Steam Oxidation of Shot Peened Austenitic Stainless Steel

By

Matthew Ian Bass

A thesis submitted to the University of Birmingham for the degree of

DOCTOR OF ENGINEERING

School of Metallurgy and Materials

The University of Birmingham

January 2017

Abstract

Shot peened steel tubing made from 304HCu-grade austenitic stainless steel was exposed to temperatures of 600-750°C in three atmospheres: vacuum, deoxygenated steam at atmospheric pressure and deoxygenated steam at 70bar.

The microstructural changes and the oxides grown on the shot peened material were observed with SEM, TEM, Vickers microhardness testing, nanohardness testing and TKD mapping. Observations were compared to thermodynamic calculations of the steel and the Cr-Mn-O systems.

It was found that the shot peened surface of 304HCu-grade steel underwent a phase transformation from an austenitic steel to a ferritic steel when exposed to temperatures of 600°C-700°C. The transformation was evident in microhardness tests, TKD and TEM observations. This phase transformation, under the conditions found in this study, is not widely discussed in the literature, but may be important to predictions of the mechanical and oxidation performance of shot peened 304HCu-grade steel components.

An estimate of the lifetime of the shot peened microstructure in service conditions was made based on microhardness. It was found that the phase transformation of shot peened material limited the predictive capabilities of this method. The shot peened microstructure was predicted to remain stable for at least 10,000hrs at 600°C and 650°C. The microstructure was predicted to be >50% recrystallized after exposure to 700°C for 10,000hrs. The microstructure was predicted to be >50% recrystallized after only 1000hrs of exposure to 750°C.

The oxides grown on shot peened 304HCu-grade steel contained $MnCr_2O_4$ spinel. A number of possible consequences of the growth of this spinel are discussed. It could not be confirmed if the growth of $MnCr_2O_4$ spinel was beneficial or detrimental to the oxidation performance of the shot peened 304HCu-grade steel used in this study. Diffusion calculations suggest that growth of the $MnCr_2O_4$ spinel is made possible by the high fraction of grain boundary material in the shot peened material, and may not be possible after the microstructure undergoes recrystallization in service conditions.

Dedicated to Trina and Chris

Acknowledgements

I would like to thank the technicians and staff of the Department of Metallurgy & Materials for their tireless efforts to keep the place running despite the best efforts of researchers, students and the architecture.

Thank you to Rengen Ding for some last minute STEM work and assistance with FIB milling.

A long-delayed thank you to Paul Brown at the University of Nottingham. Your advice and assistance during the first year of the project were helpful all the way to the very end.

Special thanks to Ian Jones for stepping in as supervisor at such a late stage.

Thank you to Brian Connolly for trusting me to finish this thesis eventually and being understanding of my leave(s) of absence.

My unending love to Trina and Chris. I would not have made it this far without you.

A big thank you to Mum & Dad for raising two really big nerds. We turned out pretty well.

Thank you to everyone who played in Oracle. You know who you are (and what you did).

Finally, I would like to acknowledge my anxiety and depression; it has been a real sonofabitch. Thank you to the Wellbeing support group, Counselling support group and the University Mental Health Student Services for helping me keep going.

Financial support for this doctorate has come from the Efficient Fossil Energy Technology centre (EFET) at the University of Nottingham, Doosan Power Systems (Renfrew) and the EPSRC.

> "Hearts starve as well as bodies,
> Give us bread, but give us roses."
> - James Oppenheim & Rose Schneiderman

Glossary of Terms and Abbreviations

α	Ferrite / Ferritic Iron
α’	Deformation Induced Martensite
γ	Austenite / Austenitic iron
Å	Angstrom. 10^{-10}m
bcc	Body Centered Cubic
BF	Bright Field
DF	Dark Field
DIM	Deformation Induced Martensite (α’)
EBSD	Electron Backscatter Diffraction
EDS	Energy Dispersive Spectroscopy
EDX	Energy Dispersive X-ray (spectroscopy)
fcc	Face Centred Cubic
GB	Grain boundary
hcp	Hexagonal Close Packed
IOZ	Internal Oxidation Zone
SAED	Selected Area Electron Diffraction
SC	Supercritical
SCS	Supercritical Steam (with low levels of O_2)
SCW	Supercritical Water (Same as SCS but with relatively high levels of O_2)
SE	Secondary Electron
SFE	Stacking Fault Energy
BSE	Back Scattered Electron
SEM	Scanning Electron Microscopy/Microscope
SS	Stainless Steel
STEM	Scanning Transmission Electron Microscopy/Microscope
TEM	Transmission Electron Microscopy/Microscope
TKD	Transmission Kikuchi Diffraction
XRD	X-ray Diffraction

Contents

1 Introduction

Stainless steels are a key material in the construction of thermal power plants such as coal, gas and nuclear power. However, new power plants are designed to work in ever higher temperature ranges and steam pressures and this is a challenge for the materials in use. For example, Tachibanawan 2 (Japan) has a steam temperature over 600°C and pressure over 26MPa [1]. This is significantly higher than in older plants, such as Drax (England) which has a steam temperature of 570°C and a pressure of 16.6MPa.

A simplified schematic of a once-through supercritical coal power plant is shown in Figure 1 with example steam temperatures and pressures shown in Table 1.

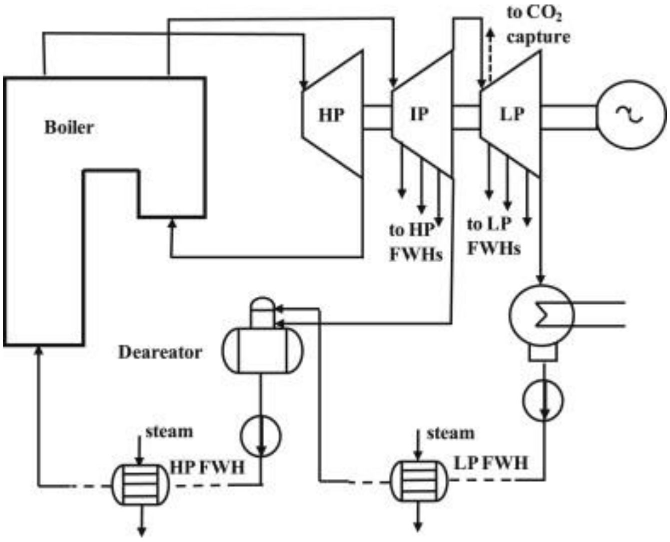

Figure 1 – Simplified diagram of water/steam flow in a theoretical ultra-supercritical (USC) coal power plant. HP: High pressure turbine, IP: Intermediate pressure turbine, LP: Low pressure turbine, FWH: Feed water heater. Taken from [2].

Steam is generated from deaerated water in the boiler and is used to drive a high-pressure turbine. The now lower-pressure steam is then re-heated in the boiler and used to drive an intermediate-pressure turbine and then a low-pressure turbine. Multiple turbines are used to covert as much energy as efficiently as possible into mechanical energy to drive electrical generators. After the steam has travelled through the turbine systems, it is condensed and re-used.

Table 1 - Steam pressures and temperatures experienced by components in a theoretical USC plant. Taken from [2].

Component	**Temperature (°C)**	**Pressure (bar)**
High pressure turbine	600	274
Intermediate pressure turbine	610	65
Low pressure turbine	269	6.5
Boiler feed water	296	290

The drive to achieve more extreme steam conditions is efficiency; an increase in steam temperature and pressure will boost the generating efficiency of a power plant[3]. Such an increase in efficiency will lower both the fuel cost and the CO_2 emissions of the plant per unit of power being produced. The reason that lowering the CO_2 emissions of power generators is important is to reduce the impact of climate change[4]. To this end governments around the world are considering implementing carbon taxes and requiring carbon capture technologies for fossil fuel burning power plants [5][6]. Electricity providers therefore face a strong economic pressure to reach higher temperatures and pressures in new plant to prepare for future regulation.

To meet the challenge of higher temperatures and pressures, new materials are being developed and tested across the world[7], for example nickel-based alloys previously used in the aero-industry and stainless steel alloys with higher chromium and nickel content. Achieving increased power plant efficiency is dependent on being able to design and produce new, cost effective materials or finding new ways to use existing materials.

This project examines the oxidation behaviour of DMV304HCu and Super304H, which are both versions of the 304HCu grade of austenitic stainless steel. 304HCu steels are already widely used in steam tubes in existing power plants. It is hoped that modifying the material's surface by shot peening will make it more resistant to oxidation in the harsh steam conditions found in thermal power plants without compromising the material's other important properties, such as creep strength and lifespan. Previous work in the literature has investigated the oxides formed on 304-grade steels in relatively oxygen-rich steam ('wet air' experiments) at atmospheric pressures. However, there are significant gaps in the literature when examining the effects of deoxygenated steam and high pressures.

The key aims of this project are to:

- Estimate the lifespan of the shot peened microstructure in the industrially important 600-700°C temperature range
- Characterize the oxides grown in deoxygenated steam on a 304-grade stainless steel alloy
- Characterize the oxides grown on the same alloys in high-pressure deoxygenated steam

Achieving these aims will provide industrially relevant information for the power generation industry. The information could be used to more reliably estimate the lifetime of shot peened materials in power plant service conditions and therefore produce electricity more cheaply and safely.

This thesis contains seven chapters and their structure is discussed below.

Chapter 2 is a literature review showing the current state of research into the questions raised by this thesis. It also serves to highlight areas of research that require further study and gaps in the literature that may, in part, be filled by this project.

Chapter 3 describes the materials and experimental techniques that were used in this research project.

Chapter 4 provides the results of experiments that investigate the lifespan of the shot peened microstructure. This includes Vickers microhardness testing and electron microscopy of the shot peened surfaces before and after exposure to elevated temperatures.

Chapter 5 includes the results of SEM, TEM and TKD observations of the oxides grown during exposure to elevated temperatures in vacuum, atmospheric pressure deoxygenated steam and higher pressure (70bar) deoxygenated steam.

Chapter 6 is a discussion of both results chapters. The observations of microstructural changes and oxide growth are used together to attempt to predict the evolution of shot peened austenitic steel components in elevated temperatures and deoxygenated steam environments.

Chapter 7 is a summary of the conclusions of this thesis and chapter 8 proposes further work that could be undertaken to refine its findings.

1.1 References

1. Bugge, J., Kjar, S., & Blum, R. (2006). High-efficiency coal-fired power plants development and perspectives. *Energy*, *31*(10–11), 1437–1445. doi:10.1016/j.energy.2005.05.025

2. Cau, G., Tola, V., & Bassano, C. (2015). Performance evaluation of high-sulphur coal-fired USC plant integrated with SNOX and CO2 capture sections. *Applied Thermal Engineering*, *74*, 136–145. doi:10.1016/j.applthermaleng.2014.03.027

3. Kaushik, S. C., Reddy, V. S., & Tyagi, S. K. (2011). Energy and exergy analyses of thermal power plants: A review. *Renewable and Sustainable Energy Reviews*, *15*(4), 1857–1872. doi:10.1016/j.rser.2010.12.007

4. Bruckner, T., Bashmakov, I. A., Mulugetta, Y., Chum, H., de la Vega Navarro, A., Edmonds, J., … Zhang, X. (2014). *Energy Systems. In: Climate Change 2014: Mitigation of Climate Change. Contribution of Working Group III to the Fifth Assessment Report of the Intergovernmental Panel on Climate Change*. New York. Retrieved from http://www.ipcc.ch/report/ar5/wg3/

5. Energy Act 2010 (c.27). (2010). London, United Kingdom: HMSO.

6. European Commission. Directive 2009/31/EC of the European Parliament and of the Council of 23 April 2009 on the geological storage of carbon dioxide and amending Council Directive 85/337/EEC, European Parliament and Council Directives 2000/60/EC, 2001/80/EC, 2004/35/EC, 2006/. , L140/114 Offical Journal of the European Union (2009). European Council. Retrieved from http://data.europa.eu/eli/dir/2009/31/oj

7. Viswanathan, R., Henry, J. F., Tanzosh, J., Stanko, G., Shingledecker, J., Vitalis, B., & Purgert, R. (2005). U.S. Program on Materials Technology for Ultra-Supercritical Coal Power Plants. *Journal of Materials Engineering and Performance*, *14*(3), 281–292. doi:10.1361/10599490524039

2 Literature Review

2.1 Austenitic Stainless Steels for use in Thermal Power Plant

2.1.1 Boiler conditions and material challenges

The latest generation of thermal power plants operate within the 'supercritical' regime. This means that the steam is a supercritical fluid and that instead of there being a liquid phase and a gas phase in the steam system at the same time, there is only a single phase present. Figure 1 is a phase diagram for water and shows its critical point. Water is supercritical if held at a pressure above P_{cr} (≈22MPa) and a temperature above T_{cr} (≈375°C).

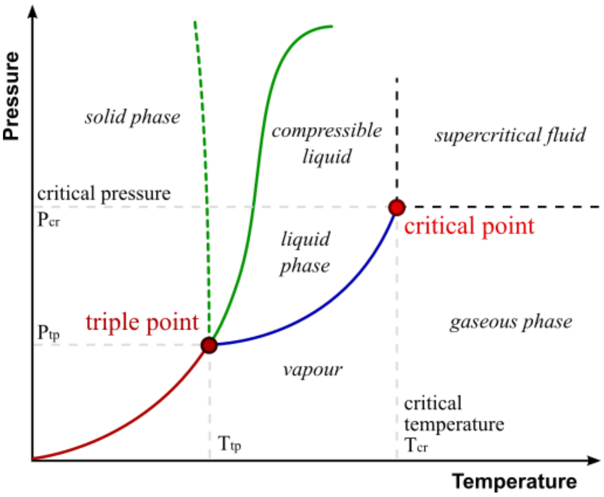

Figure 1 - Phase Diagram for Water [1]

Supercritical (SC) plants such as Tachibanawan 2 (Japan) have a steam temperature over 600°C and pressure over 26MPa [2]. This is significantly higher than in sub-critical plants, such as Drax (England) which has a steam temperature of 570°C and a pressure of 16.6MPa.

SC boilers in power plants are built to a once-through design in which the steam travels all the way through the power plant as a supercritical fluid until it is condensed at the end. The steam chemistry is carefully controlled in order to reduce corrosion in the boiler and the formation of deposits. Two of the key factors that must be controlled are the amount of oxygen present in the steam and its pH.

2.1.1.1 Oxygen Content

The EPRI (Electric Power Research Institute) is a non-profit research group that publishes industry guidelines for power plant operation and includes the major electricity utility companies in the USA as members. The EPRI recommends that oxygen content in once-through boilers be kept lower than 10ppb whenever possible and that the pH be kept between 9.2-9.6 [3]. These restrictions are needed to prevent the corrosion of plant components, and so the exact pH and oxygen contents may vary based on the materials used in a plant. Control of the pH, oxygen content and any impurities in steam are achieved by treating the feed water before it enters the boiler. There is a range of treatment methods available, including filtration systems such as condensate polishers [4] and chemicals that can be added to the feed water [5].

A significant portion of oxidation tests at elevated temperatures have historically been performed in relatively high partial pressures of oxygen due to the complexity of producing deoxygenated steam. These conditions are also referred to as 'wet air' conditions because they are not a 'pure' steam atmosphere and can contain significant amounts of N_2, CO_2 and O_2. Studies that do not specifically keep the oxygen content of the test atmosphere to a level at or below the recommended levels are listed in appendix A.1. Studies that are performed in deoxygenated steam (both sub and super critical) are listed in appendix A.2. This thesis will refer to *deoxygenated* steam as 'steam' and all other water-containing atmospheres as 'wet' (e.g. wet air, wet argon, wet hydrogen) to make a clear distinction between them.

2.1.1.2 Pressure

SC water (SCW) and SC steam (SCS) are synonymous, as both refer to water that is above the critical temperature and pressure to form a supercritical fluid. Both terms are used extensively in the literature, for example, Zhu et al. [6] use the terms SCW and SCS interchangeably, but are careful to only use 'steam' to describe steam atmospheres below the supercritical pressure. Wright & Dooley [7] only refer to SCS except for a single use of SCW, and they do not draw any distinction between the two. Guzonas & Novotny [8] only refer to SCW. A detailed study has not been performed, but it appears to the author that SCW is used in literature focused on nuclear reactors [9], waste processing and chemical engineering. SCS appears to be used almost exclusively by papers that focus on fossil-fuelled thermal power plants. This thesis will refer to SCS if conditions are supercritical *and* deoxygenated. If the oxygen content is higher than recommended power plant conditions then it will be referred to as 'SCW' to differentiate it. This is not how the terms are used in the literature, but it provides a useful nomenclature for this work.

2.1.1.3 Creep

Creep is a phenomenon experienced by metals under load and held at high temperatures, such as the conditions faced by steam pipes in power plants. Over time the metal plastically deforms and changes shape as if a stress higher than its yield point was being applied. Eventually, the metal can rupture without ever being exposed to stresses above its yield point.

The cause of this deformation can be the diffusion of metal atoms in response to stress (Nabarro-Herring and Coble creep) or the motion of dislocations in the metal crystal structure (dislocation creep) [10]. The rates of both of these mechanisms are controlled by the stress and the temperature to which a component is exposed. The higher the temperature, the higher the rate of creep and the faster a component can fail. Therefore, metals that will be exposed to high temperature loading are tested to find how much stress they can be placed under to cause them to rupture within a certain time period (usually 10,000 hours) [11].

Steel component failures in power plants are often caused at least in part by creep [12]. For example, creep can deform tubing and cause localised thinning. The thinner regions of tubing are less able to withstand high pressures and are likely to be the sites of a rupture if the problem is not addressed.

Stainless steel can exhibit higher 'creep strength', or resistance to creep, compared with martensitic and ferritic steels that are also used in power plant construction [13]. The differences between austenitic, ferritic and martensitic steels are discussed in more detail in sections 2.2.1 and 0. Each component of a power plant boiler is made from a material selected to withstand its operating conditions and to minimise cost. Austenitic steels can therefore be selected for parts exposed to higher temperatures than most ferritic and martensitic steels, though austenitic steels are usually more expensive because of higher Ni content. Figure 2 shows the temperature ranges for some important boiler components and alloys that may be selected for them.

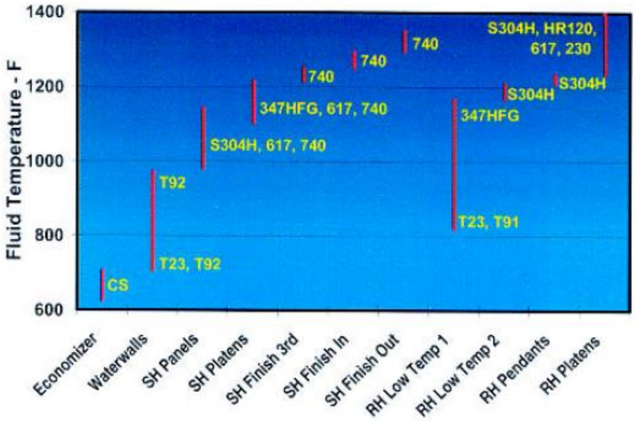

Figure 2 - Possible alloy choices for various components of a USC boiler based on the expected steam temperatures. Taken from [14].

2.1.1.4 Weldability

In order to be used in power plants any metal alloys selected must not only achieve the oxidation and creep stress requirements, but they must also be suitably weldable and fabricable [15]. Viswanathan et al. performed a study in 2005 which investigated these factors in a number of candidate metals for use in supercritical boilers [14]. It was found that the nickel-based super alloys Haynes 230 and Inconel 740 were difficult or impossible to weld using traditional techniques. However, new nickel-based alloys are being developed specifically to meet this challenge. For example, an alloy known as $FT750_{DC}$ has shown the potential for good weldability [16]. The paper does not include the same range of tests as described by Viswanathan et al. and so it is not clear if this alloy and others of its type are ready for use in full scale power plant.

2.1.1.5 Thermal Cycling

Power plants and other industrial applications include thermal cycling as a requirement for the materials used in their construction. Thermal plant is powered up and down to meet demand and is turned off completely for maintenance periods. Thermal cycling causes thermomechanical fatigue (TMF), which has its own field of study [17, 18] and will not be discussed in detail in this thesis. One of the factors that exacerbates stress in materials with oxides or multiple phases is that each of these can have a difference rate of thermal expansion. It is common for stainless steels to spall under these conditions, where cracks form in the protective oxide layer and pieces flake off, exposing new metal to atmosphere. Furthermore, spall can block pipes and damage downstream components in power plant steam systems and over time the component can become too thin to function as it loses material. Therefore, a material chosen for use in the steam systems of a power plant must be able to experience thermal cycling with an acceptable level of spallation.

2.1.2 Research Consortiums

The search for materials to meet these conditions has been going on across the globe for decades. Europe, Japan and the USA all have initiatives to find suitable alloys for use in future supercritical power plants [14, 19].

2.1.2.1 USA

A consortium of private groups and government agencies have been working in the USA under the project “Boiler Materials for Ultrasupercritical Coal Power Plants”, led by the EPRI [14]. This group is focused on identifying candidate alloys for use in high temperature steam and then developing the tools and procedures to introduce them into service and testing.

FutureGen are a group of industry partners who are attempting to design and construct a pilot integrated gasification combined cycle (IGCC) coal power plant with carbon capture and storage capability in Mattoon, Illinois.

Clean Coal Power Initiative is funded by the Department Of Energy in the USA and is designed to assign funding to projects to develop carbon capture technology. A number of new test facilities and pilot plants are being built throughout the US under this initiative.

2.1.2.2 EU

Examples of EU based research projects that are focused on the development of higher temperature thermal power plants are Thermie and a number of COST actions.

Thermie aimed to develop the technology necessary to increase the efficiency of thermal power plant and to lead the way to produce plants capable of operating at 700°C [19].

COST (European Cooperation in Science and Technology) provides organisation and funding for collaborative research in the EU. COST has actioned the development of new materials for use in power plants and continues research in other areas. For instance, COST 501 (1986-1997) developed the E911 steel, aiming to achieve steam temperatures of 620°C. COST 522 (1998-2003) continued from 501 and targeted higher pressures and temperatures [20].

COST 536 [21] seeks to develop and test new alloys for use in even higher temperature regimes and COST 538 is tasked with developing tools to test and predict the lifetimes of power plant components at higher temperatures.

The materials used in current power plants are often ferritic steels, which are mostly iron with 9-12% chromium. These materials do not have the necessary creep strength or oxidation resistance at temperatures higher than 620°C, so two other kinds of alloy are being investigated; austenitic steels and nickel-based alloys [22].

Austenitic stainless steels are alloys that contain iron, nickel and chromium and are already used in power plants today. More information will be given on these in the next section. These materials have the benefit of being more economical than Ni-alloys, as they are widely available, but they are currently limited by their creep strength and oxidation behaviour in steam above 650°C.

Above 700°C it is expected that nickel-based alloys will need to be used instead. These are much more expensive because nickel is in shorter supply than iron [23]. These alloys also require different welding techniques and can be difficult to work with.

2.2 Stainless Steel Composition & Structure

Steels describe a large range of alloys of iron that contain between 0.2-1.7% (by weight) of carbon. Above a carbon content of 1.7% the alloy is considered a cast iron [24].

1,219,715,000 tons of steel were made worldwide in the year 2009 [25], and of these 24,578,000 tons (~2%) were stainless steels [26]. Stainless steels can be used in construction in areas that are too corrosive for carbon steel or for aesthetic reasons. It is also used in medical and industrial equipment.

Stainless steels are defined as grades of steel that contain more than 10.5% chromium, with or without other alloying elements [27]. At this percentage of Cr the alloy becomes resistant to corrosion due to a layer of chromium oxide on its surface.

The composition and names of steels are defined by a number of different standards across the world. The most prevalent in the scientific literature is the American Iron and Steel Institute (AISI) system. The AISI has issued numbers for broad groups of metals that must meet standards such as composition and contamination limits. Stainless steels are given a three digit code number under the AISI system. Some metals are given longer codes including letters to designate other details of their composition. For instance, L indicates a steel that is lower in carbon than its codename may suggest. Some of these steels are listed in Table 1.

This project will be focused on investigations of the austenitic stainless steels in the 300-series, primarily steels that fall into the 304 standards. Historically, a steel is considered part of the 300 series if it is an austenitic alloy of iron, nickel and chromium[28].

Table 1-AISI composition standards for some austenitic stainless steels

AISI Steel Grade	**Composition (Weight %)***							
	C	**Mn**	**Si**	**Cr**	**Ni**	**P**	**S**	**Other**
301	0.15	2.0	1.00	16.0-18.0	6.0-8.0	0.045	0.03	
302	0.15	2.0	1.00	17.0-19.0	8.0-10.0	0.045	0.03	
302B	0.15	2.0	2.0-3.0	17.0-19.0	8.0-10.1	0.045	0.03	
304	0.08	2.0	1.00	18.0-20.0	8.0-10.5	0.045	0.03	
304H	0.04-0.10	2.0	1.00	18.0-20.1	8.0-10.5	0.045	0.03	
304L	0.03	2.0	1.00	18.0-20.2	8.0-12.0	0.045	0.03	
304LN	0.03	2.0	1.00	18.0-20.3	8.0-12.0	0.045	0.03	0.10-0.16 N
304Cu	0.08	2.0	1.00	17.0-19.0	8.0-10.0	0.045	0.03	3.0-4.0 Cu
304N	0.08	2.0	1.00	18.0-20.0	8.0-10.5	0.045	0.03	0.10-0.16 N
310	0.25	2.0	1.5	24.0-26.0	19.0-22.0	0.045	0.03	
316	0.08	2.0	1.00	16.0-18.0	10.0-14.0	0.045	0.03	2.0-3.0 Mo
347	0.08	2.0	1.00	17.0-19.0	9.0-13.0	0.045	0.03	10 x %C Nb

Sources: [29],[30],[31] * Balance: Fe

2.2.1 Ferrite and Austenite Phases

Iron is able to form different solid phases within different temperature ranges as shown in Figure 3. The two primary solid phases of iron are its ferritic and its austenitic phases.

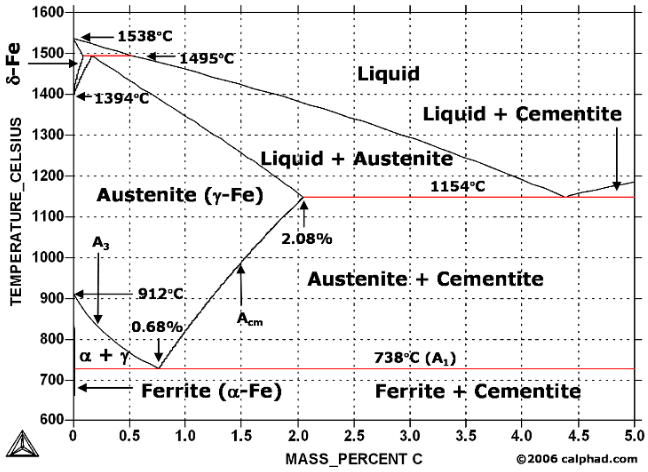

Figure 4 - Fe-C Phase Diagram[49]

The difference between each phase is its crystal structure. Ferritic iron (α), also known as ferrite, is a body centred cubic crystal (Figure 4 (a)). Austenitic iron (γ), or austenite, is a face centred cubic crystal (Figure 4 (b)). This difference in atomic arrangement gives each phase different properties, such as the ability to absorb other elements like carbon and differing permeability for elements to diffuse through the metal lattice. Table 2 shows the accepted lattice parameters for ferritic and austenitic steels. The composition of an alloy will affect its lattice parameters and this is discussed in more detail in section 2.2.3.

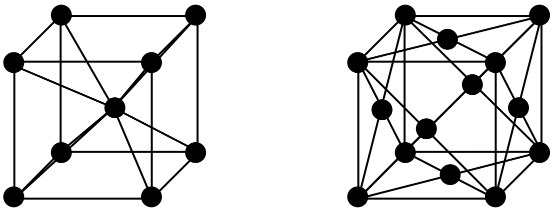

a) Body Centred Cubic (bcc)

b) Face Centred Cubic (fcc)

Figure 3 - Atomic structures of bcc and fcc unit cells

Table 3 gives values for the solubility of carbon in its austenitic (γ) and ferritic (α) structure. The carbon content of a steel affects many properties and is one of the most important elements in alloying.

Table 2 - Atomic structures and spacings of phases of iron [32]

Phase	**Structure**	**Lattice Parameter (nm)**
Ferrite (α)	bcc	0.286–0.288
Austenite (γ)	fcc	0.358–0.362

Table 3 - Solubility of Carbon in ferritic and austenitic iron [33]

Metal Phase	Temperature (°C)	Carbon Solubility (wt%)
Austenite (γ)	1150	2.04
	723	0.80
Ferrite (α)	723	0.02
	20	<0.00005

2.2.2 Martensitic Phases

A phase of iron and carbon that is not shown in Figure 3 is martensitic iron, or martensite [34]. This form of iron is a metastable phase so it is not shown on phase diagrams, which only show phases that are in thermodynamic equilibrium. A phase is called martensitic if it forms without a diffusion process.

One way in which martensite is created is when an austenitic iron containing carbon is cooled very rapidly until it becomes ferritic. Table 3 shows that ferritic iron can dissolve less carbon than austenite, so the carbon is forced out of solid solution. However, if the cooling rate is fast enough the carbon becomes trapped in interstitial sites within the metal matrix. These trapped carbon atoms change the bcc structure of ferrite to a tetragonal one, with the difference in shape dependent on the carbon content of the steel.

This is not the only kind of martensite found in iron alloys. A number of other transformation mechanisms are possible which will lead to martensitic phases with slightly different structures and morphology [35]. Some of these mechanisms are discussed in more detail in the section Deformation Induced Martensite (DIM) Transformation. These are transformations based on stress and strain in the austenitic crystal structure and they create a bcc-structured martensite instead of a tetragonal structure.

Martensitic phases of iron are metastable and can revert back to austenite or transform fully into ferrite upon an increase in temperature. The temperature at which this occurs varies with alloy composition and processing. This is discussed in more detail in the section Reversion of DIM

Martensitic steels are relatively harder and more brittle compared to ferritic and austenitic steels [33].

2.2.3 Lattice Constants in 304 Series Steel

The lattice constant of pure austenite and ferrite is known to a significant degree of accuracy. However, when alloyed with other metals the bcc and fcc crystal lattices are slightly altered by the inclusion of atoms that are larger and smaller than Fe. The change in lattice parameter caused by alloying additions can be found empirically and used to create a formula to estimate the changes given a particular alloy composition.

Dyson and Holmes [36] used XRD to find the lattice constants of 18-10 austenitic steels with different alloying additions and then calculated the change in lattice parameter that each addition caused. Further studies based on the same methodology as Dyson and Holmes found the lattice parameter coefficients for more alloying additions, such as the work of Cheng et. al. [37], Li et. al. [38] and He et. al. [39] The coefficients used in this thesis are given in Table 4.

Table 4 - Coefficients used in this study to calculate lattice parameter of Austenitic and Ferritic steel. Taken from [36] *unless otherwise noted.*

Element	Lattice Parameter Coefficient (Å/wt%) in Austenite	Lattice Parameter Coefficient (Å/wt%) in Ferrite
--	3.5780	2.8664
C	+0.0330	+0.000112974 [37]
Mn	+0.00095	+0.000542986 [38]
Ni	-0.0002	+0.00153
Cr	+0.0006	+0.000372 [39]
Cu	+0.0015	No Data Found
Nb	+0.005	No Data Found

2.2.4 Sensitization

Austenitic stainless steels suffer from a phenomenon called ‘sensitization’ if they are held in the temperature range of 600-1000°C and then cooled. The steel becomes weaker and prone to intergranular stress corrosion cracking.

Sensitization is caused by the formation of carbides at the grain boundaries of the metal. When held in the sensitizing temperature range carbides can grow, usually forming $Cr_{23}C_6$ [40]. At temperatures below the range of sensitization the formation of these carbides is not energetically favourable, and above this range the carbides can dissolve back into the metal matrix.

However, the formation of $Cr_{23}C_6$ causes depletion of the chromium from the matrix, particularly near grain boundaries, as it is incorporated within the carbide [41]. As will be discussed later, the depletion of chromium makes the steel more susceptible to corrosion. If the grain boundaries are sufficiently depleted in Cr they will not be ‘stainless’ and will be unable to form protective, compact chromia (Cr_2O_3) on exposure to sufficient concentrations of oxygen. Carbides forming in the grain boundaries and chromium depletion will allow the metal to undergo intergranular stress corrosion cracking [42], which is a known failure mechanism for critical steel components such as gas and oil pipelines [43].

The formation of σ-phase metals can also take place in these temperature regimes as shown in Figure 5. The σ-phase is made up of iron-chromium compounds such as FeCr and is very brittle at low temperatures. Steel with σ–phase present within it can have a reduced creep strength, which is a very important factor in determining the lifetime of many high temperature components [44].

One way in which carbide formation (and therefore sensitization) is reduced is to minimize the amount of carbon present in the steel. Low-carbon steel grades such as 304L and 304LN have <0.03 wt% carbon and were developed to minimize the sensitization caused by welding. The high localised temperatures and fast cooling of welding are ideal conditions to create σ-phase, carbides and thus localized Cr-depletion.

Furthermore, Parvathavarthini & Dayal found that in 316 steel the more cold worked their samples were, the more prone they were to sensitization [45]. It was also found that the samples with more cold work returned to an un-sensitized state more quickly when held at a high temperature afterwards. It is theorised that this effect is caused by the rapid diffusion of chromium and carbon through the dislocations introduced by the cold work.

Such behaviour is of interest to this study because shot peening introduces a dislocation network in the surface of a metal and if the material is exposed to sensitizing temperatures it may form carbides. These may alter the kinetics of oxidation and appear in observations of the surface layers.

2.2.5 Alloying Elements

2.2.5.1 Austenite Stabilizers and Ferrite Stabilizers

Austenitic stainless steels contain at least two other elements which have a significant effect on the steel's phase. Figure 5 is the phase diagram for Cr and Fe [46] and shows that the temperature range at which the metal is austenitic (also known as the 'gamma loop') is reduced as the proportion of Cr is increased. For this reason chromium is in a category of alloying elements known as 'Ferrite Stabilizers'. Adding more ferrite stabilizers to an alloy will increase the temperature ranges over which the metal is ferritic. The following elements are common ferritic stabilisers: chromium, silicon, aluminium, titanium, tantalum and niobium [47]. When calculating the phase of a steel alloy that includes these elements they are often given 'Chromium equivalents'. For small alloying additions it is therefore possible to use only a ternary Fe/Ni/Cr phase diagram (Figure 8) to predict the metal's phase at different temperatures and compositions [48].

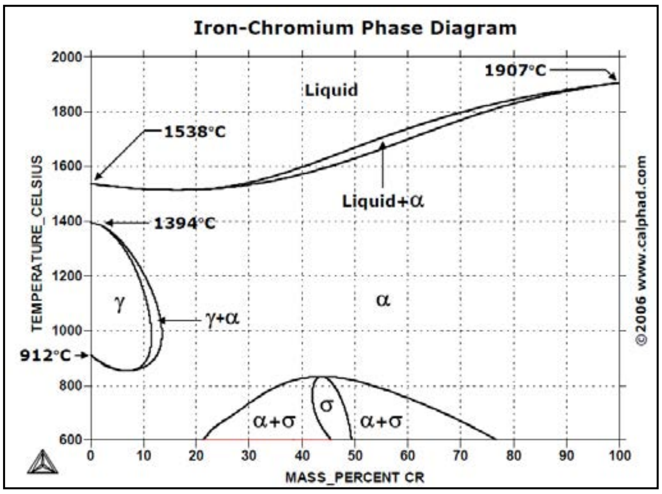

Figure 5 - Iron-Chromium Phase Diagram[49]

Figure 6 is the phase diagram for Ni and Fe [49] and shows that adding Ni to an alloy will increase the temperature range over which the metal is in the austenitic phase. Nickel is therefore an 'Austenite Stabilizer', and part of a group of materials analogous to ferrite stabilizers. The following elements are common austenite stabilizers: nickel, carbon, manganese, nitrogen and copper. Just as ferrite stabilizers are given 'chromium equivalent' values, austenite stabilizers are given as 'nickel equivalent' values.

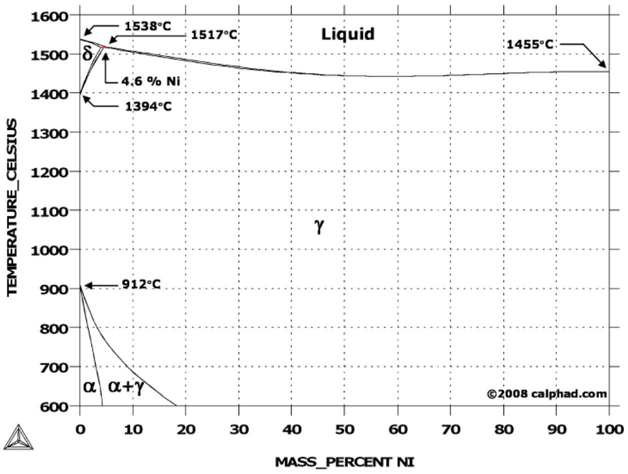

Figure 6 - Iron-Nickel Phase Diagram [30]

These 'equivalent' relationships are empirical and have been found not to be reliable if the alloy is changed significantly, such as by changing the proportion of Mn or N by more than a few percent [50], or under processing conditions that are not casting, such as welding [48]. For commercial and engineering applications it is important to take these factors into account by using a Schaeffler or Delong diagram that reflects the correct composition and processing steps, such as Figure 7, which is for welded stainless steel with low Mn and N contents. The Schaeffler diagram in Figure 7 is divided into regions of austenite (A), martensite (M) and ferrite (F), and mixtures of the three. An alloy's composition can be marked on the diagram to identify the possible phases of steel that will be formed upon welding. For example, according to Figure 7, 18-8 stainless steel can form a mixture of A+M+F when it is welded. If a change in phase is undesirable during welding then special precautions would need to be taken, such as additional heat treatments.

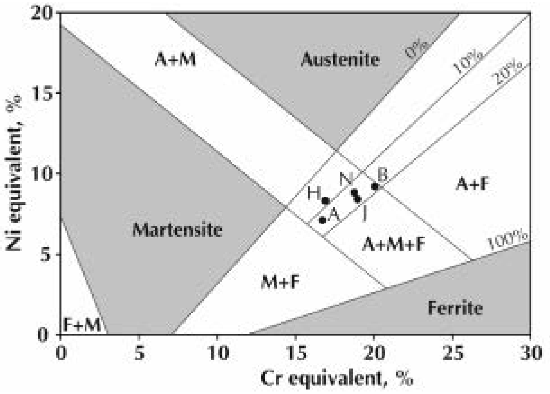

Figure 7 - Schaeffler Diagram for welded stainless steel [51]

Figure 8, is an iron/nickel/chromium phase diagram at 900°C and has the 18-8 (304) stainless steel composition noted on it. In this composition range the steel is fully austenitic at 900°C, but this may not be true at lower temperatures. Some 300-series alloys can be austenitic even at cryogenic temperatures [52]. If the steel must remain fully austenitic during its service then care must be taken not to go below the stable austenite temperature. Below this temperature it is possible that ferrite and martensite can form in the material, though the rate of transformation is temperature dependant and can be so slow that a metal remains almost entirely austenitic for many years.

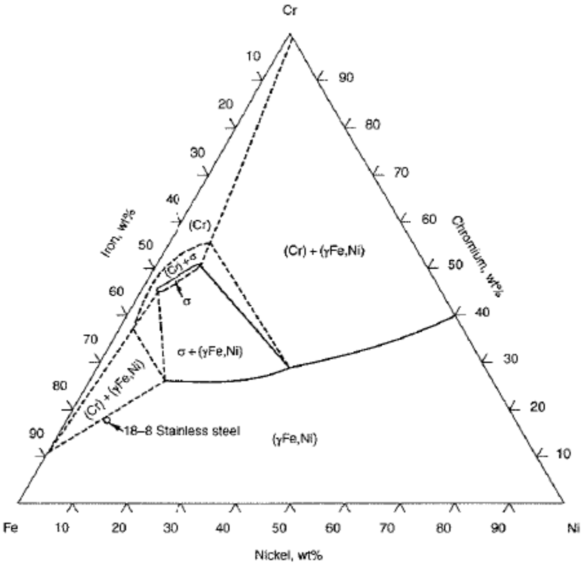

Figure 8 - Iron, nickel and chromium ternary phase diagram at 900°C [30]

2.2.5.2 Carbon

The most important alloying element in steel is carbon. As the carbon content of a steel is increased not only are the stable temperature ranges of the ferrite and austenite phases altered, but new phases and compounds appear, such as cementite (Fe_3C) and pearlite (alternating layers of cementite and ferrite). These are thermodynamically stable phases which are formed by diffusion processes, unlike the previously described martensitic transformations.

The 304 series of alloys contain 0.03-0.1 wt% of carbon. The carbon will either remain in solid solution in the austenitic steel or diffuse to grain boundaries and form carbides with metals such as Cr and Nb, depending on the alloy composition and temperature. Carbides can be desirable in some microstructures, but they can also weaken a stainless steel through sensitization, which was described earlier in section 2.2.4.

2.2.5.3 Carbides

At elevated temperatures found during annealing and in high temperature service carbon can form a variety of compounds with the metals in a steel alloy. Table 5 shows the types of carbide one can expect to precipitate in stainless steels and the elements which may form them [53, 54]. Carbides precipitate in the grain boundaries of a metal, which can 'pin' the grain boundaries to reduce recrystallization and prevent the movement of dislocations between grains, reducing creep.

Table 5 - Carbide Precipitates in Austenitic Stainless Steels

Carbide Composition	**Carbide Forming Elements**
MC	Ti, V, Cr, Zr, Nb, Mo, Hf, Ta, W
$M_{23}C_6$	Cr, Ni, Mo, Fe
M_6C	Mo, Nb, Fe, Cr, Ni, Ti, Co

2.2.5.4 Nitrogen

Nitrogen stabilizes the austenitic phase of iron and can increase the strength of a stainless steel. The strength of steel can be enhanced because nitrogen forms an interstitial solution and behaves in a similar way to carbon in locking in dislocations.

Nitrogen can also form nitrides with other elements, which can precipitate from the metal matrix. These can act as precipitate hardeners.

2.2.5.5 Nitrides

Nitrides are compounds of the base metal and nitrogen and behave much like MC-type carbides. This includes precipitating in the grain boundaries of a metal. Table 6 shows the nitrides that may form in steels. Nitrides are unlikely to be found in 300 series steels unless they have an increased nitrogen content, such as 304N and 304LN. Nitrides are often more stable than an analogous carbide at high temperatures, so nitride-forming alloys may be used when creep-resistance at high temperature is important.

Table 6 - Nitride Precipitates in Austenitic Stainless Steels

Nitride Composition	Nitride Forming Elements
MN	Ti, V, Cr, Zr, Nb, Mo, Hf, Ta, W

2.2.5.6 Nickel

As well as stabilizing the austenitic phase of steel, nickel also increases its ductility and impact strength [31]. Nickel forms a substitutional solid solution in steel. Alloys with a larger proportion of Ni will have superior corrosion resistance and higher melting points, so they are used in more demanding roles such as power plant turbine blades

2.2.5.7 Chromium

Chromium is the most important element in stainless steel for reducing corrosion because it oxidizes to form a layer of chromium-oxide (Cr_2O_3), or chromia on the surface. This passive layer protects the metal underneath from further oxidation.

As the proportion of chromium in a stainless steel is increased it will offer more protection from oxidation. This has been shown by many studies, including the work of Quaddakers et al. in a number of oxidation tests in different atmospheres [55–59]. However, increasing the amount of chromium causes the steel to become ferritic, so more nickel or manganese is needed to offset this effect to retain an austenitic structure.

Chromium also forms a phase with iron and other metals called the σ (sigma) phase. This is a combination of iron, chromium and sometimes molybdenum if it is present in the steel. The sigma phase is also discussed in more detail in section 2.2.4.

2.2.5.8 Aluminium

Aluminium can form an oxide layer on the surface of a steel in a similar way to chromium, but it is reported to be more stable at higher temperatures. Adding 2-5% Al to a stainless steel allows the formation of both aluminium and chromium oxides and changes not only the oxidation behaviour but the way in which other minor alloying additions behave. For example, Brady et al.[60] found that adding niobium and vanadium prevented oxide layers from forming in Al-containing stainless steels.

The Al-containing steels are a more recent development and can be considered a distinct group compared to traditional 300 series steels. Therefore, this review will not explore the effects of aluminium in more depth.

2.2.5.9 Molybdenum

Molybdenum forms a substitutional solid solution with stainless steel and causes it to harden. It is not thought to affect the oxidation of stainless steels to a great extent. However, different studies into its effects on 9-12%Cr ferritic steel have produced conflicting accounts, with some indicating that additional Mo provides a small improvement in oxidation resistance and others showing a minor reduction [7].

2.2.5.10 Manganese

Manganese acts as an austenite stabilizer and is used instead of nickel in the 200-grade steels for economic reasons. Adding Mn to a steel can also increase its solubility for nitrogen. However, Mn does not improve the corrosion and oxidation resistance as much as adding Ni does.

Mn is relatively mobile in austenitic steel and it has been found in many studies to be present in the surface and grain boundaries of steel in higher concentrations than in the bulk. It may also reduce the volatilization of chromium from the metal surface in wet atmospheres [7].

2.2.5.11 Silicon

Silicon is included in steels in small quantities (<0.1%) to take up oxygen during steel making, but is generally kept to very low levels to avoid changing the steel's mechanical properties. However, if the silicon content of a stainless steel is increased to 2-4% it has been found that there is an increase in its resistance to corrosion. Huntz et al. claim that this effect is caused by silicon segregating to the metal surface and forming a very thin layer of SiO_2. This layer prevents corrosion and oxidation by itself, but its primary function is to promote the growth of a chromia layer and slow the formation of iron oxides. Huntz et al. performed this experiment with ferritic 9%Cr steel and not austenitic steels, but this is in line with other literature on the subject of minor additions to stainless steels, as can be found in a review by Lepingle et al. [61].

The effect of silicon on the oxidation of austenitic stainless steels is less well understood and it has been highlighted as a target for future research in reviews of the literature.

2.2.6 Precipitates in Austenitic Stainless Steels

Temperature is a key factor for determining which alloying elements have the chance to dissolve in to or precipitate out of a solid solution. Common precipitates in steel include carbides and nitrides, the formation of which is controlled by adding or removing carbon, nitrogen and elements that more readily form carbon/nitrogen compounds. Precipitation can have both detrimental and beneficial effects on the steel microstructure, such as sensitization in some stainless steels or dispersion strengthening. Table 7 shows a summary of precipitates from a review by T. Sourmail [53]. Table 8 shows a similar summary table from a much more general review of steels by Lo, Shek & Lai [32] in 2009.

Table 7 - Precipitates and Phases of Stainless Steels (T. Sourmail) [53]

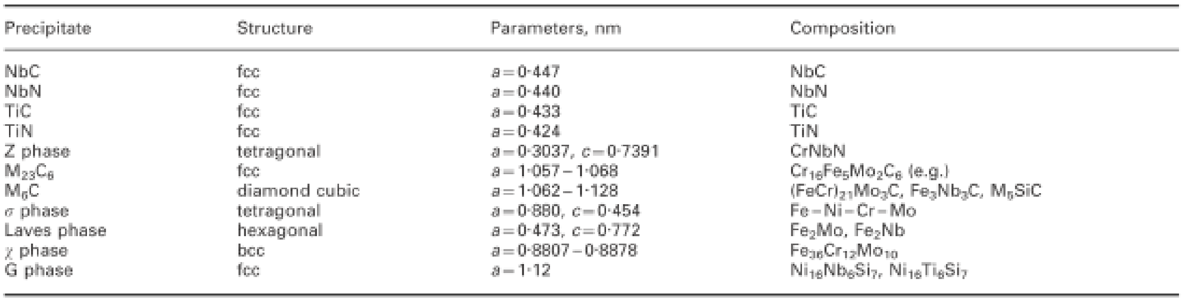

Precipitate	Structure	Parameters, nm	Composition
NbC	fcc	$a=0\cdot447$	NbC
NbN	fcc	$a=0\cdot440$	NbN
TiC	fcc	$a=0\cdot433$	TiC
TiN	fcc	$a=0\cdot424$	TiN
Z phase	tetragonal	$a=0\cdot3037$, $c=0\cdot7391$	CrNbN
$M_{23}C_6$	fcc	$a=1\cdot057-1\cdot068$	$Cr_{16}Fe_5Mo_2C_6$ (e.g.)
M_6C	diamond cubic	$a=1\cdot062-1\cdot128$	$(FeCr)_{21}Mo_3C$, Fe_3Nb_3C, M_5SiC
σ phase	tetragonal	$a=0\cdot880$, $c=0\cdot454$	Fe–Ni–Cr–Mo
Laves phase	hexagonal	$a=0\cdot473$, $c=0\cdot772$	Fe_2Mo, Fe_2Nb
χ phase	bcc	$a=0\cdot8807-0\cdot8878$	$Fe_{36}Cr_{12}Mo_{10}$
G phase	fcc	$a=1\cdot12$	$Ni_{16}Nb_6Si_7$, $Ni_{16}Ti_6Si_7$

Table 8- Precipitates and Phases of Stainless Steels (Lo, Shek & Lai) [32]

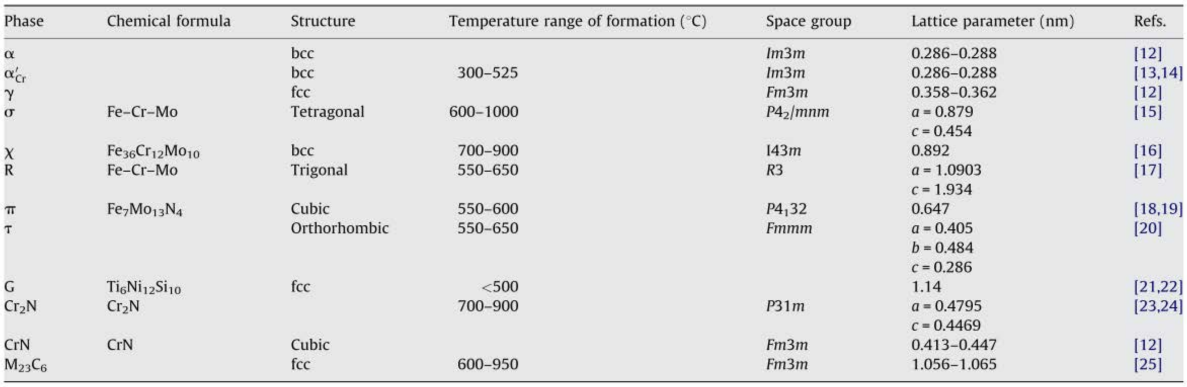

Phase	Chemical formula	Structure	Temperature range of formation (°C)	Space group	Lattice parameter (nm)	Refs.
α		bcc		$Im3m$	0.286–0.288	[12]
α'_{Cr}		bcc	300–525	$Im3m$	0.286–0.288	[13,14]
γ		fcc		$Fm3m$	0.358–0.362	[12]
σ	Fe–Cr–Mo	Tetragonal	600–1000	$P4_2/mnm$	$a=0.879$ $c=0.454$	[15]
χ	$Fe_{36}Cr_{12}Mo_{10}$	bcc	700–900	$I43m$	0.892	[16]
R	Fe–Cr–Mo	Trigonal	550–650	$R3$	$a=1.0903$ $c=1.934$	[17]
π	$Fe_7Mo_{13}N_4$	Cubic	550–600	$P4_132$	0.647	[18,19]
τ		Orthorhombic	550–650	$Fmmm$	$a=0.405$ $b=0.484$ $c=0.286$	[20]
G	$Ti_6Ni_{12}Si_{10}$	fcc	<500		1.14	[21,22]
Cr_2N	Cr_2N		700–900	$P31m$	$a=0.4795$ $c=0.4469$	[23,24]
CrN	CrN	Cubic		$Fm3m$	0.413–0.447	[12]
$M_{23}C_6$		fcc	600–950	$Fm3m$	1.056–1.065	[25]

The different precipitates listed are only some of the possible compounds and phases that form in stainless steels. The exact precipitates found in a given sample will change significantly based on its alloy composition and processing history. A paper by Ha & Jung [62] examines an austenitic steel with some of the same alloying elements (15% Cr-15% Ni-4%Mn-0.5%Si-0.4%Nb-3%Cu-1.5%Mo-0.26%N) as the 304-based steel examined in this thesis. Ha & Jung's alloy formed a combination of nitrides, carbides, copper, χ-phase and carbonitrides with each precipitate affecting the material properties in different ways.

2.2.6.1 Precipitation Strengthening

Also known as precipitation hardening. Precipitates can form in the metal matrix (inside the grains) and prevent the movement of dislocations along any slip planes they intercept. The movement of dislocations is how metals undergo plastic deformation, so reducing their mobility increases the ability of the metal to resist deformation [63]. Some alloying elements, such as carbon, strengthen the metal more effectively by remaining in the solid solution as interstitial atoms. However, at lower temperatures the alloy may not be able to dissolve enough of such elements to maintain its strength and at elevated temperatures such interstitials can become mobile enough to become ineffective. Precipitate compounds such as carbides, however, can remain stable at low and high temperatures, including temperatures above the melting point of the steel.

2.2.6.2 Carbides, Nitrides and Carbonitrides

Carbides, nitrides and carbonitrides can form in alloys with sufficient carbon and/or nitrogen available. In stainless steels iron based carbides and nitrides do not form because other elements will preferentially react to form compounds instead, such as chromium, and carbon/nitrogen concentrations are kept relatively low. However, chromium carbides and nitrides are not desirable in many stainless steels because they deplete the available chromium in the alloy, which reduces its ability to resist corrosion. Elements such as Nb and Ti are added to alloys to form carbides and nitrides instead of Cr. For example, the alloys studied in this thesis contain ~0.4% Nb and 347 grade steels contain 10x as much Nb (wt%) as C (see Table 1).

Figure 9 shows that some carbides and nitrides form in grain boundaries while others are present inside the grains. Carbides and/or nitrides forming can increase the alloy’s strength, but can also lead to enhanced corrosion and embrittlement in some situations, such as by causing sensitization (see section 2.2.4).

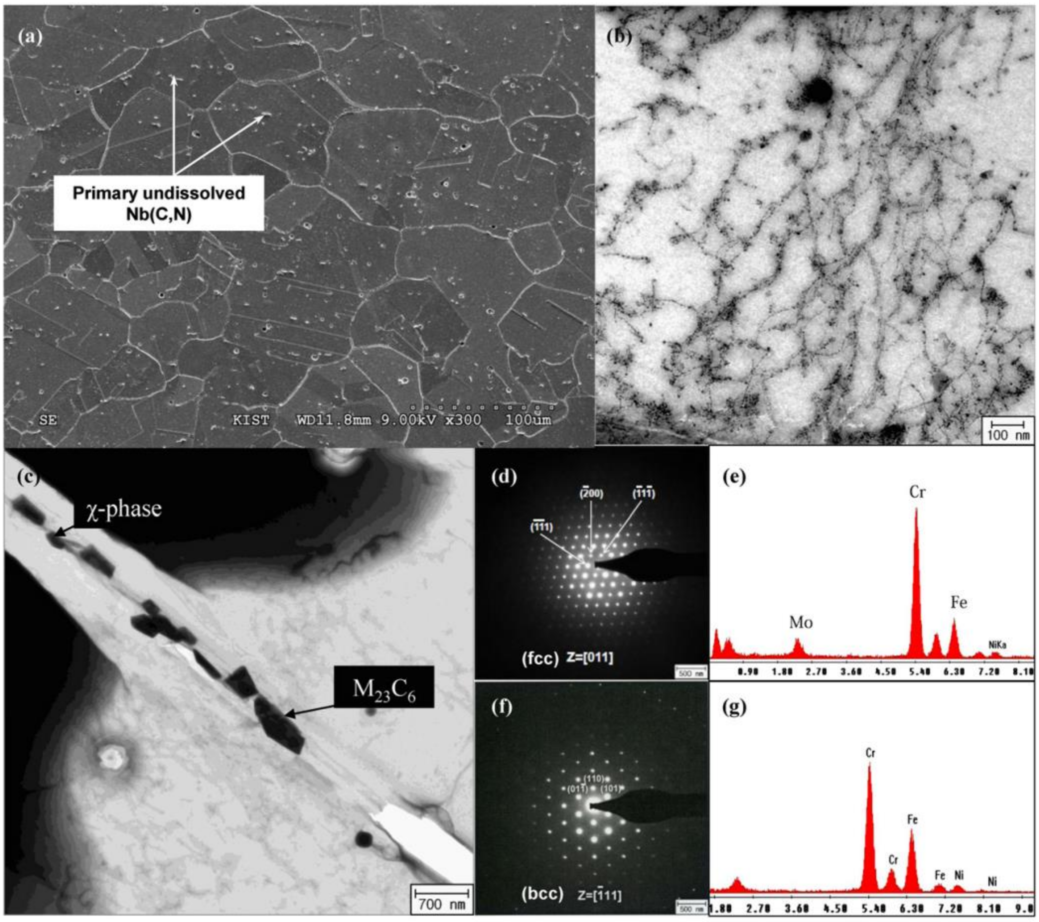

Figure 9 - Carbides and nitrides in a stainless steel [62]

2.2.6.3 Copper

304Cu-grade steels and their derivatives, such as the Super304H and DMV304HCu steels investigated in this thesis, have improved creep resistance at elevated temperatures compared to other austenitic stainless steels. The addition of 2-4% copper improves creep strength by forming a fine dispersion of Cu particles within the austenite matrix when held at elevated temperatures [64]. Cu has the same crystal structure and almost the same lattice parameters as γ, so the Cu precipitates and the Cu interstitial atoms do not cause a significant deformation of the metal matrix. The high coherence between precipitates and matrix allows the Cu precipitates to grow very slowly and remain stable at elevated temperatures, without causing the depletion of important elements such as Cr [65].

Gonzalez et. al. [66] found that copper had a significant effect on the martensitic transformation of 304 steel when cold worked. The Cu stabilized the austenite phase during cold work so it was more difficult to transform austenite into DIM.

Figure 10 shows that the increase in strength is from the copper precipitates formed during high temperature service and not simply from the presence of Cu in a substitutional solution. The improvement in yield stress becomes smaller at temperatures >300°C.

Figure 11 shows how the Cu precipitates in Super304H grow over time at 650°C. The precipitates remain <40nm in diameter for over 10,000 hours, making Cu-enriched alloys potential choices for supercritical power plant materials because of the slow rate of change in the material properties over long time scales.

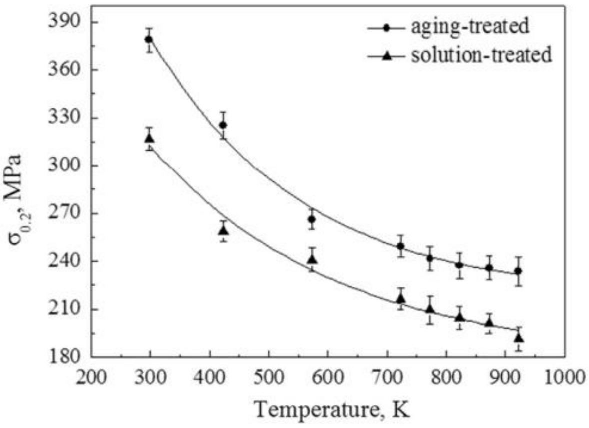

Figure 10 - Tensile yield stress of Super304H showing Cu precipitates formed during aging increase the yield stress[67]

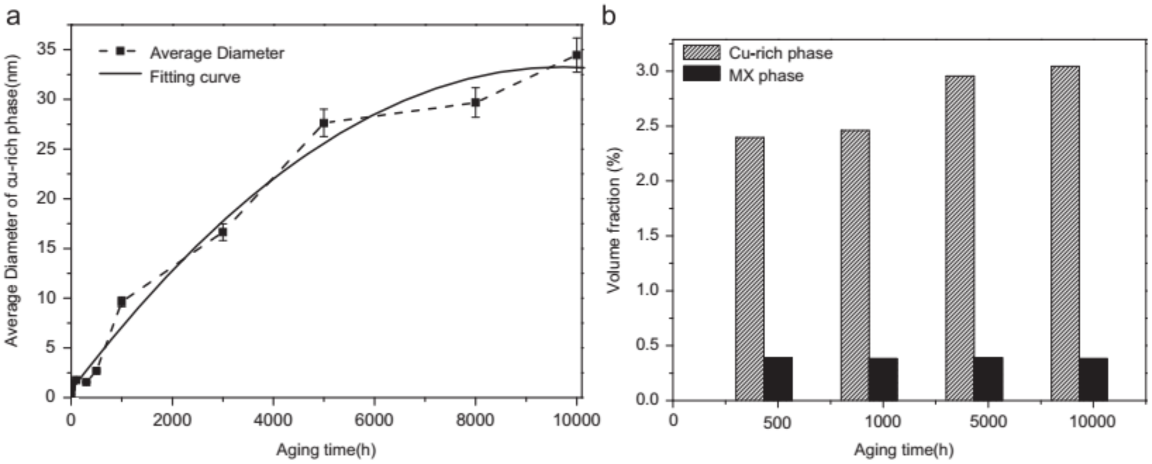

Figure 11 - Cu precipitate growth in Super304H at 650°C[68]

2.3 Shot Peening

Shot Peening is a method of surface treatment that has been around since the early 20th century. It is used to work harden a surface and to increase the fatigue life of metallic components such as gas turbine blades [69]. The technique involves bombarding an object with a large number of small projectiles to deform the surface [70].

Projectiles that are fired at a surface to shot peen it are called 'shot' and come in many varieties. The correct shot must be chosen based on the material being shot peened. Common varieties of shot include cast steel balls, cut steel wire, glass and ceramic beads. If the shot is too soft it will deform instead of the surface, but if the shot is too hard it will shatter on impact. Shot is normally re-used, so shattering significant amounts of shot will make the process more costly and may allow small, sharp fragments to be fired at the surface, causing chips or embedding the shot in the surface.

The shot is fired out of a nozzle at the target surface, powered either by a stream of compressed air or by a wheel that throws the shot outwards by centrifugal force.

2.3.1 Effects on Microstructure

The microstructure of a shot peened component can be significantly altered at the surface while the bulk of the object remains unaffected. This makes shot peening an attractive treatment for materials which suffer from cracking or corrosion on their surface. The effects of shot peening generally extend down <1mm [71], with the microstructure changing gradually over this distance.

One of the most cited reviews on shot peened microstructure is by Vöhringer [72], which provides the data shown in Table 9. Table 9 shows the variables that Vöhringer identified as the properties discussed in the literature relating to the shot peened surface state.

Table 9 - Methods and properties used to characterize the shot peened surface state. Taken from [72]

Property	Shorthand/Unit
Microhardness	HV
Residual Stress	σ^{rs}
Half width value	HW
Root-mean-squared strain	$<\varepsilon^2>^{1/2}$
Particle Size	L
Dislocation density	P_t
Almen intensity	i
Texture pole figures and lattice deformation pole figures	
Surface roughness	R
Plastic strain	ε_p
Phase fraction	f
Fraction of deformation twins	f_T
Surface yield point	$R^S{}_E$
Temperature	T

2.3.1.1 Microhardness

Microhardness profiles of shot peened materials are used extensively in the literature to identify regions of material affected by shot peening and to compare shot peened materials to one another. Compared to techniques such as microscopy and TEM, microhardness is a relatively easy characteristic to find and record.

The hardness of a metal is related to its grain size and follows the Hall-Petch relationship (see section 2.4.2). Therefore, as the grain size of a sample is reduced by shot peening, its hardness should show a corresponding increase. This relationship is well documented in the literature [73] and produces a hardness profile with the same form as the residual stress profile [74]. Work by Abbate et. al. [75, 76] showed that residual stress can also contribute to measurements of hardness made by micro-indentation. For a residual stress range of -8kbar to 4kbar (-800MPa to 400MPa) the measured hardness of machined steel tubes varied from 43 to 39 Rockwell hardness as shown in Figure 12. A residual stress of -800MPa is the same order of magnitude of stress that would be expected at the surface of a shot peened material, so the effect of residual stress on the measured hardness of shot peened metal can be assumed to be <10% in this study.

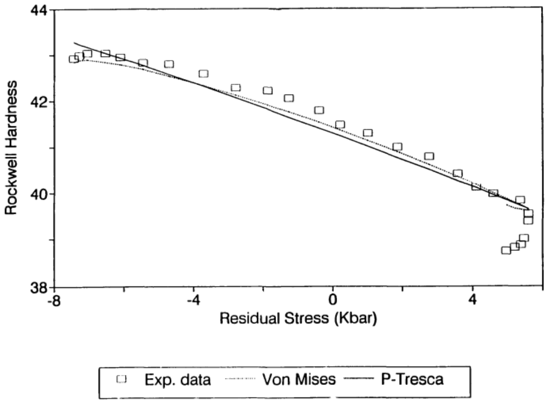

Figure 12 - Plot of Rockwell C hardness as a function of residual stress in autofretted steel tubes. Taken from [75].

More detail about hardness testing and its analysis is provided in section 2.4.

2.3.1.2 Strain and Residual Stresses

Research on shot peened steels primarily focuses on the strain and compressive stress field generated by shot peening. As the surface is shot peened it is put under compressive stress and will deform. The stresses experienced by the shot peened target can be separated into two components: Hertzian pressure and plastic stretching [77].

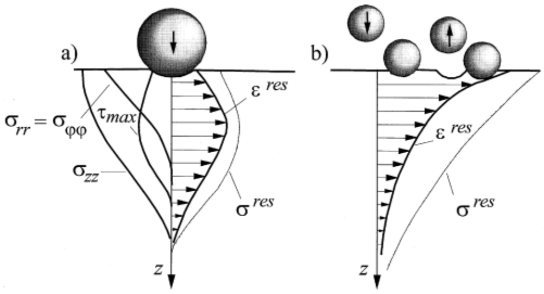

Figure 13 - Stress profiles generated by two key mechanisms during shot peening: a) Hertzian pressure and b) plastic stretching. z axis shows distance beneath shot peened surface. Horizontal axis shows relative amounts of overall residual stress (σ^{res}), strain (ε^{res}) and shear stress (τ). Taken from [77].

The compressive stress generated by plastic stretching (Figure 13 (b)) is the result of the material surface being plastically deformed relative to the sub-surface material. An impacting shot creates a 'crater' or 'dimple' on the surface and this is effectively pushing the surface material away from the impact point, or stretching it. The material further beneath and around the impact point is not stretched, so a compressive stress is created between them. The less deformed material is pushing back against the more deformed material at the surface because the less deformed material is being held in place by the rest of the workpiece. During shot peening, enough impact sites will be made so that they overlap with each other and create a layer of residual compressive stress beneath the surface across the entire shot peened area. The maximum compressive stress generated by plastic deformation will therefore be at the surface of the material, where the most deformation has occurred [72]. This is in contrast to residual stress created by Hertzian pressure.

Hertzian pressure is the stress experienced by a material due to a compressive force normal to the surface, for example, when a sphere is pressed downwards into a surface. The stress and strain that are created by Hertzian pressure has a maximum beneath the surface, as shown in Figure 13 (a). Both Hertzian pressure and plastic stretching occur during shot peening and the two effects are superimposed on each other in the residual stress profile. Plastic stretching is dominant in harder materials, such as steel, and Hertzian pressure is dominant in softer materials [72]. The general form of the residual stress within a shot peened material, with respect to distance beneath the peened surface, is given in Figure 14.

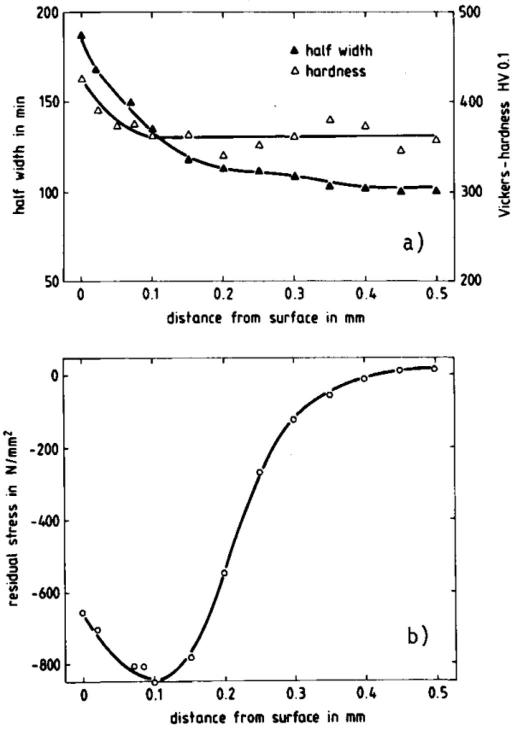

Figure 14 - Distributions of a) half-width values and Vickers hardness (HV0.1) and b) residual stresses of shot peened TiAl6V4 in an as-peened condition. Taken from [72]*.*

The compressive residual stress in shot peened components is widely acknowledged to be the key characteristic that can improve their fatigue life [73]. Therefore, understanding the residual stress profile in a shot peened component has direct application in predicting their fatigue life under high temperature conditions, because shot peened materials can 'relax' or partially return to their original state over time, especially at elevated temperatures. The stability of residual stress under thermomechanical loading has been reviewed by McClung[78] in 2006 and Soady[79] in 2013.

The strain field in a sample can be observed using XRD line broadening and diffraction techniques in a TEM [80], but these methods are not used in this thesis and they will not be described in detail.

There are models available that allow the strain field to be predicted given the material and shot parameters. For example, Hills, Waterhouse and Noble found that the residual stress field caused by shot peening was proportional to the velocity of the shot and the hardness of the impacted metal [81]. Other factors that affect the residual stress profile in shot peened metals include the angle of impact of the shot, the material and hardness of the shot and the shape of the shot [71].

2.3.1.3 Particle Size

The mechanical distortion of a surface by shot peening can give rise to a nano-crystalline surface. Metals such as austenitic stainless steels ordinarily have surface grains several micrometres in size after being cast, but after shot peening the surface can be broken up into ‘grains’ only 10nm in size [74]. However, the high strain and number of dislocations caused by shot peening make it inappropriate to think of these ‘grains’ as one would in an annealed material. The extensive cold work will introduce subgrains, dislocations and ‘cell’ structures that are discussed in more detail in the section Recrystallization of Austenitic Steels. A grain can be defined as having a certain orientation mismatch with its nearest neighbours (e.g. >15°), but with so many subgrains etc. present in the surface, it is not clear which structures can meet any such definition. This thesis will continue to use the term ‘grain size’.

It is common in the literature to find the grain size investigated by both TEM and from calculations based on XRD peak broadening [74, 82–84]. However, the grain size varies with depth so surface sensitive techniques such as XRD cannot reveal the grain size profile without additional sample processing. For example, Chu et al. [85] and Krull, Nitschke-Pagel & Wohlfahrt [86] incrementally electropolished their peened samples so that they could take XRD measurements at a range of depths. Furthermore, it was found by Tao et al. [82] that because XRD observes the top several micrometres of the sample surface it can over-estimate the average grain size at the surface. XRD produced an average grain diameter of 12nm, but TEM observations suggested that the true value was closer to 7nm.

Hassani-Gangaraj et. al. [87] prepared TEM samples from shot peened AISI 4340 by mechanical polishing of cross sections taken from different distances from the peened surface. The dislocation cell size (analogous to grain size in this study) was observed by TEM or SEM and seen to vary as shown in Figure 15. The grain size at the sample surface was found to be >100nm in size, which is at least an order of magnitude larger than in the other studies cited in this thesis. This discrepancy may be caused by a difference in behaviour of austenitic stainless steels (e.g. 304, 347 grade steels) and the AISI 4340 grade steel used by Hassani-Gangaraj et. al. However, the general trend in the data from Figure 15 may still be applicable to austenitic steels.

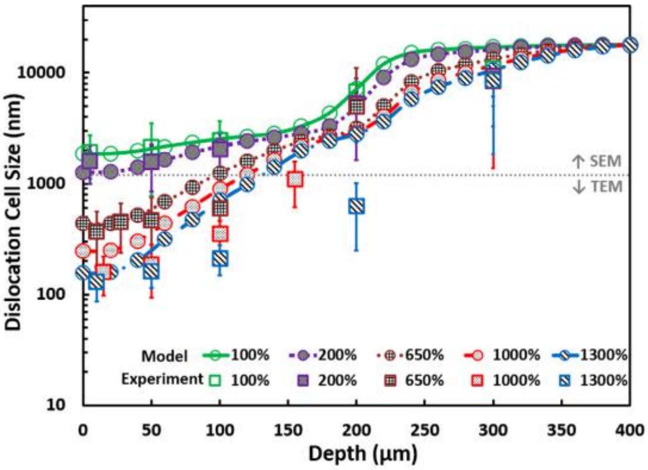

Figure 15 – Observed and modelled dislocation cell size (analogous to grain size) of AISI 4340 shot peened with different coverages (100-1300%). Taken from [87].

Table 10 shows the grain sizes found in a number of peening and surface deformation studies. Mordyuk et al. [84] also provide a summary of their own and a small collection of others' data on the grain sizes created by surface mechanical attrition treatment (SMAT), shot peening (SP), laser shot peening (LSP) and deep rolling.

The effect of grain size refinement on mechanical and chemical behaviour is being investigated due to the need for improved steel performance in chemical and power plants. For more examples, see the reviews by Fard & Guagliano [73] and Montross et al [88].

Table 10 - Grain sizes found at the surface of peened and sputtered metals

Study	**Metal**	**Treatment**	**Average Surface Grain Size (nm)**
H. Yu et al.[74]	304	USSP, ABSP	20 to 25
T. Wang, J. Yu, and B. Dong[89]	1Cr18Ni9Ti steel	SP	18
X. Peng et al. [90]	304	Sputtering	5 to 15
G. Liu, J. Lu, and K. Lu[91]	316L	USSP	15 to 20
H. Zhang et al.[83]	304	SMAT	8 to 60
N. Tao[82]	Iron	SMAT	7
X. Wang and D. Li[92]	304	Sand Blasting	20

SP = Shot Peened, USSP = Ultrasonic Shot Peened, ABSP = Air Blast Shot Peened, SMAT = Surface Mechanical Attrition Treatment

2.3.1.4 Dislocation Density

The deformation of the surface layer causes dislocations to form. The movement and formation of dislocations is central to the effects of shot peening on the mechanical behaviour of the metal, such as hardening. The density of dislocations is also important to oxidation studies. Dislocations behave as a short circuit path for atoms such as chromium to diffuse through, and therefore alter the oxidation behaviour. This is discussed in more detail in the Diffusion section.

The structure and density of dislocations are studied using TEM [85, 88, 91, 93]. However, very few papers give any quantitative values for dislocation densities.

Chu et al. provide both measured and calculated values for the dislocation densities of a low carbon steel [85]. The calculation used is an empirical one based on the measured hardness of the metal. This equation was created for use with pure iron, but was found by Chu et al. to produce results within experimental error when used with a low carbon steel. However, it is not made clear if this technique could also be used in a stainless steel, which has a higher proportion of alloyed components and an austenitic structure.

Yu et al. provide quantitative values for dislocation density in their samples of 304 steel [74] after being air-blast shot peened and ultrasonically shot peened. The values are calculated from XRD peak broadening, based on average grain size and microstrain. The calculated values were found to correspond well to TEM observations of the dislocation densities. Both of these papers indicate that a way of calculating dislocation density from hardness data or XRD peaks is possible, but the reliability of such data for stainless steels is not certain. This offers a more effective method of finding an average dislocation density than observing dislocations using a TEM, due to the larger area sampled by XRD.

2.3.1.5 Almen Intensity

Industry categorizes shot peening processes using Almen Intensity [94]. A standardized metal strip is peened in parallel to a work piece and begins to curve because of the plastic deformation of its surface. The arc-height of the curved strip is measured and the Almen intensity is calculated using this value and previously generated calibration curves. Despite the widespread use of Almen intensity in industry the intensity does not allow for the calculation of residual stresses in a shot peened sample. Guagliano [95] performed finite element calculations in order to relate the almen intensity to the residual stress created within the shot peened object. This built on previous modelling work by other groups such as Hills, Waterhouse and Noble [81].

If the Almen intensity is too high then a shot peened component can be damaged by micro-cracking [96]. If the shot impacts with too much force then in addition to the 'crater' there may also be micro-cracks beneath the impact site, as shown in Figure 16. The likelihood of micro-cracking increases with higher shot velocities and harder, more brittle target materials.

Figure 16 - Formation of micro-cracks on a shot peened surface. Taken from [96].

The formation and growth of micro-cracks reduce the fatigue performance of a component, so care must be taken when shot peening to avoid their creation [97].

2.3.1.6 Surface Roughness

Shot peening has other effects on the microstructure of surfaces. One of the most visible effects is that shot peening increases the surface roughness of a sample. This can be measured by a roughness profile and the most common values are roughness average, R_a, and the maximum peak-to-valley variation R_{max}/R_t [88]. There is a possibility that this leads to an increase in corrosion and oxidation rates in some metals and environments [98] caused by the increased surface area and possibly the nanocrystalization of the surface.

Furthermore, the roughness profile of a shot peened surface can be misleading if only the R_a and R_{max} values are considered. Figure 17 shows how surface roughness values can ignore key aspects of the profile of a shot peened surface. In the hypothetical case of Figure 17, it would be expected that surface B would be more resistant to fatigue because the rounded 'valleys' of the roughness profile do not concentrate stress to the same degree as the sharp valleys on surface A.

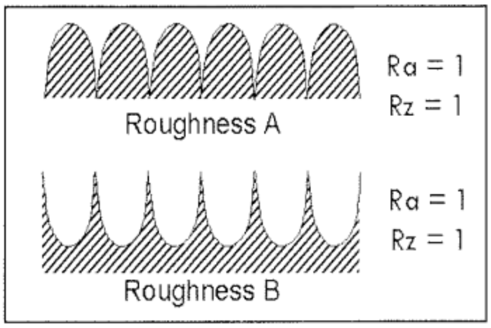

Figure 17 - Roughness comparison of two theoretical surfaces, A and B. Taken from [96]. *Both have the same values of Rougness average (R_a) and peak-to-valley variation (R_z).*

2.3.2 Deformation Induced Martensite (DIM) Transformation

Deformation Induced Martensite (DIM) has a bcc structure and is labelled as α' to differentiate it from ferrite, α. However, martensite is the name given to any phase created by transformation, not diffusion and there are a hexagonal close-packed (hcp) arrangement that is given the symbol ε and a body-centered tetragonal (bct) martensite that forms on quenching steel with a significant carbon content. DIM is formed whenever an austenitic stainless steel is deformed by mechanical work such as peening and cold rolling. Martensite can also form if an austenitic stainless steel is cooled below its martensite formation temperature (M_s), though this is not considered DIM [99].

2.3.2.1 Creating DIM

The crystallographic geometry of martensitic transformations in steel has been studied extensively, with one of the first models created by Kurdjumov & Sachs in 1930 [100]. The progress made in understanding martensitic transformation since then is described in a 2009 review by Zhang & Kelly [101] and a more in-depth discussion of some martensitic transformations can be found in [102]. The transformation of γ to α' is known to occur by two pathways, known as stress assisted martensite transformation and strain induced martensite transformation [103]. The exact pathway taken by a material being deformed will be decided by its Stacking Fault Energy (SFE).

Stress assisted martensite transformation follows the pathway shown in (1). The austenite (γ) phase is transformed first into ε martensite and then into α’ martensite. A relatively low SFE (< 20mJm^{-2}) will favour martensite formation by stress assisted martensite transformation [80].

$$\gamma \to \varepsilon \to \alpha' \tag{1}$$

Strain induced martensite transformation follows the pathway shown in (2). γ phase material transforms directly into the α’ phase, shown in Figure 18. Austenitic SS with relatively high SFE (> 20mJm^{-2}) will form martensite by strain induced martensite transformation [104].

$$\gamma \to \alpha' \tag{2}$$

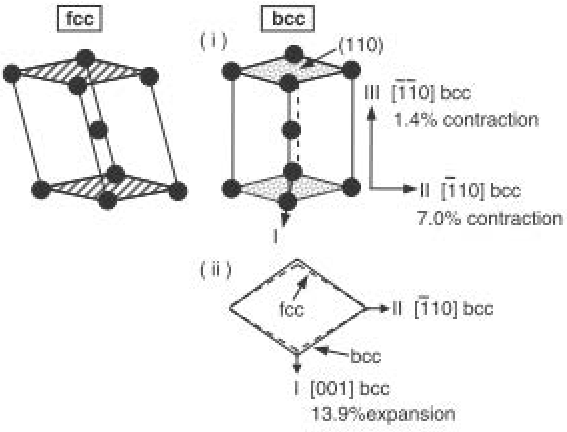

Figure 18 - Schematic illustration of lattice displacement in fcc-bcc martensitic transformation (taken from[105]*)*

304 grade steels have a SFE of around 20mJm^{-2}, which means that both mechanisms may be observed when the material is deformed [106]. In work by Zhang et. al. the pathway shown in (2) was directly observed by TEM in samples treated by surface mechanical attrition treatment [83].

DIM forms during the cold rolling of austenitic SS and is used in combination with annealing treatments to produce ultrafine grain (UFG) metal [104]. When austenitic SS is cold rolled the metal can reach a volume fraction of α’ of >75% [107] and this is related to the amount of strain that the material undergoes, as shown in Figure 19. The α’ is dispersed throughout the metal and forms in laths as shown in Figure 20.

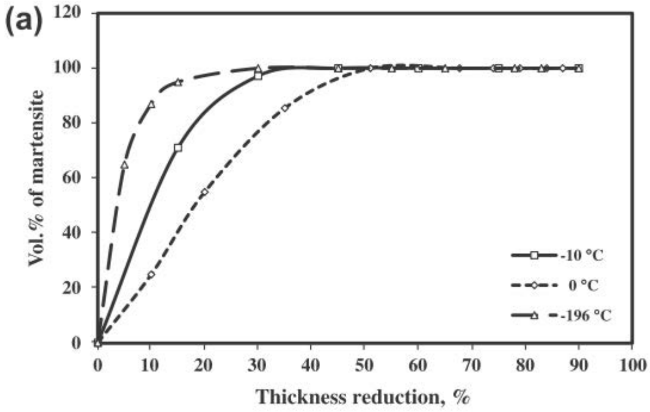

Figure 19 - Effects of rolling strain and temperature on martensite formation in 301 steel. Taken from[108]

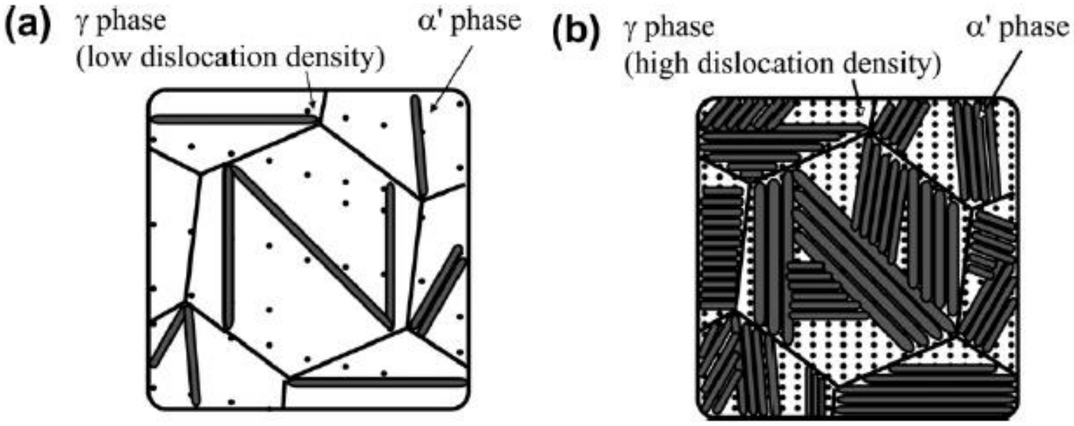

Figure 20 - Schematic diagrams taken from [109] *showing the change in the microstructure of cold rolled SUS304 steel at room temperature. The black rod-like phase shows the α' phase and the white phase containing dots shows the γ phase. The number of dots in the γ phase are proportional to the dislocation density.*

The formation of martensite in shot-peened austenitic SS is not documented in the literature to the same degree as for cold rolled steels. In a study by Ni et. al. a sample of 304 steel underwent high energy shot peening and reached a maximum volume fraction of α' of 91% at the surface [110].

2.3.2.2 Identifying DIM

In homogenous samples of metal it is possible to identify the volume fraction of α, γ and ε phases using X-ray Diffraction (XRD) and Electron Back Scatter Diffraction (EBSD), which is shown in Figure 21. Haušild et. al. have also made use of acoustic emission techniques and magnetic induction to identify the volume fractions [80].

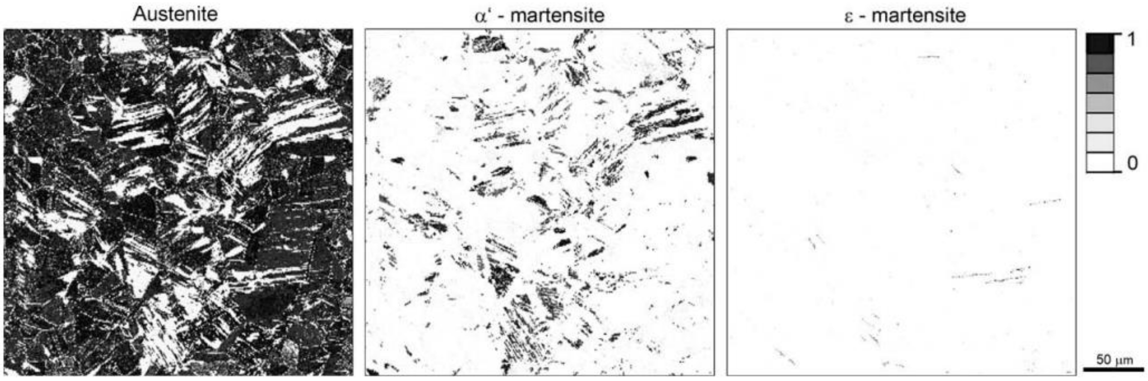

Figure 21 - EBSD images of strained AISI 301 steel. Taken from [80]

When only the surface of a sample is changed, such as by shot peening, it becomes more difficult to characterise the microstructure. The relatively shallow depth to which the material is affected (<1mm) makes it difficult to resolve microstructural changes in samples using XRD, but not impossible. Yu et. al. used XRD with samples of peened SUS304 to assess the volume fraction of α', grain size and dislocation densities with depth from the shot peened surface [74]. The findings of Yu et. al. suggest that the surface of a shot peened sample of SUS304 had a martensite fraction of up to 70%.

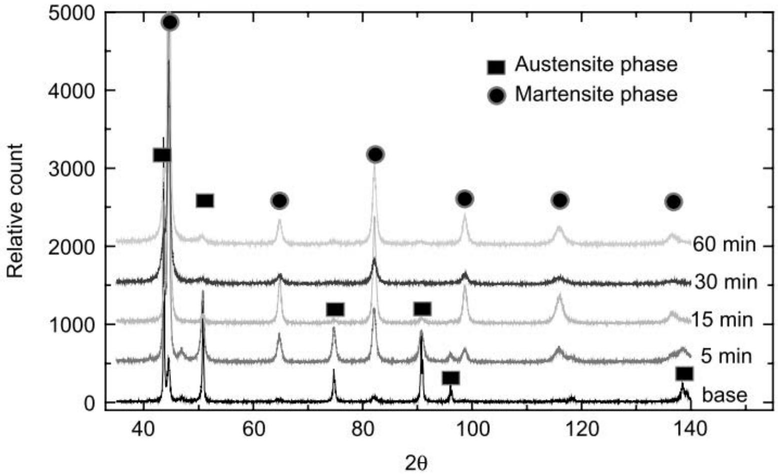

Figure 22 - XRD pattern of 304 SS samples before and after HESP treatment taken from [110]

In order to confirm the XRD observations it would be necessary to create a number of samples for observation by transmission electron microscopy (TEM). The area fraction of α' can then be more directly observed using electron diffraction techniques such as selected area electron diffraction (SAED) [109], shown in Figure 23, and Transmission Kikuchi Diffraction (TKD) [111] which is sometimes referred to as transmission electron backscatter diffraction (t-EBSD).

However, studies such as those of Karimi et. al. [112] make no distinction between α' and α, which are indistinguishable using techniques such as XRD because of their shared bcc structure. This is particularly important, and surprising, in studies of austenitic stainless steels such as 304 and 301 grades because these grades are metastable. A SS can be fully austenitic if it is cooled rapidly even if ferrite is more thermodynamically stable at room temperature. It appears to be a significant oversight on the part of the literature dealing with austenitic SS. An exception to this trend is the work of Guy, Butler & West [113] which uses TEM to show that the α’ and γ grains are related by the martensitic transformation and are not simply α and γ grains adjacent to one another. This relationship is shown in Figure 23. Care must be taken when reading the literature to separate DIM and any other γ→α transformations, which may also be called martensitic transformations.

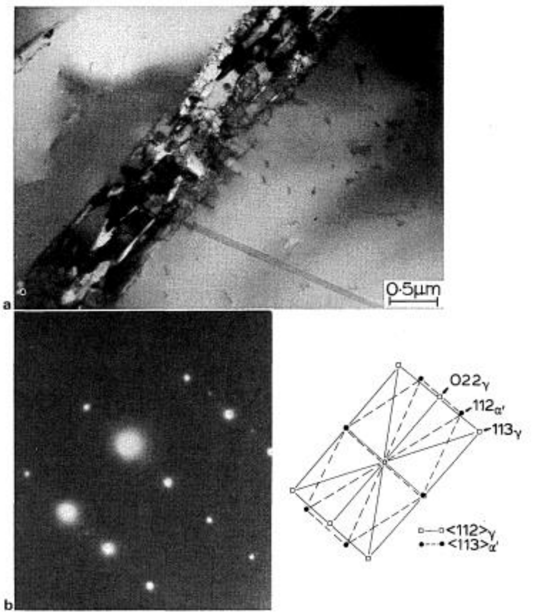

Figure 23 - TEM micrograph of 18/8 steel cooled to -196°C and then heated at 640°C for 2 min. The SAED pattern shows <112>γ and <113>α’, linking the α’ orientation to the source γ orientation. Taken from [113]

2.3.2.3 Effects of DIM

The effect of DIM on the chemical and mechanical behaviour of austenitic SS is not known in detail. Zengwu et. al. theorise that in shot peened TP304H the martensite improves the oxidation resistance of the material because chromium diffuses more readily through the α’ bcc structure [114]. This would provide very little advantage in the in-service conditions of a power plant however, because the α’ is thought to revert to γ when heated to around 550°C [104]. The dispersed α’ can still enhance the oxidation resistance of an austenitic SS by allowing the formation of a fine grain structure. The α’ provides a large number of nucleation sites that encourage many small grains to form when the steel is heated and recrystallizes. The higher volume fraction of grain boundaries offers more pathways for Cr to diffuse through to reach the surface and form protective Cr-rich oxides [115]. The shot peening process also creates a fine-grained crystal structure at the metal surface. No studies have yet decoupled these sources of grain refinement in the context of a steam oxidation study, so it is not known which has the greater part to play in improving shot peened austenitic SS oxidation performance.

The hardness of austenitic SS is also changed by the formation of DIM. α’ is harder than γ phase material. Shintani & Murata suggest that in their cold rolled SUS304 it is the volume fraction of α’ which is the dominant factor that determines sample hardness [109]. However, in work by Naraparaju et. al. the increase in hardness of 304 SS after shot peening is attributed to work hardening, with no discussion of the role of α’ [116]. In the study by Naraparaju et. al. the hardness of shot peened 304 SS returns to its previous level after heat treatment, which would cause the α’ to revert to the γ phase and also the work hardened material to relax and recrystallize. Therefore, it is not obvious which of these factors plays the dominant role in determining material hardness after shot peening.

2.3.3 Prediction of Microstructure

Models for predicting the microstructure generated by shot peening are currently being developed, for example by Bagherifard et al. [117]. Bagherifard et al. report that a finite element model developed for a flat 3D surface has performed well in predicting the residual stresses, work hardening, and depth of the nanostructured layer, but that further work is needed to predict the grain sizes. In work by Zhang et al. it was reported that the grain refinement process in 304 steel is dependent on multiple aspects of the peening regime: strain, strain rate and multidirectional repetitive loading by shots [83]. Furthermore, the low SFE of austenitic steel causes it to form different microstructures when compared to other fcc metals such as Al and Cu, and the effects of slip planes sets austenite apart from ferrite.

2.4 Hardness of Steel

Hardness is the resistance of a material to deformation under a compressive force, for example, a material is said to be harder than another if it can scratch the other material. In general terms the hardness of a material is found by applying a load and observing some resulting change in the material surface.

2.4.1 Measuring Hardness

Different loading regimes and testing methods will provide measures of ‘hardness’ specific to them and require conversions to compare the results of different techniques. In this thesis two methods were used to determine the hardness of samples: Vickers indentation and nano-indentation.

2.4.1.1 Vickers Indentation

A square-based pyramid shown in Figure 24 has a known diagonal and an angle of 136° between opposite sides at the tip. This pyramid is the ‘indenter tip’ and is pressed into a polished surface with a calibrated load for several seconds. The indentation left by the indenter tip is then measured from corner to opposite corner on both sides and the average diagonal length used in (3) to give the Vickers microhardness number, HV. HV can be converted to SI units by (4), but HV should be recorded with the applied load because materials can vary in measured hardness based on the exact load used, especially at small loads [118].

$$HV = \frac{2F}{d^2}\sin\frac{136^\circ}{2} = 1.854\frac{F}{d^2} \qquad (3)$$

$$HV_{SI} = 9.807HV \qquad (4)$$

HV = Vickers Hardness Number (kg/mm^2)
HV_{SI} = Hardness in SI units (MPa)
F = Indentation load (kg)
d = Mean diagonal length of indentation (mm)

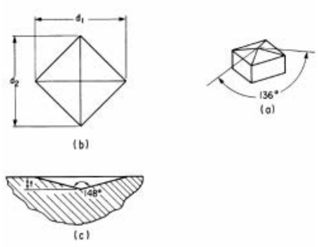

Figure 24 - Vickers microhardness indenter tip geometry. Taken from [119]

Figure 25 shows how the indenter tip causes both plastic and elastic deformation in the material being tested. When the indentation load is removed the elastic deformation can cause the indentation to ‘recover’ and leave a smaller visible indentation than it would in a material that only underwent plastic deformation. This can be important in highly elastic materials such as rubber and many polymers. In metals, the deformation does not recover significantly when the indentation load is reduced during microhardness testing [120].

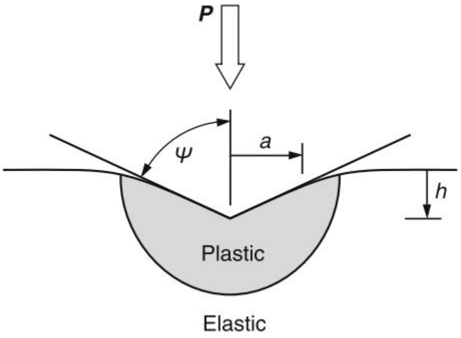

Figure 25 - Schematic diagram of elastic-plastic impression of an indenter of semi-apical angle Ψ. h is depth of indentation, a is half diagonal length of the indentation, P is the indentation load. Taken from [120]*.*

Figure 25 also shows how the plastic zone is not entirely constrained by the boundaries of the indentation (a), but includes the material surrounding the indentation. This means that indentations can be affected if the edge of the sample or other indentations are within a certain radius of the indenter tip. The size of this radius can vary depending on the mechanical characteristics of the target material, but the general ASTM recommendation for indentation spacing is shown in Figure 26. Interactions between a sample edge or other indentations is eliminated by keeping a separation of ≥2.5x the diagonal width of an indentation [121].

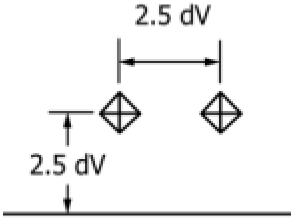

Figure 26 - Recommended distances between Vickers microhardness indentations and the edge of a sample. dV is the diagonal width of the indentation. Taken from [121]*.*

2.4.1.2 Nano-Indentation

An indenter tip is pressed into a surface by a linearly increasing load of maximum ≈200mN to a depth of <1µm and the load is then reduced at the same rate until contact with the surface is broken. The elastic deformation under the indenter tip is relieved as the load decreases, making the indenter rise up. The relationship between applied load and indenter tip depth is shown in Figure 27 and allows the calculation of the material's nanohardness by (6) and elastic modulus by (5) [118].

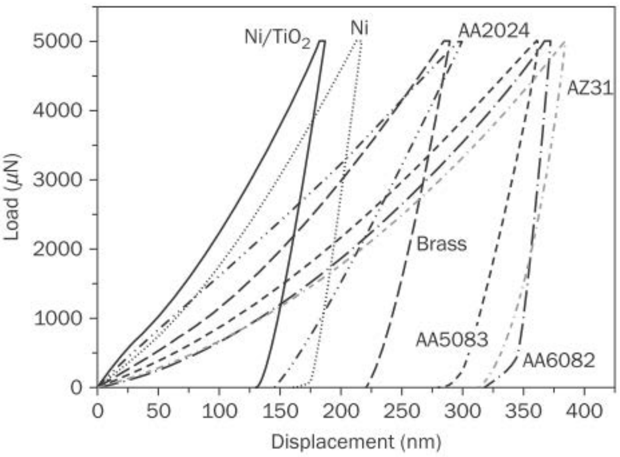

Figure 27 - Loading-unloading curves of metals and alloys for applied loads of 5000µN. Taken from [118]

$$E_r = \frac{S\sqrt{\pi}}{2\beta\sqrt{A_c}} \tag{5}$$

$$H_c = F/A_C \tag{6}$$

E_r = Elastic modulus
H_C = Contact hardness
S = Initial slope of the unloading load–displacement curve at peak load
A_C = Contact area of tip and surface
β = Constant based on indenter tip geometry
F = Indenter load

2.4.2 Hall-Petch Relationship of Grain size vs Yield Stress

Experiments by Hall [122] and Petch [123] related the grain size of a metal to its yield point. It was found that materials with relatively smaller grains would possess a higher yield point and this was attributed to the interaction of dislocations and the grain boundaries. This model proved successful and the findings are known as the Hall-Petch relationship given in (7).

$$\sigma_{lyp} \propto \frac{1}{\sqrt{d}} + \sigma_{sc} \tag{7}$$

Were σ_{lyp} is the lower yield point (kg/mm^2), σ_{sc} is the calculated yield point of a single crystal and d is the grain diameter.

Metals become harder as their grain sizes are reduced because dislocations become pinned at grain boundaries. The dislocation requires a higher energy to pass from a grain boundary and into another crystal than it does to move through the bulk of the material. Therefore, dislocations ‘pile up’ at the grain boundaries instead of moving through the bulk of the metal and allowing it to deform. This relationship does not hold for grain diameters below ≈10nm. At these scales the relationship breaks down and the smaller the grains are, the lower the metal’s yield point [124].

During annealing treatments the hardness of metals goes down as a result of recovery and recrystallization, as shown in Figure 28.

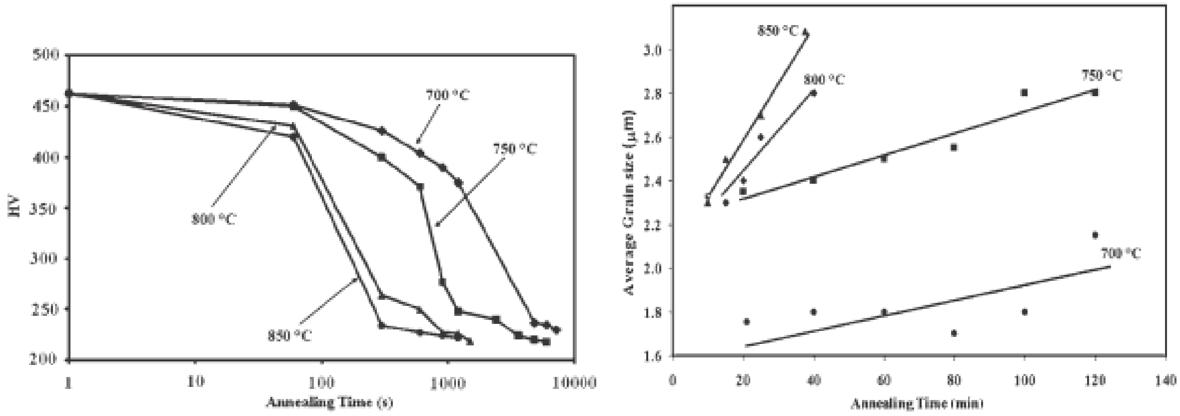

Figure 28 - Effect of annealing time and temperature on the hardness and grain size of 304 SS. Taken from [125].

2.5 Recrystallization of Austenitic Steels

Recrystallization is a process driven by minimizing energy; the atomic arrangement of the material will trend towards its lowest energy state whenever possible. However, the rate of atomic re-arrangement will be based on temperature. At higher temperatures the constituents of the steel will be able to move more easily to take new forms with the lowest energy states.

2.5.1 Stages of recrystallization

Studies of the phenomenon have identified three general behaviours of metals when they are held at temperatures high enough to allow a significant amount of self-diffusion; Recovery, Primary recrystallization and Secondary recrystallization [102, 126, 127].

2.5.1.1 Recovery

The recovery period involves a change in a deformed material's characteristics, such as hardness, partially back to the pre-deformation condition. The changes are brought about by several mechanisms related to the number and structure of dislocations in the metal lattice including those given below. Not all mechanisms have to happen and each mechanism can overlap with the others. Austenitic SS have low stacking fault energies which discourage recovery. They instead tend to undergo only recrystallization.

1.1.1.1.1 Dislocation Tangles

As a material undergoes recovery the dislocations in its lattice will begin to move by glide, climb and cross-slip. Dislocations travelling on different glide plains in a lattice will interact with each other and generate 'tangles' of dislocations such as in Figure 29. A dislocation tangle is less mobile than free dislocations and will tend to capture dislocations that move through or past it.

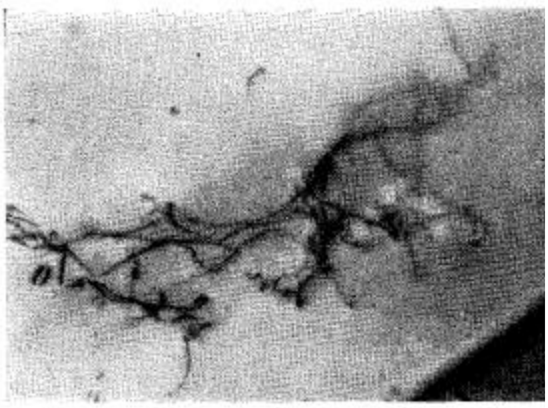

Figure 29 - TEM image of a dislocation tangle in Al. Taken from [128]

1.1.1.1.2 Cell Formation

Dislocation tangles will form a cell structure. The material within cells is still deformed and contains many defects. It is now much more difficult for a dislocation to leave a cell structure without being captured by the surrounding tangles. Such a cell structure is shown in Figure 30 (a).

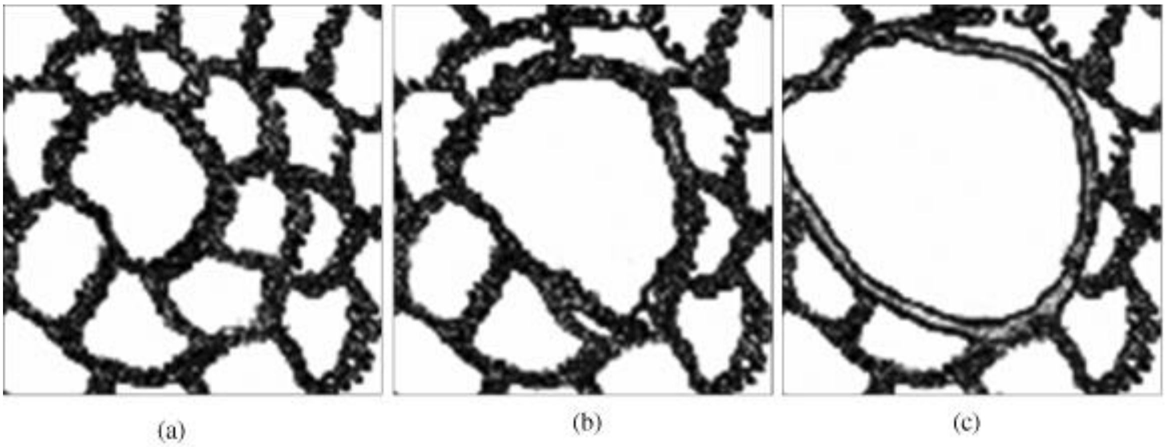

Figure 30 - The sequence shows the nucleation of a recrystallized grain starting from a subgrain: a) initial substructure; b) the larger (middle) subgrain growth over the other (smaller) ones; and c) an area free of defects associated with a large angle boundary that is being formed. [129]

1.1.1.1.3 Dislocation Annihilation

The dislocations which are still mobile inside the cell structures will interact with each other to annihilate. Parallel dislocations with opposite Burgers vectors are known as a dislocation dipole and they will tend to attract each other. When the dislocations meet they will annihilate and reduce the strain in the matrix. This process is shown in Figure 31.

1.1.1.1.4 Subgrain Formation

The tangles that make up the cell walls will take on a more ordered structure to create more clearly defined cell edges. When the edges are well defined then the cell is said to be a subgrain. Adjacent subgrains have a very low mismatch angle and still contain strain, which differentiates them from grains formed during recrystallization.

1.1.1.1.5 Subgrain Growth

Subgrains will coarsen over time in a manner which has some similarities to grain coarsening. The exact process of subgrain growth has at least two possible mechanisms, grain reorientation shown in Figure 32 and boundary migration.

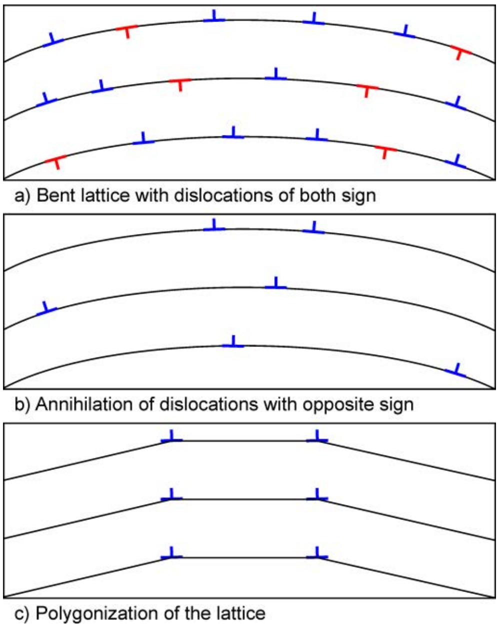

Figure 31 - Simple schematic of dislocation annihilation and lattice polygonization [130]

2.5.1.2 Primary Recrystallization

Primary Recrystallization is the creation and growth of strain-free grains with high orientation mismatch to their neighbouring grains. Throughout the primary recrystallization phase the deformed material which remains after the recovery phase will be consumed by the new strain-free grains.

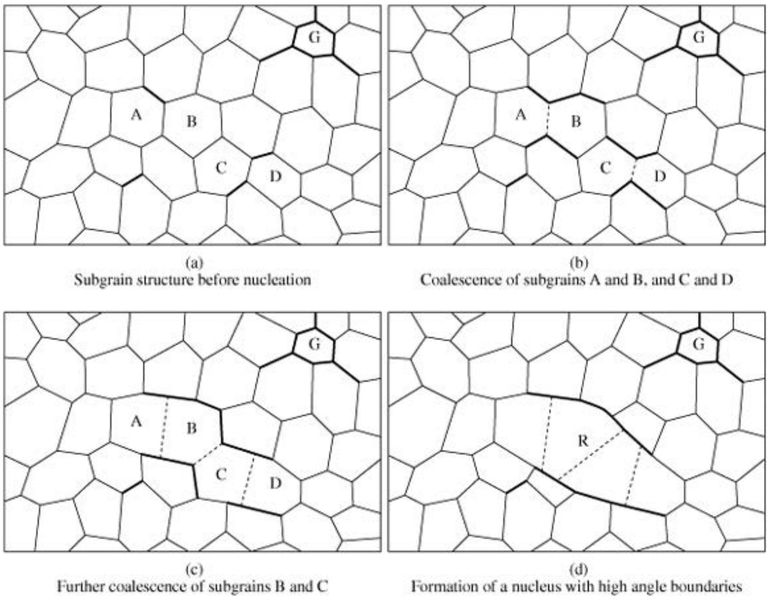

(a) Subgrain structure before nucleation (b) Coalescence of subgrains A and B, and C and D (c) Further coalescence of subgrains B and C (d) Formation of a nucleus with high angle boundaries

Figure 32 - Schematic representation of a recrystallized grain. The orientation difference of subgrains is represented by the line thickness: a) original structure; b) coalescence of pairs by elimination of common boundaries; c) coalescence of the A/B and C/Ds; and d) recrystallized grain originating from a group of coalesced subgrains. The thicker lines indicate large angle boundaries [129]

If a sufficiently high fraction of the metal undergoes recovery there will not be enough non-recovered matter remaining to undergo primary recrystallization. The need for deformed material for the new grains to grow into stems from the driving force of recrystallization; minimizing the free energy of the grains. Without the dislocations and defects found in deformed material, there is not enough energy change generated by recrystallization, and the process cannot go forwards.

Figure 33 shows the process of recrystallization as a fraction of the material against time. There are two distinct sections of the curve; nucleation and growth.

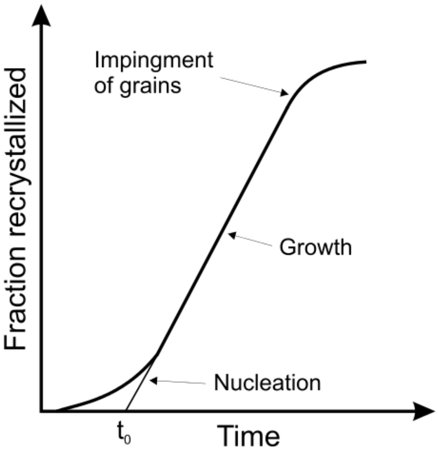

Figure 33 - The nucleation and growth kinetics of recrystallized grains in a generic deformed alloy. t_0 is the nucleation time. The gradient of the Growth line is the growth rate. Impingement of Grains describes the time at which recrystallized grains are beginning to grow up against one another. Taken from [131]

1.1.1.1.6 Nucleation

In the nucleation phase there is a delay before the recrystallized grains begin to grow. This time may include a recovery phase, but not always. The nucleation process is not strictly a single mechanism, as in precipitate nucleation, but can be many. For example, the nucleation sites can be partially recovered subgrains, areas of high dislocation density or a certain phase present in the deformed material.

1.1.1.1.7 Growth

In the growth phase the high angle grain boundaries formed during nucleation migrate through the matrix and consume the remaining deformed material. This phase will continue until the grains run out of free space to move into and begin to impinge on each other.

2.5.1.3 Secondary Recrystallization

When the deformed material has recrystallized in primary recrystallization there is very little energy to be gained by further grain growth. The free energy stored in the grain boundaries can be minimized by the grains growing larger, but this driving force is at least 2 orders of magnitude less than in primary recrystallization. Grains may be enlarged 'normally', with all the grains growing at a similar rate or 'abnormally', with only the larger grains growing at the expense of the smaller. Secondary recrystallization is seen when fully recrystallized metals are held at elevated temperatures for long periods of time.

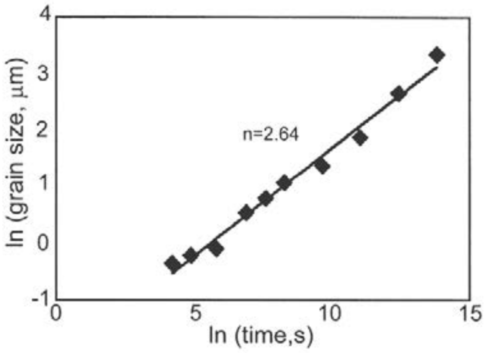

Figure 34 - Annealing of a single-phase 0.5µm-grained Al-3%Mg alloy at 250°C showing normal grain growth. Taken from [132]

2.5.2 The JMAK Model

A model commonly used to assess recrystallization is the Johnson-Mehl-Avrami-Kolmogorov (JMAK) model which can be written as (8).

$$X_R = 1 - exp[-Bt^n] \qquad (8)$$

X_R = Fraction recrystallized
t = Time
n = JMAK/Avrami exponent
B = Constant

This model is used by plotting $\ln(1/(1-X_R))$ against $\ln t$ to produce a 'JMAK plot', such as Figure 34. An ideal JMAK plot is linear and the gradient of the line is the JMAK exponent, n. The theoretical value of n is based on system geometry and the rate of nucleation, and shown in Table 11. The model requires that the nucleation sites of new grains are random, which is not found in many real-world systems. JMAK plots are commonly used in the literature to find the JMAK exponent in a series of experiments and compare it to the idealized systems. In theory, the exponent will show if the nucleation sites are randomly distributed, saturated, constantly increasing in number, or if the grain growth is restricted to one or two dimensions. This treatment is strictly qualitative.

Table 11 - Ideal JMAK Exponents

Dimensions of Growth	Nucleation Site Saturation	Constant Nucleation Rate
3	3	4
2	2	3
1	1	2

2.5.3 Predicting recrystallization

The recrystallization process in shot peened SS will cause the microstructure of the shot peened surface to change. Predicting how a shot peened surface will behave at elevated temperature may therefore be vital to a time of life calculation for component.

In isothermal conditions the rate of recrystallization is recorded as the time taken for 50% of a material to recrystallize into strain-free grains, $t_{0.5}$. By defining $t_{0.5}$ in such a way it is possible to compare different factors affecting the recrystallization of cold worked materials. The factors of interest in this thesis are those which are affected most by shot peening and in-service conditions: strain, grain size and temperature.

2.5.3.1 Strain

A material that has undergone a higher strain will recrystallize more quickly than the same material experiencing less strain [133]. The material undergoing higher strain has more stored energy that will be available for recrystallization, hence the more rapid process. A shot peened surface possesses a significant amount of strain and so should undergo primary recrystallization more rapidly than the bulk of the material, if the bulk does so at all.

2.5.3.2 Grain Size

It has been found that smaller initial grain sizes will cause faster recrystallization [126, 134, 135]. This relationship is qualitatively established in the literature but a general, quantitative relationship between grain size and recrystallization has not yet been described. Some recent discussion on initial grain size effects is included by Pous-Romero et al. in their investigation of austenitic steels in nuclear pressure vessels [136].

2.5.3.3 Temperature

The most basic model for recrystallization and grain growth based on temperature is (9) and uses empirically discovered values for C and Q. The model is not valid when used to estimate the growth rate of untested materials with unknown constants. Furthermore, the model does not take into account changing growth rates caused by differences in nucleation rates.

$$\frac{1}{t_{0.5}} = Cexp\left[\frac{-Q}{kT}\right] \tag{9}$$

$t_{0.5}$ = Time to 50% recrystallization (s)
C = Constant
Q = Activation energy of 'recrystallization' (J)
k = Boltzman constant ($m^2kg^1s^{-2}K^{-1}$)
T = Temperature (K)

The physical meaning of Q is related to the energy required to drive the recrystallization process, but this is not easily defined and is in fact a combination of factors based on the atomic species, microstructure and thermodynamics of the system. However, in the literature this model is popular because of the simplicity of plotting $\ln(t_{0.5})$ against 1/T to create plots for particular materials in defined starting states, such as Figure 35.

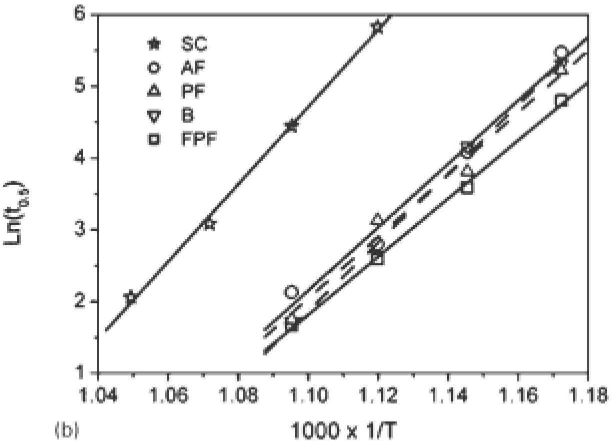

Figure 35 - Arrhenius plots of $t_{0.5}$ for cold rolled steel with different initial microstructures. Taken from [135]. *SC = strip cast, AF = acicular ferrite, PF = polygonal ferrite, B = bainite, FPF = fine polygonal ferrite.*

2.5.4 Microhardness During Recrystallization

The work of Kalu & Waryoba with drawn wires of copper showed that the progress of recrystallization could be measured by microhardness[137]. They found that the fraction of material which had recrystallized was linked to the material's microhardness by (10).

$$X_R = \frac{H_0 - H_t}{H_0 - H_{ann}} \tag{10}$$

X_R = Fraction recrystallized
H_0 = Initial microhardness
H_t = Microhardness at time t
H_{ann}= Microhardness when fully annealed

2.5.5 Reversion of DIM

As previously discussed in the section 'Deformation Induced Martensite (DIM) Transformation', shot peening transforms austenitic material into martensitic α' material. When α' is held at temperatures above ≈400°C it reverts to γ, with the rate of transformation based primarily on the annealing temperature as shown in Figure 36. However, in some studies the volume of martensite is reported to increase upon further heating as shown in Figure 37. This is because if the material is metastable it can form ferrite, which has an identical crystal structure to DIM and can be detected by the same techniques.

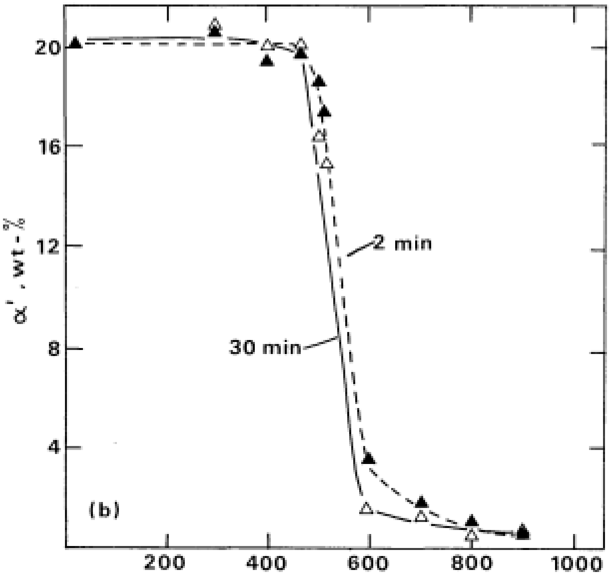

Figure 36 - Ferromagnetic content of an 18/12 steel cold rolled to a reduction of 20% at -196°C and then annealed at various temperatures. Taken from [113].

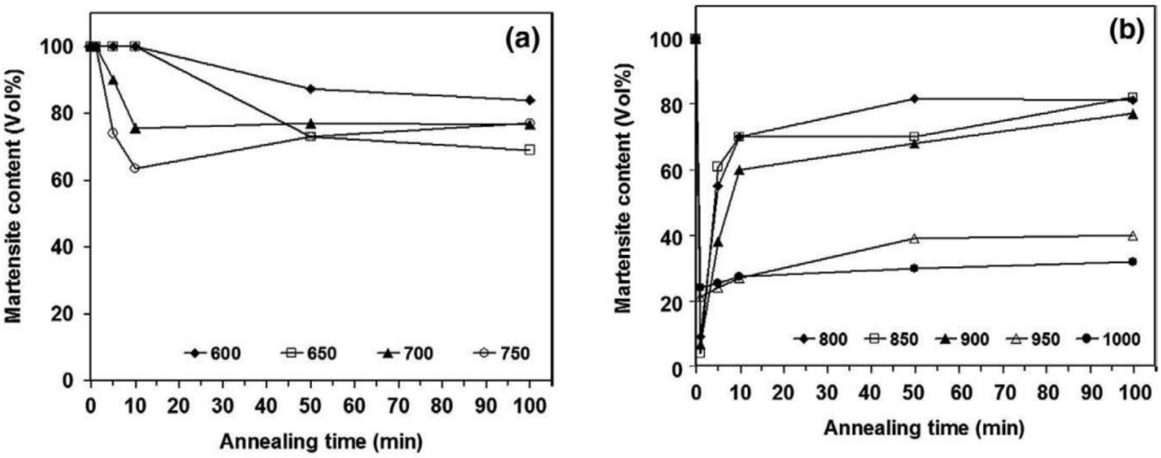

Figure 37 - Martensite content in cold rolled 301 steel when annealed at 600-1000°C. Taken from [112]

.

2.6 Diffusion

Diffusion is the net movement of molecules or atoms from a region of high concentration to a region of low concentration. Diffusion In 1 dimension is described by Fick's first law as shown in (11). [138]

$$J = -D\frac{\delta\varphi}{\delta x} \qquad (11)$$

J = Amount of substance per unit area per unit time ($mol.m^{-2}s^{-1}$)
D = Diffusion coefficient or diffusivity (m^2s^{-1})
φ = Concentration of substance per unit volume ($mol.m^{-3}$)
x = Position in 1 dimension (m)

The rate of diffusion within a metal is related to temperature by Arrhenius' equation (12).

$$D = D_0 \exp\left(-\frac{Q_d}{RT}\right) \qquad (12)$$

D = Diffusivity of a species (m^2s^{-1})
D_0 = Temperature-independent constant for matrix and diffusing species (m^2s^{-1})
Q_d = Activation energy for diffusion ($J.mol^{-1}$)
R = Gas Constant ($J.K^{-1}mol^{-1}$)
T = Temperature (K)

Q_d will depend on the mechanism of diffusion and the strength of the atomic bonds that must be broken in order for the mechanism to occur. These vary with the species involved in diffusion, the chemical make up of the matrix being diffused into, the structure of the matrix and other factors such as electrical potentials. Therefore, Q_d will be specific to each species in each matrix.

2.6.1 Bulk Diffusion

The dominant type of diffusion in large grained metals is diffusion through the bulk of the grains. This occurs through vacancy diffusion, or interstitial diffusion if the diffusing species is small enough.

Vacancy diffusion takes place when an atom moves from its location in the matrix into an adjacent vacancy. It is therefore highly dependent on the kinetic energy of the atoms (i.e. temperature) and the number of vacancies in the matrix, which is itself also heavily dependent on temperature. [138]

Interstitial diffusion occurs when an atom moves from one interstitial site to another. Only small atoms such as H, C and O can inhabit the interstitial sites within metals. Interstitial diffusion is a faster process than vacancy diffusion due to the larger availability of interstitial sites compared to vacancies in the matrix.

The activation energies and diffusion coefficients in the bulk of steels are shown in Table 12 and Table 13. The tables also include the resultant value of diffusivity at 700°C, the most relavent temperature used in this thesis. In general, the diffusivity of elements in α-Fe is an order of magnitude larger than in γ-Fe. Diffusivity will also vary depending on the steel composition, as shown for example in Figure 38. There is significant disagreement in the literature over the meaning and most useful values for diffusion data when used to model materials; there is a wide range of values between studies even if the element and alloy are the same. For example, in Table 12 the diffusivity of Fe in 18-10 steel is investigated in [139] and [140], but the diffusion coefficient at 700°C is an order of magnitude apart. A review of this data and the relevant literature is beyond the scope of this thesis.

Table 12 - Arrhenius equation diffusion data for elements in the bulk of an austenitic (fcc) Fe matrix

Element	Matrix	Q_d(kJ mol^{-1})	D_{0V} (cm^2/s)	Reference	D(700°C) (cm^2/s)
Fe	18-10 steel	280	4.40×10^{-1}	[140]	4.12×10^{-16}
Fe	19.1-19.1 steel	286.9±27.5	1.15	[141]	4.59×10^{-16}
Fe	18-10 steel	217	2.50×10^{-3}	[139]	5.63×10^{-15}
Fe	γ-Fe	284	5.00×10^{-1}	[138]	2.85×10^{-16}
Cr	19.1-19.1 steel	269.8±9.4	4.25×10^{-1}	[141]	1.40×10^{-15}
Cr	321 steel	296	5.59	[142]	7.24×10^{-16}
Cr	304 steel	283	3.06	[143]	1.98×10^{-15}
Cr	18-8 steel	230.4±7.0	5.38×10^{-3}	[144]	2.31×10^{-15}
Cr	304 steel	289	2.20	[145]	6.77×10^{-16}
Cr	310 steel	246	2.70×10^{-1}	[146]	1.69×10^{-14}
Cr	316 steel	243	6.20×10^{-2}	[147]	5.62×10^{-15}
Cr	316 steel	229	1.18×10^{-2}	[148]	6.03×10^{-15}
Cr	γ-Fe	291.8	$1.08 \times 10^{+1}$	[149]	2.35×10^{-15}
Ni	18-10 steel	301	$1.40 \times 10^{+1}$	[139]	9.77×10^{-17}
Ni	γ-Fe	280.5	7.70×10^{-1}	[149]	6.77×10^{-16}
Mn	17/18Cr-16/10Ni steels	265	4.20×10^{-1}	[150]	2.51×10^{-15}
Mn	γ-Fe	261.7	1.60×10^{-1}	[149]	1.44×10^{-15}

Table 13 - Arrhenius equation diffusion data for elements in the bulk/volume of a ferritic (bcc) Fe matrix

Element	Matrix	Q_d(kJ mol^{-1})	D_{0V}(cm^2/s)	Reference	D(700°C) (cm^2/s)
Fe	α-Fe	251	2.80	[138]	9.44×10^{-14}
Cr	446 ferritic steel	210	1.50×10^{-1}	[146]	8.02×10^{-13}
Cr	α-Fe	250.8	8.52	[149]	2.94×10^{-13}
Ni	α-Fe	245.8	1.40	[149]	8.97×10^{-14}
Mn	17/18Cr-16/10Ni steels	204	1.80×10^{-1}	[150]	2.02×10^{-12}
Mn	α-Fe	233.6	1.49	[149]	4.31×10^{-13}

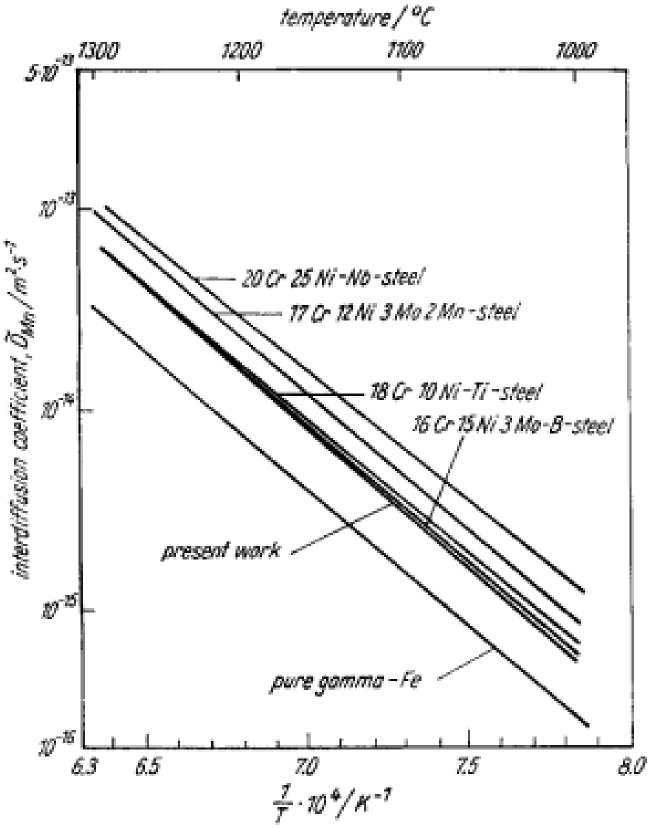

Figure 38 - Temperature dependence of the diffusion coefficients of Mn in γ-Fe and stainless steels. Taken from [150]

Bulk diffusion within metal oxides is often orders of magnitude less than in a metal. Two of the oxides studied in this thesis are $MnCr_2O_4$ spinel and Cr_2O_3 (chromia). The diffusivities of Fe, Mn and Cr in these matrices are shown in Table 14 and Figure 39. The author did not find data for the diffusivity of $MnCr_2O_4$ below 800°C and the value of bulk diffusivity at 800°C given in Table 14 is similar in size to α-Fe at that temperature. Diffusivity in chromia at 700°C is of the order 10^{-18}cm^2/s; two to four orders of magnitude below the diffusivity in the alloy.

Table 14 - Diffusivity for elements in a $MnCr_2O_4$ spinel matrix at 800°C (1073K) from [151]

Element	**D_v(cm^2/s)**	**D_{GB}(cm^3/s)**
Fe	$(1.2 \pm 0.6) \times 10^{-12}$	$(2.6 \pm 1.0) \times 10^{-15}$
Cr	$(9.7 \pm 1.3) \times 10^{-13}$	$(7.6 \pm 3.6) \times 10^{-15}$
Mn	$(1.7 \pm 1.4) \times 10^{-12}$	$(1.1 \pm 0.2) \times 10^{-14}$

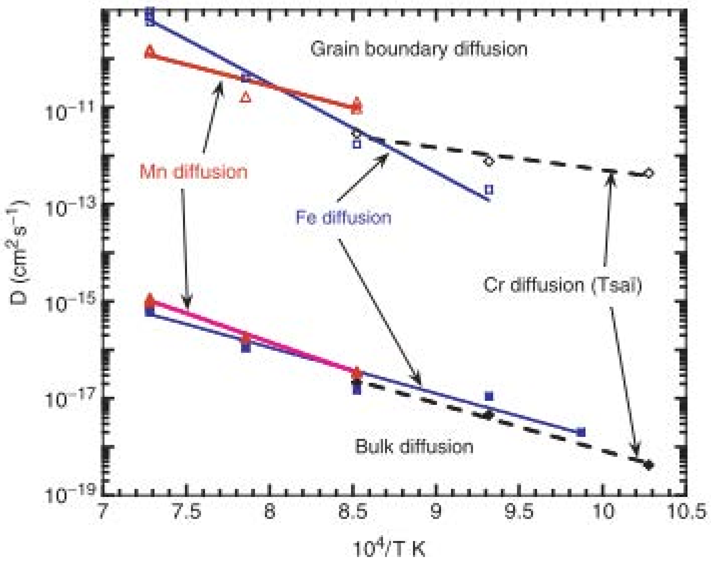

Figure 39 - Arrhenius plot of bulk and GB diffusion of Fe, Mn and Cr in polycrystalline Cr_2O_3*. Taken from* [152]

Dieckmann [153] models the diffusion of cations through magnetite by considering its crystal structure and the available Fe valences; Fe^{2+}, Fe^{3+}. The O atoms form an fcc matrix with 32 O atoms per unit cell. Fe cations are then arranged on 2 sub-lattice sites with Fe^{3+} taking up locations on an octahedral and the tetragonal sub-lattices and the Fe^{2+} cations on the octahedral sub-lattice, as shown in Figure 40. Both Fe^{2+} and Fe^{3+} can diffuse through magnetite and there are both octahedral and tetrahedral interstitial sites that can be inhabited. This is part of why magnetite is not a protective oxide.

Chromia and haematite are based on a lattice of oxygen atoms in an hcp arrangement. The cations occupy 2/3 of the octahedral sites and are all of valence (III). Higher valence cations require more energy to diffuse and there are fewer empty interstitial sites for them to move into than in a spinel structure.

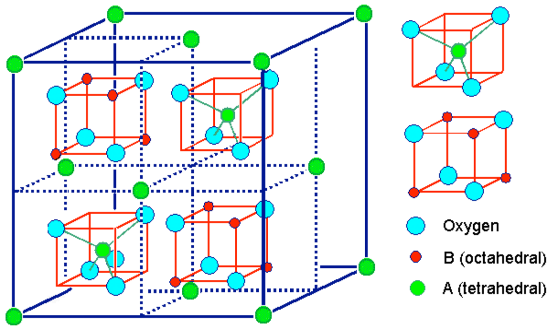

Figure 40 - Spinel lattice sites. Taken from [154]

2.6.2 Grain Boundary Diffusion

Diffusion through the GBs of a metal is a ‘short circuit’ pathway, or a ‘shortcut’ because the diffusivity within the GBs is much higher than in the bulk, as can be seen in Figure 41. In large grained metals the GBs are a very small fraction of the total volume of material, and so GB diffusion may not be significant. When a material is fine grained then the larger fractional volume of GBs will cause GB diffusion to be significant or even to be the dominant process.

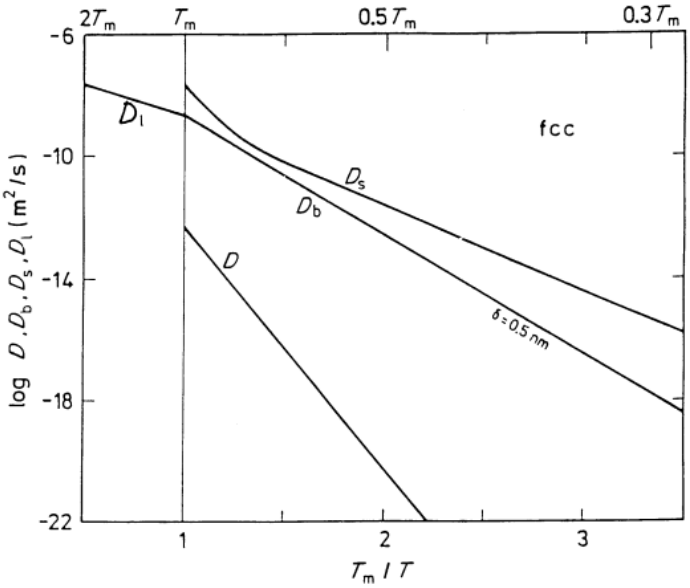

Figure 41 - Arrhenius plot for self-diffusion in fcc metals for the bulk lattice (D), along GBs (D_b), on the surface (D_s) and in the liquid phase (D_l).Taken from [155]

The model used for the diffusion processes in a GB is the Fisher model [156]. GBs in the Fisher model are thin channels of high diffusivity material of thickness δ, which is generally taken to be 0.5nm [155]. The GB is perpendicular to the surface of the material.

This geometry is used to analyse the results of radiotracer experiments in which a radioactive source material is placed on a metal surface. The diffusion profile can then be observed by removing material from the metal surface and measuring its radioactivity. The diffusion profile will have the form shown in Figure 42 and can be used to find the triple product given in (13).

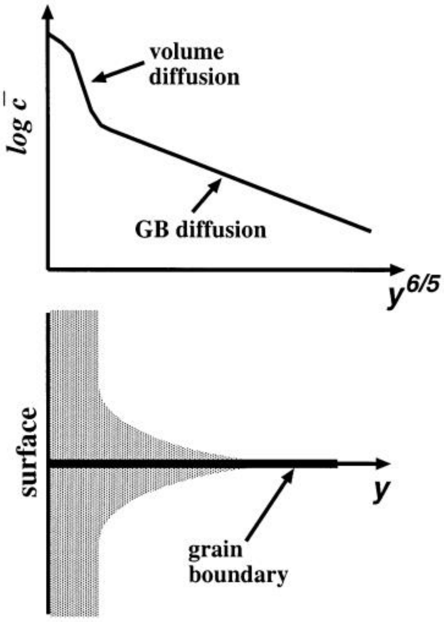

Figure 42 - Schematic shape of a diffusion profile along a GB with penetration depth (y). c is the count rate of the radioactive tracer. Taken from [155]

$$s\delta D_b = 1.322(D_v/t)^{\frac{1}{2}}\left(-\frac{\partial \ln \bar{c}}{\partial y^{\frac{6}{5}}}\right)^{\frac{5}{3}} \tag{13}$$

s = Equilibrium segregation factor (=1 in pure metal)
δ = diameter of GB
D_b = Diffusivity of GB
D_v = Diffusivity of bulk material
t = time
c = average number of radioactive decays counted
y = distance from metal surface

In order to find D_b the two other variables must be known, and this is not always possible. Therefore, the results of tests to find the diffusivity of GBs are generally given as $s\delta D_b$ in units of (m^3s^{-1}) and not just D_b (m^2s^{-1}). D_b can be expressed using Arrhenius equations, as with D_v. Table 15 provides Arrhenius data for GB diffusion in austenitic steels and Figure 43 shows the GB diffusivity of Cr and Ni found in a range of alloys.

Table 15 - Arrhenius equation diffusion data for elements in grain boundaries in an austenitic Fe matrix. Calculated values for the GB diffusivity at 700°C assume a GB thickness of 0.5nm.

Element	**Matrix**	**Q_b(kJ mol^{-1})**	**D_{0GB} (cm^3/s)**	**Reference**	**D_{GB}(700°C) (cm^2/s)**
Fe	18-10 steel	307	3.36×10^{-1}	[157]	2.22E-08
Cr	18-8 steel	226.7±4.0	1.33×10^{-4}	[144]	1.80E-07
Cr	316 steel	191	1.5×10^{-6}	[147]	1.67E-07
Ni	18-10 steel	71	2.95×10^{-12}	[139]	9.11E-07

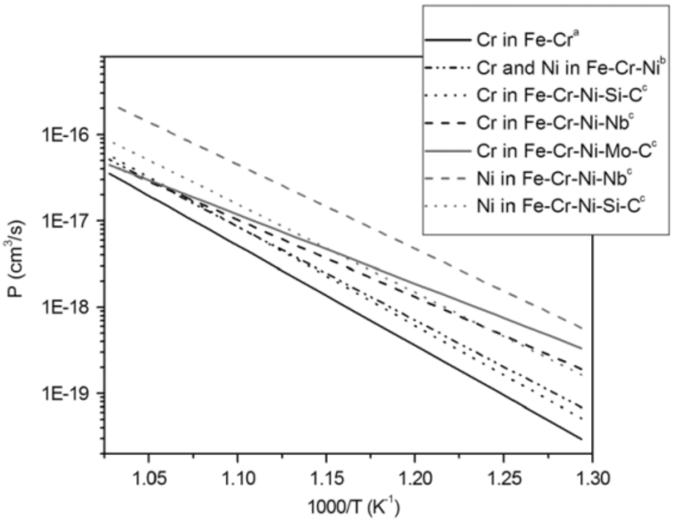

Figure 43 - Comparison of grain boundary self-diffusion coefficients in various alloys. Taken from [158]

The fraction of material in a metal that is made up of grain boundaries can be calculated by (14) from the work of Palumbo et al. [159]. It uses a regular fourteen-sided tetrakaidecahedron as the grain shape instead of the cubic or spherical grains used in many models. Figure 44 shows how the fraction of 'bulk' material to grain boundary material varies with grain size assuming a GB thickness of 1nm. The relationship is theorized to hold only when d>>Δ.

$$\boldsymbol{V_t^{IC} = 1 - \left[\frac{(d - \Delta)}{d}\right]^3} \tag{14}$$

V_t^{IC} = Intercrystalline volume fraction
d = grain diameter
Δ = thickness of grain boundary

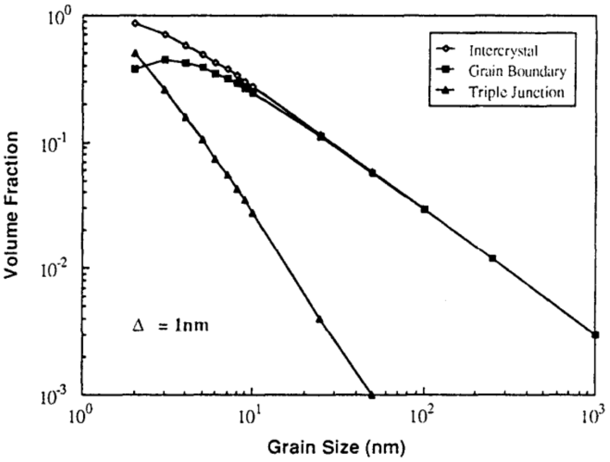

Figure 44 - Calculated volume fraction of intercrystalline material based on grain size assuming GB thickness = 1nm. Taken from [159]*.*

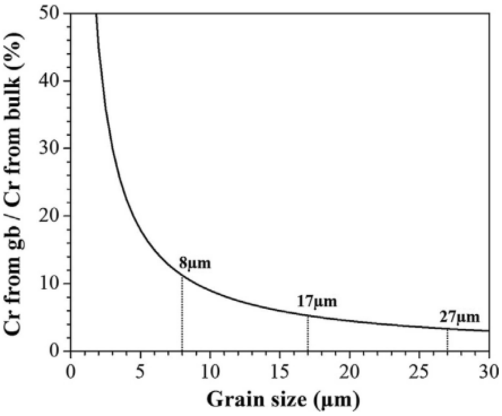

Figure 45 - Relative increase in the Cr flux via grain boundary diffusion as grain size is changed for 304Cu steel at 700°C assuming a GB width of 0.5nm. Taken from [160] *and based on* [161]*.*

2.6.3 Diffusion along Dislocations

Dislocations are able to act as rapid diffusion pathways in the bulk of the matrix, similar to low angle grain boundaries. Hart suggested this should be taken into account at low temperatures (<700°C) and over relatively short diffusion distances as early as 1957 [162]. Further work assumed that the dislocations could be modelled as so called ‘pipes’ of a fixed average diameter and possessing a higher diffusion coefficient than the bulk of the matrix, similar to GB diffusion in the Fisher model. Work by Smith in 1975 suggested that the enhanced rate of diffusion in dislocations was smaller than expected and probably less than 10^3x the bulk diffusivity [163]. The overall effect of dislocation diffusion on the diffusion of Cr in steels has been found to only be relevant at short distances and short time scales [164]. Therefore, the increased dislocation density in a shot peened SS surface could promote the formation of a protective chromia layer in the first few hours of oxidation, but this initial effect will quickly disappear. Quantifying the effect of dislocations on oxidation resistance has been attempted, such as in the work of Naraparaju [116], but only qualitative results have been found. Furthermore, Naraparaju’s work does not separate the effect of enhanced dislocation diffusivity from grain boundary diffusion, which is significant in shot peened materials.

2.7 High Temperature Oxidation of Steel

2.7.1 Oxides of Steel

For iron and pure oxygen there are multiple possible iron oxides which are thermodynamically stable, shown in (15), (16), and (17).

$$2Fe + O_2 \rightarrow 2FeO\ (Wustite) \qquad (\ 15\ )$$

$$\frac{4}{3}Fe + O_2 \rightarrow \frac{2}{3}Fe_2O_3\ (Hematite) \qquad (\ 16\ )$$

$$\frac{3}{2}Fe + O_2 \rightarrow \frac{1}{2}Fe_3O_4\ (Magnetite) \qquad (\ 17\ )$$

Hematite and Magnetite are non-protective oxides that do not discourage further oxidation. For an iron alloy to be resistant to oxidation it must contain an element that can form a stable, continuous passivating oxide layer on its surface. Passivating layers can be formed from Cr_2O_3, Al_2O_3 and SiO_2 if there is enough of the element in the alloy and if the partial pressure of oxygen and temperature are in the correct range. Steels are called ‘stainless’ if they are able to form a protective oxide layer under normal conditions, usually because they contain >10.5% Cr. A stainless steel will not oxidize to form wustite until the Cr concentration in its surface has fallen below a critical level. The exact critical concentration is uncertain, but known to be <1% and so cannot be reached under practical conditions in 300-series steels.

Some oxides share a common crystal structure with each other and can exist as mixtures. This is especially true of the spinels, which can exist as a spectrum of compounds depending on the concentrations of different cations in the metal surface and their rates of diffusion. [165]

A spinel of note is manganese chromium spinel ($MnCr_2O_4$) because of its unusual thermodynamic properties. Unlike the other spinel compositions made up of Mn, Fe and/or Cr, manganese chromium spinel is more stable in the temperature range 300-1500K than chromia. This will be discussed further in Thermodynamics of Oxidation.

The metals and oxides studied in this thesis and their crystal structures are summarised in Table 16.

Table 16 - Crystallographic data for some components and oxides of stainless steels

Material	Formula	Structure	Space Group	Lattice Constant a (Å)	Lattice Constant b (Å)	Lattice Constant c (Å)	Angle 1 (°)	Angle 2 (°)	Angle 3 (°)
Metals									
Austenite (γ)	Fe	fcc	$Fm\bar{3}m$	3.591			90	90	90
Martensite/Ferrite (α)	Fe	bcc	$Im\bar{3}m$	2.86			90	90	90
Epsilon Phase Iron (ε)	Fe	hcp	$P6_3/mmc$	2.548	2.548	4.162	90	90	120
Sigma Steel (σ)	FeCr	tetragonal	$P4_2/mnm$	8.8	8.8	4.54	90	90	90
DMV304HCu	Alloy	fcc	$Fm\bar{3}m$	3.600			90	90	90
DMV304HCu Martensite	Alloy	bcc	$Im\bar{3}m$	2.887			90	90	90
Copper	Cu	fcc	$Fm\bar{3}m$	3.615			90	90	90
Manganese	Mn	bcc	$I\bar{4}3m$	8.913			90	90	90
Chromium	Cr	bcc	$Im\bar{3}m$	2.910			90	90	90
Spinels									
Chromium Manganese Spinel	$MnCr_2O_4$	fcc	$Fd\bar{3}m$	8.43			90	90	90
Chromium Iron Spinel	$FeCr_2O_4$	fcc	$Fd\bar{3}m$	8.38			90	90	90
Iron Manganese Spinel	$MnFe_2O_4$	fcc	$Fd\bar{3}m$	8.51			90	90	90
Manganese Iron Spinel	$FeMn_2O_4$	fcc	$Fd\bar{3}m$	8.51			90	90	90
Magnetite	Fe_3O_4	fcc	$Fd\bar{3}m$	8.38			90	90	90
Corundums									
Chromia	Cr_2O_3	Trigonal	$R\bar{3}c$	4.958	4.958	13.59	90	90	120
Hematite	Fe_2O_3	Trigonal	$R\bar{3}c$	5.00	5.00	13.7	90	90	120
Other Oxides									
Wustite	FeO	fcc	$Fm\bar{3}m$	4.3			90	90	90
Manganese(II) Oxide	MnO	fcc	$Fm\bar{3}m$	4.48			90	90	90
Manganese(III) Oxide	Mn_2O_3	cubic	$Ia\bar{3}$	9.41			90	90	90
Manganese(II, III) Oxide	Mn_3O_4	tetragonal	$I4_1/amd$	5.7	5.7	9.4	90	90	90
Manganese(IV) Oxide	MnO_2	various	---						
Silica	SiO_2	various	---						

The morphologies of oxide scales are often described by their Pilling–Bedworth (PB) ratios [166]. The PB ratio of an oxide formed by the reaction in (18) is calculated with (19). A PB > 2 indicates that the oxide scale will form non-protective flakes and that it may spall. A PB < 1 indicates that an oxide layer will not be continuous enough to provide protection from oxidation. A PB between 1 – 2 is likely to be adherent to the metal surface and may provide a protective barrier that reduces cation and anion transport from/to the metal surface. The PB ratios of common steel oxides are given in Table 17.

$$aM + \frac{b}{2}O_2 \rightarrow M_aO_b \qquad (18)$$

$$PB = \frac{A_O \rho_M}{a A_M \rho_O} \qquad (19)$$

A_O = molecular weight of oxide
A_M = atomic weight of metal
ρ_M = density of metal
ρ_O = density of oxide

Table 17 - Pilling Bedworth ratios of some common metals and oxides. Taken from [167]

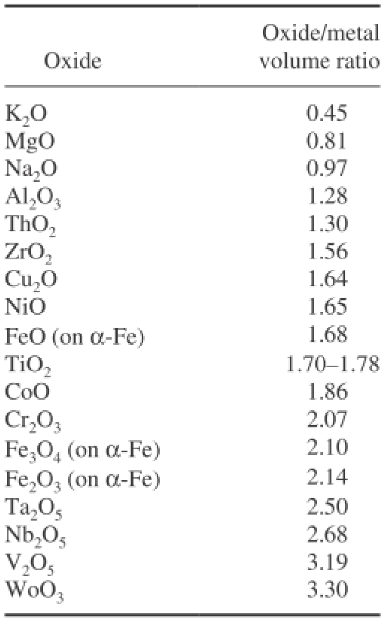

Oxide	Oxide/metal volume ratio
K_2O	0.45
MgO	0.81
Na_2O	0.97
Al_2O_3	1.28
ThO_2	1.30
ZrO_2	1.56
Cu_2O	1.64
NiO	1.65
FeO (on α-Fe)	1.68
TiO_2	1.70–1.78
CoO	1.86
Cr_2O_3	2.07
Fe_3O_4 (on α-Fe)	2.10
Fe_2O_3 (on α-Fe)	2.14
Ta_2O_5	2.50
Nb_2O_5	2.68
V_2O_5	3.19
WoO_3	3.30

2.7.2 Thermodynamics of Oxidation

An oxidation reaction will go ahead if the free energy of the reactants (G) would be lowered by the reaction. ΔG can be found for a reaction $A + B \rightarrow C$ using (20).

$$\Delta G = \Delta G^{\circ} + RT\left(\frac{p_c}{p_A p_B}\right) \qquad (20)$$

G = Gibbs free energy (J)
R = Gas Constant (J.K^{-1}mol^{-1})
T = Temperature (K)
P_A = Partial pressure of compound A (Pa)
P_B = Partial pressure of compound B (Pa)
P_C = Partial pressure of compound C (Pa)
G^0 = Free energy of formation at standard pressure (J.mol(O_2)$^{-1}$)

If a reaction is in equilibrium then ΔG = 0 and ΔG° can be expressed as shown in (21).

$$\Delta G^0 = -RT \ln k_p \qquad (21)$$

ΔG^0 = Standard Gibbs free energy of formation (J per mole O_2)
R = Gas Constant (J.K^{-1}mol^{-1})
T = Temperature (K)
k_p = Equilibrium Constant

If ΔG° < 0, the reaction can go ahead without any external energy required. This information can be used to show which oxides can be expected to form in a given temperature and partial pressure of oxygen using an Ellingham Diagram [168]. Figure 46 is an Ellingham diagram that has a number of common oxidation reactions listed on it. Each line shows the equilibrium points for the reactions at a given temperature. The more negative the ΔG° of a reaction is at a given temperature, the more stable the oxide is. Drawing a line from the O mark on the left-most line to the equilibrium point of a reaction at a given temperature and continuing that line to the p_{O2} marker will give the partial pressure of oxygen required for the oxidation reaction to go occur. If less oxygen than required is present then the reaction will be reversed and the oxide will be reduced.

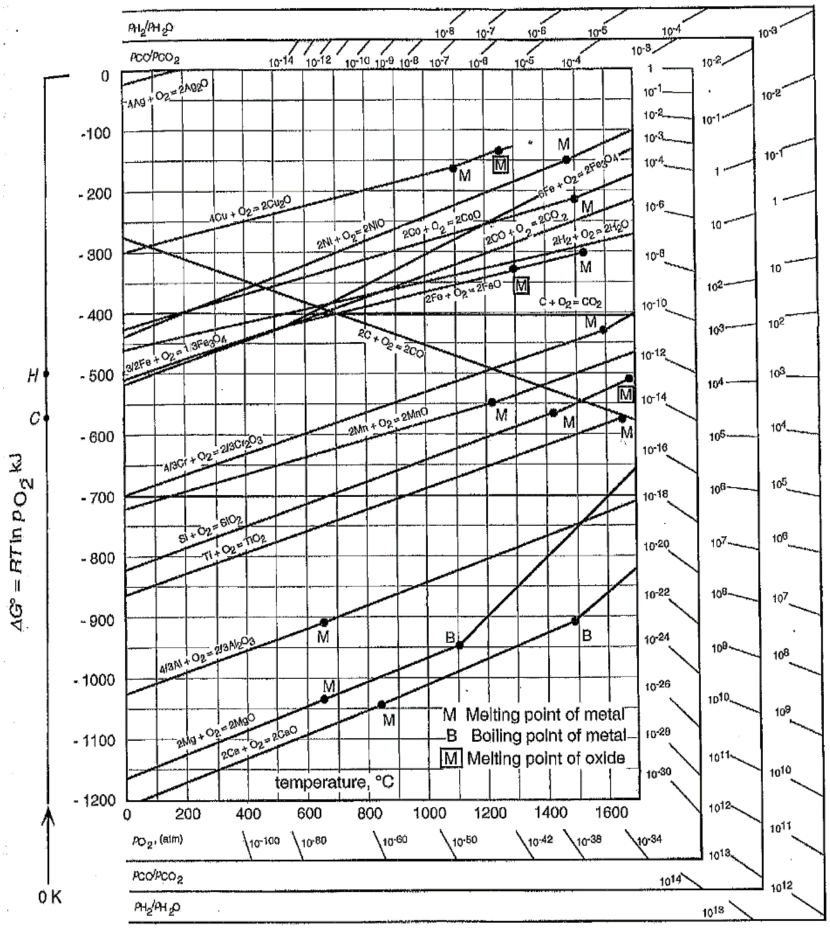

Figure 46 - Ellingham diagram for selected oxides taken from [169]

It can be seen in Figure 46 that in the range of 300-1000K the iron oxides are significantly less stable than chromia. Figure 47 shows that below 1200°C in air the oxide formed on a Cr-containing steel will be of a corundum structure. This means that if there is a high enough concentration of Cr present in the metal surface a steel will always form a protective layer of chromia when oxidized in air. Other oxides may form above the chromia layer, but the diffusion rate of cations through the chromia is greatly reduced compared to diffusion in the metal and may be too slow to support oxide growth (see Figure 39).

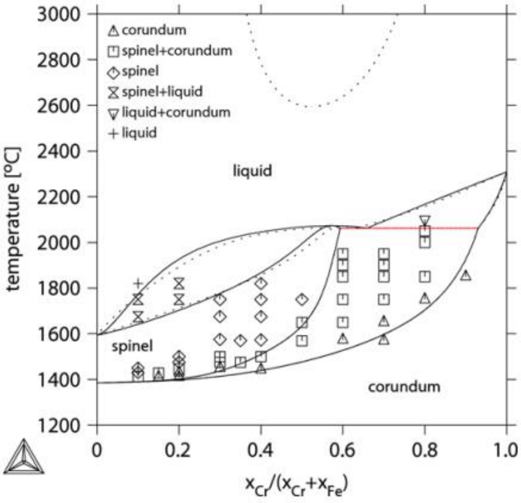

Figure 47 - Phase diagram of Cr-Fe-O in air at 1 atm. Taken from [170]

The oxide layer formed on stainless steels in most oxidizing conditions is either pure chromia or an Fe-Cr spinel, with layers above this being Fe-oxides [171], [172]. If the Cr content of the alloy was above a critical amount of Cr, N_{Cr}^{Crit}, then chromia could form. Below N_{Cr}^{Crit} the alloy would instead oxidize to form Fe-Cr spinel, with the proportion of Fe/Cr dependent on the Cr concentration. N_{Cr}^{Crit} depends on the oxidation atmosphere, temperature and surface preparation of the alloy, but generally N_{Cr}^{Crit} ≈ 15-20%wt.

The presence of water in the atmosphere further increases N_{Cr}^{Crit} and 304 steels do not reliably form chromia layers when oxidized at high temperatures in steam [173]. However, studies have found that shot peening 304 steels causes protective chromia to be formed under these conditions [98]. There is currently no model to predict N_{Cr}^{Crit} in alloys that takes all of the necessary factors into account.

2.7.2.1 Manganese Chromium Spinel

If there is sufficient Cr and Mn available at the metal surface it is possible that the oxide being formed is $MnCr_2O_4$ and this is significantly different from other spinels in regard to its thermodynamic stability. $MnCr_2O_4$ was observed in previous work with stainless steel, such as in [174], that in 1981 found that in a CO_2 atmosphere at 1123K a duplex oxide was grown, the outer layer being a $Mn(Fe,Cr)_2O_4$ spinel and the inner oxide rhombohedral Cr_2O_3. However, the potential importance of this specific spinel being formed by stainless steels in high temperature steam has only been recognized recently, such as in the 2016 work of Behnamian et al. [175], that found the spinel when oxidizing SS in 800°C supercritical water.

In 2010 Kjellqvist & Selleby built on previous modelling work of the C-Cr-Fe-Ni-O system[170] to include data for the Mn-Cr-O system[176]. The Mn-Cr-O system was also modelled by Jung [177] and Povoden et al. [178]. Figure 48 shows that in a Mn-Cr-O system **both** the spinel and chromia can be thermodynamically stable at temperatures of >500°C. Furthermore, the presence of Mn even in small fractional quantities can lead to the formation of the spinel or Mn-oxides instead of chromia.

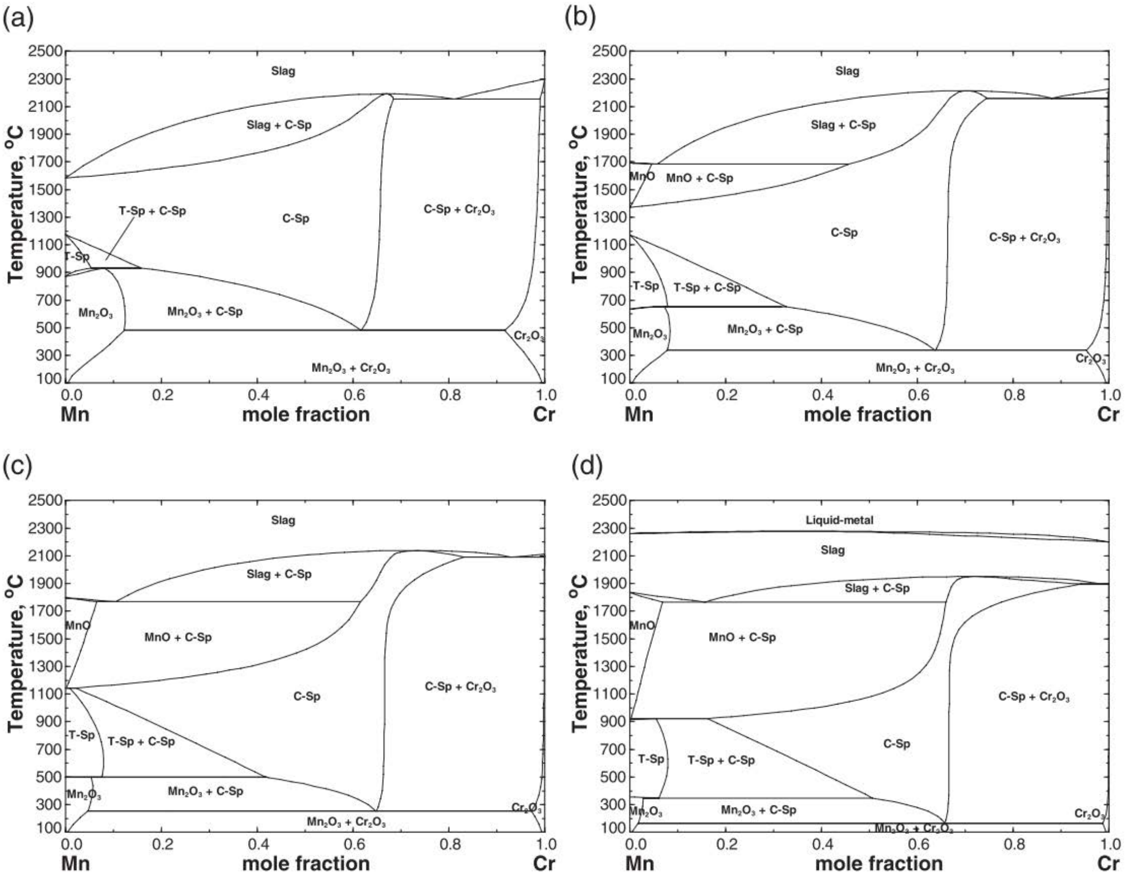

Figure 48 - Predicted phase diagrams of the Mn-Cr-O system at various oxygen partial pressures, P(O_2). Molar metal ratio vs temperature. (a) Air, (b) log P(O_2) = -3.0bar, (c) log P(O_2) = -5.0bar, (d) log P(O_2) = -8.0bar. C-Sp is the $MnCr_2O_4$ type spinel. T-Sp is Mn_3O_4 type spinel. Taken from [177]

2.7.3 Kinetics of Oxidation

For common materials there are three distinct kinetic regimes that describe the rate of oxidation; linear, logarithmic and parabolic, shown in Figure 49.

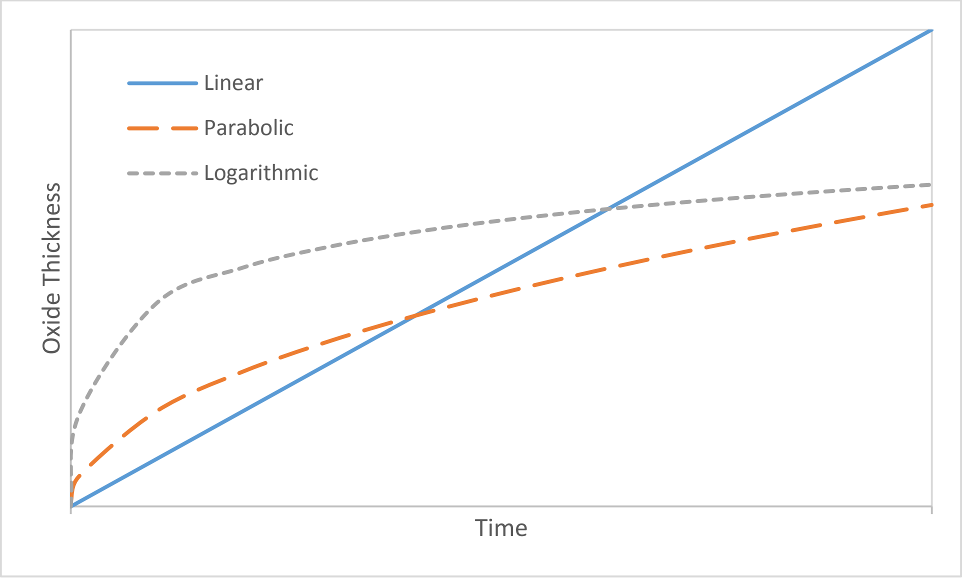

Figure 49 - Oxidation rate laws

Linear oxidation follows (22). This occurs when the oxide being formed is not protective and diffusion in the oxide layer is not the limiting factor. Logarithmic oxidation is described in (23). It is observed in very thin films less than 100nm in thickness and is associated with low temperature oxidation. The high temperature oxidation of an ideal protective oxide former is described by (24). Parabolic oxidation begins rapidly and then slows with time as the protective oxide layer grows thicker and acts as a larger and larger barrier to diffusion.

$$X = K_O t \qquad (22)$$
$$X = K_{L1} \log(K_{L2} t + K_{L3}) \qquad (23)$$
$$X^2 = K_P t \qquad (24)$$

X = oxide thickness
t = time
K_O = linear oxidation constant
K_P = parabolic oxidation constant
K_{L1}, K_{L2}, K_{L3} = logarithmic oxidation constants

2.7.3.1 Wagner's Model

Wagner created a diffusion based model of oxidation that is used as the base of most modern models [179]. Wagner's model includes the following assumptions:

- The oxide is compact and adherent
- Diffusion is the rate controlling process
- Thermodynamic equilibrium is established at both the metal/oxide and oxide/gas interface
- The oxide is stoichiometric
- Oxygen solubility in the metal is neglected

Figure 50 shows Wagner's model applied to the oxidation of Ni-Pt. The Ni anions move through the oxide by vacancy diffusion and this is the rate-limiting factor of the oxidation. Ni-Pt oxidizes according to the parabolic law, in agreement with the Wagner model.

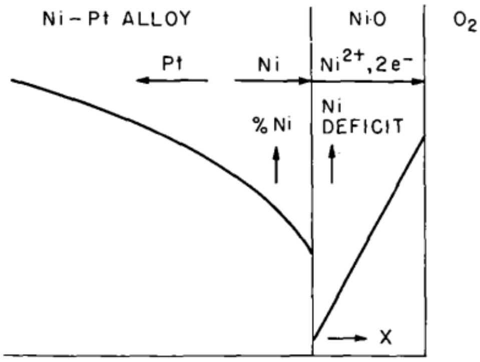

Figure 50 - Diffusion processes during the oxidation of Ni-Pt. Taken from [179]

For binary alloys with components capable of forming more than one oxide the concentration of components at the oxide/metal surface is important to determine what oxide scales will grow. Here, Wagner considers an alloy of A and B which both oxidize to AO and BO respectively. If the two oxides are both in equilibrium then:

$$\left(N_{A(i)}\right)^2 p_{ox(i)} = \pi_{ox(AO)} \text{ for oxide AO} \tag{25}$$

$$\left(N_{B(i)}\right)^2 p_{ox(i)} = \pi_{ox(BO)} \text{ for oxide BO} \tag{26}$$

$$N_B = 1 - N_A \tag{27}$$

$N_{A(i)}$ = molar fraction of element A at oxide/metal surface

$N_{B(i)}$ = molar fraction of element B at oxide/metal surface

$\pi_{ox(AO)}$ = partial pressure of dissociation of AO into A and O.

$\pi_{ox(BO)}$ = partial pressure of dissociation of BO into B and O.

$p_{ox(i)}$ = partial pressure of oxygen

As an example Wagner then assumed that $\pi_{ox(BO)} = 10\ \pi_{ox(AO)}$ to produce Figure 51, which predicts at which alloying mixtures a single phase oxide and multi-phase oxides will be present.

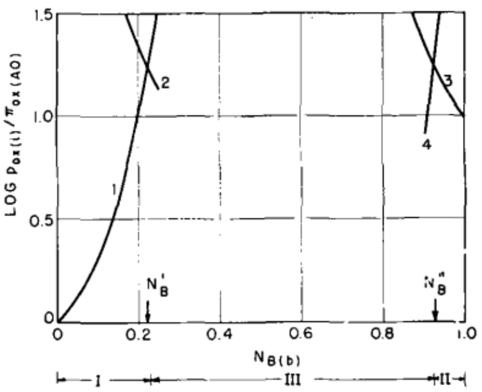

Figure 51 - Oxygen equilibrium pressures at the interface between A-B alloys and growing oxide layers of AO and BO [179]

1. *Oxygen equilibrium pressure at the metal/gas interface of the alloy and AO*
2. *Oxygen pressure for virtual equilibrium between the alloy and BO at the AO/metal interface*
3. *Oxygen equilibrium pressure at the metal/gas interface of the alloy and BO*
4. *Oxygen pressure for virtual equilibrium between the alloy and AO at the BO/metal interface*

Region I – Exclusive formation of AO, Region II – Exclusive formation of BO, Region III – Formation of both AO and BO

Wagner's model provides qualitative solutions for multicomponent alloys but has a number of shortcomings that future work has attempted to overcome. One impact of significance to SS is that the model does not account for non-reactive components and how they will become enriched by the diffusion of the oxidizing components [180]. In SS >10% of the alloy is Ni which does not form any oxides under most service conditions. The model assumes a single phase metal and does not include any effects from microstructures such as GBs and dislocations. It also does not model internal oxidation of the metal by gas species penetrating the oxide layer, which could have a considerable effect on the kinetics by altering diffusion rates from the metal.

Essuman et al. use Wagner's model to find the requirements of an Fe-Cr model alloy to form a protective, continuous chromia layer [58]. The relationships they give are (28), which is required to prevent internal oxidation and (29), which is required to grow a chromia layer. These values are for a simplified model that only forms chromia and no other oxides.

$$N_{Cr}^{(1)} > \left[\frac{\pi g^*}{3} N_O^{(S)} \frac{D_O V_m}{\widetilde{D}_{Fe-Cr} V_{CrO_{1.5}}}\right]^{\frac{1}{2}} \qquad (28)$$

$N_{Cr}^{(1)}$ = Molar fraction of Cr in alloy
$N_O^{(s)}$ = Oxygen solubility in alloy
D_O = Diffusivity of oxygen in alloy (cm^2/s)
$\widetilde{D}_{Fe-Cr}$ = Alloy interdiffusion coefficient (cm^2/s)
V_m = Molar volume of alloy
$V_{CrO_{1.5}}$ = Molar volume of oxide
g* = factor, approximated to 0.3

$$N_{Cr}^{(2)} = \frac{V_m}{32V_O}\left(\frac{\pi k_p}{\widetilde{D}_{Fe-Cr}}\right)^{\frac{1}{2}} \tag{29}$$

$N_{Cr}^{(2)}$ = Molar fraction of Cr in alloy
$\widetilde{D}_{Fe-Cr}$ = Alloy interdiffusion coefficient
V_m = Molar volume of alloy
V_O = Molar volume of oxide
k_p = parabolic rate constant (in terms of scale thickness) (cm^2/s)

(28) and (29) were used with literature data to conclude that either (i) the presence of water vapour in the atmosphere was increasing the effective value of $N_O^{(s)}$, i.e. providing a greater concentration of oxygen at the oxide surface than the atmosphere would if it was dry. Or (ii) the presence of hydrogen in the alloy was increasing the effective diffusivity of oxygen, D_O.

It is possible that $N_{Cr}^{(1)}$ and $N_{Cr}^{(2)}$ could act as a starting point for creating a model to calculate N_{Cr}^{Crit}.

2.7.4 Oxidation of Stainless Steels in Air

Figure 52 shows the typical growth curves for chromia forming steels in high temperature environments. A protective chromia layer is formed which limits the growth rate of the oxide layer to a parabolic form, because of the slower diffusion rate of cations through the oxide. The scale can then spall at (A) and the growth rate of the oxide layer increases drastically. The time (AB) is linear growth because iron is exposed to the oxidizing atmosphere and a non-protective oxide grows. At (B) the concentration of Cr has increased sufficiently to begin reforming the chromia layer and parabolic growth takes place again (BC). This general pattern is observed in the literature whenever Fe-Cr containing alloys are oxidized in a relatively oxygen-rich atmosphere [181], and many studies showing this are listed in appendix A.3.

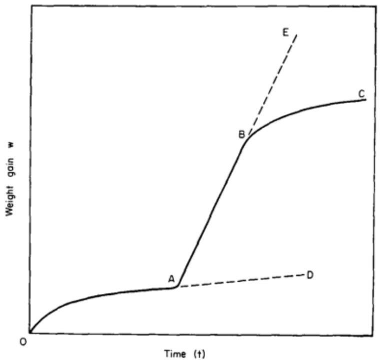

Figure 52 - Typical growth curve of iron-chromium alloys and stainless steels. Taken from [171]

In stainless steels such as 304 the oxide layer formed in air at high temperatures is not only chromia, but also spinel. In [182], Botella et al. identify a layer of $MnCr_2O_4$ spinel formed above a layer of chromia in 304 steel oxidized in air at 700°C. After oxidation of 18Cr-8Ni steel in air at 750°C Naraparaju et al. [116] found that the oxide layer formed was an Fe-Cr spinel and no chromia formed unless the surface was first shot peened. Trindade et al. [183] also found that 347 steel oxidized in air at 750°C formed a thin layer of chromia but this was below significantly thicker layers of Fe_2O_3/Fe_3O_4 and unidentified oxides of Fe, Cr and Mn. This is suggestive of a structure shown in Figure 53, and the difference in chromia formation between 18Cr-8Ni steel and 347 is caused by the slightly elevated Cr/Ni/Mn content of the 347 compared to the 18Cr-8Ni. At a lower temperature of 600°C Asterman et al. [184], [185] do not observe any spinel forming and only find chromia.

In all of the previously mentioned air oxidation experiments there would sometimes be regions of Fe-rich material on the surface described as 'nodules' or 'islands'. The islands allow a limited amount of internal oxidation beneath them. These are suggested to be locations of lower Cr concentration that are unable to form a completely protective oxide. This leads to iron cations diffusing to the gas/oxide interface and oxygen anions diffusing into the base metal, both of which are then able to make non-protective Fe-oxides that further enhance the speed of this process.

The rate-controlling factor in the oxide growth is the rate of diffusion of metal ions through the oxide scales. At temperatures >700°C the rate of diffusion increases such that iron oxides can form on the surface while the underlying chromia layer can remain intact.

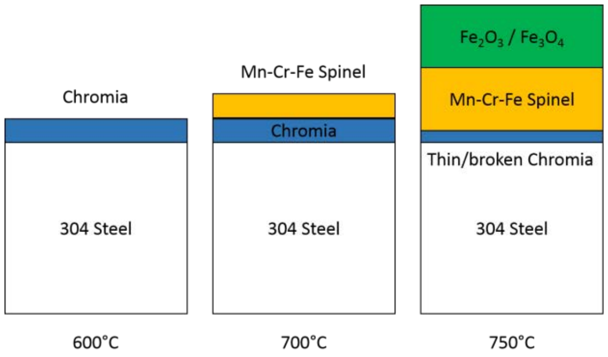

Figure 53 - Oxides grown on 304 steel at elevated temperatures in air

2.7.5 Oxidation of Austenitic Steels in 'Wet' Atmospheres

As explained in the section "Oxygen Content", this document defines a 'wet' atmosphere as one containing both water and levels of oxygen significantly higher than the recommended 10ppb for power plant steam. High oxygen conditions have the advantage of being more easily reproducible in the lab and many wet-air studies are listed in appendix A.1. It is very well established that austenitic SS will oxidize more rapidly in wet atmospheres than in dry air and it is a significant part of several literature reviews: [7, 171, 173, 186]. The oxide layers grown in wet air are thicker and more iron rich than in dry air and there can be significant internal oxidation.

In [187], Hansson et al oxidized 304 steel in wet oxygen at 600°C and found that Fe-rich oxide islands formed on the surface after only 168hrs of exposure. Figure 54 shows one such island and how it includes both internal oxidation and outward oxide growth. The base oxide that had not formed islands was a thin (<100nm) layer of corundum-type oxide richer in Cr and Mn than the base steel. No spinel was detected in the thin oxide layer despite the 8-12%wt Mn content. The oxide islands were iron-rich corundum-type oxides above the metal surface and spinel-type Fe-Cr oxides in the IOZ. Underneath the oxide crater there was a thin layer of bcc steel, but the paper does not draw any conclusions or provide further information about this particular feature.

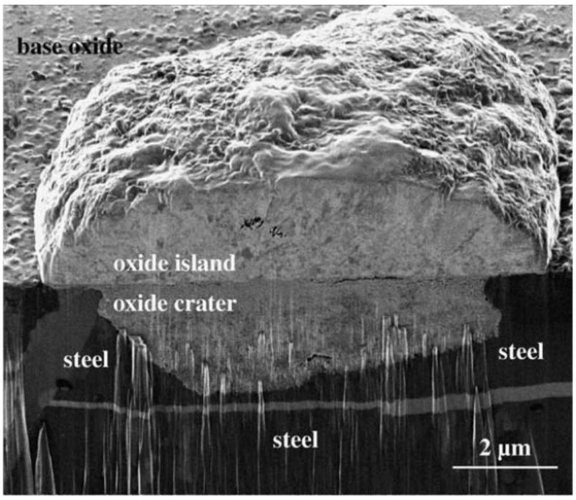

Figure 54 – FIB image of an oxide island grown on 304 steel in wet oxygen atmosphere at 600°C after 168hrs. Taken from[187]

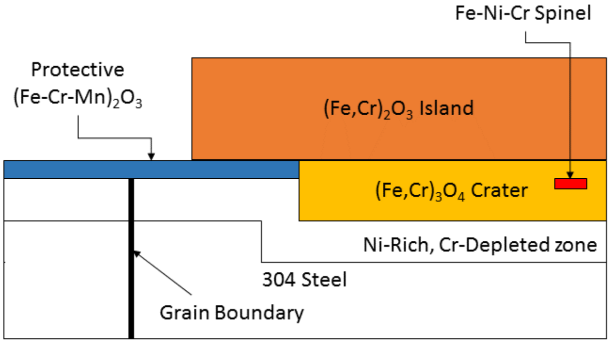

Figure 55 - Schematic of the oxides grown on 304 steel in wet oxygen atmosphere at 600°C after 168hrs.

Therefore, the introduction of water to an oxidizing environment causes an increase in external oxidation rate and promotes internal oxidation that is not seen in dry air oxidation.

2.7.6 Oxidation of Austenitic Steels in Steam

Hansson et. al. [188] found that 347 steel exposed to wet argon at 600-700°C showed significant internal oxidation after 336hrs and that much of the oxide had a spinel structure. Figure 56 (b) shows how the inward growth of the oxide was slowed and stopped at grain boundaries where Cr concentrations were enriched. The outward growth of Fe-rich spinel was accelerated by the presence of H_2 added to the wet carrier gas, which also has the effect of reducing the oxygen content of the atmosphere and may better approximate a 'steam' environment. Figure 56 (b) shows that in a 8%-H_2O atmosphere with added H_2 the internal oxidation is significantly slowed compared to atmospheres without added H_2. A possible explanation for this is that the H_2 addition enhances cation transportation and that the increased Cr availability compensates for the increased internal oxidation rate. In Figure 56

(d) shows that in a 46%-H_2O environment the higher Cr mobility may not be enough to overcome the effects of the higher H_2O content. This will be discussed in more detail in the oxidation mechanisms section. A summary of these findings are shown in Figure 57.

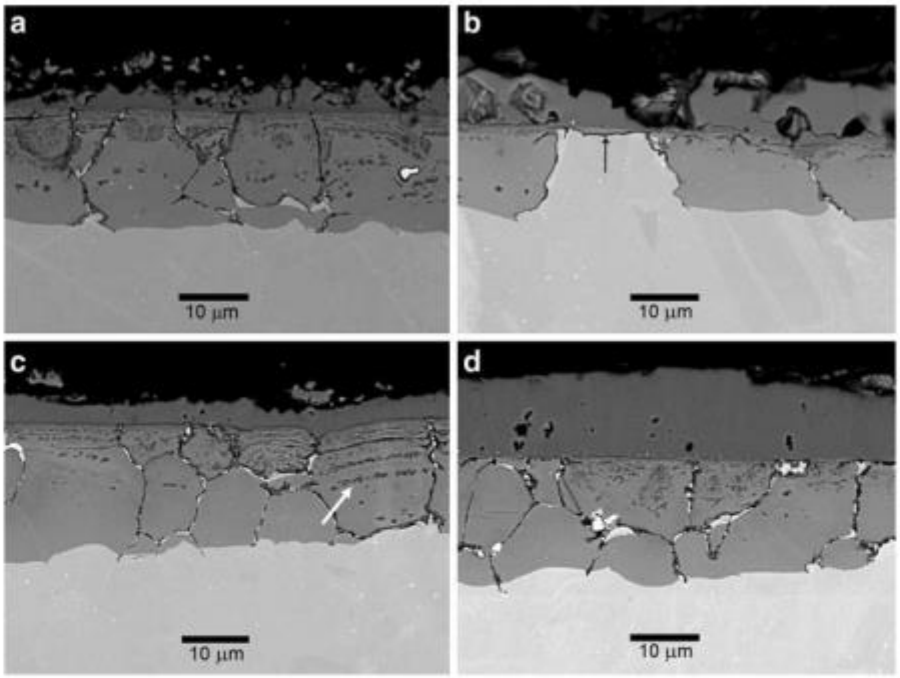

Figure 56 - BSE-SEM micrographs of 347H oxidized at 600°C for 336h in (a)Ar-8%H_2O (b)Ar-7%H_2-8%H_2O (c)Ar-46%H_2O (d)Ar-7%H_2-46%H_2O. Taken from [188]

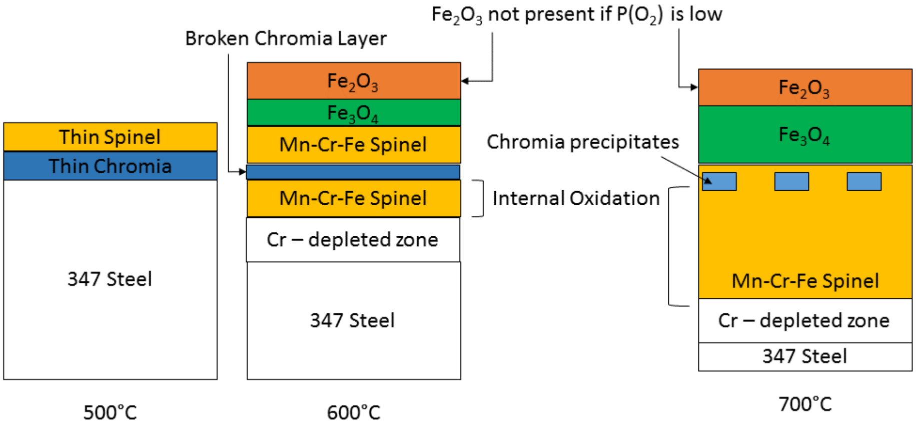

Figure 57 - Schematic of oxide layers found on 347 steel oxidized in wet argon for 336hrs.

2.7.7 Oxidation of Shot Peened Steels

A qualitative relationship between cold working and improved oxidation resistance in 304 steels has been established since the 1960’s when Warzee et al. published an experiment on the effects of different surface treatments on steel oxidation in steam between 400-600°C[189]. The oxide layers grown on ground 304 steel were much thinner and richer in Cr and Mn than in electro-polished or pickled samples. Further examination of the effects of cold work and grain size were carried out by Otsuka et al in the 1980’s-1990’s and sought to produce a model to calculate N_{Cr}^{Crit} in stainless steels [190, 191]. A very limited number of grain sizes were investigated in both papers with the key results shown in Figure 58, Figure 59 and Figure 60. The model proposed by Otsuka et al. produced a very limited dependence of $\mathrm{N_B^O(i,ii)}$ on grain size, which is the minimum amount of Cr required to grow an external protective oxide. However, a much more significant relationship was seen between $\mathrm{N_B^O(ox)}$ and grain size, which is the fraction of Cr required for a 15%Ni steel to form a protective internal oxide. It was thought that $\mathrm{N_B^O(i,ii)}$ explained line(a) in Figure 58 and that $\mathrm{N_B^O(ox)}$ explained line (b).

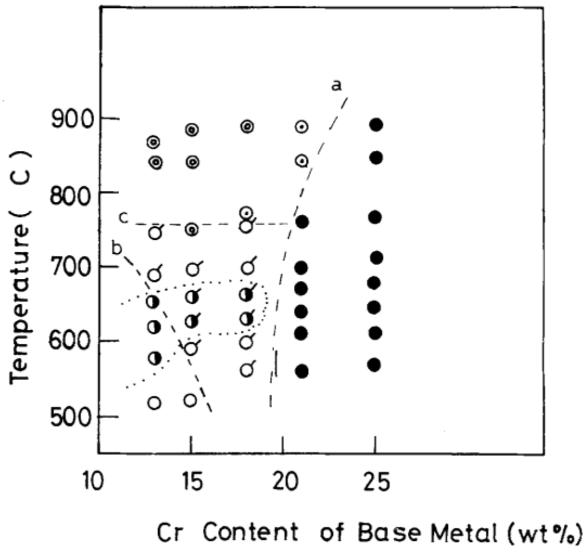

Figure 58 - Effect of Cr concentration on oxide growth characteristics in Fe-Cr-15%Ni steel with grain size ≈110µm. (●) External continuous chromia layer, (⊙) Multiple layers of internal/external oxides growing into the matrix with external iron rich oxide, (○) External spinel oxide with outer iron rich oxides, (◑) Internal oxidation stopped at grain boundaries, (○’) Limited internal oxidation, Fe-rich external oxide, (◑’) Both (○’) and (◑) observed at surface. Taken from [190].

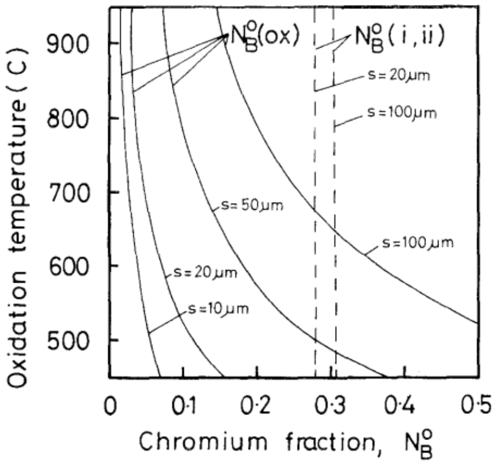

Figure 59 - Effect of grain size on calculated limiting bulk concentrations of Cr in Fe-Cr alloys. Effect of grain size on calculated limiting bulk concentrations of Cr in Fe-Cr alloys. $N_B^O(ox)$ is the minimum Cr required to grow chromia internally. $N_B^O(i, ii)$ is the minimum Cr required to grow an external chromia layer. S = grain diameter. Taken from [190].

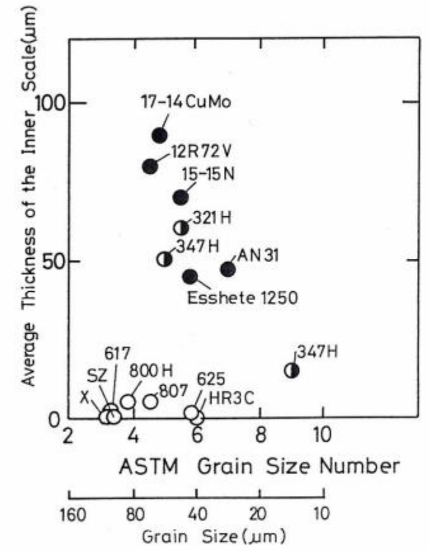

Figure 60 - Average thickness of inner oxide layer of steam-oxidized steels at 700°C for 1000hrs and their observed grain size. (●) 16wt% Cr, (◑)18% wt% Cr, (○)>20wt% Cr. Taken from [191].

Since the publication of the work of Otsuka et al. there has been little progress in modelling the processes that lead to improved oxidation resistance in shot peened austenitic SS. However, increasing interest in shot peened SS for use in SC power plants has provided a surge in research since 2009. There is now a significant number of observations on the oxidation behaviour of shot peened steels, including [98, 114, 160, 192–195].

2.7.8 Oxidation Mechanisms

The reason why oxidation is enhanced in water-containing atmospheres is not certain and several theories are put forwards in the literature. In wet atmospheres with sufficient oxygen the driving force may be chromium volatilization. Other mechanisms are suggested to be at work in steam atmospheres with a low partial pressure of oxygen; Hydrogen Enhanced Oxygen Diffusivity, Hydrogen Enhanced Cation Diffusivity, Water Vapour Enhanced Oxygen Diffusion and increased microcracking in the oxide.

2.7.8.1 Chromium Volatilization

Asteman et al. suggest that chromium is lost by the chemical reaction shown in (30) [196]. However, there is disagreement in the literature as to how much chromium can be lost through this method when there is very little oxygen present in the atmosphere. The studies performed by Asteman et al. were in wet air and in temperature ranges that encourage Cr evaporation.

$$\frac{1}{2}Cr_2O_3(s) + H_2O(g) + \frac{3}{4}O_2(g) \rightarrow CrO_2(OH)_2(g) \qquad (30)$$

It has been reported by Opilia et al. that there is a wide spread in the figures both calculated and found by experiment for the rates of the reactions involved in (30) [197, 198]. Furthermore, experiments by Quadakkers et al. show that the reaction becomes negligible at low oxygen partial pressures [59].

The potential for chromium volatilization is further complicated by the oxide morphology. If a spinel, such as Fe_3O_4, is present above a Cr-rich oxide it will act to reduce the partial oxygen pressure and the flow rate experienced by the Cr-containing oxide. An oxide that is not traditionally protective, because it does not significantly slow anion or cation diffusion, can therefore be advantageous by reducing chromium volatilization.

2.7.8.2 Hydrogen Enhanced Oxygen Diffusivity

Essuman et al. suggest that the presence of hydrogen in the metal matrix causes the matrix to expand in order to accommodate the hydrogen interstitials [58]. The larger separation between atoms in the matrix then allows oxygen anions to diffuse into the metal at an enhanced rate and raises the effective partial pressure of oxygen.

2.7.8.3 Increased Micro-cracking in Oxide

Hansson et al. suggests that the presence of water vapour causes the oxide layer to become more porous and develop microscopic cracks as it grows [188]. This could be caused by the presence of H_2 gas in the metal or oxide, by mismatches in the PB-ratio of the oxide layers or by void formation. Micro-cracks would create areas of metal that were effectively unprotected from the atmosphere. However, observing and quantifying such cracks would be extremely difficult, since most sample preparation techniques, including FIB, could introduce very small cracks or relax the oxide layers and conceal them. One possible technique to look for micro-cracking would be high resolution 3D X-ray tomography, which can provide images of the oxide layer without cross sectioning [199].

2.7.8.4 Hydroxide Diffusion

Oxidation models often assume that the process in (32) is responsible for the generation of oxygen from water vapour. Work by Wouters et al. in Ti oxidation[200] and Yuan et al. in pure Fe[201] theorize that the dominant mechanism for anion generation and transport in Fe and Ti oxides instead utilizes hydroxide ions formed by (33). This is shown schematically in Figure 61.

$$H_2O(g) \leftrightarrow H_2O(ads) \tag{31}$$

$$H_2O(ads) \leftrightarrow O_0 + H_2 + V_{Fe}^{2-} + 2e^+ \tag{32}$$

$$H_2O(ads) + V_O^{2+} \leftrightarrow OH_O^- + H_i^- \tag{33}$$

$$2H_i^- + 2e \leftrightarrow H_2 \tag{34}$$

(ads) = adsorption
O_O = Oxygen in an Oxygen site in the oxide matrix
V_{Fe}^{2-} = Iron vacancy in oxide matrix (with charge 2-)
e^+ = Electron hole
V_O^{2+} = Oxygen vacancy in oxide matrix (with charge 2+)
OH_O^- = Hydroxide Ion on Oxygen site in oxide matrix (with charge 1-)
H_i^- = Hydrogen ion on interstitial site in oxide matrix (with charge 1-)

The OH_O^- anion may pass more easily through the oxide and metal matrix because of its smaller valence. The generation of H_2 gas may further enhance oxidation by diffusing into the oxide and metal matrix were it is known to cause micro-cracking and voids.

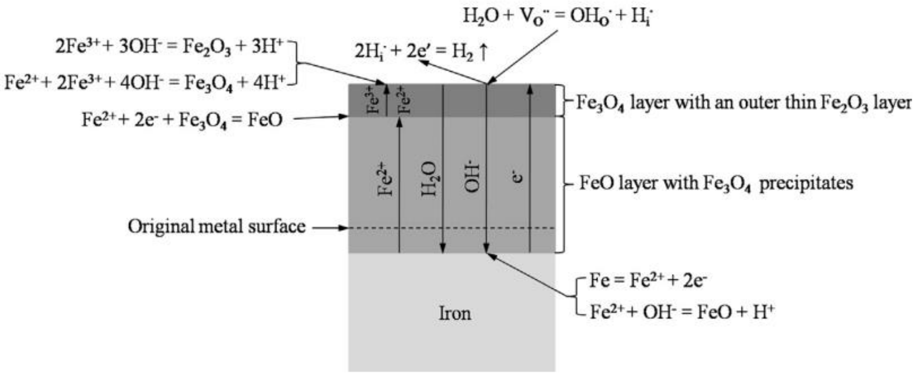

Figure 61 - Schematic illustration of oxidation process of iron in steam. Taken from [201].

2.8 Summary of Literature Review

The need for increasing efficiency in thermal power plants is driving a significant amount of research and development of new high temperature materials for use in the steam cycle. Candidate materials are required to show suitable creep strength in the new higher temperature ranges and also to resist steam-side oxidation in super critical water at higher pressures.

Much of the research being performed is focused on austenitic stainless steels such as grade 304HCu because the materials are already in use in existing power plant. Austenitic steels also offer economic benefits and better formability than nickel-based super alloys. Finding ways to improve existing alloys is therefore a high priority in materials development for thermal power plant.

This thesis will focus on the improvements in oxidation performance of shot peening austenitic stainless steels. Shot peening describes the process of bombarding a component with 'shot' at high velocity to induce a change in microstructure in the component's surface. The impact of the shot plastically deforms the object's surface and breaks down the metal grains into a finer microstructure. Studies into various forms of peening have used XRD and TEM to characterise the changes in target material microstructure, but there is not yet a model that can be used to predict the effects of the shot peening process in detail.

In this thesis the most important microstructural change caused by shot peening austenitic stainless steel will be the reduction of grain size. This is being investigated extensively in the literature in regards to the affect that grain size reduction has on austenitic steels. Shot peening is known to reduce the oxidation rate of some grades of austenitic steel, but not others, and the mechanism of improvement is not fully understood. This thesis aims to contribute to the research effort to fill the gaps in knowledge surrounding the improvement of oxidation resistance in austenitic SS.

Observing the shot peened microstructure is difficult because it so close to the surface. Studies have used TEM to image the region, but this is difficult and observes only a small area. A faster method to characterise the change in microstructure is using hardness testing. Shot peened material is harder than unaffected material and the hardness profile of a surface is frequently used to identify the depth and intensity of the changes made by shot peening. The hardness of shot peened material is linked to its microstructure through the Hall-Petch relationship. However, microhardness testing cannot take reliable measurements if the indentations are made so close to the edge that they interact with it. At such small distances it is necessary to use nanohardness testing.

In temperatures above 500°C the hardness of shot peened steel is observed to decrease over time as the shot peened region recrystallizes. There is still uncertainty in the literature as to the degree to which grain size and hardness are linked in shot peened material. The reduction in hardness can also be accounted for by relaxation and dislocation annihilation.

Shot peened stainless steel is known to resist oxidation more than untreated steel in dry and wet air. However, in power plant steam the rate of oxidation of austenitic steel grades such as 304HCu is higher than in dry conditions. The presence of water vapour causes austenitic stainless steels to oxidize internally, while in dry conditions they form an external protective oxide. The reasons for this change in behaviour are still being discussed in the literature and several mechanisms for the process have been suggested.

Models have been proposed to predict the oxidation rate of austenitic stainless steels based on their Cr content. These models, such as those of Wagner, rely on calculating the flux of Cr to the metal/oxide interface, and as such rely heavily on the data from tracer diffusion experiments. Diffusivity data in the literature shows a significant range of values and there are known short comings in the methodologies employed. Of special relevance to this thesis are the models of grain boundary diffusion; diffusion data for grain boundaries make a number of assumptions and simplifications that are known to produce conflicting data points. For example, the segregation constant, S, approaches 1 in a pure metal, but in most studies and models for steel alloys the value of 1 is still used. The thickness of grain boundaries is also open to dispute, with the literature generally using values in the range of 0.5-1nm.

This thesis will investigate the predictions of the effects of shot peening on austenitic stainless steel and its oxidation resistance.

2.9 References

1. Matthieumarechal, U. (2008). Phase Diagram of Water. *Wikipedia*. Retrieved from https://upload.wikimedia.org/wikipedia/commons/3/34/Phase-diag2.svg

2. Bugge, J., Kjar, S., & Blum, R. (2006). High-efficiency coal-fired power plants development and perspectives. *Energy*, *31*(10–11), 1437–1445. doi:10.1016/j.energy.2005.05.025

3. Electric Power Research Institute. (2002). *Cycle Chemistry Guidelines for Fossil Plants : All-volatile Treatment*.

4. EPRI. (2006). *Condensate Polishing Guidelines For Fossil Plants* (Vol. 1010181). Palo Alto.

5. EPRI. (2002). *Cycle Chemistry Guidelines for Fossil Plants: All-Volatile Treatment* (Vol. 1004187). Retrieved from http://scholar.google.co.za/scholar?q=related:gx47zJiOmXMJ:scholar.google.com/&hl=en&as_sdt=0,5#8

6. Zhu, Z., Xu, H., Jiang, D., & Zhang, N. (2016). Temperature Dependence of Oxidation Behaviour of a Ferritic–Martensitic Steel in Supercritical Water at 600–700 °C. *Oxidation of Metals*, *86*(5–6), 483–496. doi:10.1007/s11085-016-9647-7

7. Wright, I. G., & Dooley, R. B. (2010). A review of the oxidation behaviour of structural alloys in steam. *International Materials Reviews*, *55*(3), 129–167. doi:10.1179/095066010X12646898728165

8. Guzonas, D., & Novotny, R. (2014). Supercritical water-cooled reactor materials - Summary of research and open issues. *Progress in Nuclear Energy*, *77*, 361–372. doi:10.1016/j.pnucene.2014.02.008

9. Sun, C., Hui, R., Qu, W., & Yick, S. (2009). Progress in corrosion resistant materials for supercritical water reactors. *Corrosion Science*, *51*(11), 2508–2523. doi:10.1016/j.corsci.2009.07.007

10. Abe, F., Kern, T. ., & Viswanathan, R. (2008). *Creep-resistant steels*. Woodhead Publishing Limited.

11. Abe, F. (2008). Stress to produce a minimum creep rate of 10−5%/h and stress to cause rupture at 105h for ferritic and austenitic steels and superalloys. *International Journal of Pressure Vessels and Piping*, *85*(1–2), 99–107. doi:10.1016/j.ijpvp.2007.06.005

12. Pramanick, A. K., Das, G., Das, S. K., & Ghosh, M. (2017). Failure investigation of super heater tubes of coal fired power plant. *Case Studies in Engineering Failure Analysis*, *9*(May), 17–26. doi:10.1016/j.csefa.2017.06.001

13. Scheffknecht, G., & Chen, Q. (2000). Material issues for supercritical boilers. In A. Strang, W. M. Banks, R. . Conroy, G. . McColvin, J. . Neal, & S. Simpson (Eds.), *Parsons 2000: Advanced materials for 21st century turbines and power plant* (pp. 249–264). Cambridge, UK: IOM Communications Ltd.

14. Viswanathan, R., Henry, J. F., Tanzosh, J., Stanko, G., Shingledecker, J., Vitalis, B., & Purgert, R. (2005). U.S. Program on Materials Technology for Ultra-Supercritical Coal

Power Plants. *Journal of Materials Engineering and Performance*, *14*(3), 281–292. doi:10.1361/10599490524039

15. Starr, F., & Shibli, I. . (2000). Fundamental issues in the development of austenitic and nickel based alloys for advanced supercritical steam and high temperature indirect gas turbine systems. In A. Strang, W. M. Banks, R. . Conroy, G. . McColvin, J. . Neal, & S. Simpson (Eds.), *Parsons 2000: Advanced materials for 21st century turbines and power plant* (pp. 459–471). Cambridge, UK: IOM Communications Ltd.
16. Tancret, F., & Bellini, M. (2008). Properties, processability and weldability of a novel affordable creep resistant nickel base superalloy. *Materials Science and Technology*, *24*(4), 479–487. doi:10.1179/174328408X295999
17. Lancaster, R. J., Whittaker, M. T., & Williams, S. J. (2013). A review of thermo-mechanical fatigue behaviour in polycrystalline nickel superalloys for turbine disc applications. *Materials at High Temperatures*, *30*(1), 2–12. doi:10.3184/096034013X13630238172260
18. Zhang, P., Zhu, Q., Chen, G., & Wang, C. (2015). Review on Thermo-Mechanical Fatigue Behavior of Nickel-Base Superalloys. *Materials Transactions*, *56*(12), 1930–1939. doi:10.2320/matertrans.M2015323
19. Vanstone, R. . (2000). Advanced (700°C) pulverised fuel power plant. In A. Strang, W. M. Banks, R. . Conroy, G. . McColvin, J. . Neal, & S. Simpson (Eds.), *Parsons 2000: Advanced materials for 21st century turbines and power plant* (pp. 91–97). Cambridge, UK: IOM Communications Ltd.
20. Staubli, M. ., Mayer, K.-H., Kern, T. ., & Vanstone, R. . (2000). COST 501/COST 522 - The european collaboration in advanced steam turbine materials for ultra efficicent, low emission steam power plant. In A. Strang, W. M. Banks, R. . Conroy, G. . McColvin, J. . Neal, & S. Simpson (Eds.), *Parsons 2000: Advanced materials for 21st century turbines and power plant* (pp. 98–122). Cambridge, UK: IOM Communications Ltd.
21. COST. (n.d.). COST Action 536 - Alloy development for Critical Components of Environmental friendly Power plantT (ACCEPT). *COST website*. Retrieved August 26, 2010, from http://w3.cost.eu/index.php?id=248&action_number=536
22. Pint, B. a. (2013). High-Temperature Corrosion in Fossil Fuel Power Generation: Present and Future. *Jom*, *65*(8), 1024–1032. doi:10.1007/s11837-013-0642-z
23. Oshima, T., Habara, Y., & Kuroda, K. (2007). Efforts to Save Nickel in Austenitic Stainless Steels. *ISIJ International*, *47*(3), 359–364. doi:10.2355/isijinternational.47.359
24. Ashby, M. F., & Jones, D. R. H. (1988). *Engineering materials 2: an introduction to microstructures, processing and design*. Oxford: Pergamon Press. Retrieved from http://books.google.com/books?id=wkOl953ZG-UC&pgis=1
25. World Steel Association. (2010). World Steel Production 2009.
26. International Stainless Steel Forum. (2009). 2009 Stainless and Heat Resisting Steel Crude Steel Production. Retrieved from http://www.worldstainless.org
27. Gardner, L. (2005). The use of stainless steel in structures. *Progress in Structural*

Engineering and Materials, *7*(2), 45–55. doi:10.1002/pse.190

28. Cobb, H. M. (2007). The naming and numbering of stainless steels. *Advanced Materials & Processes*, *165*(9), 39–44.

29. Oberg, E., Horton, H. L., Jones, F. D., & Ryffel, H. H. (2008). *Machinery's Handbook*. (F. D. Jones, H. H. Ryffel, C. J. McCauley, & R. M. Heald, Eds.) (28th ed.). Industrial Press. Retrieved from http://books.google.com/books?id=ZaqAPwAACAAJ&pgis=1

30. Davis, J. R. (Ed.). (1998). *Metals Handbook* (Desk ed. ,.). Materials Park, OH: ASM International.

31. Steiner, R., & ASM. (1990). *ASM Handbook, Volume 1: Properties and Selection: Irons, Steels, and High-Performance Alloys*. ASM International. Retrieved from http://books.google.com/books?id=IsiPbwAACAAJ&pgis=1

32. Lo, K. H., Shek, C. H., & Lai, J. K. L. (2009). Recent developments in stainless steels. *Materials Science and Engineering: R: Reports*, *65*(4–6), 39–104. doi:10.1016/j.mser.2009.03.001

33. Honeycombe, R. W. K., & Hadeshia, H. K. D. H. (1995). *Steels: microstructure and properties* (2nd ed.). London: Edward Arnold. Retrieved from http://books.google.com/books?id=8okWjoJhP5AC&pgis=1

34. F. C. Hull. (1973). Delta Ferrite and Martnesite Formation in Stainless Steels. *Welding journal*, (May), 193–203. Retrieved from http://ww.aws.org/wj/supplement/WJ_1973_05_s193.pdf

35. Olson, G. B., & Cohen, M. (1976). A general mechanism of martensitic nucleation: Part II. FCC to BCC and other martensitic transformations. *Metallurgical Transactions A*, *7*(12), 1905–1914. doi:10.1007/BF02659823

36. Dyson, D. J., & Holmes, B. (1970). Effect of Alloying Additions on the Lattice Parameter of Austenite. *Journal of the Iron and Steel Institute*, *208*, 469.

37. Cheng, L., Böttger, a., de Keijser, T. H., & Mittemeijer, E. J. (1990). Lattice parameters of iron-carbon and iron-nitrogen martensites and austenites. *Scripta Metallurgica et Materialia*, *24*(3), 509–514. doi:10.1016/0956-716X(90)90192-J

38. Li, C. M., Sommer, F., & Mittemeijer, E. J. (2002). Characteristics of the alpha to gamma transformation in Fe-Mn alloys. *Materials Science and Engineering A*, *325*(1–2), 307–319. doi:10.1016/S0921-5093(01)01459-9

39. He, X., Yang, W., Qu, Z., & Fan, S. (2009). Effects of irradiation on chromium's behavior in ferritic/martensitic FeCr alloy. *Frontiers of Energy Power Engineering China*, *3*(2), 181–183. doi:10.1007/s11708-009-0025-x

40. Ortner, S. R. (1991). A STEM study of the effect of precipitation on grain boundary chemistry in AISI 304 Steel. *Acta metallurgica et materialia.*, *39*(3), 341–350.

41. Trillo, E., Beltran, R., Maldonado, J. G., Romero, R. J., Mun, L. E., Fisher, W. W., & Advani, A. H. (1995). Combined effects of deformation (strain and strain state), grain size, and carbon content on carbide precipitation and corrosion sensitization in 304 stainless

steel. *Materials Characterization*, *35*(2), 99–112. doi:10.1016/1044-5803(95)00072-0

42. Kina, A., Souza, V., Tavares, S., Pardal, J., & Souza, J. (2008). Microstructure and intergranular corrosion resistance evaluation of AISI 304 steel for high temperature service. *Materials Characterization*, *59*(5), 651–655. doi:10.1016/j.matchar.2007.04.004

43. Otegui, J. L. (2014). Challenges to the integrity of old pipelines buried in stable ground. *Engineering Failure Analysis*, *42*, 311–323. doi:10.1016/j.engfailanal.2014.04.025

44. Smith, J., & Farrar, R. (1993). Influence of microstructure and composition on mechanical properties of some AISI 300 series weld metals. *International materials reviews*, *38*(1), 3–9. doi:10.1179/095066093790150910

45. Parvathavarthini, N. (2002). Influence of chemical composition, prior deformation and prolonged thermal aging on the sensitization characteristics of austenitic stainless steels. *Journal of Nuclear Materials*, *305*(2–3), 209–219. doi:10.1016/S0022-3115(02)00915-7

46. Calphad. (2000). Iron-Chromium Phase Diagram. Retrieved from http://www.calphad.com/iron-chromium.html

47. Andrews, J. (1965). Empirical formulae for calculation of some transformation temperatures. *Journal of the Iron and Steel Institute*, *203*(7), 721.

48. Raghavan, V., & Antia, D. P. (1994). The chromium equivalents of selected elements in austenitic stainless steels. *Metallurgical and Materials Transactions A*, *25*(12), 2675–2681. doi:10.1007/BF02649220

49. Calphad. (n.d.). Fe-Ni Phase Diagram Calphad. Calphad. Retrieved September 9, 2016, from http://www.calphad.com/iron-nickel.html

50. Onozuka, M., Saida, T., Hirai, S., Kusuhashi, M., Sato, I., & Hatakeyama, T. (1998). Low-activation Mn–Cr austenitic stainless steel with further reduced content of long-lived radioactive elements. *Journal of Nuclear Materials*, *255*(2–3), 128–138. doi:10.1016/S0022-3115(98)00031-2

51. Pawlak, S. (2007). Austenite stability in the high strength metastable stainless steels. *Journal of Achievements in Materials and Manufacturing Engineering*, *22*(2), 2–5. Retrieved from http://www.doaj.org/doaj?func=fulltext&aId=477905

52. Read, D., & Reed, R. (1981). Fracture and strength properties of selected austenitic stainless steels at cryogenic temperatures. *Cryogenics*, *21*(7), 415–417. doi:10.1016/0011-2275(81)90175-2

53. Sourmail, T. (2001). Precipitation in creep resistant austenitic stainless steels. *Materials Science and Technology*, *17*(January), 1–14.

54. Pierson, H. O. (1996). *Handbook of Refractory Carbides and Nitrides - Knovel*. Noyes: William Andrew Publishing. Retrieved from https://app.knovel.com/web/toc.v/cid:kpHRCN0005/viewerType:toc/root_slug:handbook-refractory-carbides/url_slug:kt0019FPZD

55. Ennis, P., & Quadakkers, W. (2007). Mechanisms of steam oxidation in high strength martensitic steels. *International Journal of Pressure Vessels and Piping*, *84*(1–2), 75–81. doi:10.1016/j.ijpvp.2006.09.007

56. Nieto Hierro, L., Rohr, V., Ennis, P. J., Schütze, M., & Quadakkers, W. J. (2005). Steam oxidation and its potential effects on creep strength of power station materials. *Materials and Corrosion*, *56*(12), 890–896. doi:10.1002/maco.200503920

57. Urek, J., Wessel, E., Niewolak, L., Schmitz, F., Kern, T., Singheiser, L., & Quadakkers, W. (2004). Anomalous temperature dependence of oxidation kinetics during steam oxidation of ferritic steels in the temperature range 550–650 °C. *Corrosion Science*, *46*(9), 2301–2317. doi:10.1016/j.corsci.2004.01.010

58. Essuman, E., Meier, G. H., Żurek, J., Hänsel, M., & Quadakkers, W. J. (2008). The Effect of Water Vapor on Selective Oxidation of Fe–Cr Alloys. *Oxidation of Metals*, *69*(3–4), 143–162. doi:10.1007/s11085-007-9090-x

59. Quadakkers, W. J., Żurek, J., & Hänsel, M. (2009). Effect of water vapor on high-temperature oxidation of FeCr alloys. *JOM*, *61*(7), 44–50. doi:10.1007/s11837-009-0102-y

60. Brady, M., Yamamoto, Y., Santella, M., & Pint, B. (2007). Effects of minor alloy additions and oxidation temperature on protective alumina scale formation in creep-resistant austenitic stainless steels. *Scripta Materialia*, *57*(12), 1117–1120. doi:10.1016/j.scriptamat.2007.08.032

61. Lepingle, V., Louis, G., Allue, D., Lefebvre, B., & Vandenberghe, B. (2008). Steam oxidation resistance of new 12%Cr steels: Comparison with some other ferritic steels. *Corrosion Science*, *50*(4), 1011–1019. doi:10.1016/j.corsci.2007.11.033

62. Ha, V. T., & Jung, W. S. (2012). Creep behavior and microstructure evolution at 750°C in a new precipitation-strengthened heat-resistant austenitic stainless steel. *Materials Science and Engineering: A*, *558*, 103–111. doi:10.1016/j.msea.2012.07.090

63. Hosford, W. F. (2009). *Mechanical Behavior of Materials:* (2nd ed.). Cambridge: Cambridge University Press. doi:10.1017/CBO9780511810923

64. Bai, J. W., Liu, P. P., Zhu, Y. M., Li, X. M., Chi, C. Y., Yu, H. Y., … Zhan, Q. (2013). Coherent precipitation of copper in Super304H austenite steel. *Materials Science and Engineering A*, *584*, 57–62. doi:10.1016/j.msea.2013.06.082

65. Sen, I., Amankwah, E., Kumar, N. S., Fleury, E., Oh-ishi, K., Hono, K., & Ramamurty, U. (2011). Microstructure and mechanical properties of annealed SUS 304H austenitic stainless steel with copper. *Materials Science and Engineering: A*, *528*(13–14), 4491–4499. doi:10.1016/j.msea.2011.02.019

66. Gonzalez, B. ., Castro, C. S. ., Buono, V. T. ., Vilela, J. M. ., Andrade, M. ., Moraes, J. M. ., & Mantel, M. . (2003). The influence of copper addition on the formability of AISI 304 stainless steel. *Materials Science and Engineering: A*, *343*, 51–56. doi:10.1016/S0921-5093(02)00362-3

67. Ou, P., Xing, H., Wang, X. L., & Sun, J. (2014). Tensile yield behavior and precipitation strengthening mechanism in Super304H steel. *Materials Science and Engineering A*,

600, 171–175. doi:10.1016/j.msea.2014.01.085

68. Chi, C., Yu, H., Dong, J., Liu, W., Cheng, S., Liu, Z., & Xie, X. (2012). The precipitation strengthening behavior of Cu-rich phase in Nb contained advanced Fe–Cr–Ni type austenitic heat resistant steel for USC power plant application. *Progress in Natural Science: Materials International*, *22*(3), 175–185. doi:10.1016/j.pnsc.2012.05.002

69. Zhuang, W., & Wicks, B. (2003). Mechanical Surface Treatment Technologies for Gas Turbine Engine Components. *Journal of Engineering for Gas Turbines and Power*, *125*(4), 1021. doi:10.1115/1.1610011

70. Marsh, K. J. (Ed.). (1993). *Shot Peening: Techniques and Applications*. London: Chameleon Press Ltd.

71. Verpoort, C. M., & Gerdes, C. (1989). Influence of Shot Peening on Material Properties and the Controlled Shot Peening of Turbine Blades. In A. Niku-Lari, J. S. Eckersley, & J. Champaigne (Eds.), *Shot Peening Theory and Application* (pp. 11–70). Gournay Sur Marne, France: IITT International.

72. Vohringer, O. (1987). Changes in the state of the material by Shotpeening. In H. Wohlfahrt, R. Kopp, & O. Vohringer (Eds.), *3rd International Conference on Shotpeening (ICSP3)* (pp. 185–204). Oberursel: DGM Informationsgesellschaft Verlag.

73. Fard, S. B., & Guagliano, M. (2009). Effects of surfaces nanocrystallization induced by shot peening on material properties : a Review. *Frattura ed Integrità Strutturale*, *7*, 3–16. doi:10.3221/IGF-ESIS.07.01

74. Yu, H., Dong, J. L., Yoo, D. H., Shin, K., Jung, J. S., Pyoun, Y., & Cho, I. (2009). Effect of Ultrasonic and Air Blast Shot Peening on the Microstructural Evolution and Mechanical Properties of SUS304. *Journal of the Korean Physical Society*, *54*(3), 1161. doi:10.3938/jkps.54.1161

75. Abbate, A., Frankel, J., & Scholz, W. (1993). *Measurement and Theory of the Dependence of Hardness on Residual Stress*. WATERVLIET NY. Retrieved from http://www.dtic.mil/docs/citations/ADA267553

76. Frankel, J., Abbate, A., & Scholz, W. (1993). The effect of residual stresses on hardness measurements. *Experimental Mechanics*, *33*(2), 164–168. doi:10.1007/BF02322494

77. Schiffner, K., & Droste Gen. Helling, C. (1999). Simulation of residual stresses by shot peening. *Computers and Structures*, *72*(1), 329–340. doi:10.1016/S0045-7949(99)00012-7

78. McClung, R. C. (2007). A literature survey on the stability and significance of residual stresses during fatigue. *Fatigue and Fracture of Engineering Materials and Structures*, *30*(3), 173–205. doi:10.1111/j.1460-2695.2007.01102.x

79. Soady, K. A. (2013). Life assessment methodologies incoroporating shot peening process effects: mechanistic consideration of residual stresses and strain hardening Part 1 - effect of shot peening on fatigue resistance. *Materials Science and Technology*, *29*(6), 637–651. doi:10.1179/1743284713y.0000000222

80. Haušild, P., Davydov, V., Drahokoupil, J., Landa, M., & Pilvin, P. (2010). Characterization

of strain-induced martensitic transformation in a metastable austenitic stainless steel. *Materials & Design*, *31*(4), 1821–1827. doi:10.1016/j.matdes.2009.11.008

81. Hills, D. A., Waterhouse, R. B., & Noble, B. (1983). An analysis of shot peening. *The Journal of Strain Analysis for Engineering Design*, *18*(2), 95–100. doi:10.1243/03093247V182095

82. Tao, N. (2002). An investigation of surface nanocrystallization mechanism in Fe induced by surface mechanical attrition treatment. *Acta Materialia*, *50*(18), 4603–4616. doi:10.1016/S1359-6454(02)00310-5

83. Zhang, H., Hei, Z., Liu, G., Lu, J., & Lu, K. (2003). Formation of nanostructured surface layer on AISI 304 stainless steel by means of surface mechanical attrition treatment. *Acta Materialia*, *51*(7), 1871–1881. doi:10.1016/S1359-6454(02)00594-3

84. Mordyuk, B., Milman, Y., Iefimov, M., Prokopenko, G., Silberschmidt, V., Danylenko, M., & Kotko, a. (2008). Characterization of ultrasonically peened and laser-shock peened surface layers of AISI 321 stainless steel. *Surface and Coatings Technology*, *202*(19), 4875–4883. doi:10.1016/j.surfcoat.2008.04.080

85. Chu, J., Rigsbee, J., Banas, G., & Elsayedali, H. (1999). Laser-shock processing effects on surface microstructure and mechanical properties of low carbon steel. *Materials Science and Engineering: A*, *260*(1–2), 260–268. doi:10.1016/S0921-5093(98)00889-2

86. Krull, P., Nitschke-Pagel, T., & Wohlfahrt, H. (1999). Stability of Residual Stresses in Shot Peened and High Pressure Water Peened Stainless Steels at Elevated Temperatures. In A. Nakonieczny (Ed.), *7th International Conference on Shot Peening (ICSP7)*. Warsaw: Institute of Precision Mechanics.

87. Hassani-Gangaraj, S. M., Cho, K. S., Voigt, H. J. L., Guagliano, M., & Schuh, C. A. (2015). Experimental assessment and simulation of surface nanocrystallization by severe shot peening. *Acta Materialia*, *97*, 105–115. doi:10.1016/j.actamat.2015.06.054

88. Montross, C., Wei, T., Ye, L., Clark, G., & Mai, Y.-W. (2002). Laser shock processing and its effects on microstructure and properties of metal alloys: a review. *International Journal of Fatigue*, *24*(10), 1021–1036. doi:10.1016/S0142-1123(02)00022-1

89. Wang, T., Yu, J., & Dong, B. (2006). Surface nanocrystallization induced by shot peening and its effect on corrosion resistance of 1Cr18Ni9Ti stainless steel. *Surface and Coatings Technology*, *200*(16–17), 4777–4781. doi:10.1016/j.surfcoat.2005.04.046

90. Peng, X., Yan, J., Zhou, Y., & Wang, F. (2005). Effect of grain refinement on the resistance of 304 stainless steel to breakaway oxidation in wet air. *Acta Materialia*, *53*(19), 5079–5088. doi:10.1016/j.actamat.2005.07.019

91. Liu, G., Lu, J., & Lu, K. (2000). Surface nanocrystallization of 316L stainless steel induced by ultrasonic shot peening1. *Materials Science and Engineering A*, *286*(1), 91–95. doi:10.1016/S0921-5093(00)00686-9

92. Wang, X. Y., & Li, D. Y. (2002). Mechanical and electrochemical behavior of nanocrystalline surface of 304 stainless steel. *Electrochimica Acta*, *47*(24), 3939–3947. doi:10.1016/S0013-4686(02)00365-1

93. Altenberger, I. (2003). An in situ transmission electron microscope study of the thermal stability of near-surface microstructures induced by deep rolling and laser-shock peening. *Scripta Materialia*, *48*(12), 1593–1598. doi:10.1016/S1359-6462(03)00143-X

94. SAE International. (2010). Procedures for Using Standard Shot Peening Almen Strip. SAE International.

95. Guagliano, M. (2001). Relating Almen intensity to residual stresses induced by shot peening: a numerical approach. *Journal of Materials Processing Technology*, *110*(3), 277–286. doi:10.1016/S0924-0136(00)00893-1

96. Higounenc, O. (2005). Correlation of shot peening parameters to surface characteristic. In *International Conference on Shot Peening 9* (pp. 28–35). Paris. doi:DC10503A36FF6CDD2BC9A73FFFFFD62A

97. Kim, J. C., Cheong, S. K., & Noguchi, H. (2013). Evolution of residual stress redistribution associated with localized surface microcracking in shot-peened medium-carbon steel during fatigue test. *International Journal of Fatigue*, *55*, 147–157. doi:10.1016/j.ijfatigue.2013.06.010

98. Lee, H., Kim, D., Jung, J., Pyoun, Y., & Shin, K. (2009). Influence of peening on the corrosion properties of AISI 304 stainless steel. *Corrosion Science*, *51*(12), 2826–2830. doi:10.1016/j.corsci.2009.08.008

99. Djaziri, S., Li, Y., Nematollahi, G. A., Grabowski, B., Goto, S., Kirchlechner, C., … Dehm, G. (2016). Deformation-Induced Martensite: A New Paradigm for Exceptional Steels. *Advanced Materials*, *28*(35), 7753–7757. doi:10.1002/adma.201601526

100. Kurdjumov, G., & Sachs, G. (1930). Over the mechanisms of steel hardening. *Z. Phys.*, *64*, 325–43.

101. Zhang, M. X., & Kelly, P. M. (2009). Crystallographic features of phase transformations in solids. *Progress in Materials Science*, *54*(8), 1101–1170. doi:10.1016/j.pmatsci.2009.06.001

102. Porter, D. A., & Easterling, K. E. (1992). *Phase Transformations in Metals and Alloys* (2nd ed.). Boca Raton: CRC Press.

103. Shen, Y. F., Li, X. X., Sun, X., Wang, Y. D., & Zuo, L. (2012). Twinning and martensite in a 304 austenitic stainless steel. *Materials Science and Engineering: A*, *552*, 514–522. doi:10.1016/j.msea.2012.05.080

104. Poulon, A., Brochet, S., Vogt, J.-B., Glez, J.-C., & Mithieux, J.-D. (2009). Fine Grained Austenitic Stainless Steels : The Role of Strain Induced Alpha Martensite and the Reversion Mechanism Limitations. *ISIJ International*, *49*(2), 293–301. doi:10.2355/isijinternational.49.293

105. Takaki, S., Fukunaga, K., Syarif, J., & Tsuchiyama, T. (2004). Effect of Grain Refinement on Thermal Stability of Metastable Austenitic Steel. *Materials Transactions*, *45*(7), 2245–2251. doi:10.2320/matertrans.45.2245

106. Rhodes, C. G., & Thompson, A. W. (1977). The composition dependence of stacking fault energy in austenitic stainless steels. *Metallurgical Transactions A*, *8*(12), 1901–

1906. doi:10.1007/BF02646563

107. De, A., Murdock, D., Mataya, M., Speer, J., & Matlock, D. (2004). Quantitative measurement of deformation-induced martensite in 304 stainless steel by X-ray diffraction. *Scripta Materialia*, *50*(12), 1445–1449. doi:10.1016/j.scriptamat.2004.03.011

108. Eskandari, M., Zarei-Hanzaki, A., & Abedi, H. R. (2013). An investigation into the room temperature mechanical properties of nanocrystalline austenitic stainless steels. *Materials and Design*, *45*, 674–681. doi:10.1016/j.matdes.2012.08.042

109. Shintani, T., & Murata, Y. (2011). Evaluation of the dislocation density and dislocation character in cold rolled Type 304 steel determined by profile analysis of X-ray diffraction. *Acta Materialia*. doi:10.1016/j.actamat.2011.03.055

110. Ni, Z., Wang, X., Wang, J., & Wu, E. (2003). Characterization of the phase transformation in a nanostructured surface layer of 304 stainless steel induced by high-energy shot peening. *Physica B: Condensed Matter*, *334*(1–2), 221–228. doi:10.1016/S0921-4526(03)00069-3

111. Trimby, P. W. (2012). Orientation mapping of nanostructured materials using transmission Kikuchi diffraction in the scanning electron microscope. *Ultramicroscopy*, *120*, 16–24. doi:10.1016/j.ultramic.2012.06.004

112. Karimi, M., Najafizadeh, A., Kermanpur, A., & Eskandari, M. (2009). Effect of martensite to austenite reversion on the formation of nano/submicron grained AISI 301 stainless steel. *Materials Characterization*, *60*(11), 1220–1223. doi:10.1016/j.matchar.2009.04.014

113. Guy, K. B., Butler, E. P., & West, D. R. F. (1983). Reversion of bcc (alpha) martensite in Fe-Cr-Ni austenitic stainless steels. *Metal Science*, *17*(April), 167–176.

114. Zengwu, Y., Min, F., Xuegang, W., & Xingeng, L. (2011). Effect of Shot Peening on the Oxidation Resistance of TP304H and HR3C Steels in Water Vapor. *Oxidation of Metals*, *77*(1–2), 17–26. doi:10.1007/s11085-011-9270-6

115. Cissé, S., Laffont, L., Tanguy, B., Lafont, M.-C., & Andrieu, E. (2012). Effect of surface preparation on the corrosion of austenitic stainless steel 304L in high temperature steam and simulated PWR primary water. *Corrosion Science*, *56*, 209–216. doi:10.1016/j.corsci.2011.12.007

116. Naraparaju, R., Christ, H.-J., Renner, F. U., & Kostka, a. (2012). Dislocation engineering and its effect on the oxidation behaviour. *Materials at High Temperatures*, *29*(2), 116–122. doi:10.3184/096034012X13322687148749

117. Bagherifard, S., Ghelichi, R., & Guagliano, M. (2010). A numerical model of severe shot peening (SSP) to predict the generation of a nanostructured surface layer of material. *Surface and Coatings Technology*, *204*(24), 4081–4090. doi:10.1016/j.surfcoat.2010.05.035

118. Charitidis, C. a, & Koumoulos, E. P. (2012). *Nanomechanical properties and nanoscale deformation of PDMS nanocomposites*. *Plastics, Rubber and Composites* (Vol. 41). Woodhead Publishing Limited. doi:10.1179/1743289810Y.0000000037

119. Yovanovich, M. M. (2006). Micro and Macro Hardness Measurements , Correlations , and Contact Models. In *44th AIAA Aerospace Sciences Meeting and Exhibit* (pp. 1–28). Reno. Retrieved from http://www.mhtlab.uwaterloo.ca/pdf_papers/mhtl06-2.pdf

120. Lawn, B. R., & Cook, R. F. (2012). Probing material properties with sharp indenters: A retrospective. *Journal of Materials Science*, *47*(1), 1–22. doi:10.1007/s10853-011-5865-1

121. ASTM International. (2017). ASTM E384-17 Standard Test Method for Microindentation Hardness of Materials. West Conshohocken, PA: ASTM International. doi:10.1520/E0384-10.2

122. Hall, E. O. (1951). The Deformation and Ageing of Mild Steel: III Discussion of Results. *Proceedings of the Physical Society. Section B*, *64*(9), 747–753. doi:10.1088/0370-1301/64/9/303

123. Petch, N. (1953). The cleavage strength of polycrystals. *Journal of Iron and Steel Institute*, *174*, 25.

124. Aifantis, K. E., & Konstantinidis, A. a. (2009). Hall–Petch revisited at the nanoscale. *Materials Science and Engineering: B*, *163*(3), 139–144. doi:10.1016/j.mseb.2009.05.010

125. Bakhsheshi-Rad, H. R., Haerian, B., Najafizadeh, a, Idris, M. H., Kadir, M. R. a., Hamzah, E., & Daroonparvar, M. (2013). Cold deformation and heat treatment influence on the microstructures and corrosion behavior of AISI 304 stainless steel. *Canadian Metallurgical Quarterly*, *52*(4), 449–457. doi:10.1179/1879139513Y.0000000101

126. Humphreys, F. J., & Hatherly, M. (1995). *Recrystallization and Related Annealing Phenomena*. Oxford: Elsevier Science Ltd.

127. Padilha, A. F., Plaut, R. L., & Rios, P. R. (2003). Annealing of Cold-worked Austenitic Stainless Steels. *ISIJ International*, *43*(2), 135–143. doi:10.2355/isijinternational.43.135

128. Wilsdorf, H. G. F., & Schmitz, J. (1962). The Observation and Interpretation of Dislocation Tangles in the Easy Glide Range of Aluminum. *Journal of Applied Physics*, *33*(5), 1750–1754. doi:10.1063/1.1728823

129. Rios, P. R., Siciliano Jr, F., Sandim, H. R. Z., Plaut, R. L., & Padilha, A. F. (2005). Nucleation and growth during recrystallization. *Materials Research*, *8*(3), 225–238. doi:10.1590/S1516-14392005000300002

130. Puppet, S. (2006). The polygonization of a metallic lattice during recovery. *Wikimedia Commons*. Retrieved September 27, 2016, from https://upload.wikimedia.org/wikipedia/en/b/b6/Polygonization.png

131. Puppet, S. (2005). Nucleation and growth kinetics of recrystallised grains in a generic deformed alloy. *Wikimedia Commons*. Retrieved from https://en.wikipedia.org/wiki/File:RXkinetics.svg

132. Humphreys, F. J., & Hatherly, M. (2004). Continuous Recrystallization During and after Large Strain Deformation. In *Recrystallization and Related Annealing Phenomena* (pp. 451–467). Elsevier. doi:10.1016/B978-008044164-1/50018-9

133. Cuddy, L. J. (1981). Microstructures developed during thermomechanical treatment of HSLA steels. *Metallurgical Transactions A*, *12*(7), 1313–1320. doi:10.1007/BF02642345

134. Kazeminezhad, M. (2008). On the modeling of the static recrystallization considering the initial grain size effects. *Materials Science and Engineering: A*, *486*(1–2), 202–207. doi:10.1016/j.msea.2007.08.071

135. Xu, W., & Ferry, M. (2010). Recrystallisation textures in cold rolled low carbon steel containing ferritic and bainitic microstructures. *Materials Science and Technology*, *26*(10), 1159–1172. doi:10.1179/174328409X441274

136. Pous-Romero, H., Lonardelli, I., Cogswell, D., & Bhadeshia, H. K. D. H. (2013). Austenite grain growth in a nuclear pressure vessel steel. *Materials Science and Engineering: A*, *567*, 72–79. doi:10.1016/j.msea.2013.01.005

137. Kalu, P. N., & Waryoba, D. R. (2007). A JMAK-microhardness model for quantifying the kinetics of restoration mechanisms in inhomogeneous microstructure. *Materials Science and Engineering: A*, *464*(1–2), 68–75. doi:10.1016/j.msea.2007.01.124

138. Callister, W. D., & Rethwisch, D. G. (2007). *Materials science and engineering: an introduction* (Vol. 7). Wiley New York.

139. Marchive, D., Duc, D., Treheux, D., & Guiraldenq, P. (1975). Bulk and grain boundaries diffusion of tin in 18-10 austenitic stainless-steel - study of ferritization process at high-temperature. *Comptes Rendus Hebdomadaires des Seances de l'Academie des Sciences Serie C*, *280*(1), 25–28.

140. Juve - Duc, D., Treheux, D., & Guiraldenq, P. (1978). Autodiffusion en volume et intergranulaire du 59Fe dans une austenite a 18% Cr et 10% de tres haute purete. *Scripta Metallurgica*, *12*(12), 1107–1110. doi:10.1016/0036-9748(78)90084-4

141. Million, B., Růžičková, J., & Vřešťál, J. (1985). Diffusion in FeNiCr alloys with an FCC lattice. *Materials Science and Engineering*, *72*(1), 85–100. doi:10.1016/0025-5416(85)90069-2

142. Daruvala, H. S., & Bube, K. R. (1979). Tracer diffusion of chromium in 321 stainless steel. *Journal of Nuclear Materials*, *87*(1), 211–213. doi:10.1016/0022-3115(79)90143-0

143. Daruvala, H. S., & Bube, K. R. (1979). Tracer diffusion of chromium in 304 stainless steel. *Materials Science and Engineering*, *41*(2), 293–295. doi:10.1016/0025-5416(79)90151-4

144. Tokei, Z., Hennesen, K., Viefhaus, H., & Grabke, H. J. (2000). Diffusion of chromium in ferritic and austenitic 9-20wt% chromium steels. *Materials Science and Technology*, *16*(October), 1129–1138.

145. Thorvaldsson, T., & Salwén, A. (1984). Measurement of diffusion coefficients for Cr at low temperatures in a type 304 stainless steel. *Scripta Metallurgica*, *18*(7), 739–742. doi:10.1016/0036-9748(84)90331-4

146. Williams, P. I., & Faulkner, R. G. (1987). Chemical volume diffusion coefficients for stainless steel corrosion studies. *Journal of Materials Science*, *22*(10), 3537–3542. doi:10.1007/BF01161455

147. Smith, A. F. (1975). The Diffusion of Chromium in Type 316 Stainless Steel. *Metal Science*, *9*(1), 375–378. doi:10.1179/030634575790444270

148. Patil, R. V., & Sharma, B. D. (1982). Lattice and grain-boundary diffusion of 59 Fe in 316 stainless steel. *Metal Science*, *16*(8), 389–392. doi:10.1179/030634582790427406

149. Smithells, C. J. (2004). Diffusion in metals. In W. F. Gale & T. C. Totemeier (Eds.), *Smithells Metals Reference Book (Eighth Edition)* (8th Editio., pp. 13-1-13–120). Oxford: Butterworth-Heinemann. doi:10.1016/B978-0-7506-7509-3.50016-6

150. Tariq, M., & Bergner, D. (1988). Interdiffusion of Mn in austenitic and ferritic CrNi steels. *Crystal Research and Technology*, *23*(12), 1503–1515. doi:10.1002/crat.2170231217

151. Gilewicz-Wolter, J., Dudała, J., Żurek, Z., Homa, M., Lis, J., & Wolter, M. (2005). Diffusion of chromium, manganese, and iron in MnCr2O4 spinel. *Journal of Phase Equilibria and Diffusion*, *26*(5), 561–564. doi:10.1007/s11669-005-0051-2

152. Sabioni, a. C. S., Huntz, a. M., Borges, L. C., & Jomard, F. (2007). First Study of Mn diffusion in Cr2O3 polycrystals and thin films by SIMS. *Philosophical Magazine*, *87*(12), 1921–1937. doi:10.1080/14786430601120462

153. Dieckmann, R. (1998). Point defects and transport in non-stoichiometric oxides: Solved and unsolved problems. *Journal of Physics and Chemistry of Solids*, *59*(97), 507–525. doi:10.1016/S0022-3697(97)00205-9

154. Tem5psu. (2014). AB2O4 spinel. Wikimedia. Retrieved from https://upload.wikimedia.org/wikipedia/commons/c/c9/AB2O4_spinel.png

155. Mishin, Y., & Herzig, C. (1999). Grain boundary diffusion: recent progress and future research. *Materials Science and Engineering: A*, *260*(1–2), 55–71. doi:10.1016/S0921-5093(98)00978-2

156. Fisher, J. C. (1951). Calculation of diffusion penetration curves for surface and grain boundary diffusion. *Journal of Applied Physics*, *22*(1), 74–77. doi:10.1063/1.1699825

157. Juve-Duc, D., & Treheux, D. (1984). Influence du soufre sur la diffusion intergranulaire dans la solution solide austenitique Fe-Cr-Ni (18% Cr, 10% Ni). *Acta Metallurgica*, *32*(11), 2063–2068. doi:10.1016/0001-6160(84)90185-8

158. Hansson, A. N., Hattel, J. H., Dahl, K. V, & Somers, M. A. J. (2009). Modelling Cr depletion under a growing Cr2O3 layer on austenitic stainless steel: the influence of grain boundary diffusion. *Modelling and Simulation in Materials Science and Engineering*, *17*(3), 35009. doi:10.1088/0965-0393/17/3/035009

159. Palumbo, G., Thorpe, S. J., & Aust, K. T. (1990). On the contribution of triple junctions to the structure and properties of nanocrystalline materials. *Scripta Metallurgica et Materialia*, *24*(7), 1347–1350. doi:10.1016/0956-716X(90)90354-J

160. Kim, J.-H., Kim, B. K., Kim, D.-I., Choi, P.-P., Raabe, D., & Yi, K.-W. (2015). The role of grain boundaries in the initial oxidation behavior of austenitic stainless steel containing alloyed Cu at 700°C for advanced thermal power plant applications. *Corrosion Science*, *96*, 52–66. doi:10.1016/j.corsci.2015.03.014

161. Lobb, R. C., & Evans, H. E. (1981). Formation of protective oxide film on chromium-depleted stainless steel. *Metal Science*, *15*(6), 267–274. doi:10.1179/msc.1981.15.6.267

162. Hart, E. W. (1957). On the role of dislocations in bulk diffusion. *Acta Metallurgica*, *5*(10), 597. doi:10.1016/0001-6160(57)90127-X

163. Smith, A. F. (1975). Low-Temperature Diffusion of Chromium in a Fine-Grained Austenitic Stainless Steel with Varying Dislocation Densities. *Metal Science*, *9*(1), 425–429. doi:10.1179/030634575790444342

164. Grabke, H. J., Muller-Lorenz, E. M., Strauss, S., Pippel, E., & Woltersdorf, J. (1998). Effects of Grain Size, Cold Working, and Surface Finish on the Metal-Dusting Resistance of Steels. *Oxidation of Metals*, *50*(3/4), 241–254. doi:10.1023/A:1018888321213

165. Kurepin, V. a. (2005). A thermodynamic model of Fe-Cr spinels. *Contributions to Mineralogy and Petrology*, *149*(5), 591–599. doi:10.1007/s00410-005-0669-4

166. Pilling, N. B., & Bedworth, R. E. (1923). The oxidation of metals at high temperatures. *Journal of the Institute of Metals*, *29*, 529–582.

167. Roberge, P. R. (2012). Handbook of corrosion engineering [electronic resource]. McGraw-Hill: New York.

168. Ellingham, H. J. T. (1944). Reducibility of oxides and sulfides in metallurgical processes. *Journal of the Society of Chemical Industry*, *63*(5), 125–133. Retrieved from http://openlibrary.org/works/OL11235195W/Reducibility_of_oxides_and_sulphides_in_metallurgical_processes

169. Gaskell, D. R. (2008). *Introduction to the Thermodynamics of Materials* (5th ed.). New York: Taylor & Francis Group.

170. Kjellqvist, L., Selleby, M., & Sundman, B. (2008). Thermodynamic modelling of the Cr-Fe-Ni-O system. *Calphad: Computer Coupling of Phase Diagrams and Thermochemistry*, *32*(3), 577–592. doi:10.1016/j.calphad.2008.04.005

171. Wood, G. C. (1962). The oxidation of iron-chromium alloys and stainless steels at high temperatures. *Corrosion Science*, *2*(3), 173–196. doi:10.1016/0010-938X(62)90019-7

172. PRAZAK, M., PRAZAK, V., & CIHAL, V. (1958). UBER DEN AUFBAU DER PASSIVSCHICHT AUF CHROMSTAHLEN. *ZEITSCHRIFT FUR ELEKTROCHEMIE*, *62*(6–7), 739–745.

173. Fry, A., Osgerby, S., & Wright, M. (2002). *Oxidation of Alloys in Steam Environments - A Review*.

174. Tempest, P. A., & Wild, R. K. (1981). The nature of the oxide formed on 20%Cr/25%Ni/Nb steel oxidised at 1123k in co2. *Journal of Nuclear Materials*, *102*(1–2), 183–191. doi:10.1016/0022-3115(81)90558-4

175. Behnamian, Y., Mostafaei, A., Kohandehghan, A., Amirkhiz, B. S., Serate, D., Sun, Y., … Luo, J. L. (2016). A comparative study of oxide scales grown on stainless steel and nickel-based superalloys in ultra-high temperature supercritical water at 800°C. *Corrosion Science*, *106*, 188–207. doi:10.1016/j.corsci.2016.02.004

176. Kjellqvist, L., & Selleby, M. (2010). Thermodynamic assessment of the Cr-Mn-O system. *Journal of Alloys and Compounds*, *507*(1), 84–92. doi:10.1016/j.jallcom.2010.04.252

177. Jung, I. (2006). Critical evaluation and thermodynamic modeling of the Mn–Cr–O system for the oxidation of SOFC interconnect. *Solid State Ionics*, *177*(7–8), 765–777. doi:10.1016/j.ssi.2006.01.012

178. Povoden, E., Nicholas Grundy, A., & Gauckler, L. J. (2006). Thermodynamic reassessment of the Cr−O system in the framework of solid oxide fuel cell (SOFC) research. *Journal of Phase Equilibria and Diffusion*, *27*(4), 353–362. doi:10.1007/s11669-006-0007-1

179. Wagner, C. (1952). Theoretical Analysis of the Diffusion Processes Determining the Oxidation Rate of Alloys. *Journal of the Electrochemical Society*, *99*(10), 369–380. Retrieved from http://scitation.aip.org/dbt/dbt.jsp?KEY=JESOAN&Volume=99&Issue=10

180. Danielewski, M., & Wierzba, B. (2008). Diffusion processes determining the oxidation rate of multicomponent alloys. *Corrosion Science*, *50*(4), 1161–1168. doi:10.1016/j.corsci.2007.11.024

181. Mamede, A. S., Nuns, N., Cristol, A. L., Cantrel, L., Souvi, S., Cristol, S., & Paul, J. F. (2016). Multitechnique characterisation of 304L surface states oxidised at high temperature in steam and air atmospheres. *Applied Surface Science*, *369*, 510–519. doi:10.1016/j.apsusc.2016.01.185

182. Botella, J., Merino, C., & Otero, E. (1998). A Comparison of the High-Temperature Oxidation of 17Cr-2Ni and 18Cr-8Ni Austenitic Stainless Steels at 973 K. *Oxidation of Metals*, *49*(3–4), 297–324. doi:10.1023/A:1018830424480

183. Trindade, V. B., Krupp, U., Wagenhuber, P. E.-G., & Christ, H.-J. (2005). Oxidation mechanisms of Cr-containing steels and Ni-base alloys at high-temperatures -. Part I: The different role of alloy grain boundaries. *Materials and Corrosion*, *56*(11), 785–790. doi:10.1002/maco.200503879

184. Asteman, H., Svensson, J.-E., & Johansson, L.-G. (2002). Oxidation of 310 steel in H2O/O2 mixtures at 600°C : the effect of water-vapour-enhanced chromium evaporation. *Corrosion Science*, *44*, 2635–2649.

185. Asteman, H., Svensson, J., Norell, M., & Johansson, L. (2000). Influence of Water Vapor and Flow Rate on the High-Temperature Oxidation of 304L ; Effect of Chromium Oxide Hydroxide Evaporation. *Oxidation of Metals*, *54*(1/2), 11–26.

186. Saunders, S., Monteiro, M., & Rizzo, F. (2008). The oxidation behaviour of metals and alloys at high temperatures in atmospheres containing water vapour: A review. *Progress in Materials Science*, *53*(5), 775–837. doi:10.1016/j.pmatsci.2007.11.001

187. Halvarsson, M., Tang, J., Asteman, H., Svensson, J., & Johansson, L. (2006). Microstructural investigation of the breakdown of the protective oxide scale on a 304 steel in the presence of oxygen and water vapour at 600°C. *Corrosion Science*, *48*(8), 2014–2035. doi:10.1016/j.corsci.2005.08.012

188. Hansson, a. N., Pantleon, K., Grumsen, F. B., & Somers, M. a. J. (2009). Microstructure

Evolution During Steam Oxidation of a Nb Stabilized Austenitic Stainless Steel. *Oxidation of Metals*, *73*(1–2), 289–309. doi:10.1007/s11085-009-9182-x

189. Warzee, M., Hennaut, J., Maurice, M., Sonnen, C., Waty, J., & Berge, P. (1965). Effect of Surface Treatment on the Corrosion of Stainless Steels in High-Temperature Water and Steam. *Journal of The Electrochemical Society*, *112*(7), 670. doi:10.1149/1.2423661

190. Otsuka, N., Shida, Y., & Fujikawa, H. (1989). Internal-external transition for the oxidation of Fe-Cr-Ni austenitic stainless steels in steam. *Oxidation of Metals*, *32*(1–2), 13–45. doi:10.1007/BF00665267

191. Otsuka, N., & Fujikawa, H. (1991). Scaling of Austenitic Stainless Steels and Nickel-Base Alloys in High-Temperature Steam at 973 K. *CORROSION*, *47*(4), 240–248. doi:10.5006/1.3585251

192. Ueda, M., Inoue, Y., Ochiai, H., Takeyama, M., & Maruyama, T. (2013). The effect of water vapor on the transition from internal to external oxidation of austenitic steels at 1,073 K. *Oxidation of Metals*, *79*(5–6), 485–494. doi:10.1007/s11085-012-9350-2

193. Yan, J., Gao, Y., Gu, Y., Sun, F., Yang, Z., Lu, J., … Li, Y. (2016). Role of Grain Boundaries on the Cyclic Steam Oxidation Behaviour of 18-8 Austenitic Stainless Steel. *Oxidation of Metals*, *85*(3–4), 409–424. doi:10.1007/s11085-015-9603-y

194. Yunhai, M., Haibo, W., Rui, F., Qiang, L., & Kexian, S. (2014). THE EFFECT OF SHOT PEENING ON THE OXIDATION RESISTANCE OF SUPER304H STEELS IN WATER VAPOR. In *ENERGY MATERIALS CONFERENCE PROCEEDINGS 2014* (pp. 251–259). OSNEY MEAD, OXFORD OX2 0EL, ENGLAND: BLACKWELL SCIENCE PUBL.

195. Ren, X., Sridharan, K., & Allen, T. R. (2010). Effect of grain refinement on corrosion of ferritic-martensitic steels in supercritical water environment. *Materials and Corrosion*, *61*(9), 748–755. doi:10.1002/maco.200905446

196. Asteman, H., Svensson, J.-E., & Johansson, L.-G. (2004). Effect of Water-Vapor-Induced Cr Vaporization on the Oxidation of Austenitic Stainless Steels at 700 and 900°C. *Journal of The Electrochemical Society*, *151*(3), B141. doi:10.1149/1.1644138

197. Opila, E. J., Jacobson, N. S., Myers, D. L., & Copland, E. H. (2006). Predicting Oxide Stability in High-Temperature Water Vapor. *JOM*, (January).

198. Opila, E. J., Myers, D. L., Jacobson, N. S., Nielsen, I. M. B., Johnson, D. F., Olminsky, J. K., & Allendorf, M. D. (2007). Theoretical and Experimental Investigation of the Thermochemistry of CrO 2 (OH) 2 (g). *The Journal of Physical Chemistry A*, *111*(10), 1971–1980. doi:10.1021/jp0647380

199. Marchesini, S., Chapman, H. N., Hau-Riege, S. P., London, R. A., Szoke, A., He, H., … Weierstall, U. (2003). Coherent X-ray diffractive imaging: applications and limitations. *Optics Express*, *11*(19), 2344. doi:10.1364/OE.11.002344

200. Wouters, Y., Galerie, A., & Petit, J.-P. (1997). Thermal oxidation of titanium by water vapour. *Solid State Ionics*, *104*(1–2), 89–96. doi:10.1016/S0167-2738(97)00400-1

201. Yuan, J., Wang, W., Zhu, S., & Wang, F. (2013). Comparison between the oxidation of iron in oxygen and in steam at 650-750°C. *Corrosion Science*, *75*, 309–317.

doi:10.1016/j.corsci.2013.06.014

3 Methodology

3.1 Materials Used

Two alloys were used in the experiments in this study, DMV304HCu supplied by Salzgitter Mannesmann Stainless Tubes and Super 304H supplied by Sumitomo Metal (now Nippon Steel & Sumitomo Metal). The compositions provided by the manufacturers of these alloys are given in Table 1. The alloys were supplied in the form of tubes and were cut into sections. The tubes were first sliced into 10-15mm sections by circular saw. Each ring was then cut into 1/6$^{\text{ths}}$ with a SiC circular saw, as shown in Figure 1.

Table 1 - Alloy Compositions

Alloy	**Composition (Weight %)**									
	Fe	**Cr**	**Ni**	**Cu**	**Mn**	**Nb**	**Si**	**N**	**C**	**Al**
DMV304HCu	Balance	18.13	9.03	3.05	0.76	0.43	0.27	0.11	0.087	0.006
Super 304H	Balance	18.0	9.0	3.00	0.8	0.40	0.20	0.1	0.1	0

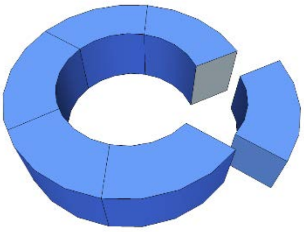

Figure 1 - Sample geometry

The internal surfaces of the tubes had been processed by the manufacturer; detailed information about the material processing parameters is not available, but the general principle of shot peening a steel tube is shown in Figure 2. Compressed air is used to propel shot from a nozzle positioned inside the tubes. The nozzle is rotated and the tube is moved in order to peen the entirety of the inner tube surface. Fired shot is collected at the end of the tube and reused in the process.

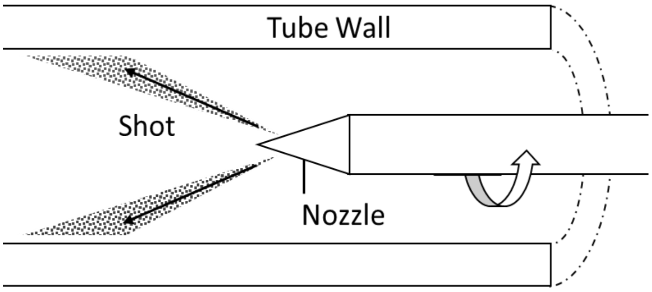

Figure 2 - The shot peening process for a steel tube. The nozzle is moved over the tube surface and rotated as it sprays the shot.

One of the DMV304HCu tubes had been shot peened and a second tube had been shot peened twice by repeating the same process. One of the Super304H tubes was shot peened and the other had been pickled. The four types of sample material and their tube dimensions are summarized in Table 2. The sample types are given short names for ease of reference during the rest of this thesis.

After being cut, the samples were ultrasonically cleaned in a water/detergent mix and any remaining burrs were filed off. Samples were filed or polished as little as possible in order to maintain the as-manufactured surfaces.

Table 2 - Tube Parameters

Sample Designation	Alloy	Shot peened	Outer Diameter (mm)	Inner Diameter (mm)	Wall Thickness (mm)
SP1	DMV304HCu	Yes	45.0	26.6	9.2
SP2	DMV304HCu	Yes - Twice	45.0	26.6	9.2
S304	Super 304H	No	42.3	31.2	5.6
SSP	Super 304H	Yes	41.3	28.5	6.4

3.2 Phase Diagrams

Phase diagrams for DMV304HCu and a generic grade 304 steel were plotted using Thermo-calc software with the TCFE 7/8 thermodynamics databases. Phase diagrams for the Mn-Cr-O system were plotted using Thermo-calc and the TCOX6 thermodynamics database.

3.3 Heat Treatment

Samples of S304 and SSP were wrapped in tantalum foil and encapsulated in evacuated silica vessels to reduce the presence of oxygen as much as possible and then heated in a furnace. Samples of SP1 and SP2 were not wrapped in foil or encapsulated and were instead heat treated in an argon-backfilled vacuum furnace that reached maximum pressures of <10^{-7}mbar while operating. This was deemed a low enough pressure to prevent significant oxidation using thermodynamic data from Ellingham diagrams. The samples were heated for 1, 10, 100 and 1000 hours at the temperatures 600°C, 650°C, 700°C and 750°C. The temperature was controlled by a microcontroller and thermocouple with a target rate of change of temperature of <10°C/min for both heating and cooling.

3.4 Steam Exposure

Samples to be oxidized in steam at atmospheric pressure were placed into a rig of the design shown in Figure 3. The water used to generate steam was deoxygenated by bubbling nitrogen through it inside metal barrels for > 24hrs. The nitrogen gas pressure was also used to force the deoxygenated water through to the furnaces to ensure a deoxygenated environment. The oxygen content of the feedwater was measured with an Orbisphere Electrochemical oxygen sensor and was kept below 10ppb. The flow rate of the feedwater was measured with a flowmeter with a needle valve. The flowrate was kept within a range of 10-20cc/min. The flow rate and oxygen content of the steam could not be measured directly. The temperature inside the tube furnaces was monitored with thermocouples positioned adjacent to the samples. The temperatures of the samples themselves were not measured to avoid disrupting the steam flow. A water trap positioned at the end of the furnace was used to condense the steam and to prevent oxygen ingress into the furnace.

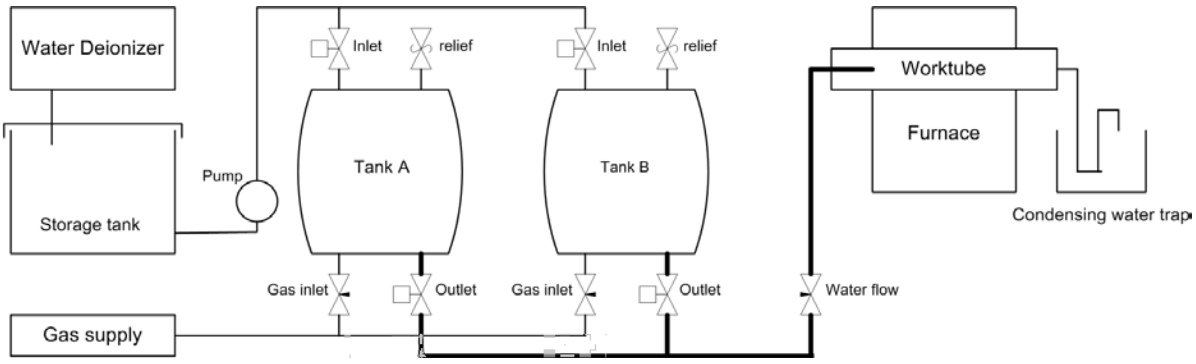

Figure 3 - Schematic of steam oxidation rig used at University of Birmingham

Samples oxidized in high pressure steam were exposed to flowing 70bar steam at 700°C at the National Physics Laboratory, UK. The samples had the same geometry and materials as those used in atmospheric steam oxidation, with a hole drilled adjacent to the outer ring surface. The samples were suspended in the steam rig with Pt wire.

3.5 Etching

Samples were prepared for optical and scanning electron microscopy by electroetching. Chemical etchants such as Kallings Solution failed to bring out the microstructure near the shot peened surfaces in sample cross sections and appeared to always over-etch this region compared to the bulk material.

The mounted cross sections were ground with P220 and P1200 grit paper and then polished with cloths impregnated with diamond suspensions of particle sizes 9µm, 3µm and then 1µm. The final polishing stage was to a <1µm finish with silica oxide suspension. The polished sample was then submerged in a 3:2 mixture of nitric acid (HNO_3) and distilled water (H_2O). The sample was then electroetched at room temperature with a voltage range of 1-6V and a current density of >20mA/cm2 in order to highlight the grain boundaries in the metal

3.6 Microhardness Testing

The microhardness of as-received and heat treated samples was studied by examining the Vickers hardness with a Struers Durascan Microhardness Tester equipped with a square pyramid indenter and 40x optical zoom. The load used to make the indentations was kept at 0.05kg throughout all of the tests so all hardness measurements could be directly compared to each other. Vickers testing gives the result of the microhardness tests in the Vickers Pyramid Number (HV) scale, with the indenter load recorded with each reading in the format xHV(l), were x is the hardness number and l is the applied load in kg.

Some samples were mounted in Bakelite, but this practice was discontinued when SEM imagery showed that the edge retention was poor. The majority of samples were mounted in 'Epofix' epoxy resin in a vacuum. This material is much softer than Bakelite but has superior edge retention and is cold-setting.

The samples were polished by the same method described previously in section 3.5, through several intermediate stages to a <1µm silica finish. Some samples were etched after being hardness tested to allow for optical and electron microscopy observations of the metal microstructure.

The Durascan Microhardness Tester could be automated through its control software to perform indentations, image the indents with an optical microscope, measure the size of the indents from the images and then move on to the next site to repeat the process. In most cases the automated imaging did not work because the system could not satisfactorily focus with the 40x optical microscope. After the indents were created the author had to manually focus the microscope and take additional images for analysis. The control software also failed to reliably measure the indents automatically due to the small size of the indents and the presence of scratches, grain boundaries and other features which made edge detection too complex. The author used the in-built features of the control software to manually highlight the indentations before the hardness number was recorded.

For indentations used to assess hardness depth profiles the recorded images of the indentations were then used to find the distance of the indentation centres from the edge of the sample. This analysis was performed in Image J software by manual measurement of the images.

3.7 Nanohardness Testing

Nanohardness testing was performed by Mike Davies and Nicola Everitt at the University of Nottingham. Cross-sectional samples of SSP and S304 were assessed with a standard depth vs. load hysteresis nanoindentation experiment and were performed on a Nanotest (Micro Materials Ltd., UK). The load on the indenter was increased at a set rate up to the pre-selected maximum load. There was then a pause to allow visco-elastic processes to relax before unloading began. There was a pause in unloading at approximately 10% of maximum load to collect data for a thermal drift correction.

The experiments were performed to a maximum load of 5mN; the loading time was set at 20s and the unloading time at 20s. The dwell at peak load was set at 15s; this was selected after initial experiments to determine the time for any visco-elastic depth change to reach a steady state. 5 rows of 15 indentations were made on each sample. The first indent in each row was made 20µm from the treated surface with subsequent indents placed 20µm apart moving into the sample.

The raw data was analysed using conventional methods popularised by Oliver and Pharr [1] to determine hardness and reduced modulus. The reduced modulus is the combined elastic response of the indenter and sample to the applied load. In order to determine the Young’s modulus is it necessary to know the Poisson’s ratio of the material. However, in this instance because the same experimental set up was used for both samples the reduced moduli can be directly compared without having to calculate the Young’s modulus values.

From each set of indentations the hardness and reduced modulus of equivalent indentations were combined to generate mean values i.e. the 5 hardness values from the first indentation in each of the rows were averaged to give a mean value for the hardness at that depth. This was done at all 15 depths to generate a map of the hardness and modulus moving into the sample.

3.8 Creating TEM Foils With a Focused Ion Beam

Transmission Electron Microscopy (TEM) was needed to characterise the sub-surface region of shot peened material and this required that TEM foils be prepared from the samples. Attempts were made to use both electro-polishing and tripod polishing to create TEM foils, but the author was unsuccessful. A brief description of these techniques is included below.

In Electropolishing [2] a 3mm disc is prepared from the sample and thinned, usually mechanically, to a thickness of the order 100µm. The disc is then placed into an electropolishing machine that sprays an electrolyte onto one or both sides of the sample. The disc can be held at a voltage which encourages the corrosive mixture to work and will be switched off as soon as the disc is found to be perforated. The region around the perforation will have been thinned to electron transparency. It is difficult to control where the disc will perforate and if the sample is not a homogenous material it can be polished unevenly. Electropolishing is used to create stress-free samples from the bulk region of metal samples. It is not suitable for examining thin oxidized surfaces because it is very difficult to create disc-shaped cut outs with the oxide layer in the centre and to ensure that the desired location is thinned.

Tripod polishing [3] is a mechanical means to reduce a sample to electron transparency. The technique involves grinding a small sample, generally around 3mm squared in size and around 100µm thick, on a sequence of diamond impregnated polishing discs. The sample is fixed to a tripod polisher to do this. The tripod polisher is a hand-held device with three 'legs' that can have their height adjusted by micrometres. Changing the leg heights affects the angle of the sample being polished and allows thinning to a wedge that is electron transparent at the tip. Tripod polishing can be used to prepare both planar and cross sectional samples, but the mechanical polishing process can introduce stress into the sample surface. While theoretically possible to prepare samples of the oxidized metal surfaces in this study, the author's attempts were unsuccessful

A Focused Ion Beam (FIB) was used to perform the in-situ lift-out technique[4] using FEI Quanta200 3D DualBeam FIB/SEMs at the University of Birmingham, the University of Nottingham and the Materials Research Facility (MRF) at Culham Centre for Fusion Energy (CCFE). The in-situ lift-out technique is an established method of sample preparation within the literature. However, FIB preparation of TEM samples can cause damage to the foils.

One form of damage is the implantation of the incident ion species into the sample surface. The incident ions are left embedded in the sample surface, with the depth of penetration depending on beam energy and angle and the materials involed. In a study on copper [5], Kiener et al. found that after milling with a Ga FIB, samples had a Ga concentration of up to 20% (atomic weight) in the top several nm and 2% (atomic weight) at 50nm below the surface.

Furthermore, it has been found that the surface can be melted and become amorphous when it is scanned by a FIB [6]. Approximately 5nm below a surface has been seen to become amorphous in a study operating in the same beam energy regime as in the current study (<30keV) on Si (100) wafers [7].

The various forms of damage that FIB can inflict upon a sample must be accounted for when observations are made. When a sample is treated with FIB it can be imaged in-situ by observing secondary electrons and secondary ions. Many devices that use FIB are also equipped with SEM and are dual-beam FIB-SEMs because they can image using both the FIB and an electron beam.

In the current study there was no detected increase in Ga content of the material studied by EDX and TKD techniques and the surfaces of the samples were protected by a layer of platinum or tungsten deposited prior to milling. These steps minimized the damage caused to the sample by the FIB during its processing.

Figure 4 shows the process of creating a cross-sectional TEM foil with the in-situ lift-out technique. First, a protective coating such as tungsten is deposited over the area that will become the foil, shown in Figure 4 (a).

Figure 4 (b) shows the excavation of trenches on either side of the foil. These were large deep and large enough to allow access to the material on both sides and underneath the final foil. Metal was gradually removed to enlarge the trenches until they impinged on the coated area, shown in Figure 4 (c).

The milling was performed in stages, starting with a high beam current for coarse milling and then gradually reduced to prevent damage during fine milling. The currents used were 50, 30, 15, 7, 3nA in this phase of the preparation. The exact currents selected varied depending on the FIB equipment being used, but the differences did not cause any noticeable variation between foils.

The majority of the metal connecting the TEM foil to the sample was then removed as shown in Figure 4 (d) leaving part of the material intact to keep the foil in place for the attachment of a probe. Figure 4 (e) is a plane view of (d) to show all of the material that was removed.

Figure 5 shows the probe that was used to remove the TEM foil after tungsten was deposited to weld the foil and probe together. The remaining point of contact between the metal and the TEM foil was then removed by FIB and the foil lifted free of the sample.

The TEM foil was then welded onto a copper grid (Figure 6) and the final thinning was then performed. The sample was thinned at a beam current of 30pA until it became electron transparent.

During preparation the sample was imaged using both FIB and SEM. When imaging with FIB the accelerating voltage was kept below 30kV and FIB imaging was not used during the final thinning stage to minimize damage to the surface.

Figure 7 shows an electron transparent TEM foil after it has been thinned by FIB and the regions of damage that were caused by this particular foil being thinned for too long at too high a beam current.

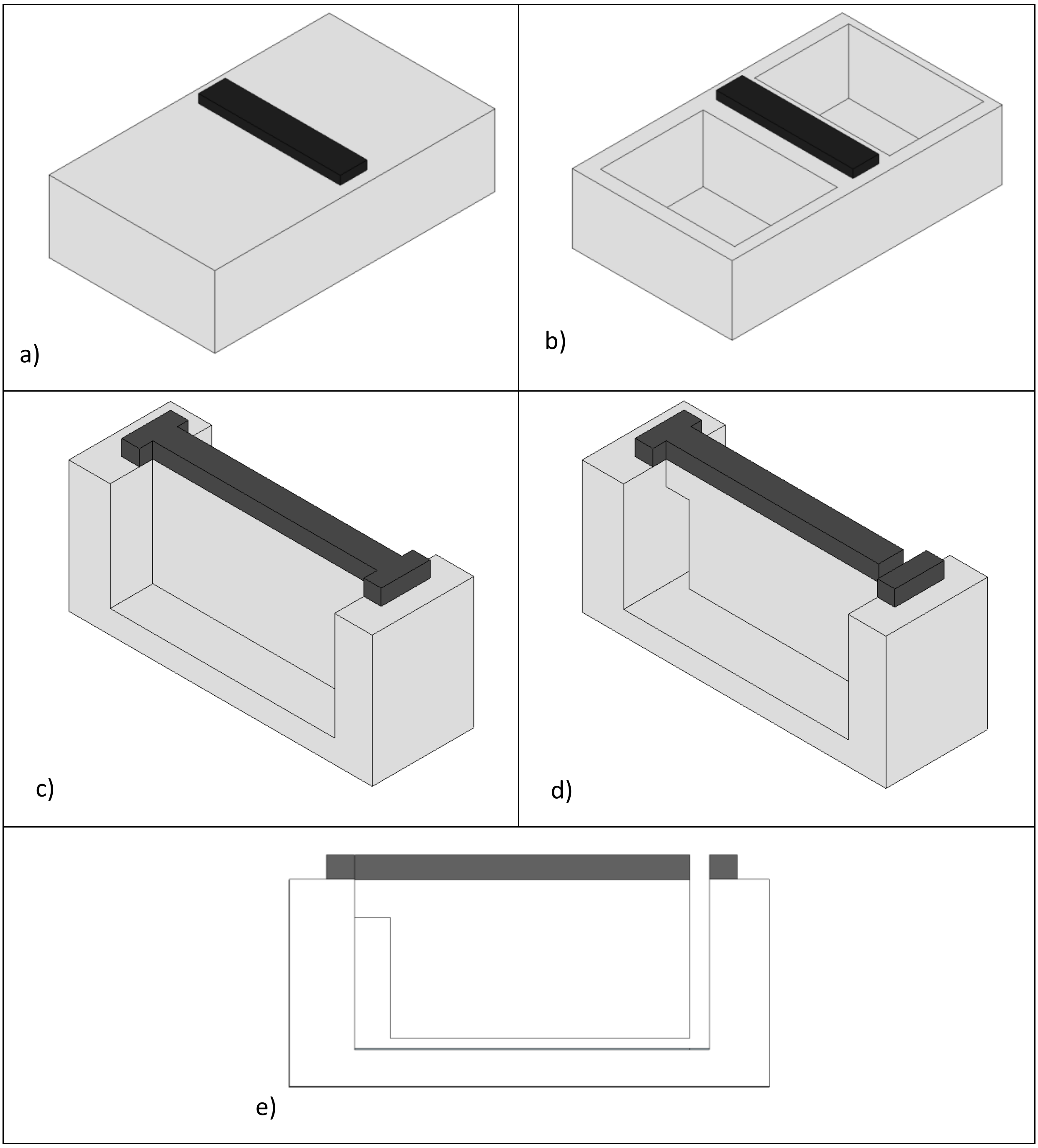

Figure 4 – Initial steps of the in-situ lift-out technique

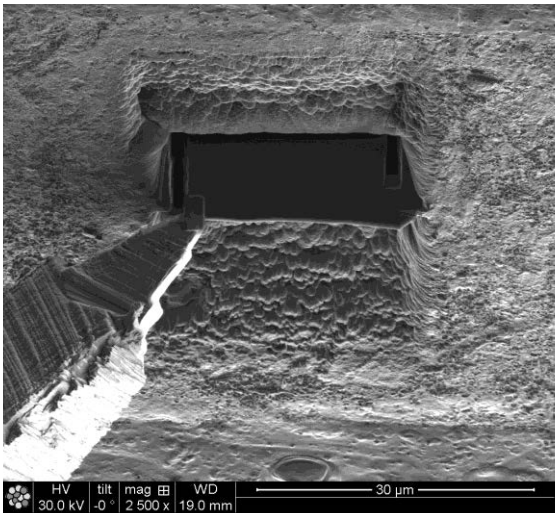

Figure 5 - Probe being attached to in-situ TEM foil by deposited W. Probe is on the left side of the image. The foil orientation is 180° to that shown in Figure 4(e)

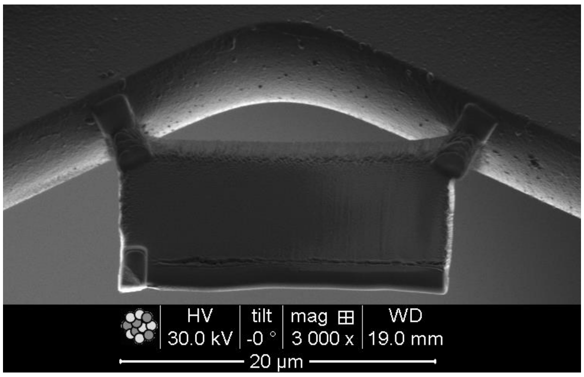

Figure 6 - TEM foil attached to Cu grid by deposited W. The protective W coating and the metal/gas interface being investigated is at the bottom of the foil in this orientation.

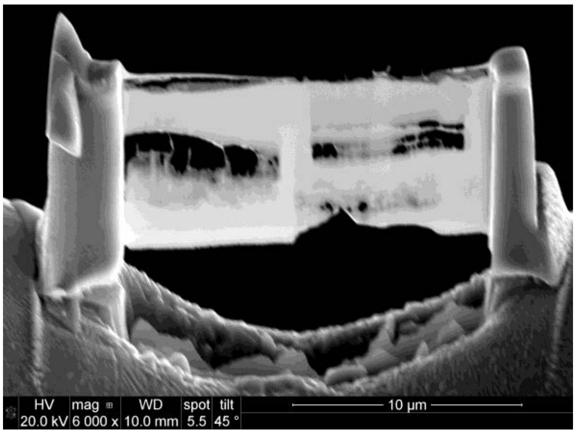

Figure 7 - TEM foil thinned to electron transparency by FIB. Some regions of this foil were thinned away completely, including much of the protective W coating at the top.

3.9 Scanning Electron Microscopy (SEM)

SEM observations were made using a Phillips XL-30 SEM with an Oxford Instruments Inca EDS system and a JEOL 6060 SEM. Secondary electron observations were made with the XL-30 at an accelerating voltage of 20 kV and a working distance of 10mm. EDS observations were made under the same conditions. The Inca EDS system was calibrated with a nickel standard.

Secondary electron observations were made with the JEOL 6060 at an accelerating voltage of 20kV and a working distance of 12mm. The same conditions were also used to make back scattered electron (BSE) observations.

3.10 Transmission Electron Microscopy (TEM)

TEM observations were performed with a JEOL 2100 TEM at the University of Birmingham Centre for Electron Microscopy. All observations were performed at an accelerating voltage of 200kV. Digital Images were acquired with a Gatan Model 830 SC2000 Orius CCD using the Gatan DigitalMicrograph software. Measurements were taken with the aid of the DiffTools plug-in [8]. EDX data were acquired with an Oxford Instruments Inca X-sight EDS system that was calibrated with a copper and aluminium standard.

Brightfield (BF) and Darkfield (DF) techniques were used to observe the oxide and metal morphologies [9]. Selected Area Electron Diffraction (SAED) patterns were used to identify crystal structures and were analysed as discussed in section 3.10.1.

3.10.1 TEM Diffraction Rings

SAED patterns from nanocrystalline materials were analysed using the Diffraction Ring Profiler software [10]. Simulated diffraction ring profiles were generated from crystallographic data using the GDIS software [11]. Crystallographic reconstructions were created from lattice constants and space groups using the VESTA software [12].

3.10.2 Steel Lattice Constants

Lattice constants for the DMV304HCu and Super304H steels are shown in Table 3. The values were calculated using the methods and data in literature review section 2.2.3 (Lattice Constants in 304 Series Steel).

Table 3 - Calculated lattice constants for steels examined in this thesis

Material	**Lattice Constant (Å)**
DMV304HCu (fcc)	3.60
DMV304HCu (bcc)	2.89
Super304H (fcc)	3.60
Super 304H (bcc)	2.89

3.11 Transmission Kikuchi Diffraction (TKD)

TKD was used to map the phases present in TEM foils prepared by FIB. TKD has been developed more recently and is less commonly used than the similar technique of EBSD, so an overview of TKD is included below in the section Principles of Transmission Kikuchi Diffraction.

TKD was performed at the Materials Research Facility (MRF) at Culham Centre for Fusion Energy (CCFE) using a TESCAN Mira3 XMH SEM. The TKD patterns were acquired by an Oxford Instruments NordlysNano EBSD Detector and analysed with HKL AZTec software. An X-Max 80 EDS detector was used to acquire EDS data from the samples. Additional grain, phase and orientation maps were created using the MTex Toolkit, a set of tools for MATLAB software.

TKD patterns were indexed against FCC iron, BCC iron, manganese-chromium-spinel and Chromia. Other materials were present in some samples but TEM and EDX were used to identify them, not TKD.

3.11.1 Principles of Transmission Kikuchi Diffraction

TKD is also known as transmission-EBSD (t-EBSD) because the two techniques use common equipment and analysis methods to produce orientation and phase maps. A comparison of the geometry of the EBSD and TKD methods are shown in Figure 8. In EBSD [13], grain orientations are found by imaging the Kikuchi patterns of backscattered electrons generated at the sample surface by a scanning electron beam in an SEM [14]. Kikuchi patterns can be indexed to reveal a crystal's structure and orientation. In TKD, the same Kikuchi patterns are used but they are generated by electrons that have been transmitted through an electron transparent sample [15].

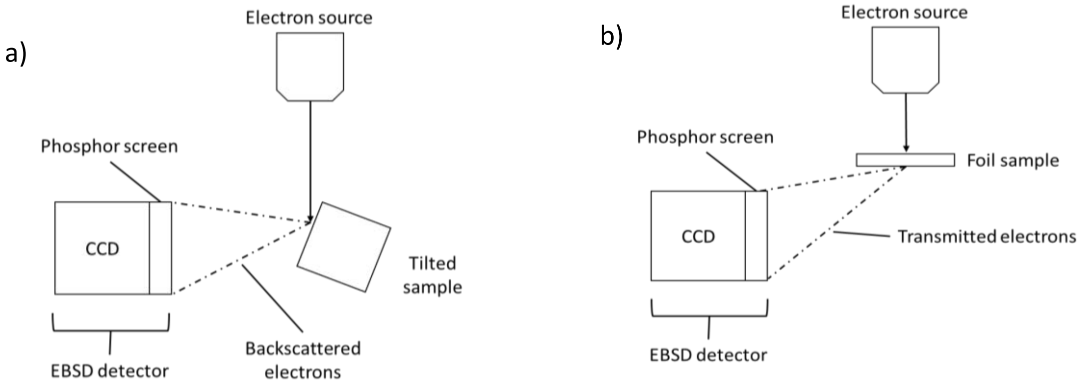

Figure 8 - Sample and detector geometries of (a)EBSD and (b) TKD mapping

Both techniques require that the EBSD detector cover as wide an angle as possible to image a significant portion of the Kikuchi pattern, and that it must be close to the sample surface to detect a strong signal. The best conditions for EBSD mapping are therefore achieved by tilting the sample to ≈70° relative to the incident electron beam and positioning the detector at ≈90° to the incident beam and as close as possible to the sample surface. The high incident angle of the electron beam creates a larger interaction volume (shown in

Figure 9 (a)) in the sample surface than in TKD and limits the resolution of EBSD to >20nm [16].

In TKD the sample is electron transparent and the Kikuchi patterns are generated by electrons being diffracted by a smaller angle than in EBSD. This geometry makes the interaction volume of the electron beam and the sample much smaller, as shown in Figure 9 (b). Reducing the interaction volume improves the resolution of the technique to be able to observe features of the order of 2nm in size and reduces the background noise.

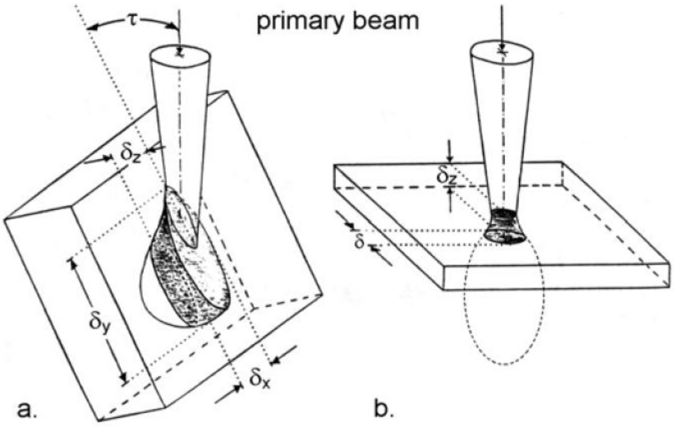

Figure 9 – Interaction volumes and spatial resolutions (δ) in (a)EBSD and (b) TKD. Taken from [16].

Kikuchi patterns are observed as the electron beam is scanned across a sample and are indexed to identify crystal structure and orientation. This data can be used to generate phase maps to highlight different crystal structures or orientation maps to show the orientation relationships between different grains.

3.12 Identifying Grain Size by SEM

The diameter of grains >10µm below the surface was assessed by mounting the materials as cross-sectional samples in cold-setting Epo-Fix resin. Each sample was then ground and polished to a <1µm finish, electro-etched and then observed using a JEOL 6060 SEM. Grain sizes were established using the linear intercept method [17, 18]. For the bulk grain size in areas unaffected by shot peening, 5-10 lines were drawn vertically and horizontally across SEM images taken at a 500x magnification. The number of times that a line crossed over a grain boundary and the length of a line were recorded and used to find the average grain diameter of a sample, its standard deviation and its standard error.

An analysis of the change in grain size with distance from the shot peened surface was performed by marking lines on images parallel to the shot peened edge at intervals of 10µm as shown in Figure 10. The distance of the line from the surface, the number of grain boundary intercepts and the length of the lines were then recorded to create a profile of grain sizes with changing depth.

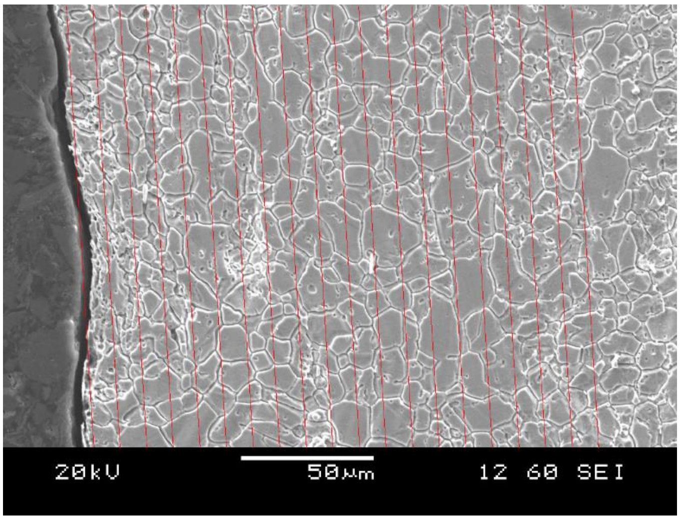

Figure 10 - SEM image of a cross section through the shot peened edge of etched SP1 with markers showing 10µm increments from the surface

3.13 Identifying Grain Size by TEM

The grain size of material <10µm from the shot peened surface could not be found with optical or scanning electron microscopy because of the small scales involved (10-100nm) and because etching of the samples did not highlight the grain structure in the region. TEM foils were observed in darkfield and brightfield TEM modes. Brightfield images contained the most grains but were too complex for automated processing and interception analysis. The brightfield images were loaded into graphical editing software (GIMP[19]) and combined to form a very large, complete image of the entire foil. The visible grains were highlighted by hand in different colours to construct a second, simplified image. The simplified image was then processed with the ImageJ software[20] by detecting the edges in the image and the edges were 'Skeletonized' to reduce all the grain boundaries to a width of 1 pixel. The skeletonized image was then analysed using the ImageJ particle detection plugin 'Particles4'[21] to provide information on the grain sizes and their locations.

DF images only showed a small number of randomly distributed grains in a single image, but they were of much higher contrast and amenable to automated processing. The DF images were thresholded individually in order to keep only the brightest grains in each image. GIMP was then used to 'despeckle' the image and remove noise which would create false grains of <1nm size when analysed. Some images were 'cleaned' by hand to remove badly-thresholded sections. This was only performed when a large grain was observed clearly in DF and BF images but was not continuous after thresholding. The thresholded images were then analysed with ImageJ particle analysis to detect grains and record the following data for each:

- X/Y Pixel coordinates of grain centre
- Area of grain (px)
- Fitted Ellipsoid major and minor radii

The grains were then arranged into size categories and the fraction of each category that made up the total highlighted area was found. Therefore, for a given area of grains highlighted in DF images it was possible to observe the grain size distribution.

3.14 Measuring Oxide Thickness

The oxide layers being examined in this study were too thin to observe in SEMs and would often be damaged during cross-sectional mechanical polishing. The oxide thicknesses were therefore measured on the TEM foils prepared by the in-situ lift-out technique using FIB. TEM brightfield images were taken of the foils and then loaded into GIMP, a graphical editing program. The oxide was then highlighted in black, the base metal in grey and everything else (mostly empty space) in white. A script was then run in ImageJ to find the closest distance from points at a regular spacing on the oxide/gas interface to the underlying base metal. These values were then recorded and used to produce a profile of the oxide thickness, which could be analysed numerically. Detailed instructions and the script used to measure the oxide thickness are included in appendix B.

3.15 References

1. Oliver, W. C., & Pharr, G. M. (1992). An improved technique for determining hardness and elastic modulus using load and displacement sensing indentation experiments. *Journal of Materials Research*, *7*(6), 1564–1583. doi:10.1557/JMR.1992.1564

2. Garcia-Borquez, A., & Kesternich, W. (1993). Controlled Depth and Cross-Section Preparation Techniques for Transmission Electron Microscopy Subsurface Studies in Metals. *Microscopy Research and Technique*, *25*, 255–263. doi:10.1002/jemt.1070250307

3. Benedict, J., Anderson, R., & Klepeis, S. (1991). Recent developments in the use of the tripod polisher for tem specimen preparation. In R. Anderson, B. Tracy, & J. Bravman (Eds.), *Specimen preparation for transmission electron microscopy of materials - III* (pp. 121–140). Pittsburgh: Materials Research Society.

4. Langford, R. M., & Rogers, M. (2008). In situ lift-out: steps to improve yield and a comparison with other FIB TEM sample preparation techniques. *Micron*, *39*(8), 1325–30. doi:10.1016/j.micron.2008.02.006

5. Kiener, D., Motz, C., Rester, M., Jenko, M., & Dehm, G. (2007). FIB damage of Cu and possible consequences for miniaturized mechanical tests. *Materials Science and Engineering: A*, *459*(1–2), 262–272. doi:10.1016/j.msea.2007.01.046

6. Bals, S., Tirry, W., Geurts, R., Yang, Z., & Schryvers, D. (2007). High-quality sample preparation by low kV FIB thinning for analytical TEM measurements. *Microscopy and microanalysis : the official journal of Microscopy Society of America, Microbeam Analysis Society, Microscopical Society of Canada*, *13*(2), 80–6. doi:10.1017/S1431927607070018

7. Basnar, B., Lugstein, A., Wanzenboeck, H., Langfischer, H., Bertagnolli, E., & Gornik, E. (2003). Focused ion beam induced surface amorphization and sputter processes. *Journal of Vacuum Science & Technology B: Microelectronics and Nanometer Structures*, *21*(3), 927. doi:10.1116/1.1565345

8. Mitchell, D. R. G. (2008). DiffTools: electron diffraction software tools for DigitalMicrograph. *Microscopy research and technique*, *71*(8), 588–93. doi:10.1002/jemt.20591

9. Williams, D., & Carter, C. (2009). *Transmission Electron Microscopy* (2nd Ed.). New York: Springer Science.

10. Zhang, L., Holt, C. M. B. B., Luber, E. J., Olsen, B. C., Wang, H., Danaie, M., … Mitlin, D. (2011). High Rate Electrochemical Capacitors from Three - Dimensional Arrays of Vanadium Nitride - Functionalized Carbon Nanotubes. *The Journal of Physical Chemistry C*, *115*, 24381–24393. doi:10.1021/jp205052f

11. Fleming, S., & Rohl, A. (2005). GDIS: a visualization program for molecular and periodic systems. *Zeitschrift für Kristallographie - Crystalline Materials*. doi:10.1524/zkri.220.5.580.65071

12. Momma, K., & Izumi, F. (2008). VESTA: a three-dimensional visualization system for electronic and structural analysis. *Journal of Applied Crystallography*, *41*(3), 653–658.

doi:10.1107/S0021889808012016

13. Wilkinson, A. J., & Hirsch, P. B. (1997). Electron diffraction based techniques in scanning electron microscopy of bulk materials. *Micron*, *28*(4), 279–308. doi:10.1016/S0968-4328(97)00032-2

14. Humphreys, F. J. (2001). Grain and subgrain characterisation by electron backscatter diffraction. *Journal of Materials Science*, *36*(16), 3833–3854. doi:10.1023/A:1017973432592

15. Sneddon, G. C., Trimby, P. W., & Cairney, J. M. (2016). Transmission Kikuchi diffraction in a scanning electron microscope: A review. *Materials Science and Engineering R: Reports*, *110*, 1–12. doi:10.1016/j.mser.2016.10.001

16. Schwarzer, R. A. (2008). Spatial Resolution in ACOM - What Will Come After EBSD. *Microscopy Today*, *16*(1 (January)), 34–37.

17. ASTM International. (2015). ASTM E1382-97 Standard Test Methods for Determining Average Grain Size Using Semiautomatic and Automatic Image Analysis. doi:10.1520/E1382

18. ASTM International. (2014). ASTM E112-13: Standard Test Methods for Determining Average Grain Size, 1–28. doi:10.1520/E0112-13.1.4

19. The GIMP Team. (2016). GIMP. Retrieved from https://www.gimp.org/

20. Rasband, W. S. (n.d.). ImageJ. Bathesda: U. S. National Institutes of Health. Retrieved from http://imagej.nih.gov/ij/

21. Landini, G. (2008). Advanced shape analysis with ImageJ. In *Proceedings of Second ImageJ User and Developer Conference* (pp. 116–121). Luxembourg. Retrieved from http://www.mecourse.com/landinig/software/software.html

4 Results: The Effects of Heat Treatment on Shot Peened Microstructure

4.1 Microhardness Tests

4.1.1 Bulk Microhardness

Hardness tests were performed on cross-sectioned samples mounted in epofix resin and polished to a <1µm silica finish. The as-peened samples had HV microhardness shown in Table 1. Bulk hardness tests were taken >2mm from the shot peened surface to avoid being affected by residual stresses from the shot peening, as discussed in literature review section 2.3.

Table 1 - Microhardness in the bulk of the as-peened samples

Material	**Bulk Microhardness (HV0.05)**	**Standard Deviation**
SSP	195	6
SP1	221	8
SP2	226	15
S304	264	10

The bulk microhardness of the SP1, SP2 and SSP samples exposed to high temperatures in a vacuum for 1-1000hrs are shown in Figure 1, Figure 2 and Figure 3 respectively. The error bars show the standard error of the hardness measurements rather than the standard deviation. This is in order to illustrate the effect of heat treatment on the mean hardness, and not the range of hardness values throughout the samples.

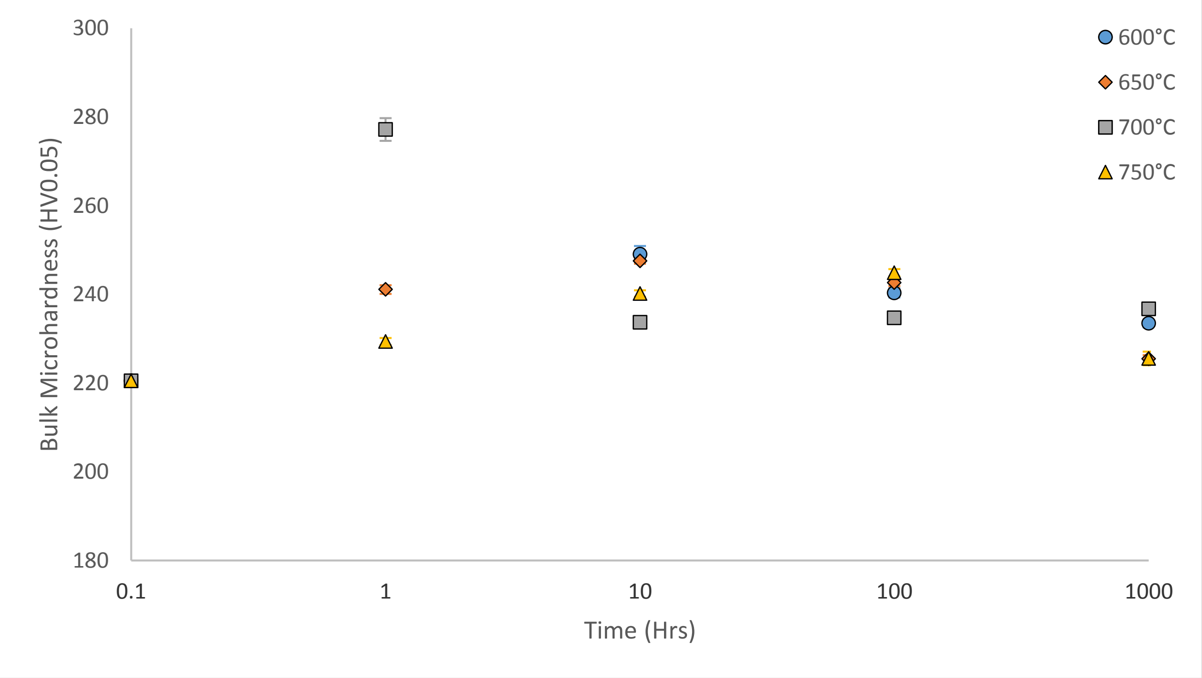

Figure 1 - Bulk microhardness of SP1 after heat treatments in vacuum

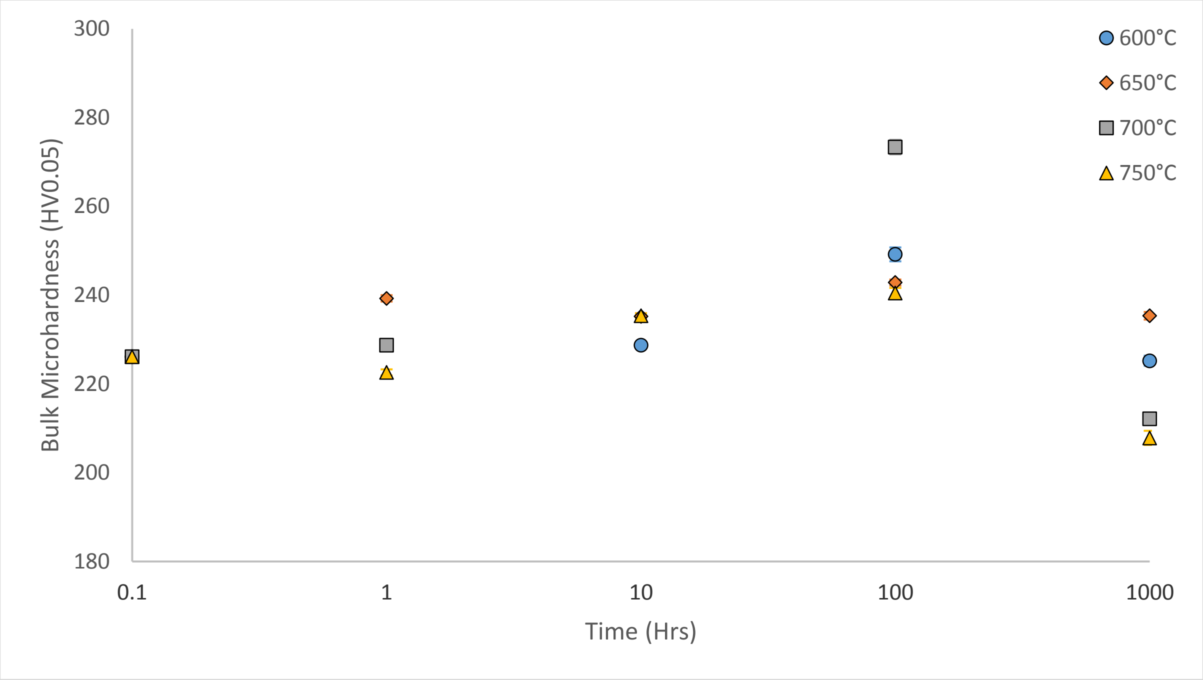

Figure 2 - Bulk microhardness of SP2 after heat treatments in vacuum

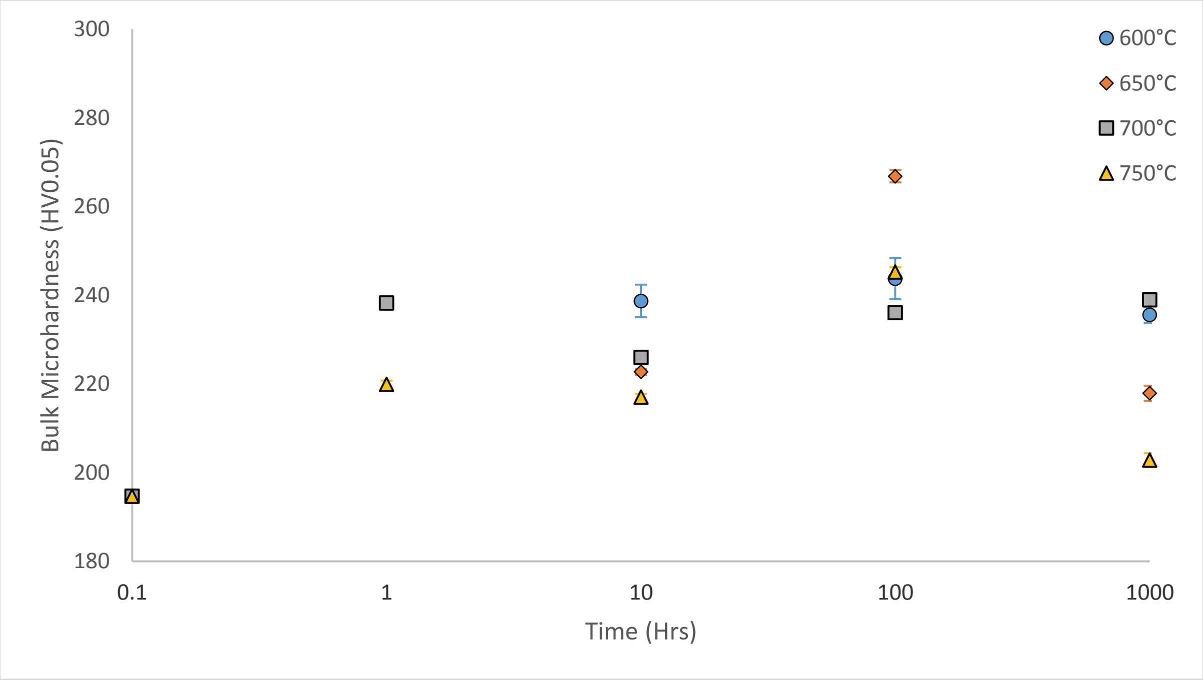

Figure 3 - Bulk microhardness of SSP after heat treatments in vacuum

All of the samples show an increase in hardness up to 100hrs into the heat treatment. After 1000hrs all of the samples had undergone a reduction in hardness relative to their peak values, but only SP2 samples had actually gone lower than their initial hardness, and only at 700°C and 750°C.

4.1.2 Surface Microhardness Profiles

The microhardness profiles of the as-peened samples of SP1, SP2, SSP and as-received S304 are shown in Figure 4, Figure 5, Figure 6 and Figure 7, respectively. The distance from the surface is based on the location of the tip of the indenter, and therefore the centre of each indentation. The bulk microhardness is also included for comparison. Bulk microhardness values are mean values from >25 hardness measurements taken >2mm from the surface.

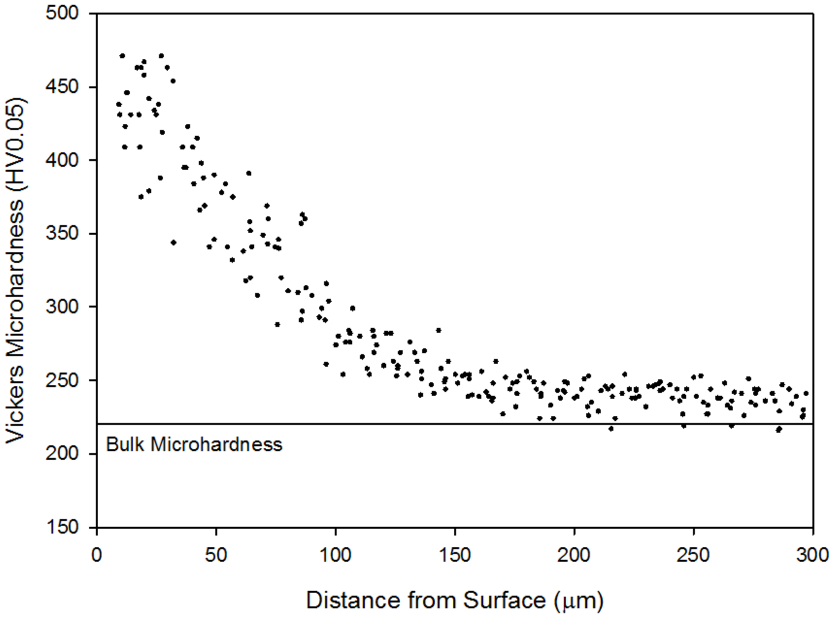

Figure 4 - Microhardness profile of as-peened SP1

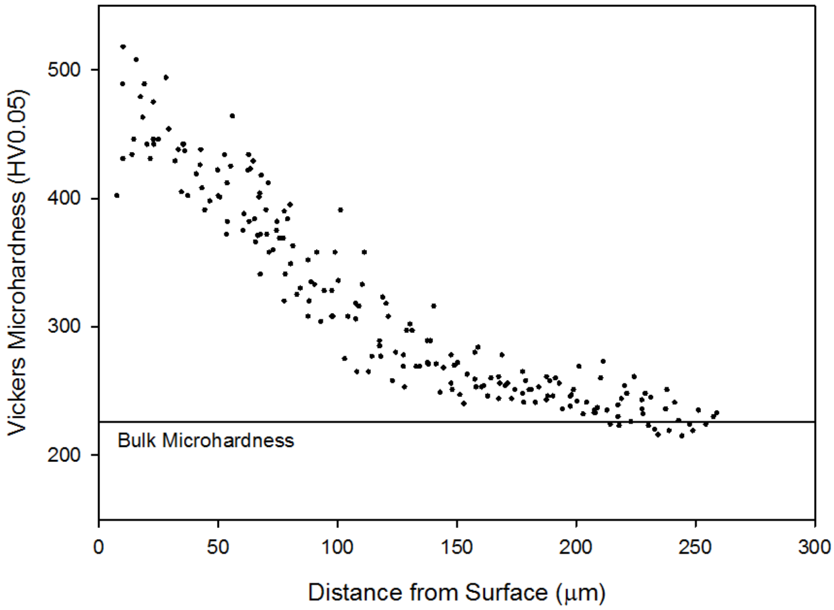

Figure 5 - Microhardness profile of as-peened SP2

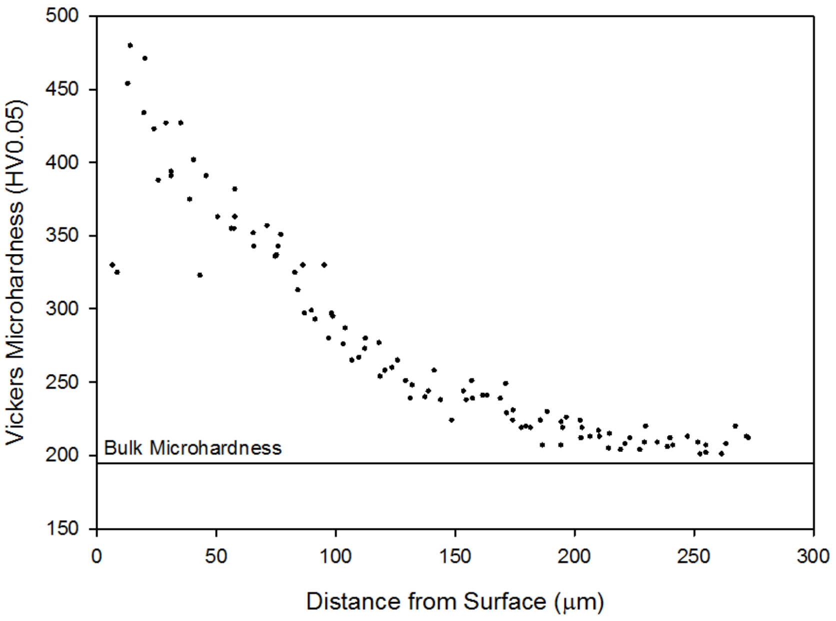

Figure 6 - Microhardness profile of as-peened SSP

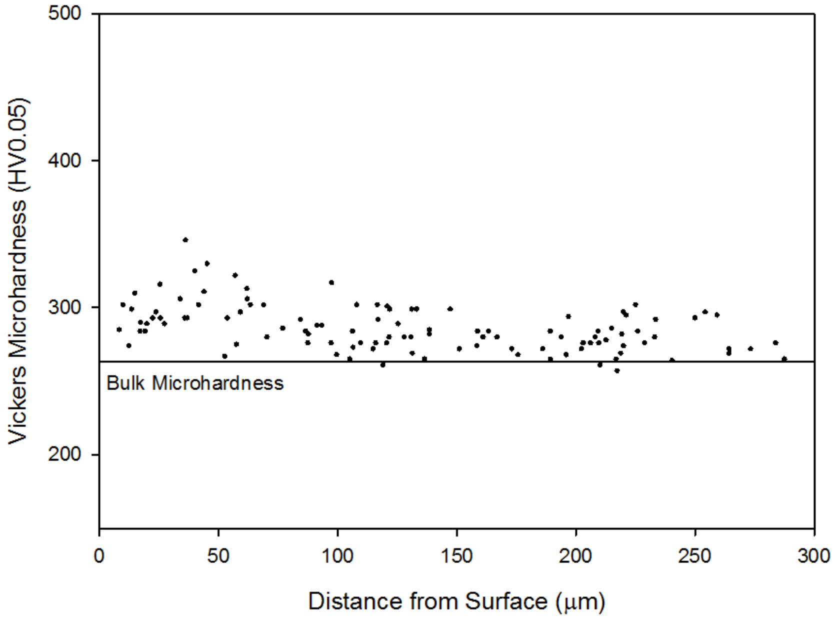

Figure 7 - Microhardness profile of as-received S304 (pickled surface)

Each microhardness profile was fitted to a curve by regression. The model curve was chosen as a Gaussian profile (1) in order to identify the peak hardness value and the distance from the surface of the peak hardness. Fitted curves for Figure 4 - Figure 7 are shown individually in Figure 8 and are all plotted on the same axis in Figure 9. The parameters of the curves are given in Table 2.

$$f(x) = y_0 + a \cdot exp\left[-0.5\left(\frac{|x - x_0|}{b}\right)^c\right] \tag{1}$$

y_0 = Bulk microhardness (found by regression)
a = Peak microhardness – y_0 (found by regression)
b = Variable found by regression
c = Variable found by regression
x = Distance from surface (µm)
x_0 = Distance from the surface of the peak microhardness (found by regression)

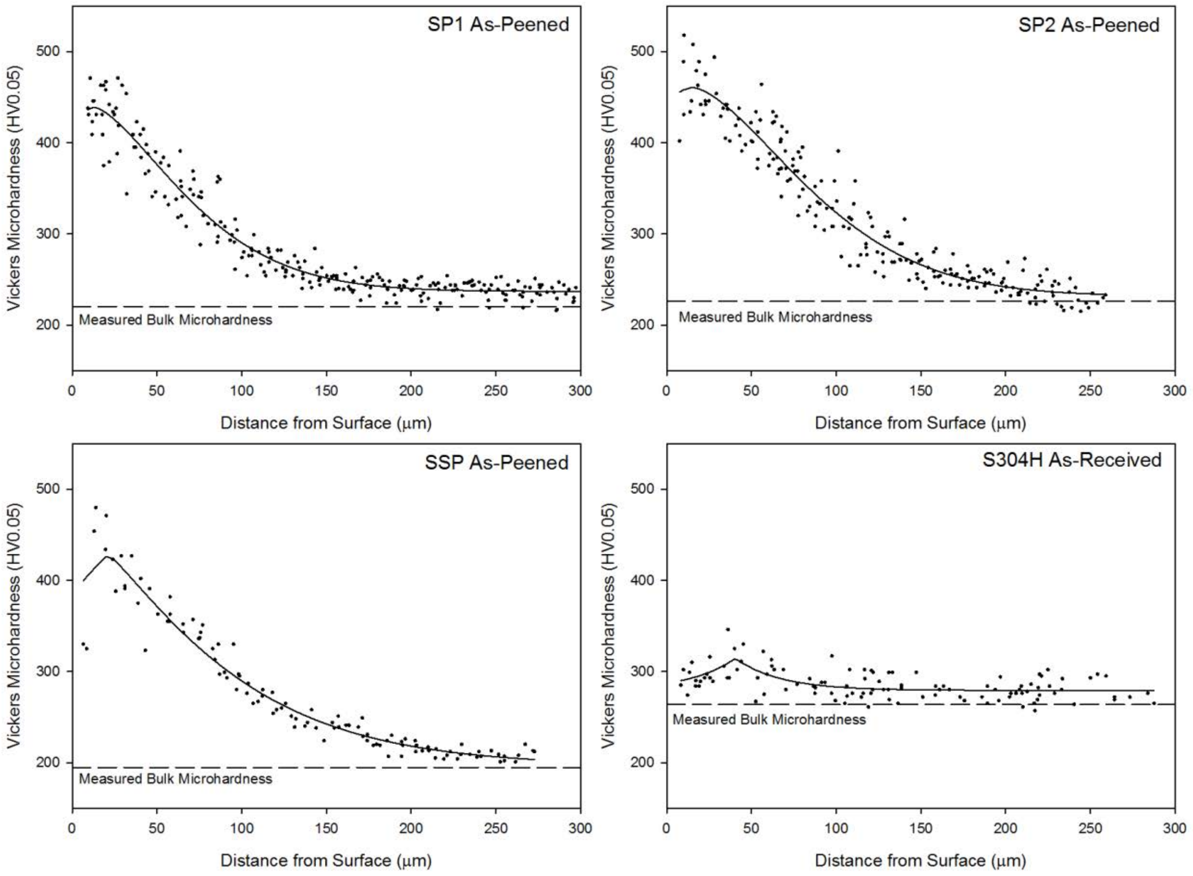

Figure 8 - Microhardness profiles and fitted curves of as-peened SP1, SP2, SSP and as-received S304H. Curves were fitted to a Gaussian profile (1) with parameters given in Table 2.

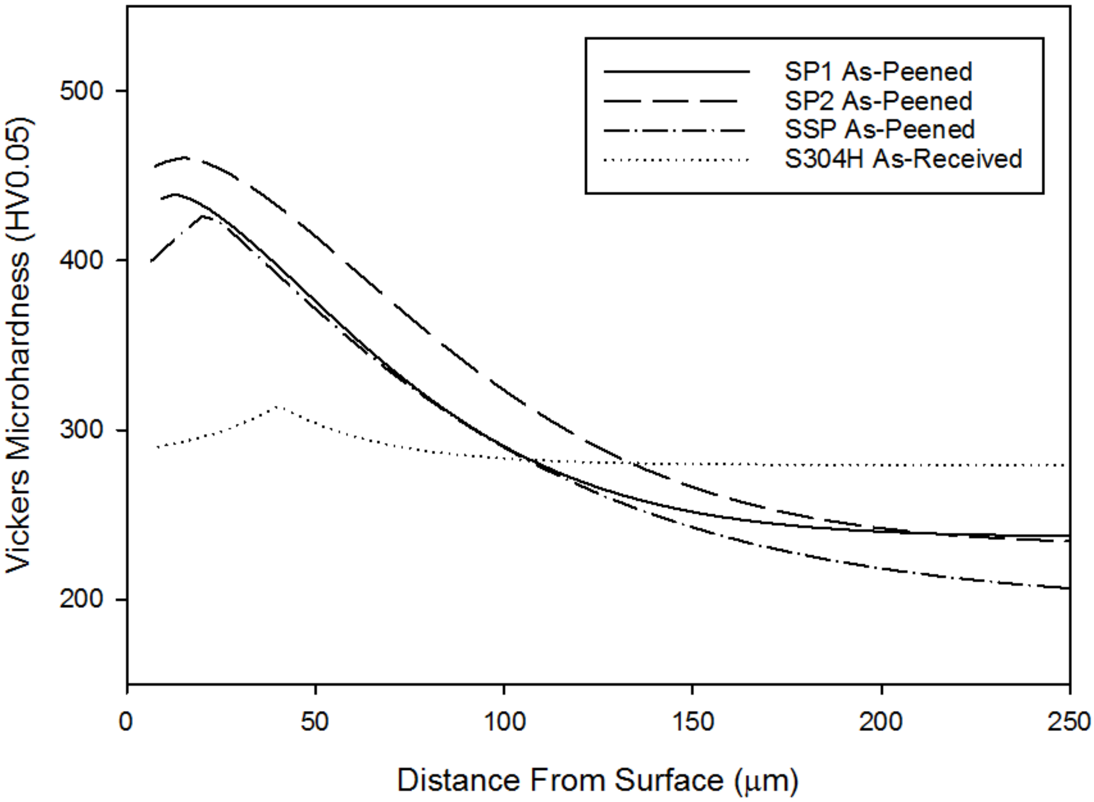

Figure 9 – Fitted curves of the microhardness profiles of the as-peened/as-received materials. Curves were fitted to Gaussian profiles (1) with parameters given in Table 2.

The shot peened materials reached a peak microhardness of ≈450 HV0.05 at <25µm distance from the shot peened surface. The hardness of all three shot peened materials then returned to values above the measured bulk microhardness at a depth of 150-200µm. The values found for bulk microhardness from the curve fits (y_0) were all within 2 standard deviations of the measured bulk microhardness.

Table 2 - Parameters for fitted curves of microhardness profiles in Figure 9. Errors are standard errors.

Material	**a**			**b**			**c**			**x_0**			**y_0**		
SP1	202	±	5	45	±	5	1.5	±	0.1	13	±	4	237	±	2
SP2	229	±	8	58	±	6	1.6	±	0.2	15	±	6	232	±	5
SSP	231	±	16	47	±	5	1.2	±	0.2	21	±	3	197	±	9
S304H	35	±	9	14	±	8	1.0	±	0.5	40	±	3	279	±	2

The fitted curve for S304 had a small peak that could have been scatter in the data. The small peak compared to the scatter showed that the microhardness at the sample edge could be considered the same as that found in the bulk. The S304H sample was not expected to show any clear peaks in microhardness because it had a pickled surface instead of being shot peened. However, the S304 bulk hardness was the highest of all four materials. There is no apparent difference between S304 and SSP that would explain the higher relative hardness of S304. SSP and S304 are from the same supplier, are ostensibly of the same composition, and the different surface treatments (shot peening and pickling) should not have changed the bulk hardness of either samples significantly. S304 was not investigated in any other experiments in this thesis, so the discrepancy will remain an open question.

4.1.3 Limitations of Microhardness Testing Near a Shot Peened Edge

As was discussed in the literature review section 2.4.1.1, it is recommended that indentations used for testing microhardness are made no closer than 2.5x the length of the indentation diagonal to each other or a sample edge. The ideal separation between two indentations or an indentation and a sample edge is therefore dependant on the hardness of the material being tested. The size of an indentation and the hardness of material are related by (2).

$$HV = \frac{2F}{d^2}\sin\frac{136°}{2} = 1.854\frac{F}{d^2} \qquad (2)$$

HV = Vickers Hardness Number (kg/mm^2)
F = Indentation load (kg)
d = Mean diagonal length of indentation (mm)

This relationship allows the calculation of the minimum Vickers microhardness that can be safely measured at a given distance from a sample edge. Any microhardness measurements made that are below this minimum microhardness will be too close to a sample edge to satisfy the ASTM standard, and may underestimate the microhardness. This data is plotted for the indentation load used in this study (0.05kg) in Figure 10. The harder the material, the smaller the indentation made during testing and therefore readings taken closer to the edge can be considered free from interference caused by the presence of the edge.

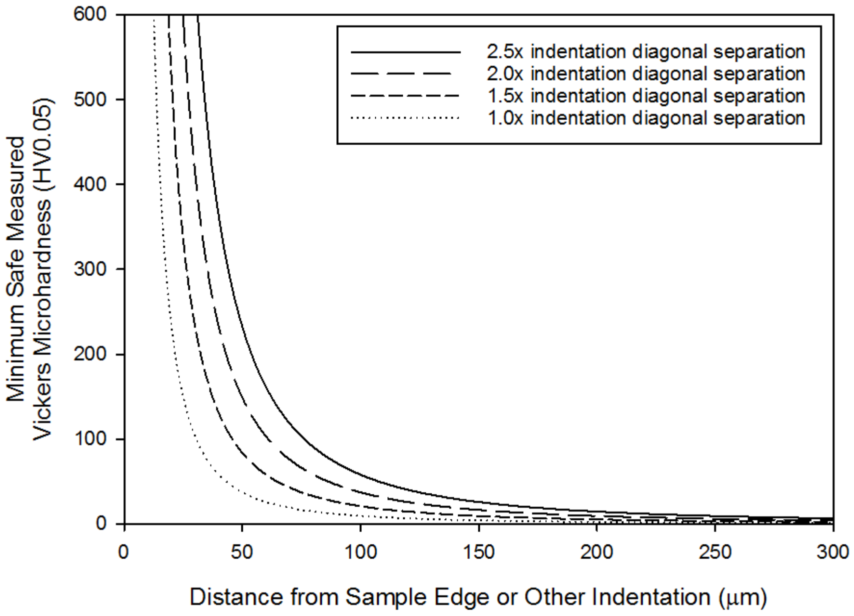

Figure 10 - Minimum Vickers microhardness that can be reliably measured at a given distance between indentations or from the sample edge for an indentation load of 0.05kg. Indentations and a sample edge must be separated by at least 2.5x the indentation diagonal in order to comply with the ASTM standard for Vickers microhardness testing.

These margins are plotted with the data from Figure 8 in Figure 11. At distances less than the 2.5x separation distance from the edge, the actual microhardness values are likely to be higher than the measured values. The difference between measured microhardness and actual microhardness will increase as the measurements are taken closer to the sample edge because the amount of material in the plastic zone beneath the indenter tip is reduced by its intersection with the sample edge.

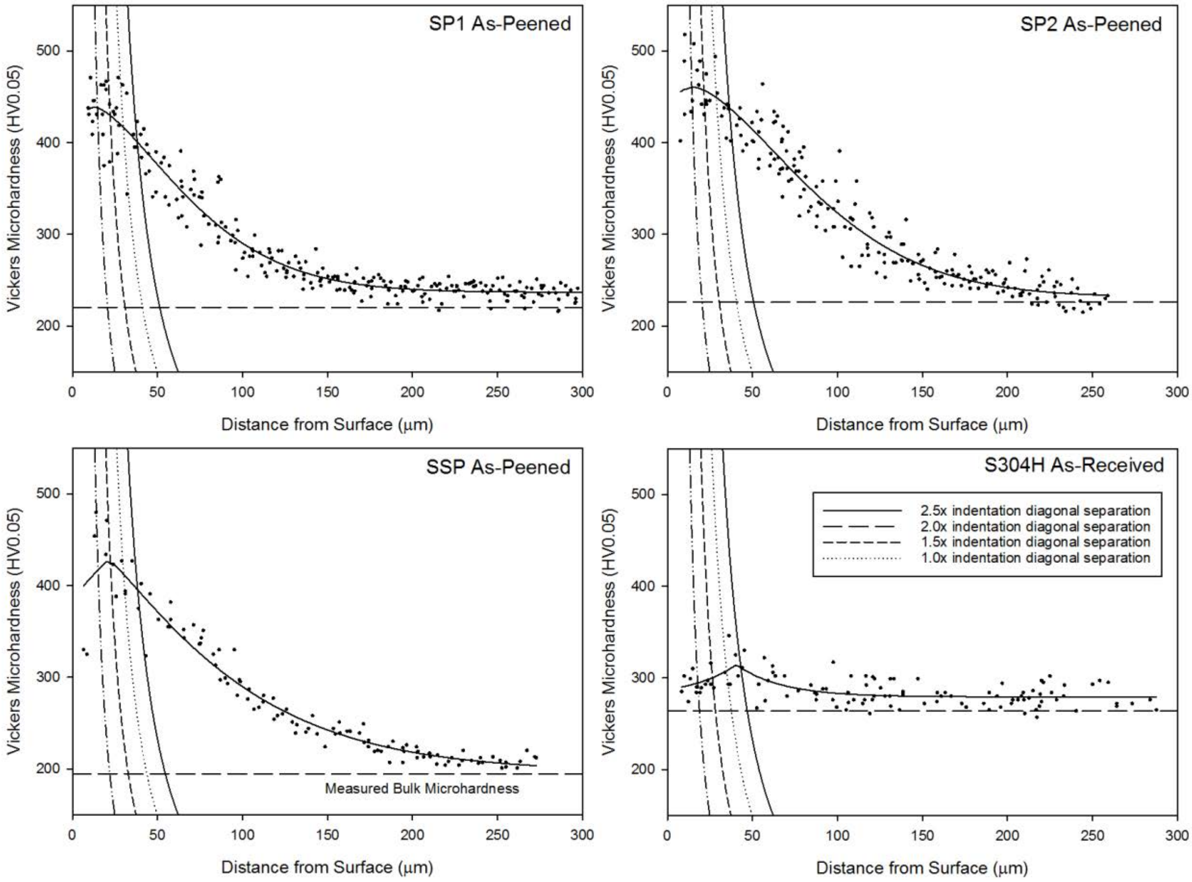

Figure 11 - Microhardness profiles and fitted curves of as-peened SP1, SP2, SSP and as-received S304H in Figure 8 with minimum separation distances from Figure 10 added to the axis. Only points to the right/above the 2.5x indentation diagonal separation line satisfy the ASTM standard for minimum distance from the sample edge. Horizontal dotted line is measured bulk microhardness.

Figure 11 shows that in all of the as-peened/as-received materials the measured peak microhardness of the material is being influenced by the indenter tip's proximity to the sample edge. If a smaller indentation load or a nano-hardness tester were to be used instead, the measured microhardness would reach higher values closer to the sample edge.

It is not possible within the limitations of the present work to calculate the actual microhardness of the material at distances closer than the 2.5x minimum separation from the presented data. However, these results would be consistent with the actual peak microhardness being located at the sample edge and the microhardness profile resembling an exponential decay curve such as one shown in Figure 12. This estimation is not mathematically rigorous and is only used to suggest a likely qualitative trend.

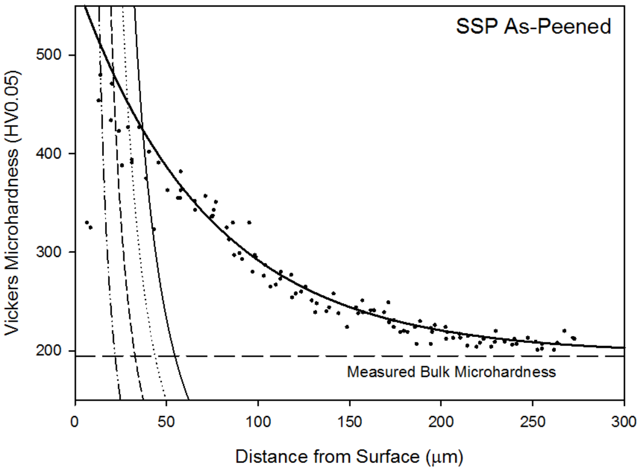

Figure 12 - Estimation of microhardness profile of as-peened SSP accounting for proximity to the sample edge.

4.1.4 Surface Microhardness Profiles After Heat Treatment

The microhardness profiles of SP1, SP2 and SSP after being heated in a vacuum at 600°C, 650°C, 700°C and 750°C for up to 1000hrs are shown in Figure 13 to Figure 24. Each plot includes the minimum safe microhardness values shown in Figure 10 and a fitted curve described by (1). The parameters of the fitted curves are given in Table 3.

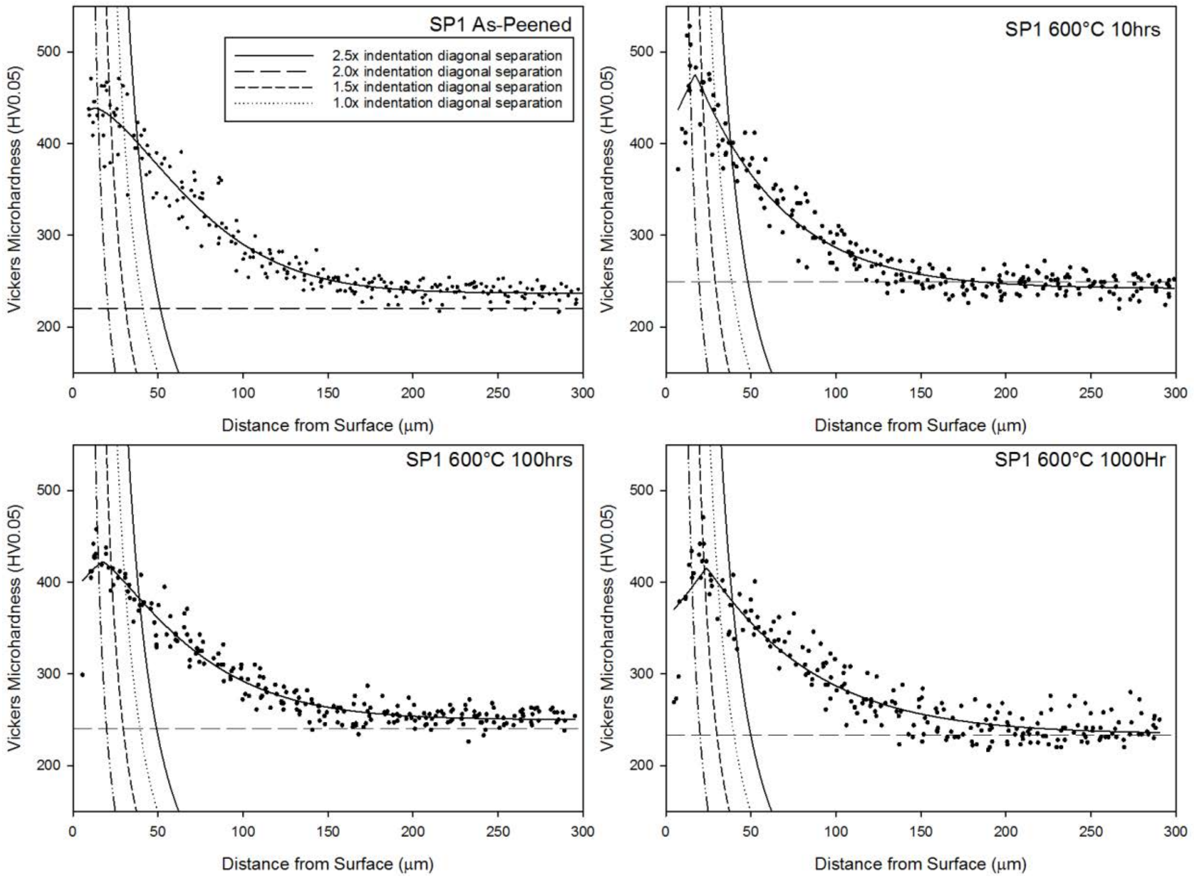

Figure 13 - Microhardness profiles of SP1 after being heated in a vacuum at 600°C for 10, 100 and 1000hrs. Horizontal dotted lines are measured bulk microhardness values taken from the same samples at distances >1mm from the shot peened surface.

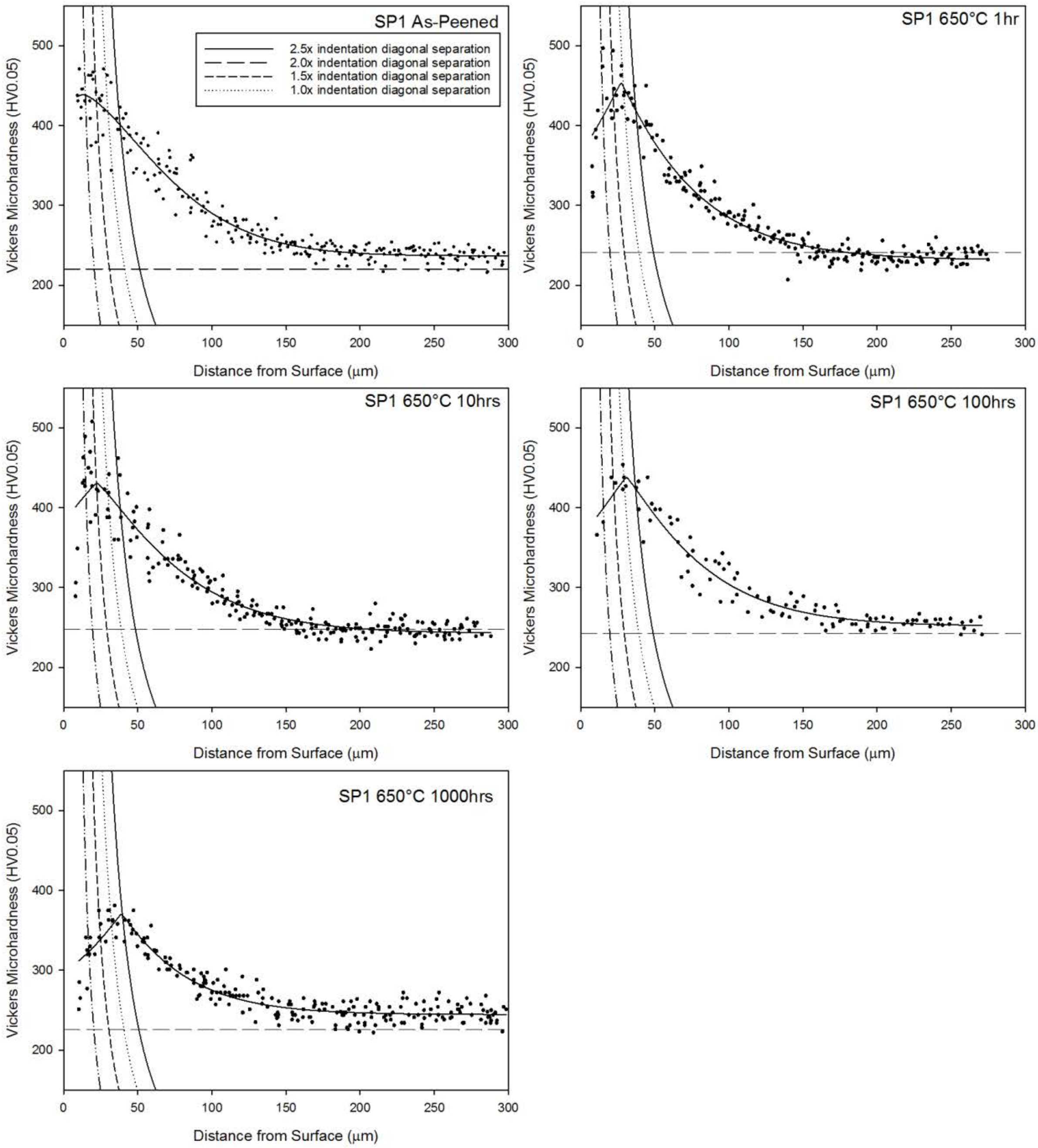

Figure 14 - Microhardness profiles of SP1 after being heated in a vacuum at 650°C for 1, 10, 100 and 1000hrs. Horizontal dotted lines are measured bulk microhardness values taken from the same samples at distances >1mm from the shot peened surface.

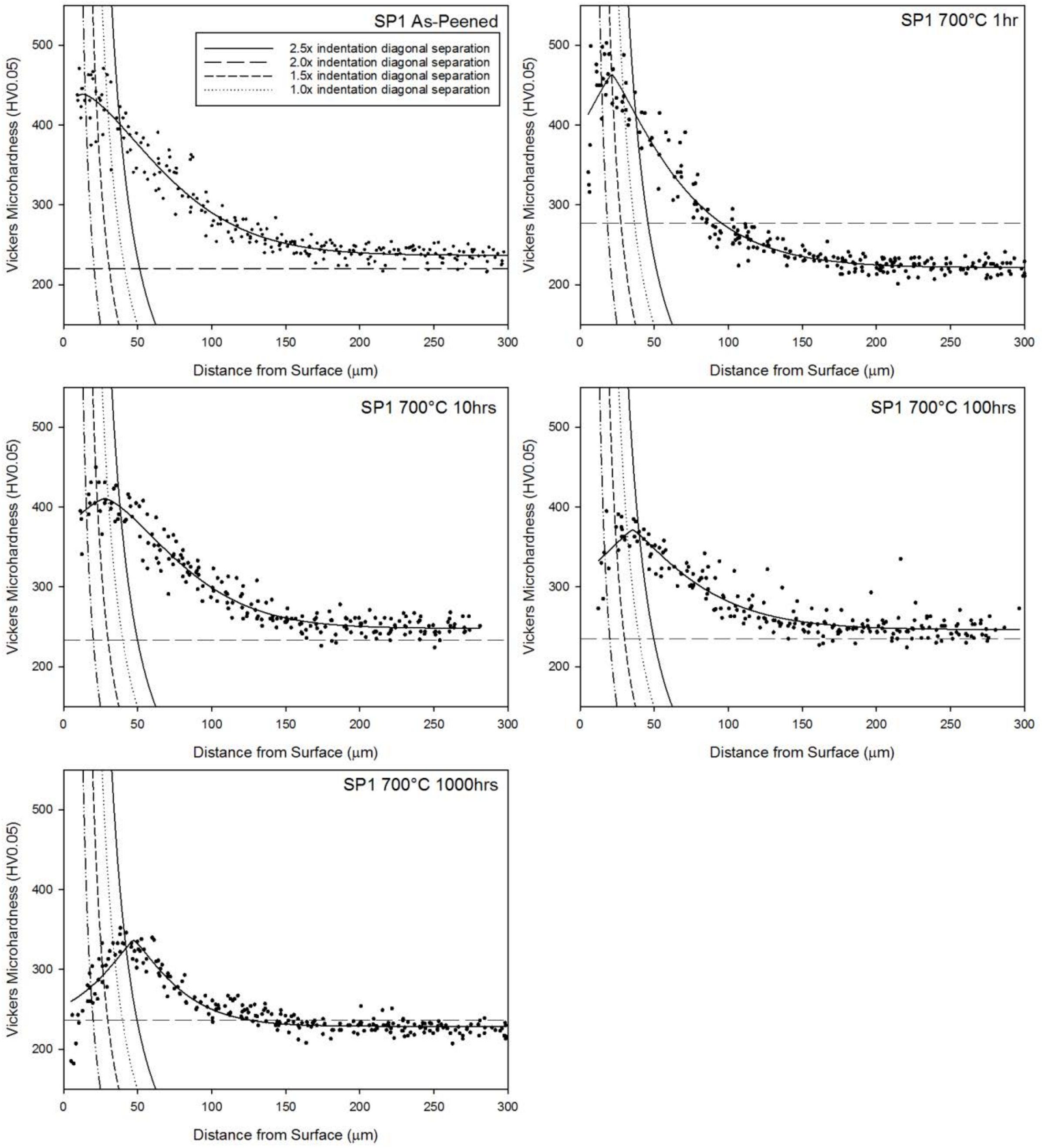

Figure 15 - Microhardness profiles of SP1 after being heated in a vacuum at 700°C for 1, 10, 100 and 1000hrs. Horizontal dotted lines are measured bulk microhardness values taken from the same samples at distances >1mm from the shot peened surface.

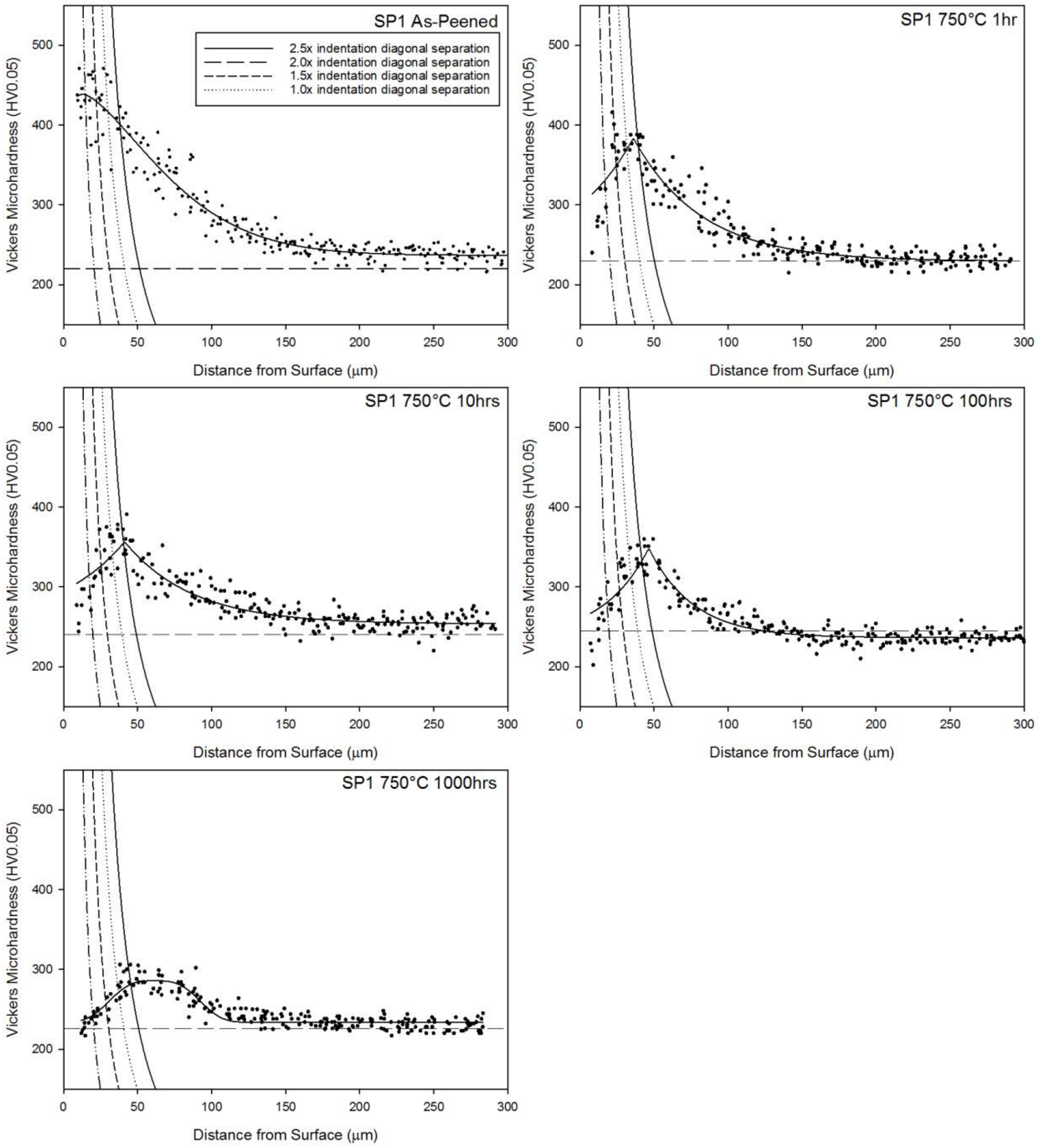

Figure 16 - Microhardness profiles of SP1 after being heated in a vacuum at 750°C for 1, 10, 100 and 1000hrs. Horizontal dotted lines are measured bulk microhardness values taken from the same samples at distances >1mm from the shot peened surface.

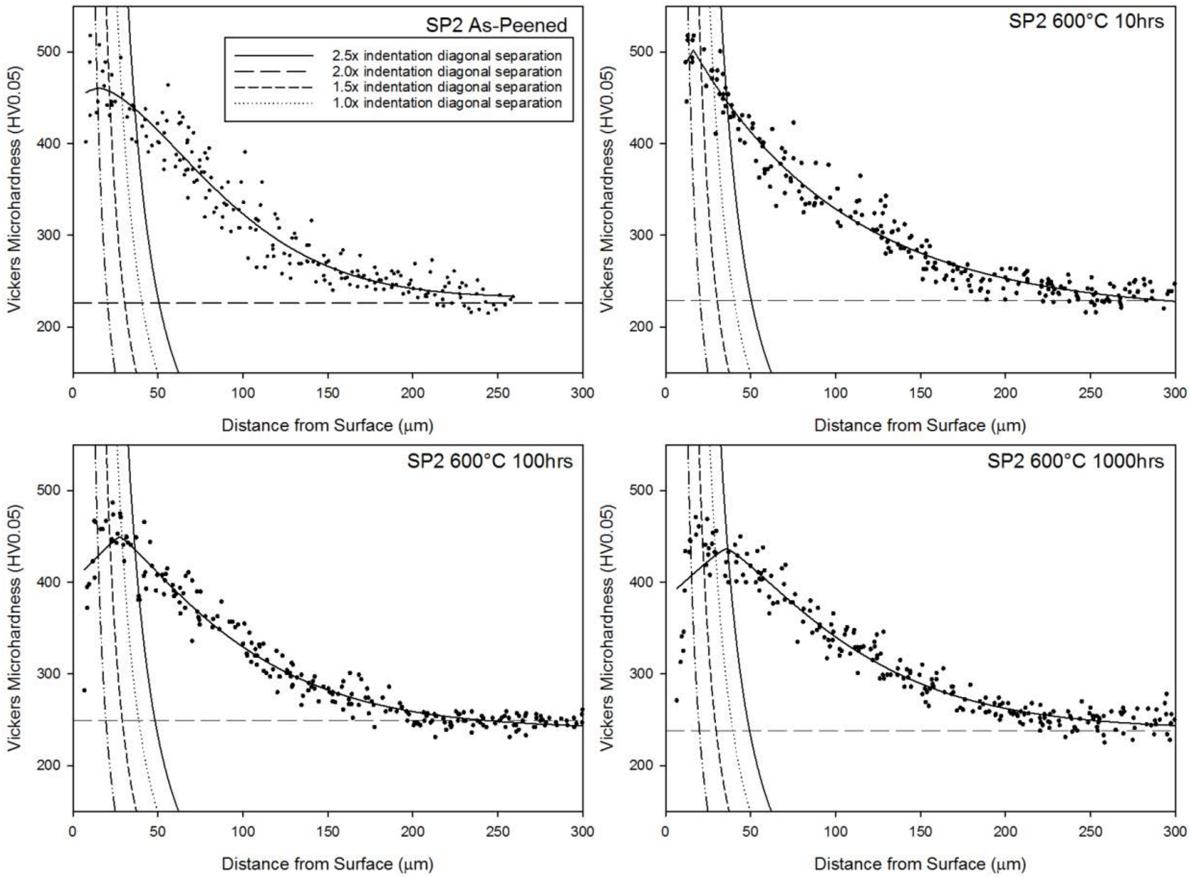

Figure 17 - Microhardness profiles of SP2 after being heated in a vacuum at 600°C for 10, 100 and 1000hrs. Horizontal dotted lines are measured bulk microhardness values taken from the same samples at distances >1mm from the shot peened surface.

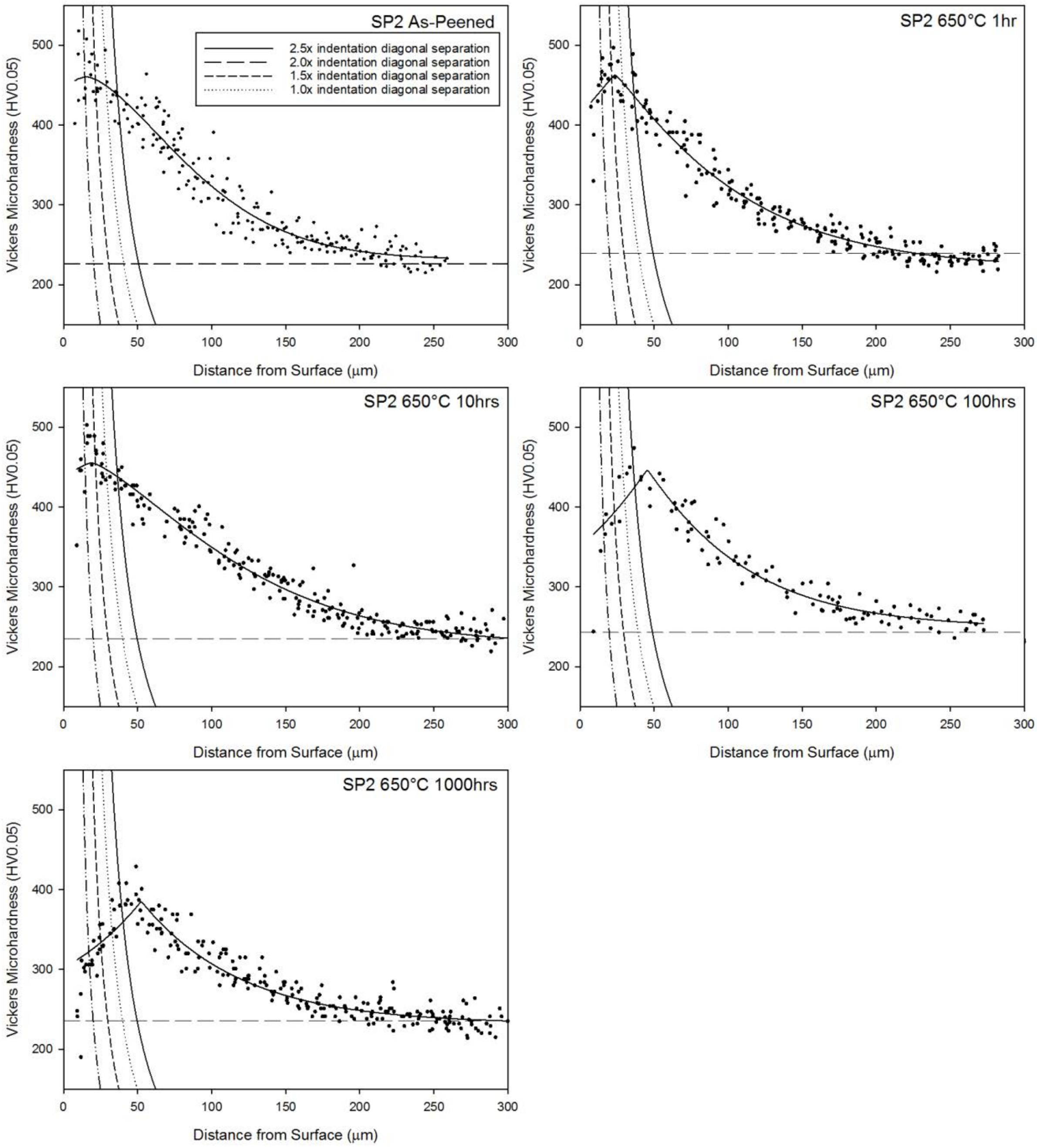

Figure 18 - Microhardness profiles of SP2 after being heated in a vacuum at 650°C for 1, 10, 100 and 1000hrs. Horizontal dotted lines are measured bulk microhardness values taken from the same samples at distances >1mm from the shot peened surface.

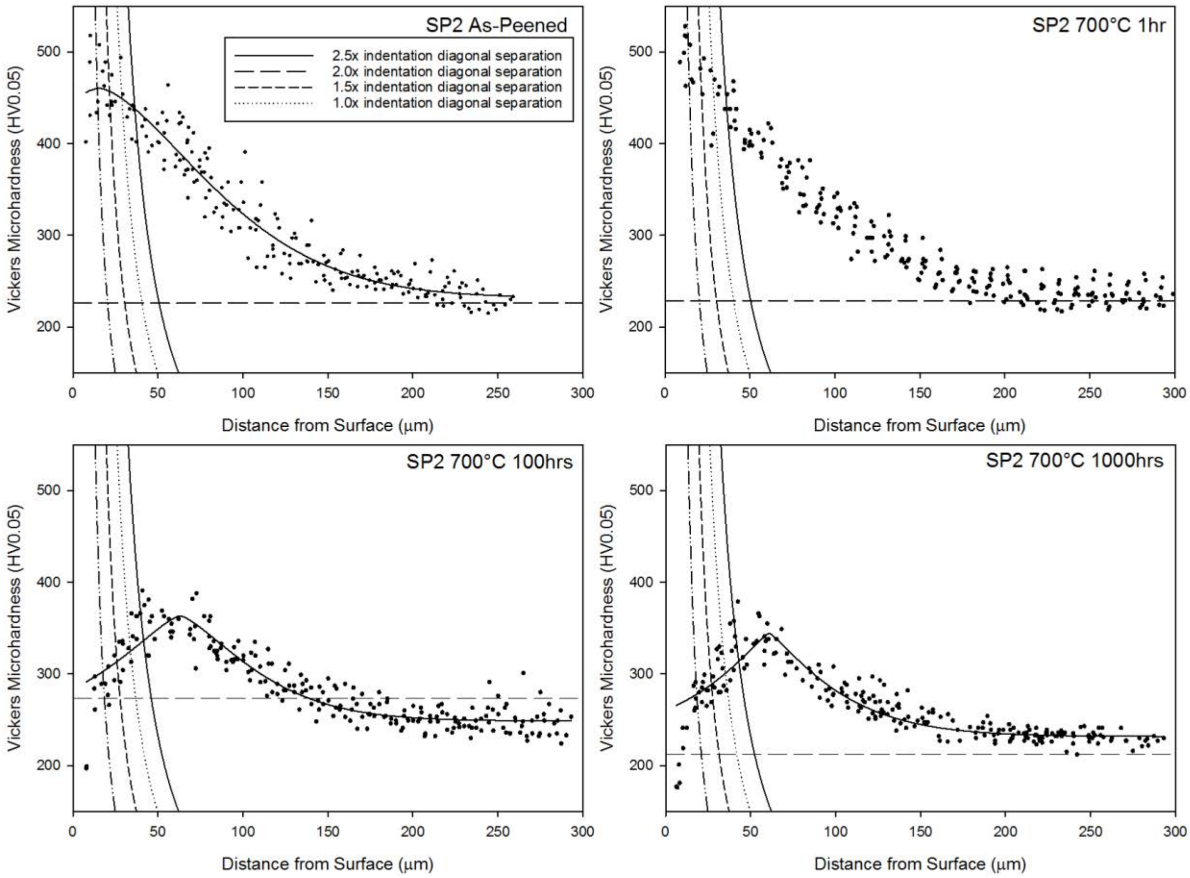

Figure 19 - Microhardness profiles of SP2 after being heated in a vacuum at 700°C for 1, 100 and 1000hrs. Horizontal dotted lines are measured bulk microhardness values taken from the same samples at distances >1mm from the shot peened surface.

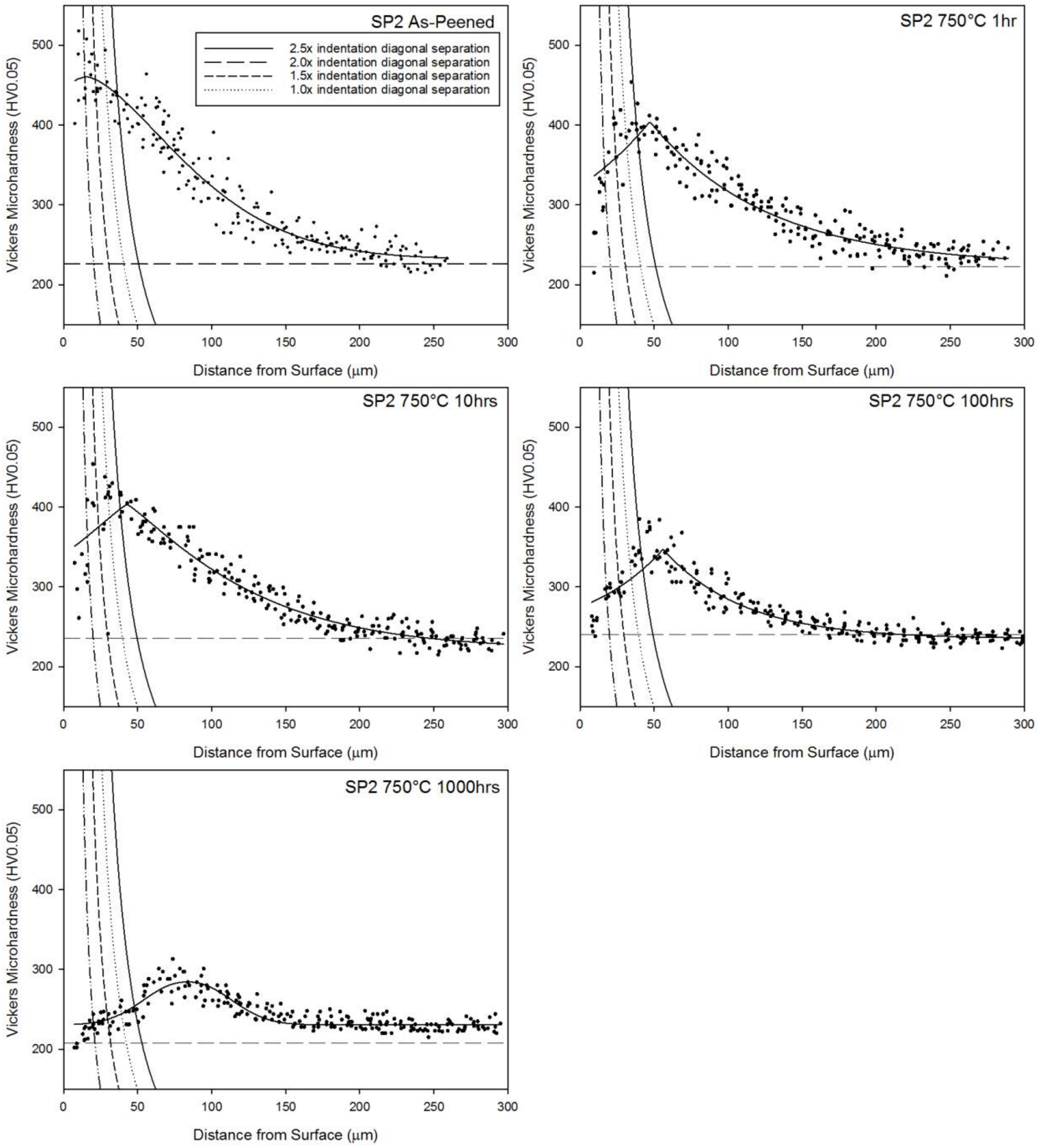

Figure 20 - Microhardness profiles of SP2 after being heated in a vacuum at 750°C for 10, 100 and 1000hrs. Horizontal dotted lines are measured bulk microhardness values taken from the same samples at distances >1mm from the shot peened surface.

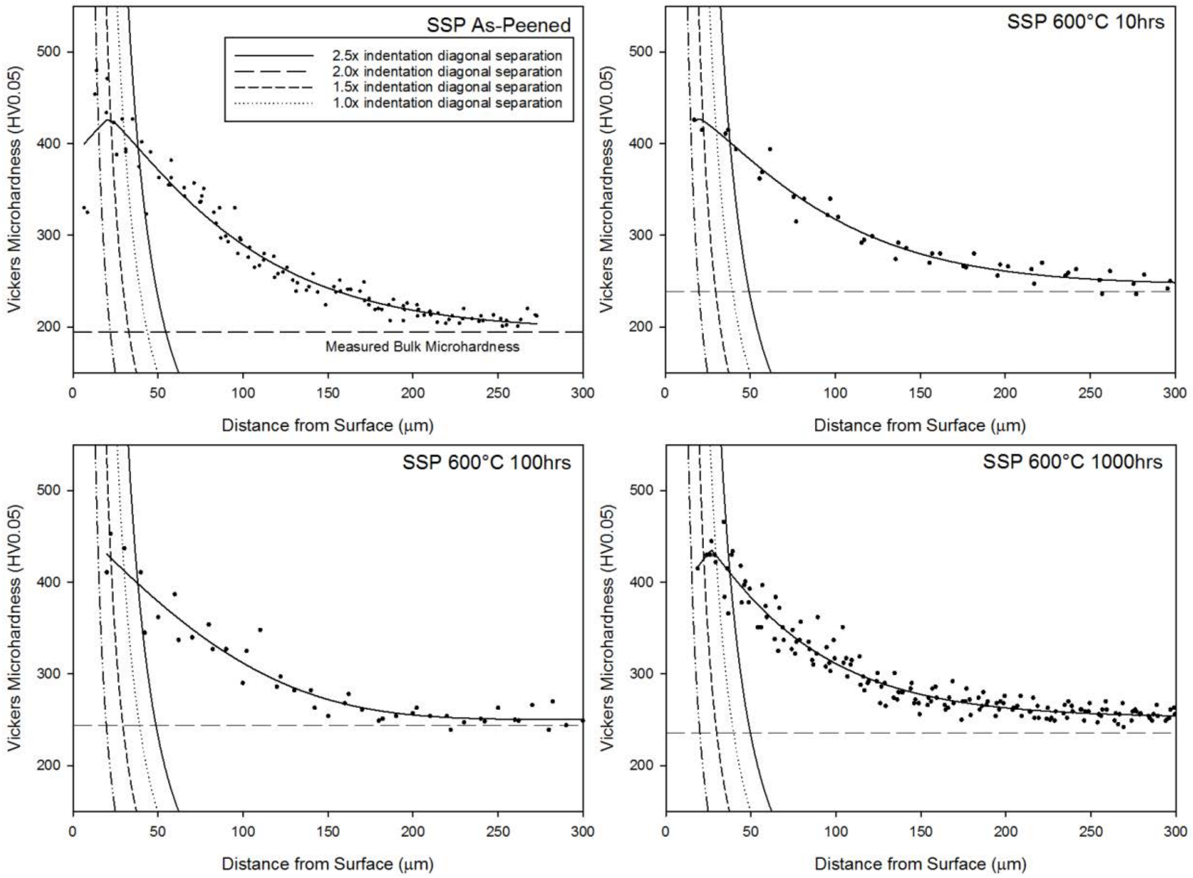

Figure 21 - Microhardness profiles of SSP after being heated in a vacuum at 600°C for 10, 100 and 1000hrs. Horizontal dotted lines are measured bulk microhardness values taken from the same samples at distances >1mm from the shot peened surface.

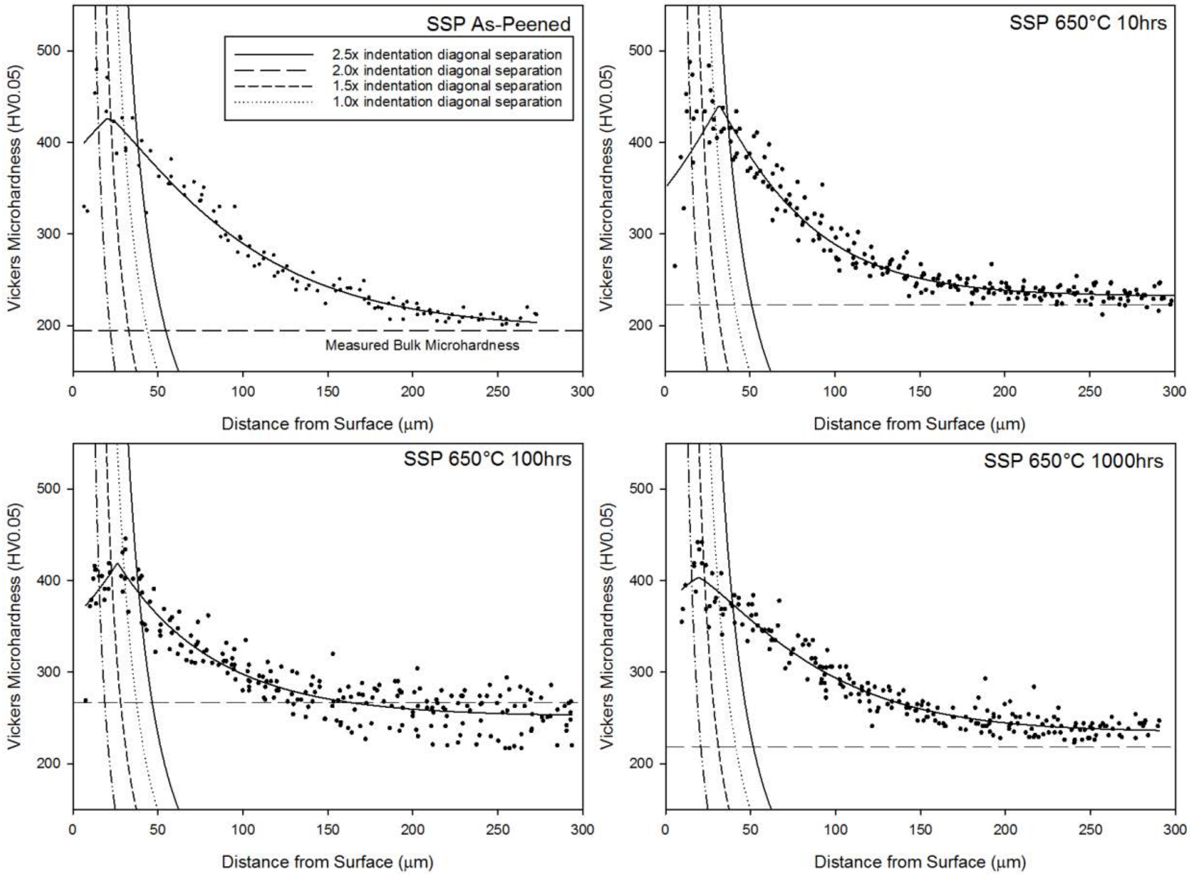

Figure 22 - Microhardness profiles of SSP after being heated in a vacuum at 650°C for 10, 100 and 1000hrs. Horizontal dotted lines are measured bulk microhardness values taken from the same samples at distances >1mm from the shot peened surface.

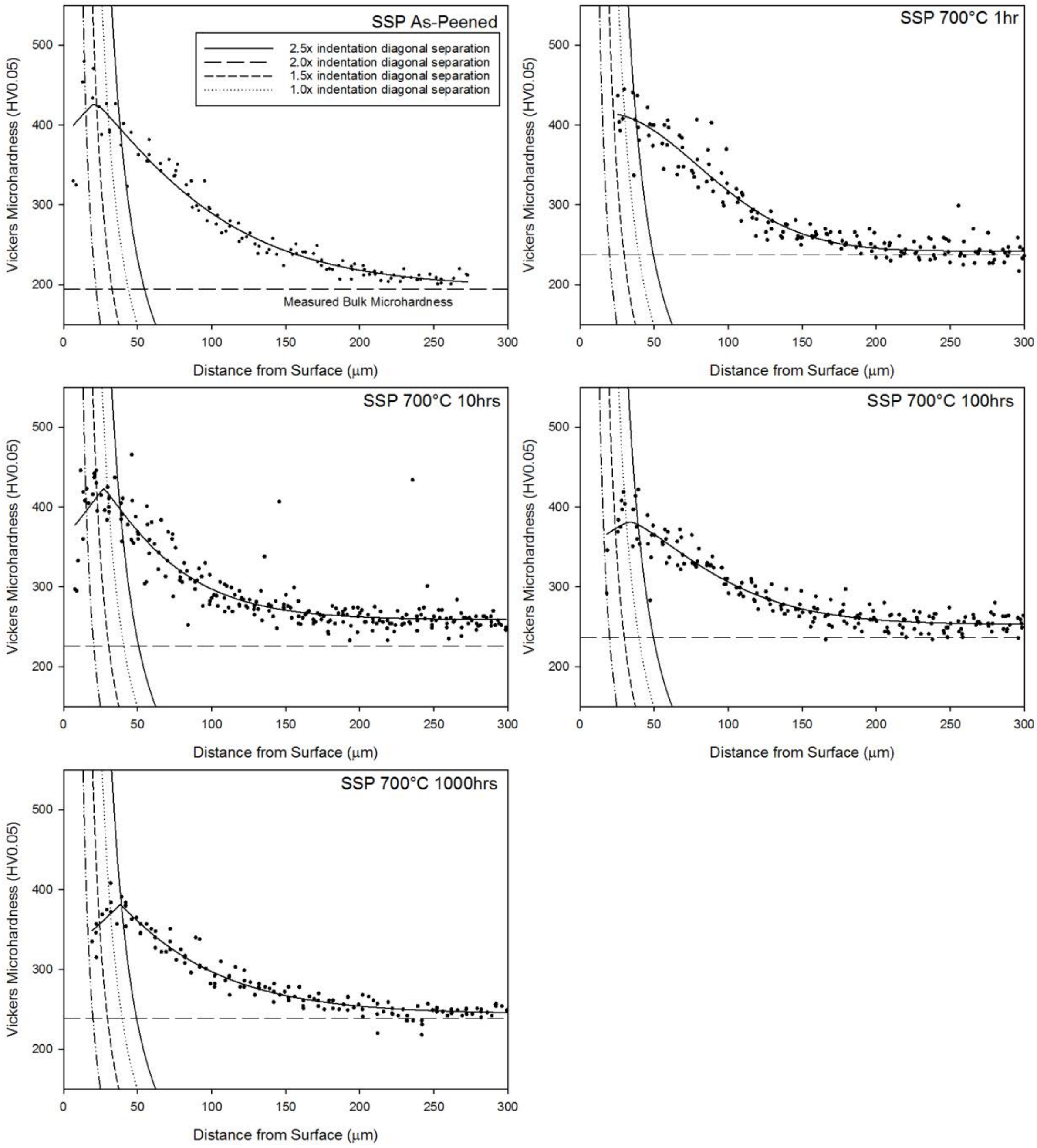

Figure 23 - Microhardness profiles of SSP after being heated in a vacuum at 700°C for 1, 10, 100 and 1000hrs. Horizontal dotted lines are measured bulk microhardness values taken from the same samples at distances >1mm from the shot peened surface.

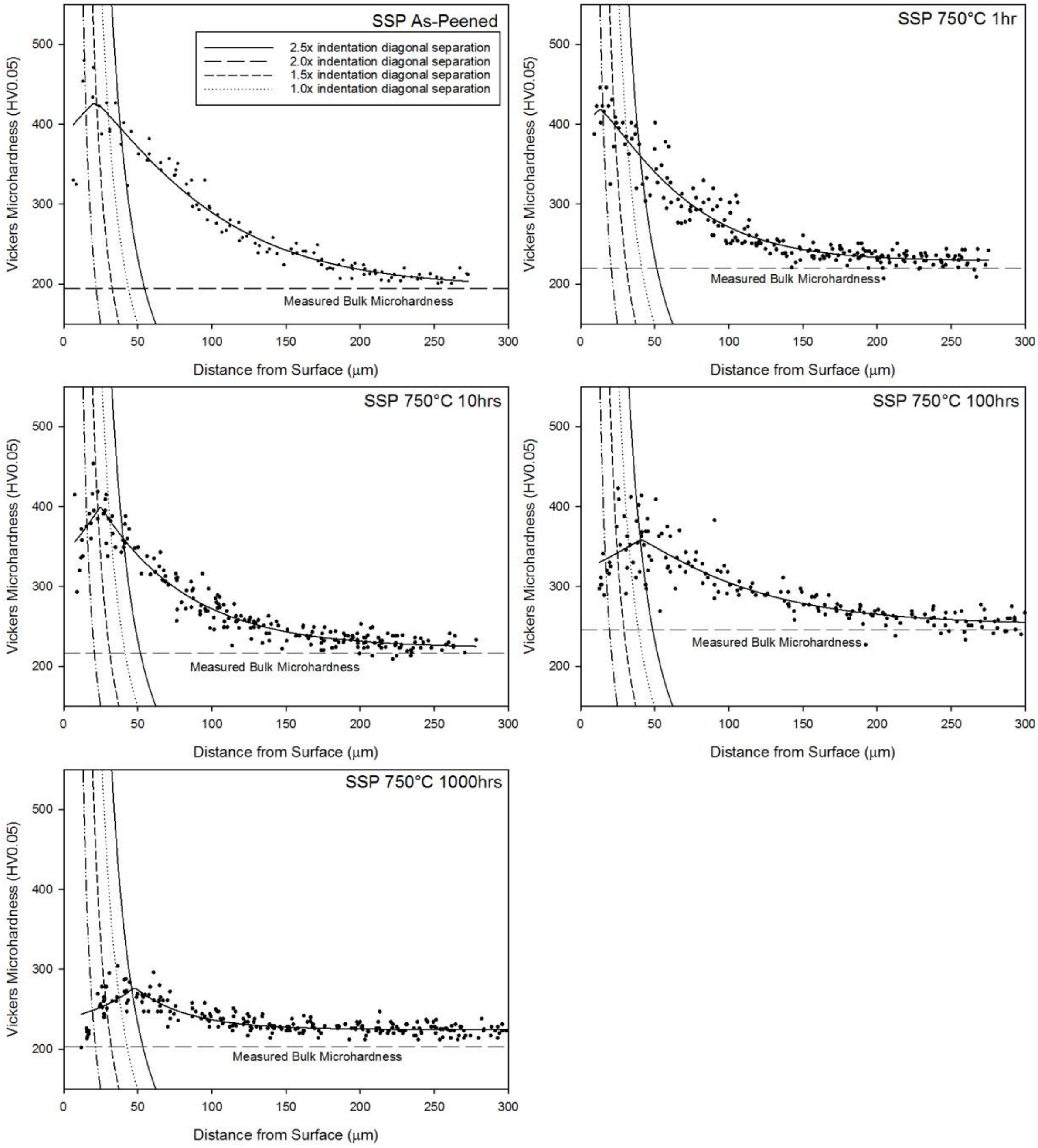

Figure 24 - Microhardness profiles of SSP after being heated in a vacuum at 750°C for 1, 10, 100 and 1000hrs. Horizontal dotted lines are measured bulk microhardness values taken from the same samples at distances >1mm from the shot peened surface.

Table 3 - Curve parameters for Figure 13 to Figure 24. Items marked with (*) are manual fits. Errors are standard errors.

Material	Heat Treatment Temp (°C)	Heat Treatment Time (hrs)	a	b	c	x_0	y_0	a Error	b Error	c Error	x_0 Error	y_0 Error	Measured y_0 (HV0.05)	Measured y_0 standard deviation (HV0.05)	Calculated Peak Microhardness (HV0.05)
SP1	0	0	202	45	1.5	13	237	5	5	0.1	4	2	221	8	439.0
SP2	0	0	229	58	1.6	15	232	8	6	0.2	6	5	226	15	460.7
SSP	0	0	231	47	1.2	21	197	16	5	0.2	3	9	195	6	427.8
S304H	0	0	35	14	1.0	40	279	9	8	0.5	3	2	264	10	314.3
SP1	600	10	234	26	1.0	17	242	9	3	0.1	1	3	249	24	476
SP1	600	100	173	36	1.2	17	250	6	3	0.1	2	2	240	10	423
SP1	600	1000	182	32	1.1	24	234	10	4	0.1	2	4	233	11	416
SP1	650	1	223	27	1.1	27	232	8	2	0.1	1	3	241	12	454
SP1	650	10	188	35	1.2	22	243	9	4	0.1	2	4	248	8	431
SP1	650	100	187	31	1.1	31	252	11	4	0.1	2	4	243	9	438
SP1	650	1000	126	23	1.1	39	245	8	3	0.1	1	2	225	11	371
SP1	700	1	243	30	1.2	21	221	8	2	0.1	1	2	277	32	464
SP1	700	10	163	41	1.5	28	248	5	3	0.1	2	2	234	10	411
SP1	700	100	125	30	1.2	35	246	7	4	0.2	2	2	235	12	372
SP1	700	1000	108	20	1.2	47	229	6	2	0.1	1	1	237	9	337
SP1	750	1	154	23	1.0	36	230	10	3	0.1	1	3	229	10	384
SP1	750	10	103	23	1.0	41	254	8	4	0.1	1	3	240	9	357
SP1	750	100	112	15	1.0	46	236	7	2	0.1	1	1	245	10	349
SP1	750	1000	52	28	3.2	61	234	3	2	0.5	1	1	226	7	286
SP2	600	10	287	45	1.0	16	216	12	3	0.1	2	7	229	8	502
SP2	600	100	210	46	1.2	27	240	7	3	0.1	2	4	249	20	450
SP2	600	1000	197	51	1.3	36	240	9	4	0.1	2	5	225	14	437
SP2	650	1	242	47	1.1	24	221	10	3	0.1	1	6	239	9	463
SP2	650	10	228	69	1.4	19	228	9	5	0.1	4	7	235	9	456

Material	Heat Treatment Temp (°C)	Heat Treatment Time (hrs)	a	b	c	x_0	y_0	a Error	b Error	c Error	x_0 Error	y_0 Error	Measured y_0 (HV0.05)	Measured y_0 standard deviation (HV0.05)	Calculated Peak Microhardness (HV0.05)
SP2	650	100	198	35	1.0	45	249	19	5	0.2	2	10	243	9	447
SP2	650	1000	154	33	1.0	52	232	11	4	0.1	1	6	235	11	386
SP2 *	700	1				11	230						229	8	430
SP2	700	100	115	34	1.4	63	249	8	4	0.2	1	3	273	21	364
SP2	700	1000	113	26	1.2	61	232	8	3	0.2	1	3	212	7	345
SP2	750	1	180	40	1.0	47	224	17	5	0.1	1	11	223	9	405
SP2	750	10	182	49	1.2	43	222	14	4	0.1	2	8	235	7	404
SP2	750	100	113	27	1.0	56	235	14	6	0.2	2	5	241	14	347
SP2	750	1000	54	29	2.2	84	231	3	2	0.3	1	1	208	7	284
SSP	600	10	181	48	1	20	246	10	7	0	5	4	239	16	427
SSP *	600	100				22	250						244	20	430
SSP	600	1000	183	34	1	27	253	7	3	0	2	2	236	10	436
SSP	650	10	209	28	1	32	232	14	4	0	2	4	223	9	441
SSP	650	100	168	29	1	26	252	12	4	0	1	4	267	18	420
SSP	650	1000	169	44	1	19	235	6	4	0	2	3	218	8	404
SSP	700	1	173	63	2	19	242	16	29	1	35	2	238	25	415
SSP	700	10	164	28	1	27	259	11	4	0	2	3	226	8	423
SSP	700	100	129	44	1	34	253	6	5	0	3	2	236	19	382
SSP	700	1000	137	34	1	38	244	7	3	0	1	3	239	18	382
SSP	750	1	190	35	1	13	229	8	4	0	3	3	220	10	419
SSP	750	10	177	30	1	25	223	10	3	0	1	4	217	9	400
SSP	750	100	106	43	1	41	252	10	7	0	3	6	245	13	359
SSP	750	1000	53	18	1	48	225	7	5	0	1	1	203	7	277

4.1.4.1 Change in Peak Microhardness

The peak microhardness of the fitted curves for SSP, SP1 and SP2 are shown in Figure 25. The peak microhardness increased compared to the as-peened material after samples were heat treated at 600°C, 650°C and 700°C for up to 10hrs. The peak microhardness then decreased between 10-1000hrs, except for SSP at 600°C, which remained mostly unchanged. At a heat treatment temperature of 750°C the peak microhardness of all three shot peened materials decreased even after only 1hr of exposure and continued to decrease up to the maximum time of exposure of 1000hrs.

At distances less than the recommended 2.5x indentation diagonal separation from the sample edge, the measured microhardness did not fall below the bulk microhardness. This was true even after heat treatment at 750°C for 1000hrs. Taking microhardness measurements so close to the sample edge would cause the microhardness to be underestimated, so in all cases it can be assumed that the shot peened surface retained an elevated microhardness compared to the bulk of the material even after heat treatment.

Figure 26 shows the peak microhardness values of the three materials heat treated at the same temperature plotted together. These data were fitted to a curve of formula (3) in order to observe general trends and to predict the peak microhardness of samples heat treated for up to 10,000hrs. It must be noted that there is significant scatter in the data and there are too few data to make these trends anything more than a very rough estimate.

$$P(t) = P_0 + q \cdot \ln(t) \qquad (3)$$

P = Peak microhardness
t = Heat treatment time (hrs)
P_0 = Coefficient found by regression
q = Coefficient found by regression

The fitted curves have the parameters given in Table 4. The coefficient q increases in magnitude as the temperature increases, in line with the trends seen for each material individually.

Table 4 - Parameters of fitted curves in Figure 26 using (3)

Heat Treatment Temperature (°C)	P_0	q
600	483	-8.5
650	466	-10.0
700	437	-12.5
750	415	-17.2

The decrease in peak microhardness over time can be used to estimate the recrystallization of the shot peened material. This will be discussed in section 6.2.2.

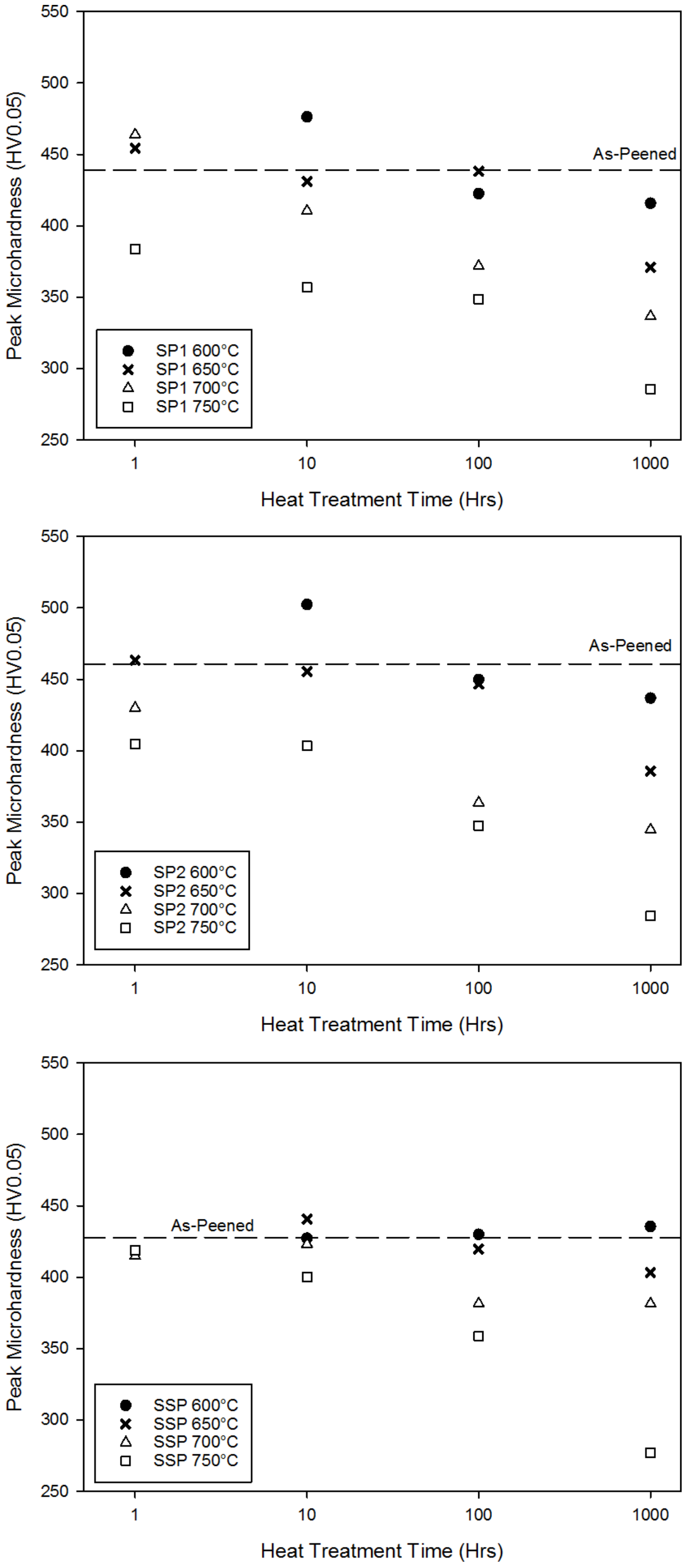

Figure 25 - Peak microhardness of fitted curves of SP1, SP2 and SSP microhardness profiles after heat treatments

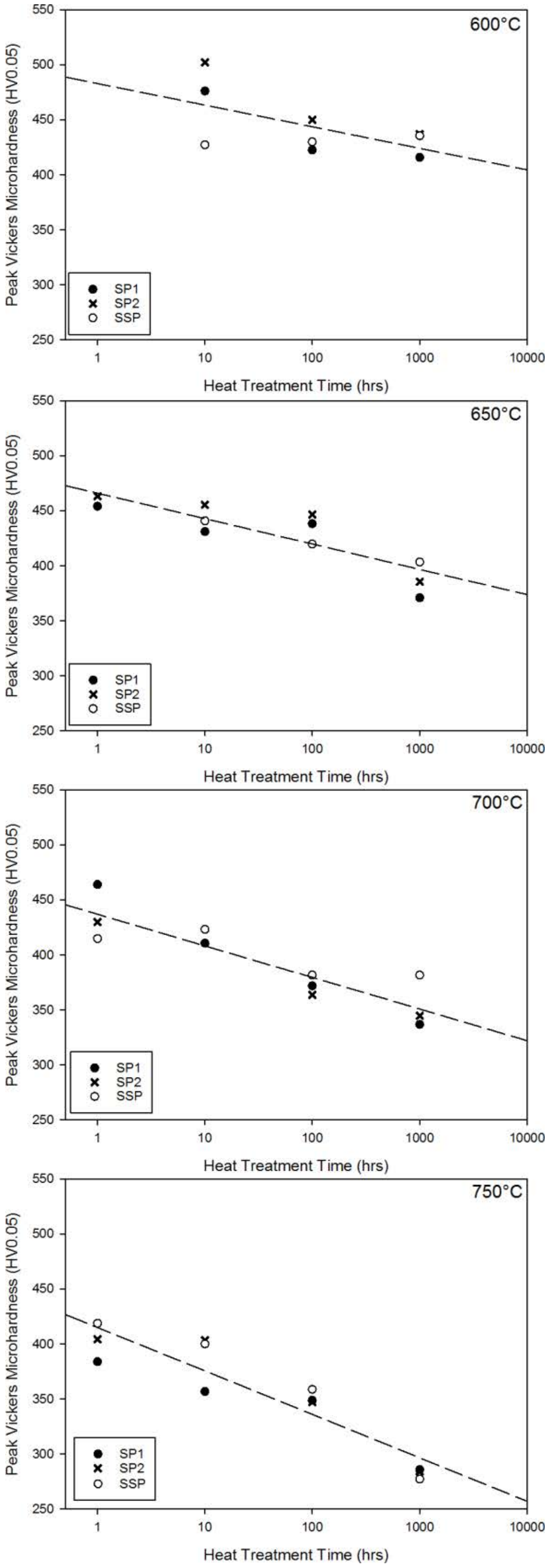

Figure 26 - Peak Vickers Microhardness of SP1, SP2 and SSP after heat treatment at 600°C, 650°C, 700°C and 750°C. Trend line is a fit of all three materials using (3) with parameters given in Table 4

4.1.4.2 Change in Distance of Peak Microhardness from the Surface

The distances of the peak microhardness from the shot peened surface after heat treatments are shown in Figure 27. The distance of the peak microhardness from the shot peened surface tends to increase the longer a sample is heat treated and the higher the treatment temperature. This trend is in line with the observation that heat treatment reduces the hardness of the shot peened region of material; the microhardness peak will move away from the sample edge as the indentations made by the microhardness tester become larger as discussed in section 4.1.3.

Three exceptions to this trend are SP2 heated at 700°C for 1hr and SSP heat treated at 700°C and 750°C for 1hr. These have peaks located closer to the sample surface than in the as-peened materials. Of these, the samples heat treated at 700°C only differ from the as-peened material by a small amount and could be explained by scatter in the data.

When SSP was heat treated at 650°C the location of peak microhardness moved closer to the shot peened material over time. However, this is the result of a discrepancy in the curve fit for the SSP sample heat treated at 650°C for 10hrs. After assessing this fitted curve by eye, the author believes the peak microhardness was located ≈25µm from the surface. This change would make the trend for SSP heat treated at 650°C almost flat and like SSP heat treated at 600°C.

For a non-peened material of constant hardness the distance of the peak microhardness from the sample edge would be expected to be linked to the size of the indentation being made as discussed in section 4.1.3. Therefore, the distance between sample edge and peak microhardness should not be greater than, at most, the 2.5x diagonal separation distance for the sample bulk microhardness. However, it is seen in several instances that this is not the case, such as in SP2 heat treated at 750°C for 1hr or more, and SP2 heat treated at 700°C and 650°C for 100hrs or more.

In the cases of SP2 heat treated at 750°C for 1hr and 10hrs, and SP2 heat treated at 650°C for 10hrs, the disparity is caused by the choice of a symmetrical peak for the curve fit. In these profiles the rise to peak microhardness is much more steep closer to the sample edge than the fall from peak microhardness to the bulk microhardness. This asymmetry causes the fitted curve peak to be placed further away from the shot peened sample edge, and the actual measured peak microhardness was still less than 2.5x the indentation diagonal away from the sample edge.

However, this explanation is not applicable for the curve fits of SP2 heat treated at 750°C for 100hrs and 1000hrs, 700°C for 100hrs and 1000hrs and 650°C for 1000hrs. In these instances the fitted curves show a peak microhardness at a distance from the shot peened edge greater than the 2.5x indentation diagonal expected for the sample bulk microhardness.

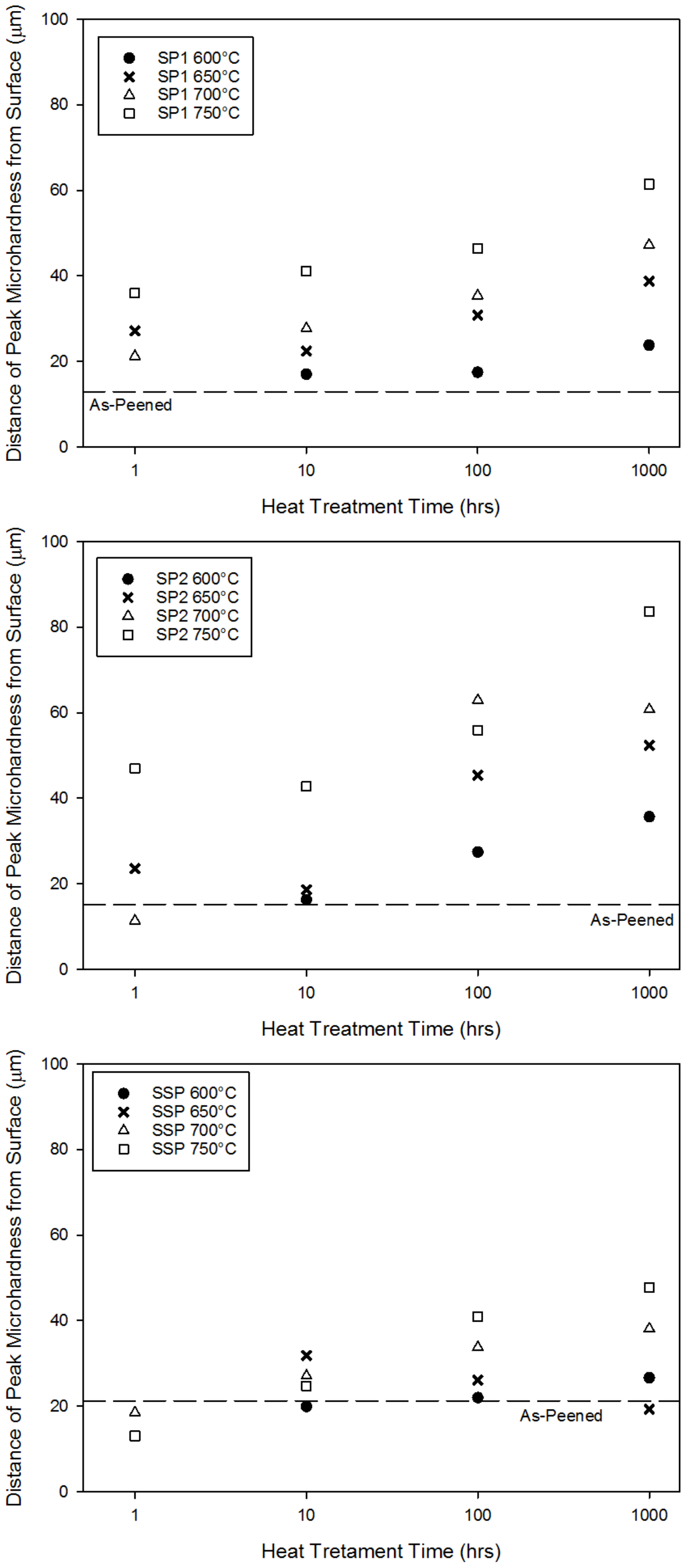

Figure 27 - Distance of peak microhardness from the shot peened surface found by curve fitting of microhardness profiles of SP1, SP2 and SSP after heat treatment.

4.1.5 Nanohardness Profiles

A nano-indenter was used to record the hardness profiles of S304 and SSP as shown in Figure 28. The indenter did not measure the hardness closer than 20µm from the edge, though In theory the nano-indenter should have been able to take measurements <1µm from the sample edge. However, in practice the operator feared that the material in that region could damage the indenter tip due to non-uniform flatness and unfamiliarity with the shot peened material. Further nano-indentation testing could be undertaken if these issues are overcome in future work.

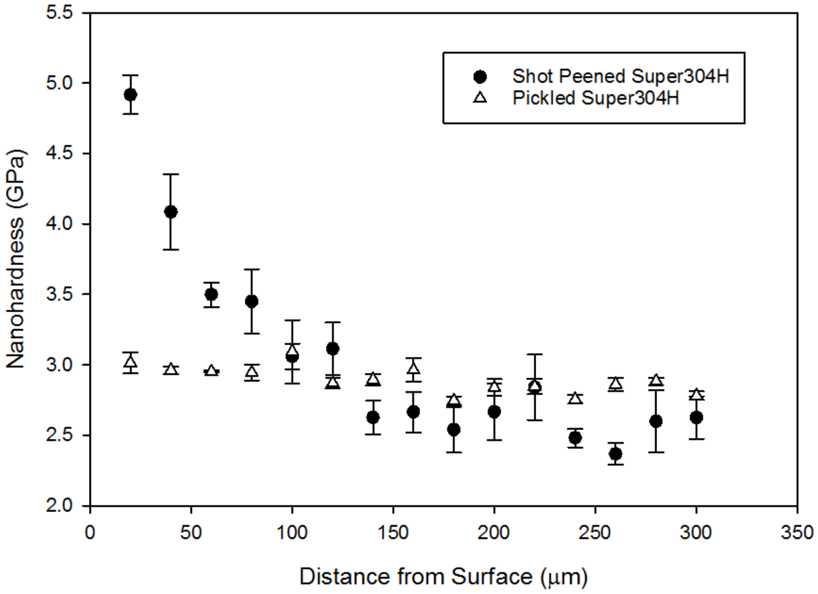

Figure 28 - Nanohardness profiles of SSP and S304. Error bars are standard errors.

The nano-hardness profile of the S304 material did not show an increase in hardness near the sample edge, unlike the microhardness profile. The nano-hardness of S304 near the sample edge was 3.0±0.1GPa and can be converted to a Vickers microhardness number using (4) to 307±8 HV. This is within the range of values found by microhardness testing.

$$HV_{SI} = 9.807HV \qquad (4)$$

HV = Vickers Hardness Number (kg/mm^2)

HV_{SI} = Hardness in SI units (MPa)

The SSP nano-hardness was at its highest value closest to the shot peened surface, as would be expected if indentation tests could be taken without interference from proximity to the sample edge. The maximum nano-hardness of SSP was 5.0 ± 0.1 GPa, which converts to a Vickers hardness of 501 ± 14 HV. This is in agreement with the highest individual values recorded during the microhardness tests, though the peak microhardness of the fitted curve of as-peened SSP is only ≈430 HV(0.05), due to the lower microhardness values taken closer to the sample edge.

4.2 Grain Size

4.2.1 Bulk Grains

The bulk grain sizes of the examined materials are given in Table 5. All the materials had similar bulk grain sizes with overlapping ranges of standard deviation.

Table 5 - Bulk grain sizes in the samples before heat treatments

Material	**Mean Grain Size (µm)**	**Standard Error (µm)**	**Standard Deviation (µm)**
S304	13.1	0.2	2.6
SSP	11.9	0.1	1.8
SP1	10.4	0.1	1.5
SP2	11.5	0.2	1.9

These values can be used with equation (14) in section 2.6.2 to find the volume fraction of GB material in the bulk of the material, shown in Table 6. GB thickness is taken to be 0.5nm in accordance with the literature.

Table 6 - Calculated volume fraction of intercrystalline material in the bulk

Material	$\boldsymbol{V_t^{IC}}$
S304	1.14E-04
SSP	1.26E-04
SP1	1.45E-04
SP2	1.31E-04

4.2.2 Near-Surface Grains (SEM)

Figure 29 and Figure 30 show the grain size in the shot peened regions of SP1 and SP2 respectively. These results were observed using SEM after sample cross sections were chemically etched. This technique could not be used to observe grains in the material <10µm from the shot peened surface because the grain structure in this region was damaged by the chemical etching. Both materials show a trend of grain size increasing to the bulk grain size within the first 100µm depth.

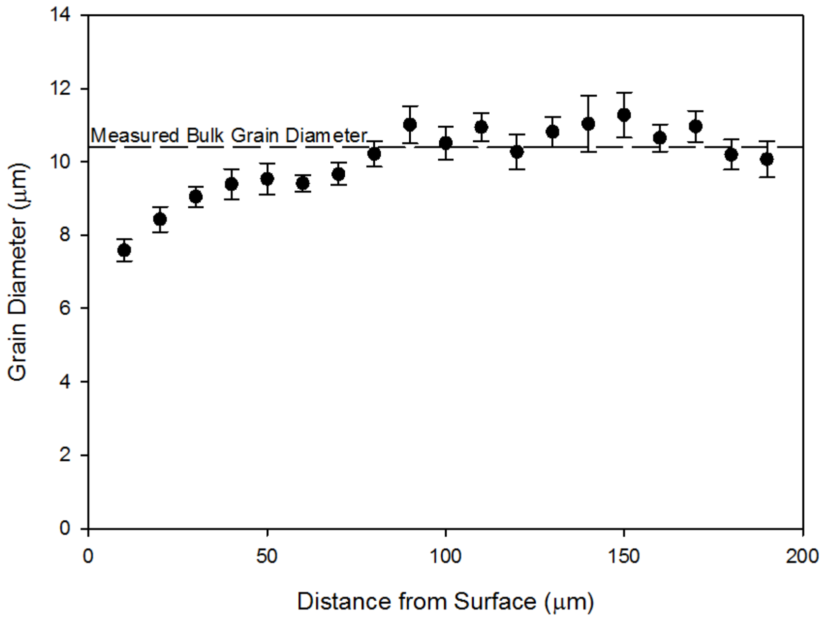

Figure 29 - Profile of the grain diameter at increasing distance from the shot peened surface in SP1. Error bars are standard error.

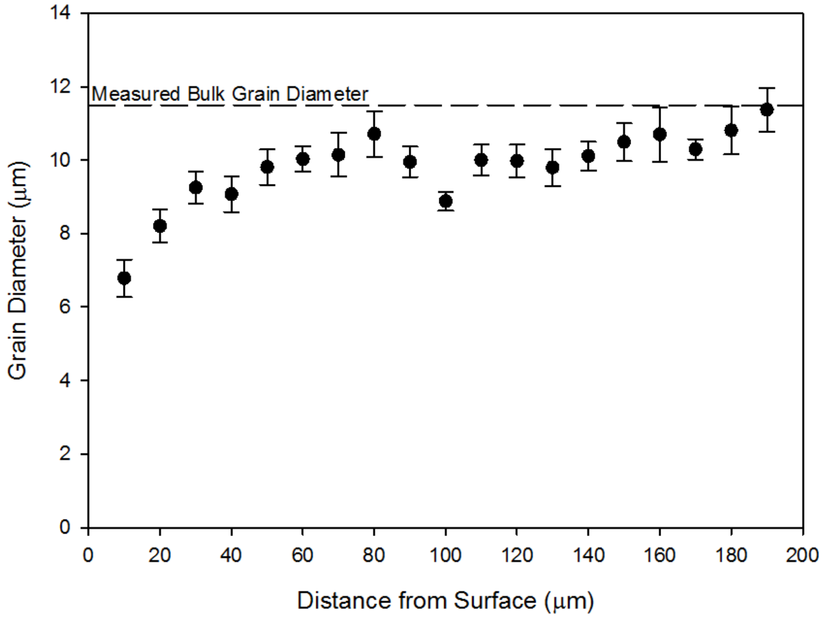

Figure 30 - Profile of the grain diameter at increasing distance from the shot peened surface in SP2. Error bars are standard error.

Lines of best fit were generated for both profiles using (5) and fitted using a non-linear least-squares fit. These are shown in Figure 31 and Figure 32.

$$d = \frac{ax}{x + b} \qquad (5)$$

d = Grain diameter (µm)
x = Distance from shot peened surface (µm)
a = Bulk grain size found by regression (µm)
b = Constant found by regression (µm)

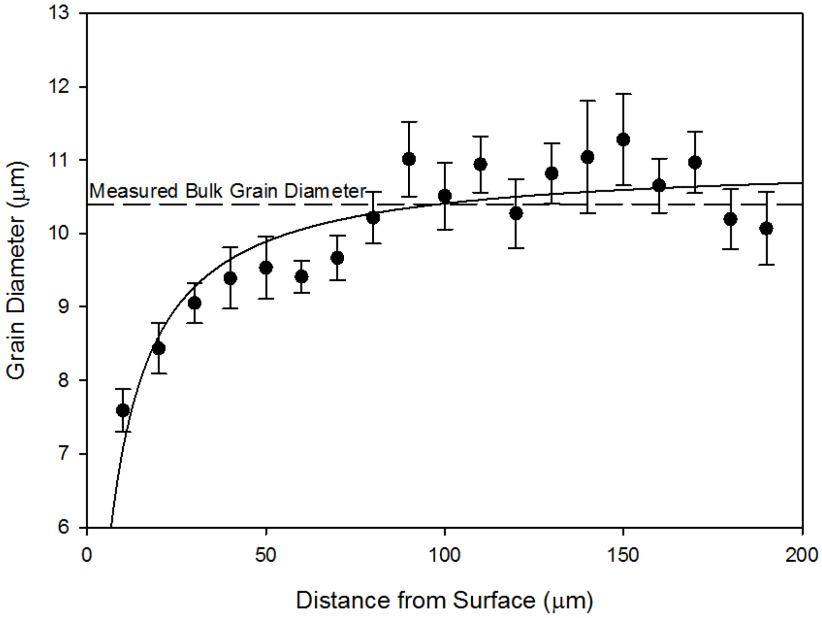

Figure 31 - Profile of the grain diameter at increasing distance from the shot peened surface in SP1. Error bars are standard error. The equation for the fitted line is (5) with constants a=11.0±0.2, b=5.5±0.9

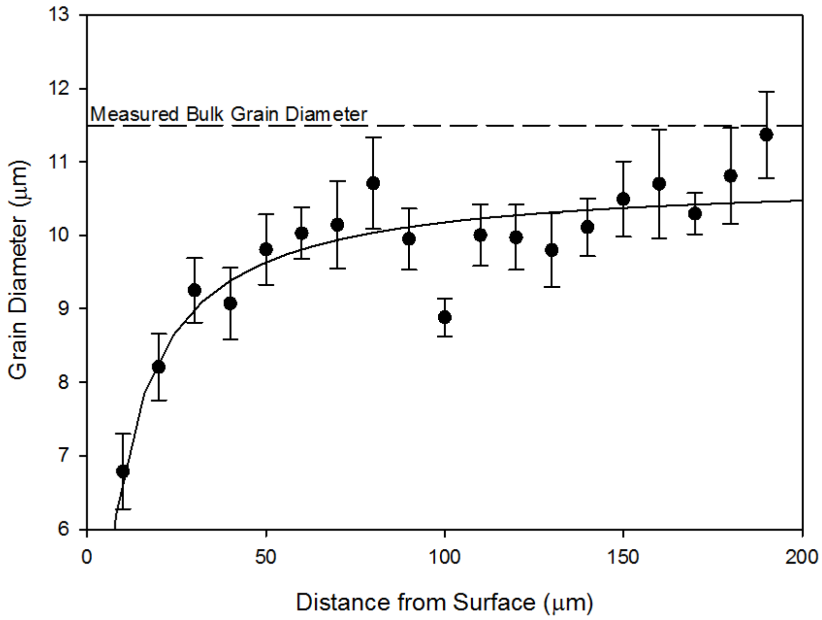

Figure 32 - Profile of the grain diameter at increasing distance from the shot peened surface in SP2. Error bars are standard error. The equation for the fitted line is (5) with constants a=10.8±0.2, b=6.0±1.0

The grain diameter at a distance of 100µm from the surface for SP2 in Figure 32 appears to lie outside of the general trend. Figure 33 shows the same plot and fitted line if this point is ignored, and demonstrates that ignoring this value does not significantly change the fitted curve.

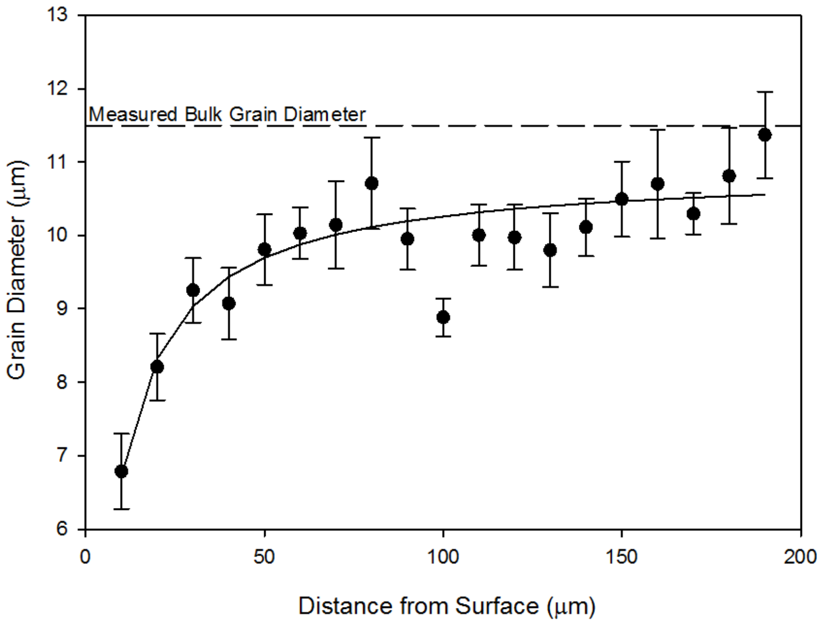

Figure 33 - Profile of the grain diameter at increasing distance from the shot peened surface in SP2. Error bars are standard error. The equation for the fitted line is (5) with constants a=10.9±0.1, b=6.2±0.8

4.2.3 Near-Surface Grains (TEM)

4.2.3.1 Darkfield TEM

Figure 34 shows a BF image of a cross section through a shot peened surface. The material is nanocrystalline and the grain sizes in the TEM images are more difficult to analyse than in the SEM. TEM images contain 3D information because the electron beam travels through and interacts with the entire thickness of the TEM foil. The TEM images are therefore 2D representations of a 3D structure and this makes grain boundaries much less defined when multiple grains fit inside the thickness of the foil, as is the case in a shot peened microstructure.

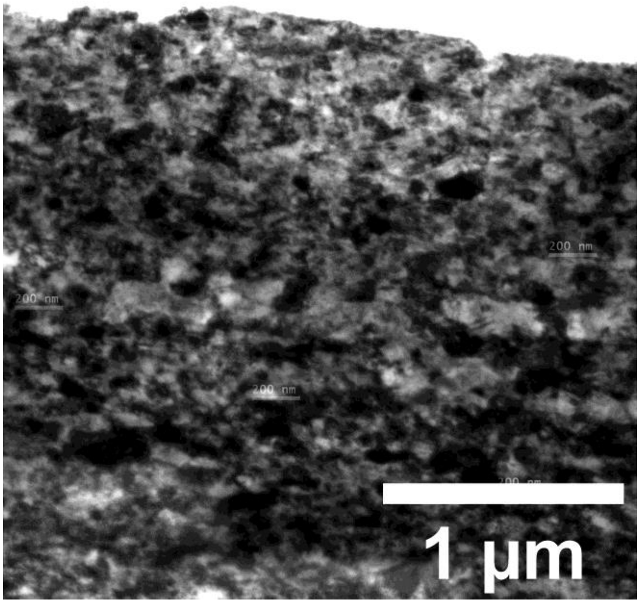

Figure 34-Brightfield TEM composite image of a SP2 surface cross section

Figure 35 shows a darkfield (DF) image of a similar microstructure. DF images are created by inserting an objective aperture in the TEM that only allows electrons that have been diffracted by a specific direction. In DF images the contrast is generated primarily by the differing orientations of the grains and most of the material is excluded. DF images can therefore be more readily analysed to yield grain size information.

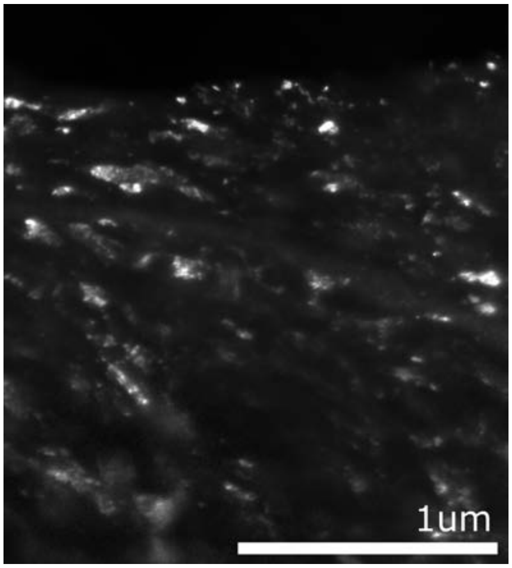

Figure 35 - Darkfield TEM composite image of SP1 surface cross section. The shot peened surface is at the top and includes clearly defined grains. The TEM foil is thicker further away from the shot peened surface and the grains can become less defined in the image.

An objective aperture was used to isolate a small range of angles of the α(110)/γ(111) peaks, which are both within 1° of each other and can therefore both contribute to the DF images. These peaks were also chosen because they are the strongest diffraction peaks for both α and γ. After thresholding the DF images the grain populations were characterised with the particle analysis features of ImageJ to find the grain sizes and locations. The total area of the grain populations categorized by grain size are shown in Table 7. Table 8 shows the same data for samples that were heat treated in vacuum for 1000hr at 700°C.

Table 7 - Grains in Shot Peened Surfaces Highlighted by DF Imaging in As Received Material

Grain Size Lower Limit (um^2)	**Grain Size Upper Limit (um^2)**	**SP1**		**SP2**	
		Highlighted Area (um^2)	**Area Fraction**	**Highlighted Area (um^2)**	**Area Fraction**
0	10^{-5}	0.000	0.01%	0.000	0.20%
10^{-5}	10^{-4}	0.005	0.66%	0.002	4.82%
10^{-4}	10^{-3}	0.070	8.53%	0.006	16.36%
10^{-3}	10^{-2}	0.471	57.33%	0.027	78.62%
10^{-2}	10^{-1}	0.275	33.48%	0.000	0.00%
10^{-1}	1	0.000	0.00%	0.000	0.00%
1	10	0.000	0.00%	0.000	0.00%
	Total:	0.821	100.00%	0.034	100.00%

Table 8 - Grains in Shot Peened Surfaces Highlighted by DF Imaging in Material Heat-Treated in Vacuum at 700°C for 1000hrs

Grain Size Lower Limit (um²)	**Grain Size Upper Limit (um²)**	**SP1**		**SP2**		**SSP**	
		Area (um²)	**Area Fraction**	**Area (um²)**	**Area Fraction**	**Area (um²)**	**Area Fraction**
0	10^{-5}	0.000	0.00%	0.000	0.00%	0.000	0.00%
10^{-5}	10^{-4}	0.011	0.22%	0.006	0.07%	0.007	0.10%
10^{-4}	10^{-3}	0.121	2.49%	0.089	0.96%	0.156	2.14%
10^{-3}	10^{-2}	0.516	10.61%	0.532	5.75%	0.693	9.47%
10^{-2}	10^{-1}	1.523	31.32%	1.506	16.27%	1.451	19.82%
10^{-1}	1	2.692	55.35%	2.411	26.03%	5.011	68.47%
1	10	0.000	0.00%	4.715	50.92%	0.000	0.00%
	Total:	4.864	100.00%	9.260	100.00%	7.319	100.00%

Heat treatment of shot peened material in a vacuum caused the grain size to increase significantly in all of the samples examined. The majority of shot peened material was made up of grains between 0.001 µm² to 0.01µm² in size. This corresponds to a grain diameter of 18nm to 56nm for an idealized circular grain. After heat treatment the region was mostly made up of grains between 0.01µm² to 1µm² in size.

There was a notable difference between SP1 and SP2 material in both the as-peened and post-heat treatment conditions. SP2 had a larger fraction of small grains compared to SP1 in the as-peened condition. This could reasonably be assumed to be a result of the additional shot peening. After heat treatment the SP2 material had a larger fraction of large grains compared to post-heat treatment SP1. The SP2 material was more deformed than the SP1 and could therefore undergo more significant recrystallization.

The limited area sampled in the DF observations makes it difficult to determine if this difference holds true across all SP1 and SP2 material or if this was only a local characteristic.

4.2.3.2 Brightfield TEM

The technique described in Methodology section 3.13 was used to create grain boundary maps of shot peened material after heat treatment and exposure to steam atmospheres. The full grain boundary maps can be found in appendix C. The fraction of material within a range of grain areas was then calculated. Table 9 shows the area fractions observed in SP1 material after being heat-treated in vacuum at 700°C for 1000hrs and Table 10 shows the same for SP1 material after exposure to atmospheric pressure steam at 700°C for 1000hrs.

The total area sampled in both cases is at least an order of magnitude larger than the area sampled with DF imaging. However, the technique is very labour intensive and only two detailed grain maps could be prepared.

After heat treatment and steam exposure both samples of SP1 showed grain enlargement compared to the as-peened material and had broadly similar distributions of grain area fractions. The results from DF and BF imaging for SP1 material heat treated in vacuum (Table 8 and Table 9) are comparable, with both techniques finding the majority of grains to be from 10^{-2} to 1µm^2 in size. DF imaging found a larger fraction of <10^{-3}µm^2 grains than BF imaging because grains of such small size are difficult to resolve with the relatively low contrast of BF images.

Table 9 - Area made up of different grain sizes of SP1 after exposure to vacuum at 700°C for 1000hrs. Data is from appendix C 1.1

Grain Size Lower Limit (um^2)	Grain Size Higher Limit (um^2)	Total Area (um^2)	Area Fraction
0	10^{-5}	0.00	0%
10^{-5}	10^{-4}	0.00	0%
10^{-4}	10^{-3}	0.07	0%
10^{-3}	10^{-2}	5.09	7%
10^{-2}	10^{-1}	30.34	43%
10^{-1}	1	30.27	43%
1	10	4.62	7%
10	+	0	0%
	Total:	70.39	100%

Table 10 - Area made up of different grain sizes of SP1 after exposure to atmospheric pressure steam at 700°C for 1000hrs. Data is from appendix C 1.2

Grain Size Lower Limit (um^2)	Grain Size Upper Limit (um^2)	Total Area (um^2)	Area Fraction
0	10^{-5}	0.00	0%
10^{-5}	10^{-4}	0.00	0%
10^{-4}	10^{-3}	0.07	0%
10^{-3}	10^{-2}	11.83	12%
10^{-2}	10^{-1}	46.02	47%
10^{-1}	1	39.72	40%
1	10	1.20	1%
10	+	0.00	0%
	Total:	98.83	100%

The grain map of SP1 after heat treatment in vacuum at 700°C for 1000hrs and the grain map of SP1 after exposure to atmospheric pressure steam at 700°C for 1000hrs were used to plot grain size profiles based on the depth from the surface. The intercept method used to find grain size profiles in SEM images was used to produce Figure 36. The linear fit of the steam exposure data has the equation $d = 0.028D + 93.1$, where d = grain size (nm) and D = distance from metal/oxide interface (nm).

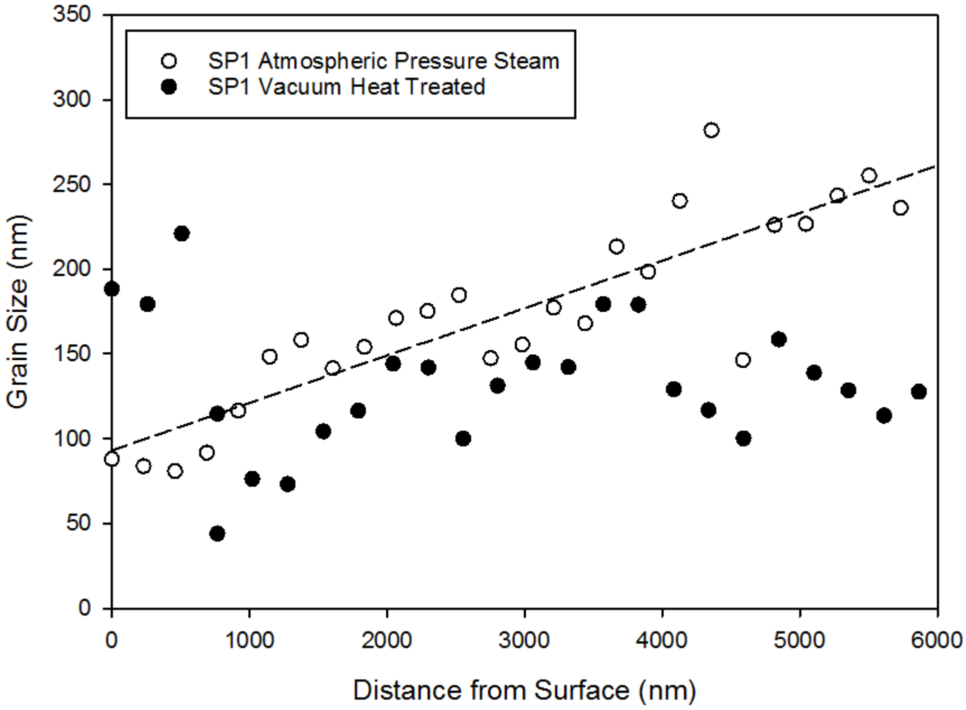

Figure 36 - Grain Size Profile of SP1 after heat treatment in vacuum at 700°C for 1000hr and SP1 after exposure to atmospheric pressure steam at 700°C for 1000hrs. The data is based on intercept analysis of a grain map produced from TEM-BF images. Distance from surface is relative to the metal/oxide interface. Dashed line is a linear fit to the steam exposure data.

4.3 Austenite & Ferrite Content

BF images of cross sections taken through the shot peened regions of SSP such as Figure 37 showed laths that are characteristic of DIM in the literature. However, the SAED pattern of Figure 37 identifies the lathes to be austenite. Other SAED patterns such as Figure 38 and Figure 39 showed that the as-peened materials (SP1, SP2 and SSP) were all fully austenitic at the surface.

Therefore, the materials must have undergone additional treatments after being shot peened to revert the DIM to austenite.

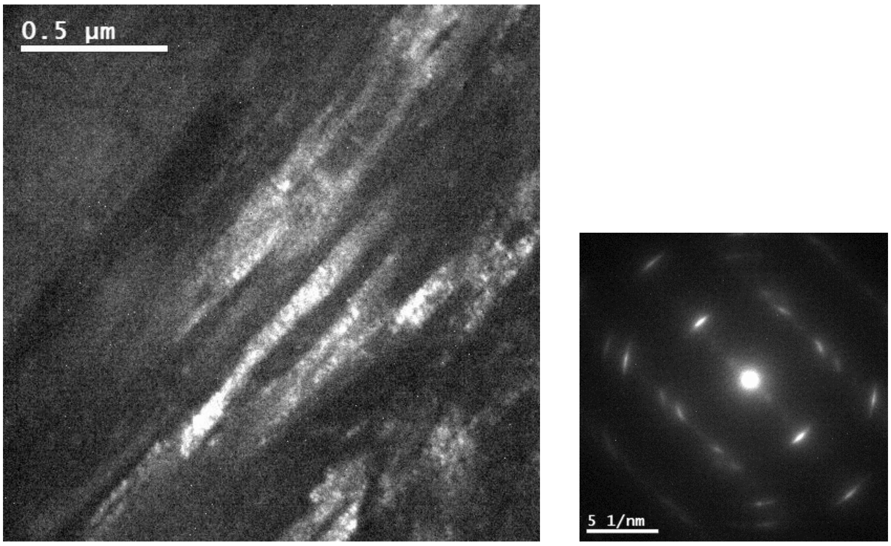

Figure 37 -Brightfield TEM image of lathes observed in shot peened Super304H. The SAED pattern is shown adjacent to the image and is identified by the angles and spacings as austenite

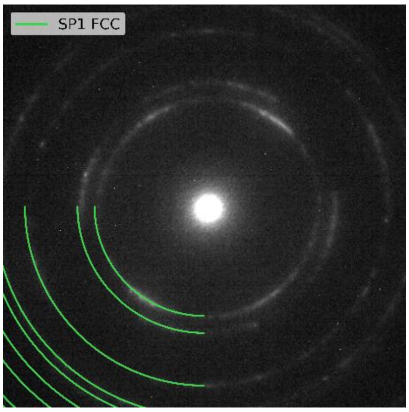

Figure 38 - SAED pattern from top layer of SSP. Overlay is simulated austenite

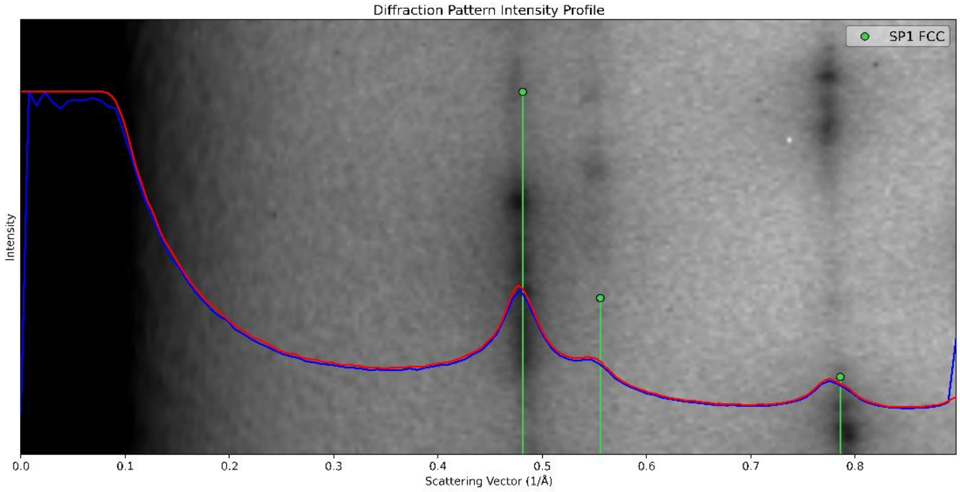

Figure 39 - Polar profile of SAED pattern of the surface layer of SP2. Marked peaks are simulated austenite

4.3.2 Diffraction Simulations

Electron diffraction peaks simulated for austenite, ferrite, chromia, $MnCr_2O_4$ and Fe_3O_4 at 200kV are shown in Figure 40, Figure 41 and Figure 42, respectively. The peaks are labelled with their plane and planar spacing. These simulations were used to perform SAED pattern analysis.

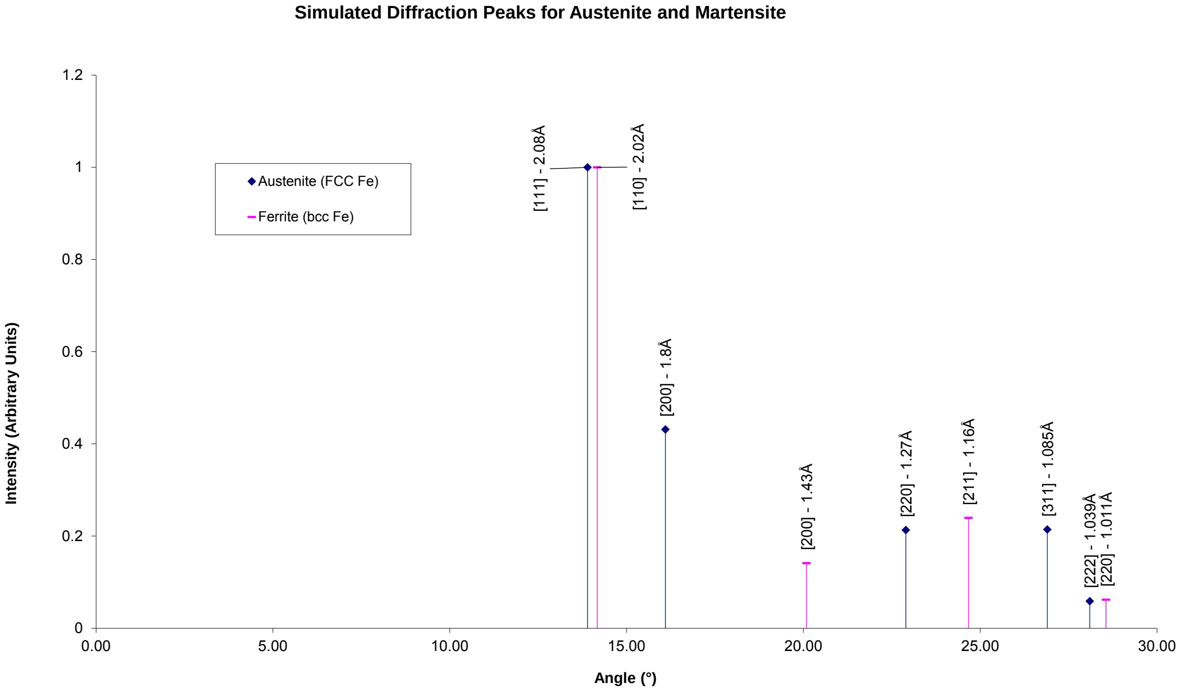

Figure 40 - Simulated electron diffraction pattern for austenite and ferrite

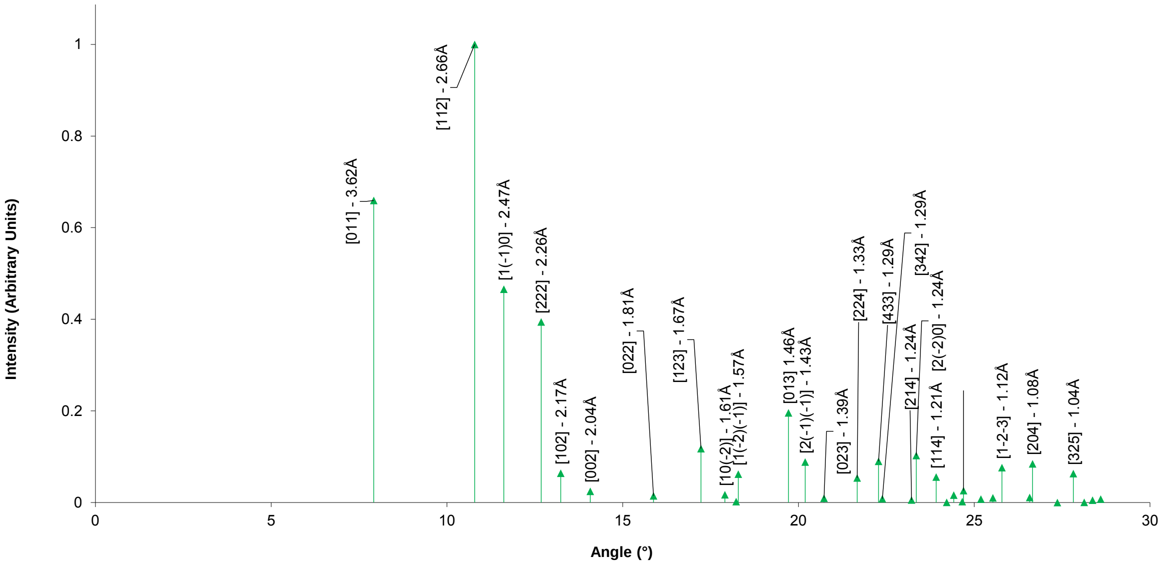

Figure 41 - Simulated electron diffraction pattern for chromia

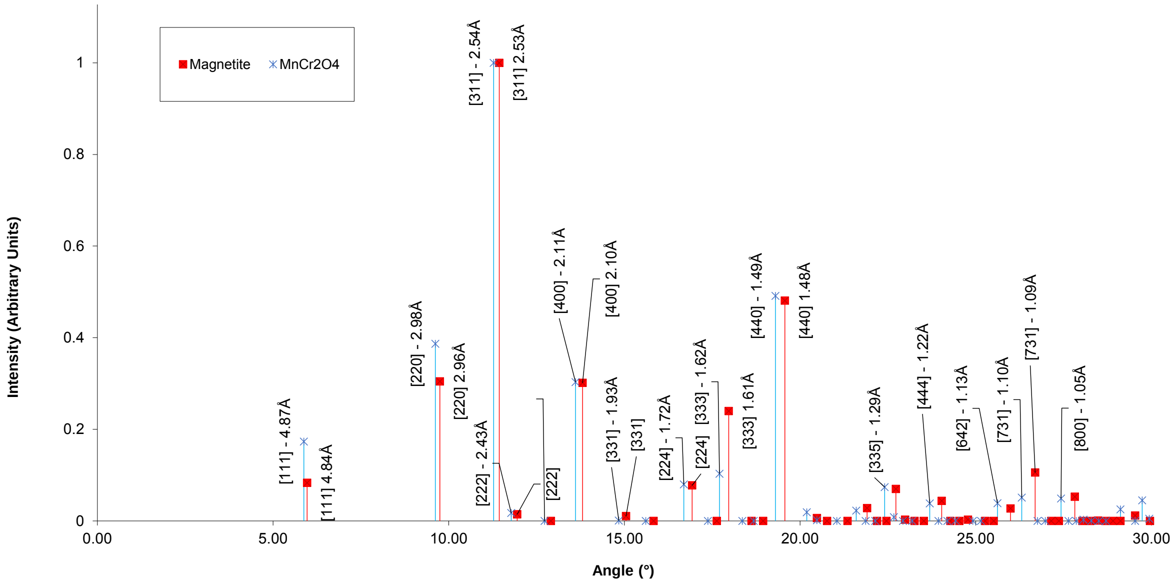

Figure 42 - Simulated electron diffraction pattern for Magnetite and $MnCr_2O_4$

4.3.3 Thermodynamic Calculations

The temperature/phase diagram for DMV304HCu was calculated in Thermo-calc and is shown in Figure 43. The molar faction of bcc phases in DMV304HCu are shown in Figure 44. At room temperature the equilibrium composition of DMV304HCu was calculated to have both α and γ present as shown in Table 11.

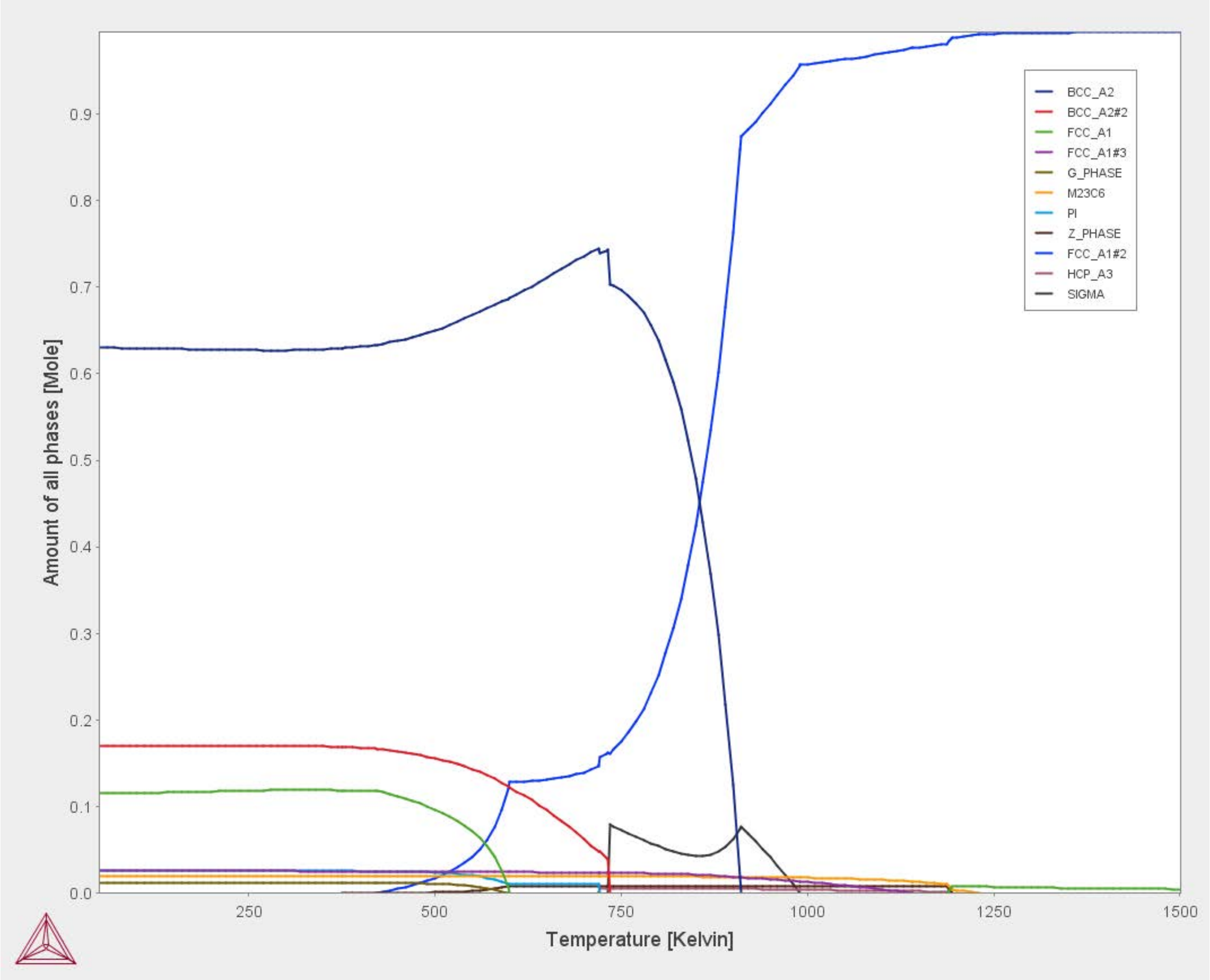

Figure 43 -Equilibrium Phases of DMV304HCu with changing temperatures calculated with Thermo-calc. Ferrite = BCC_A2, BCC_A2#2. Austenite = FCC_A1, FCC_A1#2, FCC_A1#3

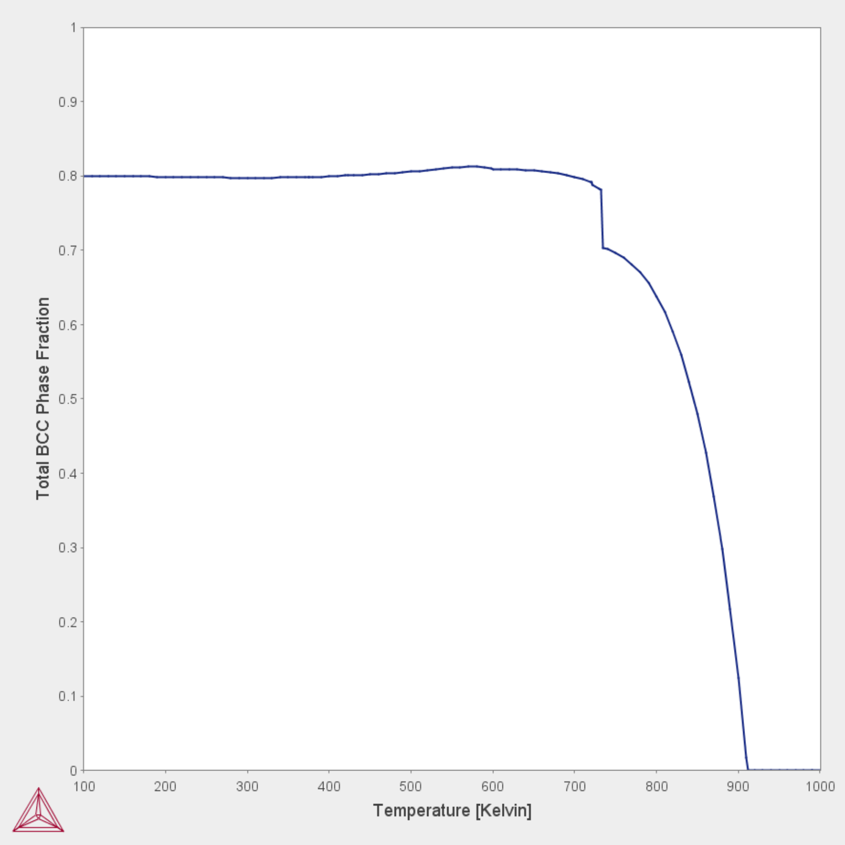

Figure 44 – Molar fraction of BCC Phases in DMV304HCu with changing temperature. Calculated with Thermo-calc.

Table 11 - Calculated stable phases in DMV304HCu at room temperature (300K)

Crystal Structure	**Molar Fraction of total**
bcc	0.80
fcc	0.14
Other	0.06

4.3.4 Effects of Heat Treatment

After exposure to temperatures of 700°C for 1000 hours the samples were found to have recrystallized and developed bcc grains in the shot peened region. Figure 45, Figure 46 and Figure 47 show SAED patterns of the shot peened regions of SSP, SP1 and SP2 respectively and all showed both α and γ diffraction peaks.

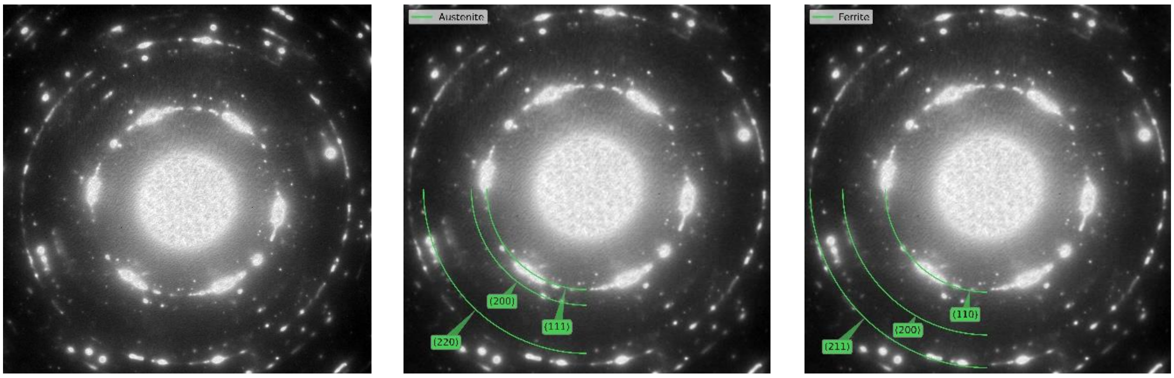

Figure 45 - SAED pattern from SSP heat treated at 700°C for 1000hrs. Simulated rings for (i)austenite and (ii)ferrite are superimposed. Austenite and ferrite are both visible in the DP.

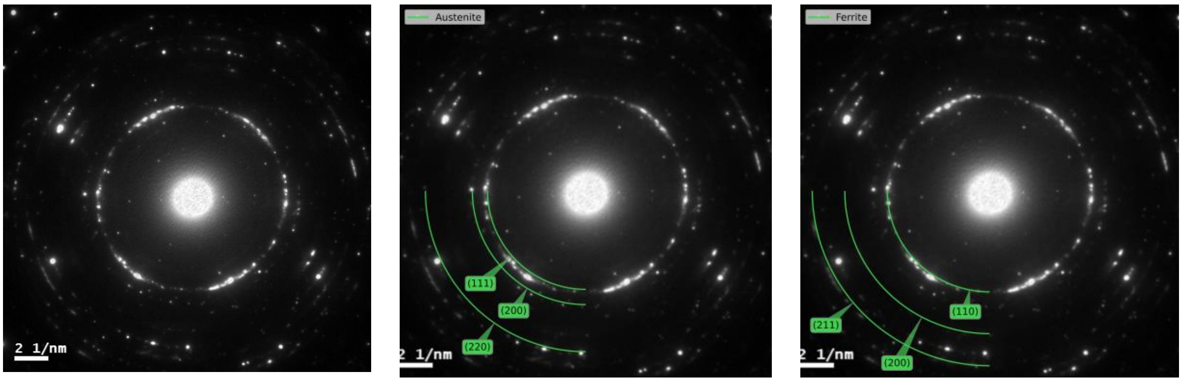

Figure 46 - SAED pattern from SP1 heat treated at 700°C for 1000hrs. Simulated rings for (i)austenite and (ii)ferrite are superimposed. Austenite and ferrite are both visible in the DP.

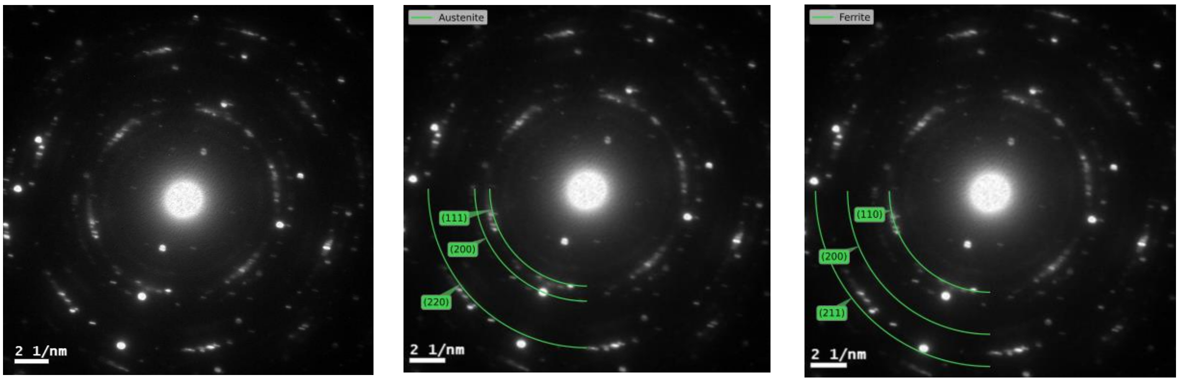

Figure 47 - SAED pattern from SP2 heat treated at 700°C for 1000hrs. Simulated rings for (i)austenite and (ii)ferrite are superimposed. Austenite and ferrite are both visible in the DP.

Figure 48 shows a combination of TKD and EDX maps taken of the oxide and underlying metal of SSP heat treated at 700°C in vacuum for 1000hrs. The SE image in Figure 48 (a) has the TKD and EDX mapped region highlighted as ‘Map Data 1’. The material towards the top of the SE image is the protective W coating used during the in-situ lift-out technique to protect the oxide layer from damage, but this material is not within the mapped area.

The TKD map (Figure 48 (b)) confirms the presence of both bcc and fcc regions in the metal beneath the oxide layer. EDX maps for Fe, Cr and Mn are shown in Figure 48 (c) and these show that the bcc regions are part of the underlying base alloy and not oxides. The fcc material at the top of the image is in the oxide layer and consists of a Mn-Cr-rich spinel. Spinel and fcc Fe were not distinguishable from each other by TKD mapping.

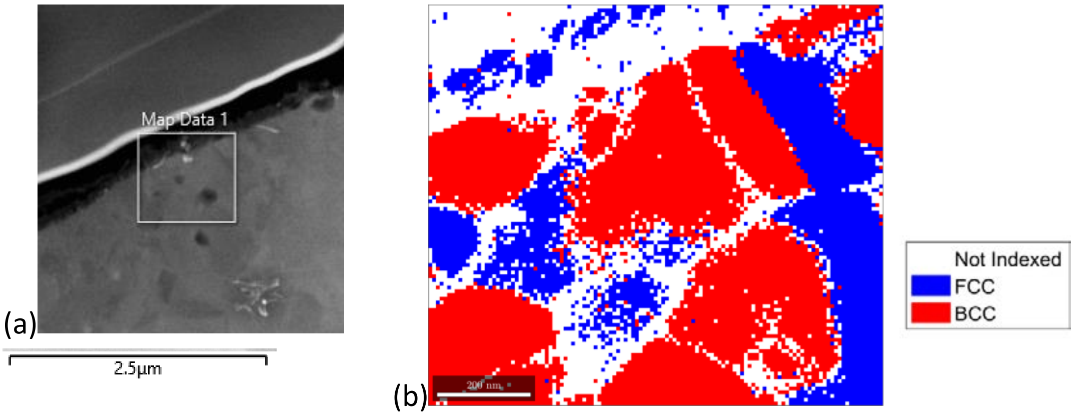

(c) (i) Cr (ii) Mn (iii) Fe

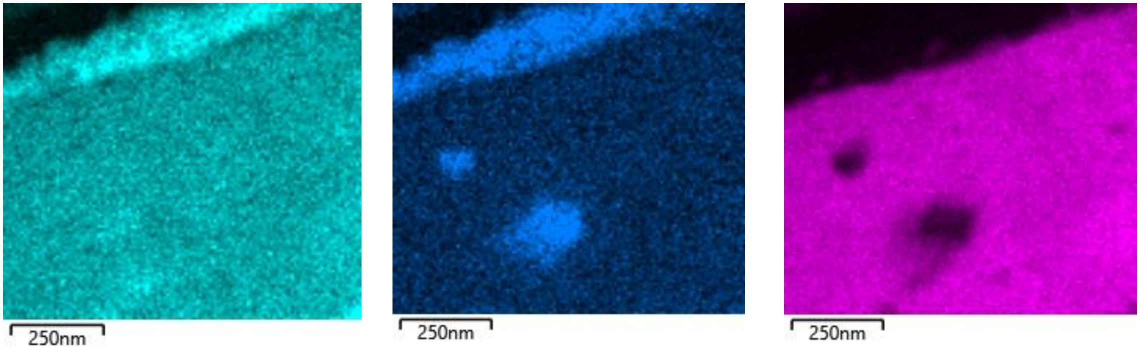

Figure 48 – (a)SE image of FIB-produced TEM foil of SSP heat treated in vacuum at 700°C for 1000Hrs. (b)Phase map of highlighted region of (a). (c)EDX images of highlighted region: (i)Cr (ii)Mn (iii)Fe

Thermodynamic simulations were generated using DICTRA software in order to understand the possible causes of ferrite growth at elevated temperatures. Figure 49 shows the growth rate of a simulated ferrite grain into an austenite grain at 750K. Simulations run at 800K, 850K and 900K also showed ferrite growth. A simulation run at 950K was unable to converge on a solution in the time available and simulations run at 1000K showed no growth of the ferrite grain, which is to be expected from Figure 44. The simulations suggest that ferrite can grow at very slow rates in a narrow range of temperatures below 1000K.

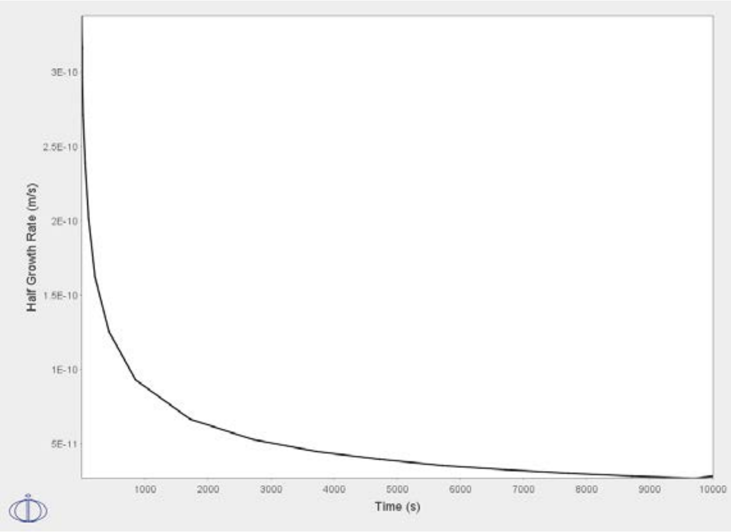

Figure 49 - DICTRA simulation of a ferrite grain growing into an austenite grain in DMV304HCu at 750K (477°C).

4.3.5 Effects of Exposure to Steam

TKD showed that exposure to high pressure, deoxygenated steam at 700°C for 1000hrs caused recrystallization to a mixed fcc/bcc structure. Figure 50 shows a TKD-derived phase map of SP1 exposed to high pressure steam. Note that the TKD system could not reliably distinguish between γ and $MnCr_2O_4$ because they are both of the same space group and the difference in lattice parameters did not have a resolvable effect on their Kikuchi patterns. γ and $MnCr_2O_4$ are combined in Figure 50 and are listed as fcc. The majority of the mapped region is bcc.

The largest grains in Figure 50 are bcc, while the fcc grains are smaller and found in clusters. This suggests that the bcc material is recrystallizing and the grains are coalescing to form larger, strain-free grains as described in the literature review section 2.5.1.2 (Primary Recrystallization). The fcc grains are at an earlier stage of recrystallization than the bcc material.

Figure 51 shows TKD data from a sample of SP1 material exposed to flowing deoxygenated steam at atmospheric pressure at 700°C for 1000Hrs. This also demonstrates the presence of a mixed fcc/bcc structure below the oxide layer. The majority of the mapped area in the SP1 exposed to atmospheric-pressure steam had an fcc crystal structure. However, there is not enough data in the small number of samples examined with TKD to provide a conclusive fcc/bcc ratio.

Exposure to high pressure steam may promote the growth of bcc material in the shot peened material more than exposure to atmospheric pressure steam, or the differences may be caused by variability in oxygen content and/or temperature in the steam oxidation rigs.

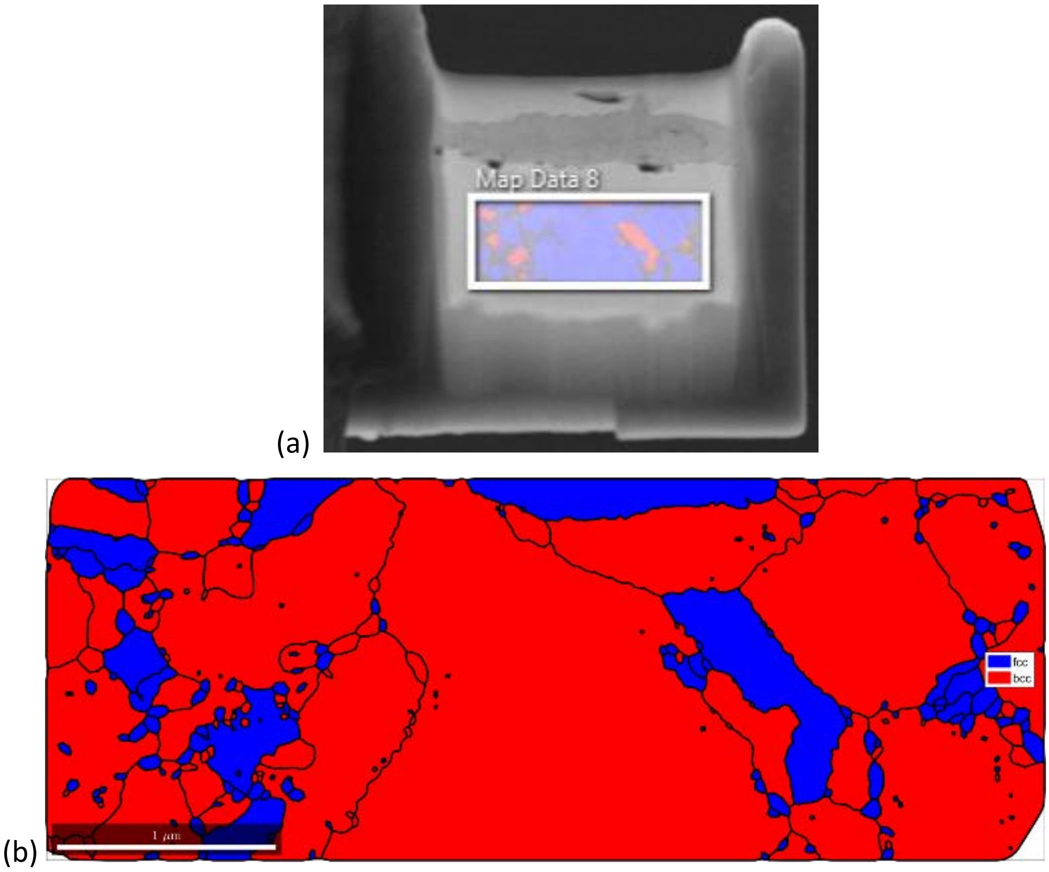

Figure 50 - (a) SE image of TEM foil from SP1 exposed to high pressure steam at 700°C for 1000hrs. (b) TKD Phase map of the highlighted region of (a) showing grains of fcc and bcc crystal structure. The black lines show grain boundaries.

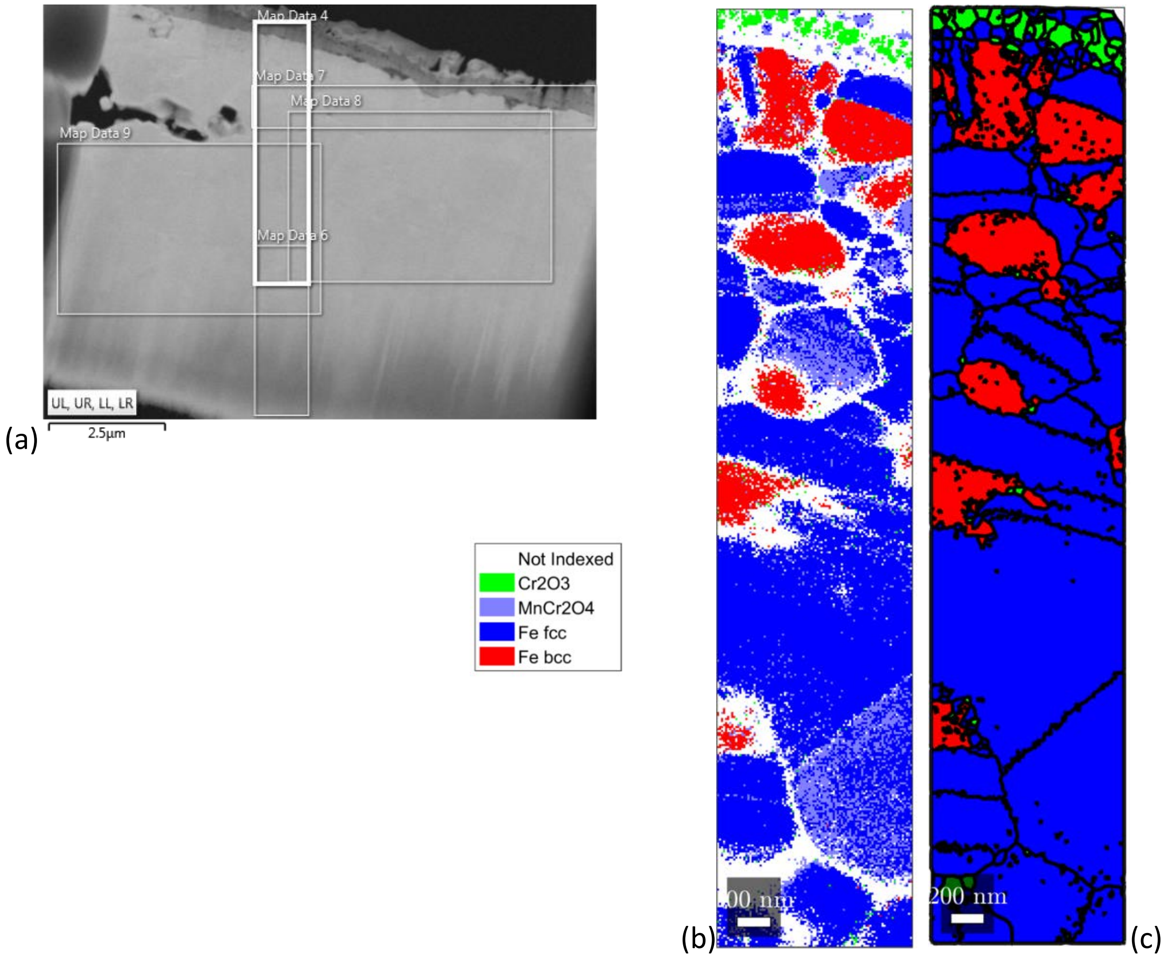

Figure 51 – (a) SE image of SP1 exposed to flowing steam at atmospheric pressure at 700°C for 1000Hrs. (b)TKD phase map of the highlighted region 'Map Data 4' in (a). (c) Grain map generated from (b) assuming that all material indexed as MnCr$_2$O$_4$ was Fe fcc.

4.4 Summary of Results

Profiles of microhardness were taken for SP1, SP2 and SSP material in the as-peened condition and after heat treatment for 1-1000hrs at 600-750°C. All samples showed an increase to peak microhardness within 50µm of the shot peened surface and then a drop off to the bulk microhardness within 200µm. The microhardness profiles were each fitted to a Gaussian function to make comparisons between them.

The use of microhardness indentation testing led to the appearance of the peaks in the microhardness profiles, because the test underestimates microhardness when used within a certain distance of a sample edge. Nanohardness testing did not show this behaviour. The hardest material is assumed to have been at the shot peened surface.

Exposure to temperatures of 600-750°C in vacuum for >1000hrs caused a reduction in peak microhardness in all samples except for SSP at 600°C. The reduction was larger for longer exposure times and for higher temperatures.

Exposure to temperatures of 600-650°C for 1-10hrs in vacuum caused the peak microhardness of all samples to increase from their as-peened condition.

Exposure to temperatures of 600-750°C in vacuum caused an increase in the distance of peak microhardness from the shot peened surface. The increase was larger for longer exposure times and for higher temperatures. This is caused by the link between the indentation size and proximity to the sample edge.

The change in peak microhardness of a shot peened 304HCu grade steel was predicted for temperatures of 600-750°C up to an exposure time of 10,000hr.

The effect of shot peening on grain size was assessed by SEM and TEM. Grain sizes increased from a minimum at the shot peened surfaces to the bulk grain size over a distance of 100-200µm. This correlates with the change in hardness over the same region. At distances >10µm from the surface the grain sizes were fitted to (5) and gave a calculated bulk grain size of 11.0±0.2 µm for SP1 and 10.8±0.2 µm for SP2.

Darkfield imaging showed that the grain size at the shot peened surface was of the order of 18nm-56nm in as-peened materials. After exposure to vacuum at 700°C for 1000hrs the SP1, SP2 and SSP all had larger grains than before heat treatment, with SP2 showing the largest difference in grain size. SP1 material showed the same trend when exposed to 700°C steam at atmospheric pressure for 1000hrs.

The as-peened material was fully austenitic but TKD and SAED showed that the shot peened region contained ferrite after exposure to elevated temperatures. Thermodynamic simulations were conducted that suggested austenite could undergo transformation to ferrite at temperatures <950K (<677°C).

5 Results: Oxidation of Shot Peened Austenitic Stainless Steel

5.1 Oxide Thermodynamics

Figure 1 shows an Ellingham diagram with a compilation of oxidation reactions that are relevant for the DMV304HCu alloy. This study only calculated the equilibrium line for reaction (1); the others are commonly available in the literature. The values for ΔG° of (1) were calculated from the work of Kjellqvist & Selleby [1].

$$\frac{1}{2}Mn + Cr + O_2 \rightarrow \frac{1}{2}MnCr_2O_4 \qquad (1)$$

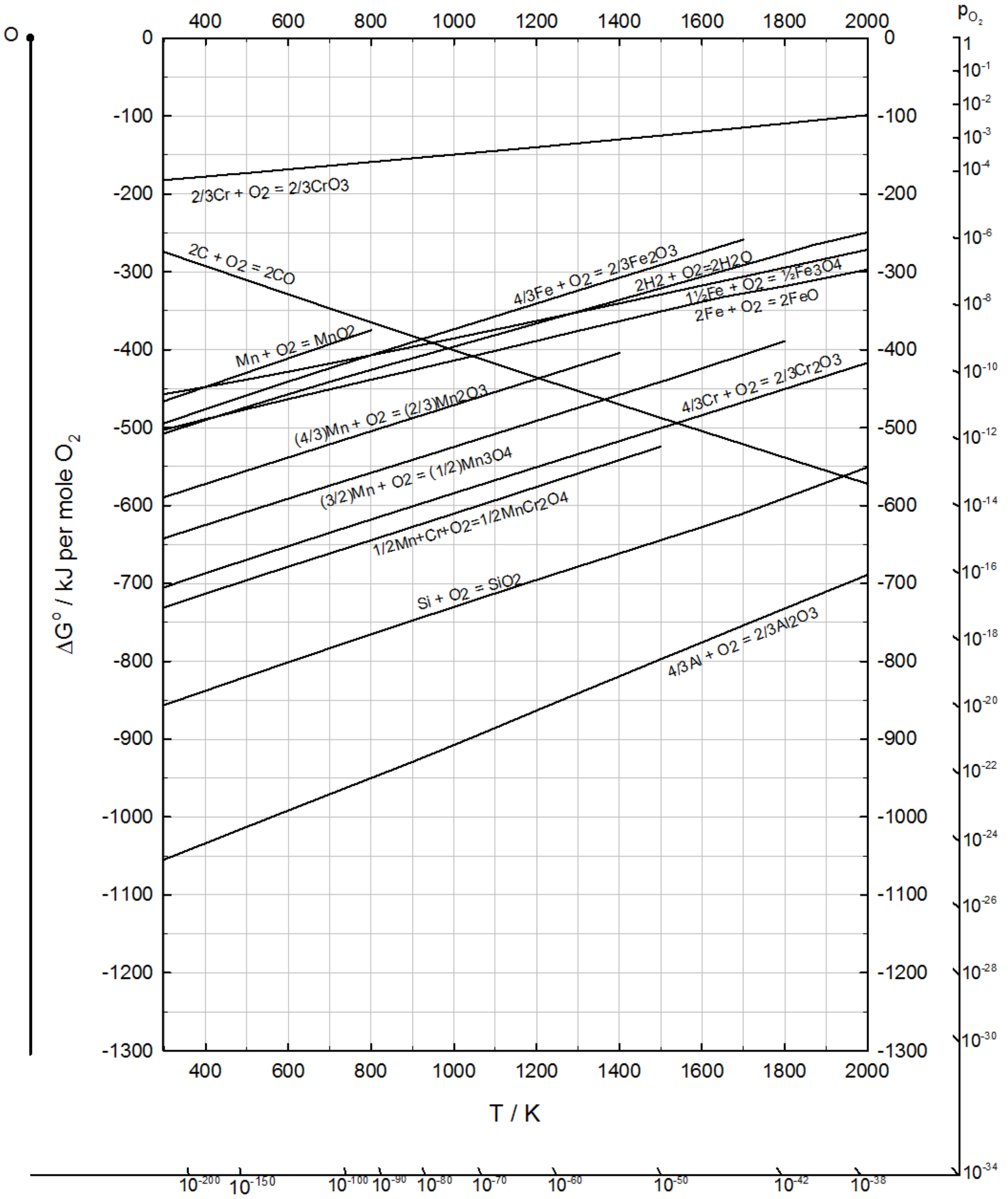

Figure 1 - Ellingham diagram of relevant oxides of stainless steel

5.1.1 The Cr-Mn-O oxide phases

Figure 2 is a phase diagram of Cr, Mn and O at atmospheric partial pressure of O_2. The diagram was created with Thermo-Calc using the TCOX6 database. The Cr-Mn-O system was chosen because it represents the chemistry present at the oxide/gas interface; Fe and Ni diffuse much more slowly through the oxide than Mn, and Cr is present in the oxide due to preferential oxidation.

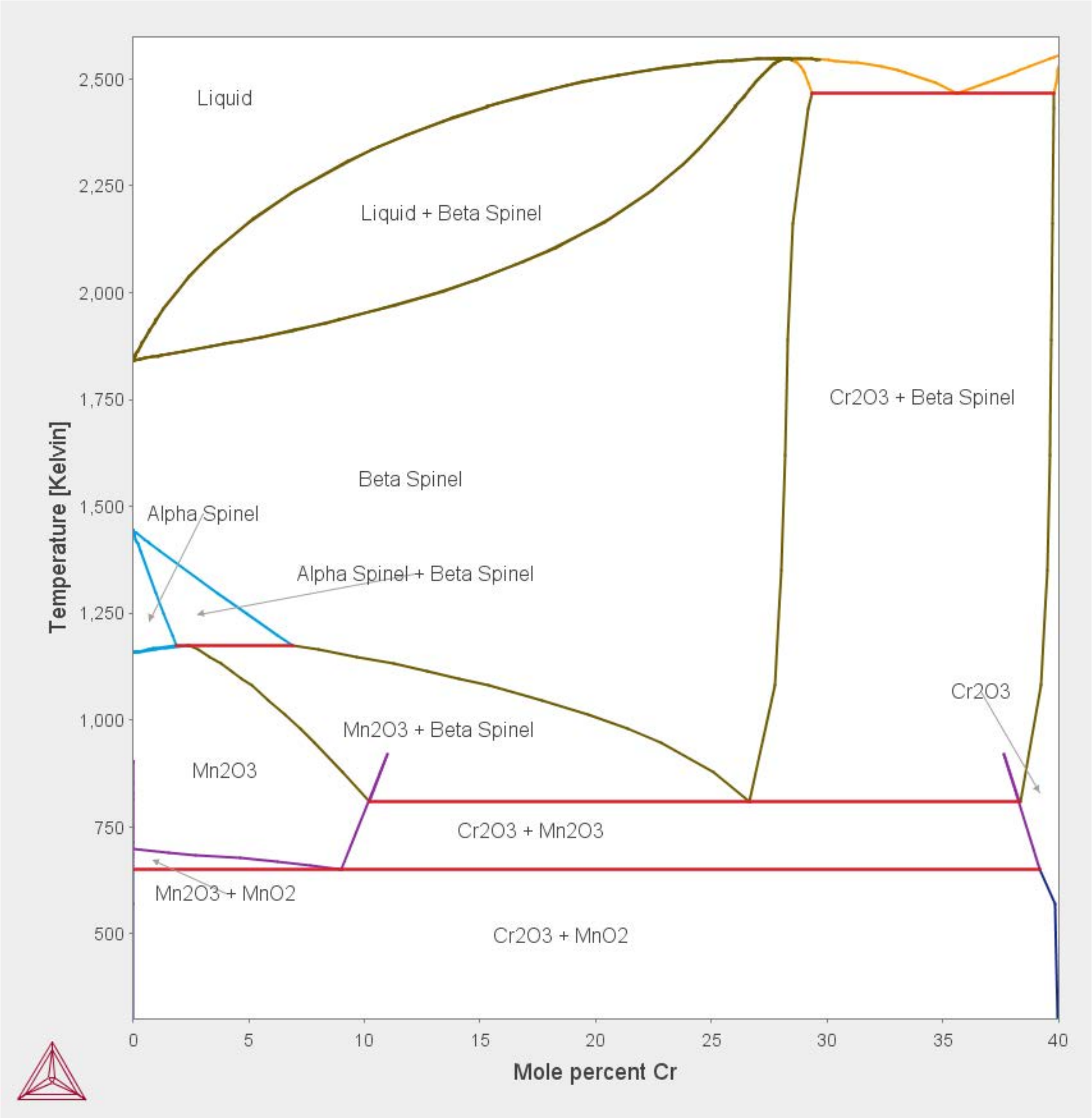

Figure 2 - Phase diagram of an Mn-Cr-O system in atmospheric partial pressure of O_2. Alpha Spinel phase is Mn_3O_4. Beta Spinel phase is $MnCr_2O_4$.

Figure 2 shows that if a small amount of Mn is present then a mixed phase of chromia and Mn-containing oxides will be thermodynamically stable. In the temperature range observed in this study (600-750°C / 873-1023K) it would be expected to find mixed phases of chromia, Mn_2O_3 and $MnCr_2O_4$ depending on the Mn content.

The Mn contents of DMV304HCu and Super304H are expected to be ≈2%wt, making the chromia layer stable without forming a mixed phase for 873-1023K. However, after the initial chromia layer is formed the diffusion rate of Mn through chromia will increase the Mn concentration and lead to the growth of $MnCr_2O_4$ as well. At lower temperatures (≈ <800K) Mn_2O_3 would be formed instead of $MnCr_2O_4$.

Figure 3 is a phase diagram for Cr, Mn and O at a partial pressure of O_2 in an idealized 24MPa deoxygenated power plant steam. The low oxygen concentration makes the $MnCr_2O_4$ phase stable over a larger range of concentrations of Mn than for atmospheric partial pressures. The temperature range of Mn_2O_3 is reduced to <500K, ensuring that it will not be stable at the temperatures examined in this study. Furthermore, if the concentration of Mn is sufficiently high then Mn_3O_4 could be stable across the whole 873-1023K temperature range. Details of the power plant steam calculations are given in Appendix D.

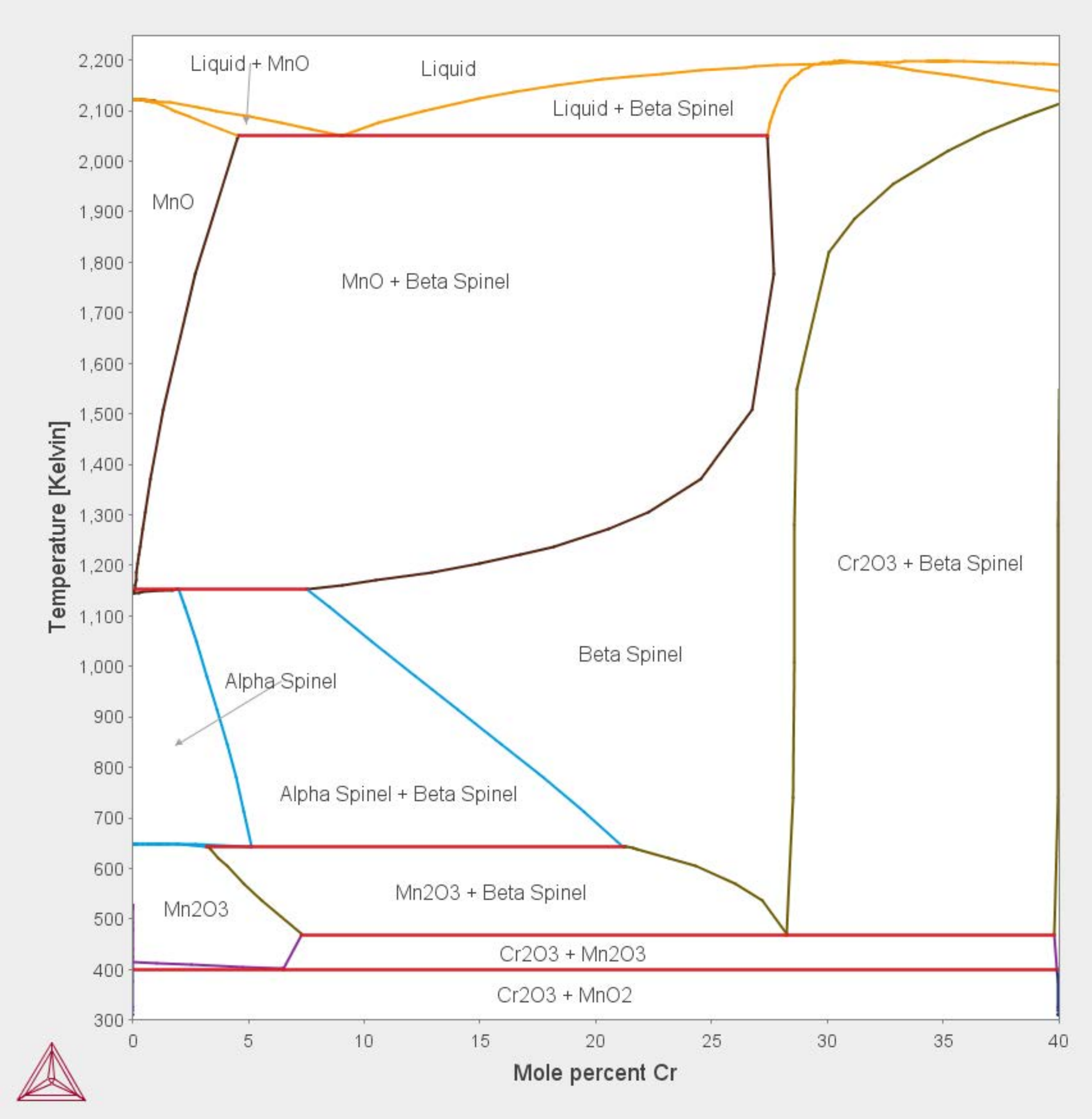

Figure 3 - Phase diagram of an Mn-Cr-O system with pO_2 of an idealized power plant steam at 24MPa pressure. Alpha Spinel phase is Mn_3O_4. Beta Spinel phase is $MnCr_2O_4$.

5.2 Oxide layer thickness

The thickness of oxides grown on shot peened material under different conditions was measured as described in Methodology section 3.14. Table 1 shows the thickness of the oxide layer in samples in the as-peened condition and after exposure to elevated temperatures in vacuum, atmospheric pressure steam (atm) and high pressure steam at 70bar (hp).

Table 1 - Oxide layer thickness in samples exposed to elevated temperatures

Material	Temp (°C)	Atmosphere	Exposure Time (hrs)	Oxide Thickness (nm)	Standard Deviation (nm)	Standard Error (nm)
SP1	--	--	0	87.9	16.5	0.8
SSP	700	Vacuum	1000	252.8	131.5	6.6
SP1	700	Vacuum	1000	215.3	43.4	2.2
SP2	700	Vacuum	1000	149.9	60.6	3.0
SP1	700	Steam (atm)	1000	482.5	131.7	9.7
SP1	700	Steam (hp)	1000	520.5	134.0	7.9

The oxide on the as-peened material was <100nm in thickness with a standard deviation of ≈20%.

5.2.1 Effects of Heat Treatment

After exposure to 700°C in vacuum the SSP material had the thickest oxide layer out of the three and was 25% thicker than for SP1. The SSP oxide (see Figure 4) also showed significant variation in thickness, having a standard deviation of ≈50%.

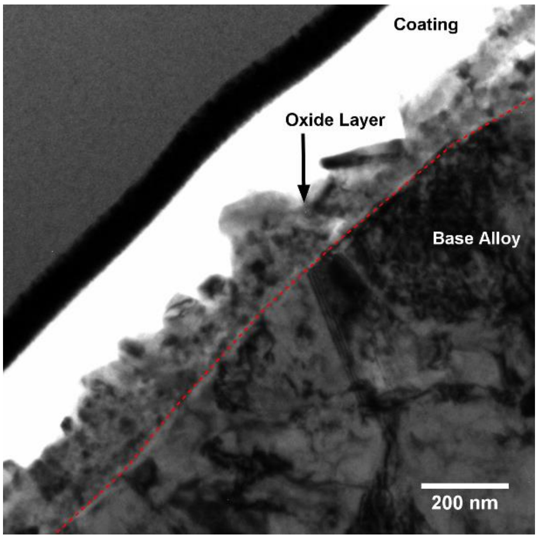

Figure 4 - Brightfield TEM image of the oxide layer formed on SSP after 1000hrs in vacuum at 700°C. Dotted line shows the location of the metal/oxide interface.

By comparison, the oxide grown on SP1 material (see Figure 5) was more uniform. Figure 6 shows a DF image of the oxide layer on SP1 created with electrons from the $MnCr_2O_4$ (311) peak. DF imaging and grain maps created from BF images showed that the oxide grains were columnar when grown on both SP1 and SP2. Figure 7 shows a grain map of a section of oxide from heat-treated SP1. A grain map covering a larger area of the heat-treated SP1 oxide can be found in appendix C 1.2

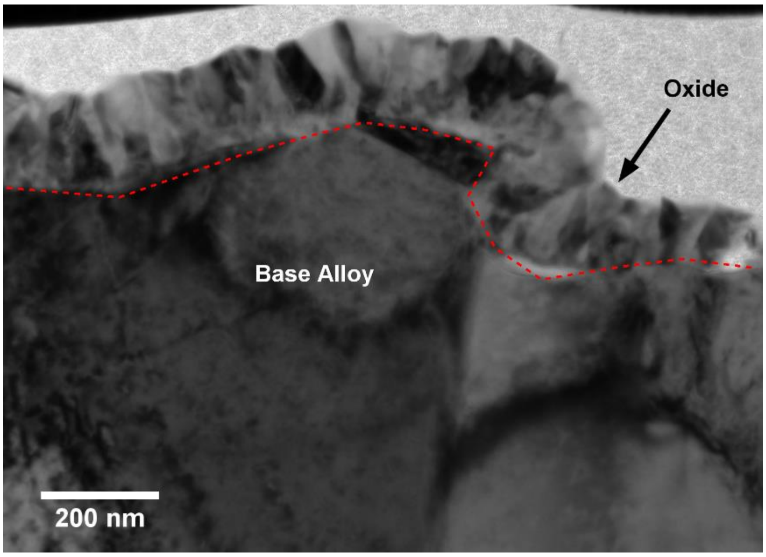

Figure 5 - Brightfield TEM image of the oxide layer formed on SP1 after 1000hrs in vacuum at 700°C. Dotted line shows the location of the metal/oxide interface.

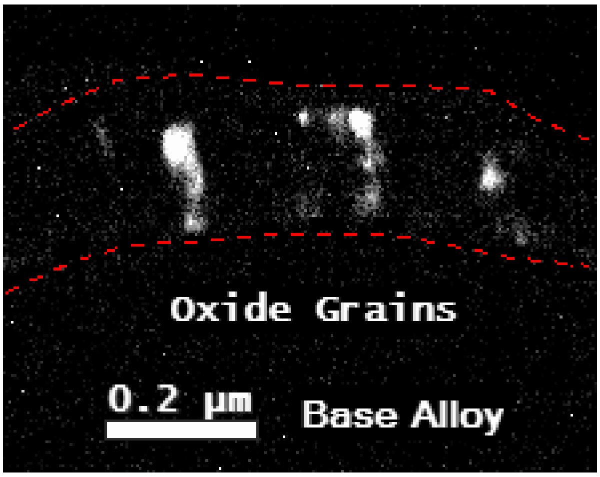

Figure 6 - Darkfield TEM image of the oxide layer formed on SP1 after 1000hrs in vacuum at 700°C. Imaged electrons are from the $MnCr_2O_4$ [311] peak. Dotted lines show the boundaries of the oxide layer.

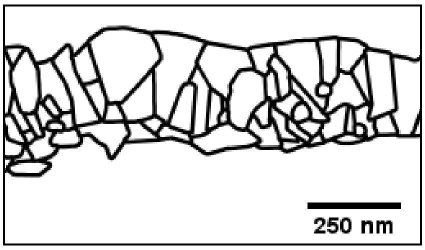

Figure 7 - Grain map of the oxide grown on SP1 after 1000hrs in vacuum at 700°C. Base alloy is to the bottom of the image.

5.2.2 Effects of Steam Exposure

Figure 8 shows a representative brightfield image of the steam-grown oxide layer. SP1 material exposed to atmospheric pressure steam at 700°C grew an oxide layer that was ≈5x as thick as in the as-peened condition, or just greater than 2x the thickness of the oxide grown in vacuum. The oxide layer thickness had a standard deviation of ≈25%; the oxide was observed to be made of many small grains and not columnar grains as seen in vacuum heat treated SP1 (Figure 9 (B)). In areas of the oxide layer that were thicker, the grains appeared to be larger and the oxide grew further outward from the surface (Figure 9 (A)). A grain map covering a larger area of the oxide layer can be seen in appendix C.2.2.

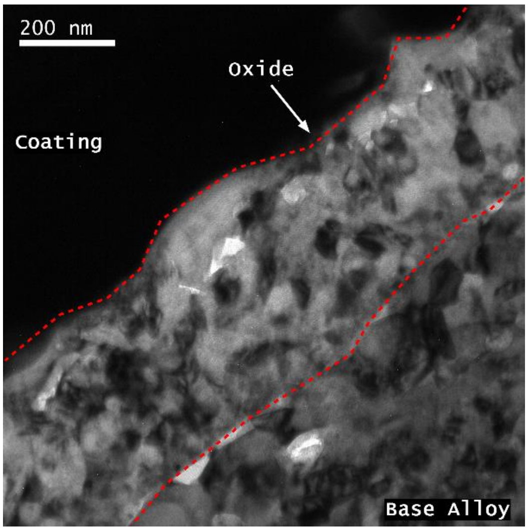

Figure 8 - Brightfield TEM image of the oxide layer formed on SP1 after 1000hrs in atmospheric pressure steam at 700°C. The dotted lines show the locations of the metal/oxide and oxide/gas interfaces. Coating is W deposited on the surface during TEM foil preparation to protect the oxide layer.

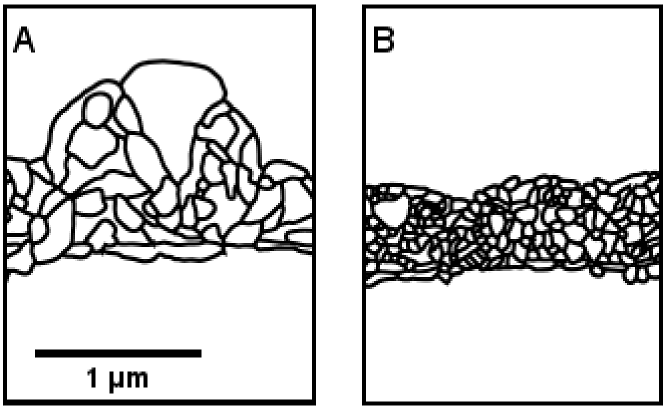

Figure 9 - Grain maps of the oxide layer formed on SP1 after 1000hrs in atmospheric pressure steam at 700°C. Base alloy is at the bottom of the image. (A) shows a region of relatively large grains. (B) shows a region of small grains.

SP1 material exposed to 70bar steam at 700°C for 1000hr grew an oxide layer ≈10% thicker than in atmospheric pressure steam and included oxide whiskers growing out of the oxide/gas interface (see Figure 10). The whiskers were not included in the calculations of oxide thickness because they are so thin and contained little material. The oxide layer thickness had a standard deviation of ≈25%, comparable with the oxide grown in atmospheric pressure steam.

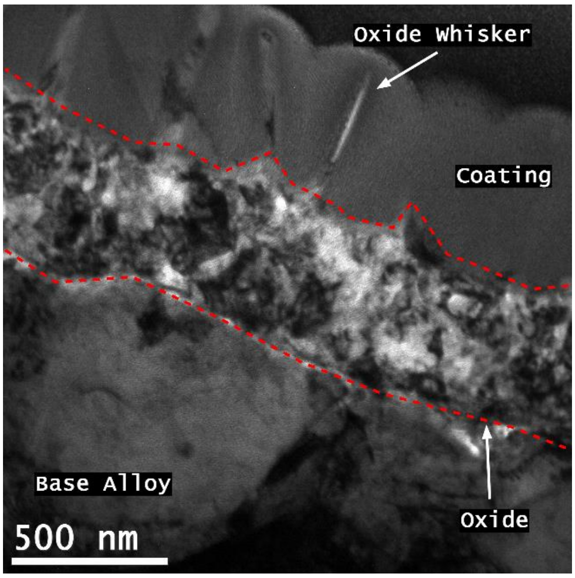

Figure 10 - Brightfield TEM image of the oxide layer formed on SP1 after 1000hrs in 70bar steam at 700°C. The dotted lines show the location of the metal/oxide and oxide/gas interfaces. Coating is W deposited on the surface during TEM foil preparation to protect the oxide layer.

5.3 Oxide Composition

5.3.1 Heat Treated in Vacuum

Figure 11 shows an SAED pattern of oxide grown on SP1 in vacuum after 1000hrs at 700°C. The diffraction rings showed that the oxide layer was a spinel with a lattice spacing consistent with both $MnCr_2O_4$ and Fe_3O_4. Figure 12 includes TEM-EDX data for two points on the oxide layer, showing that the spinel was $MnCr_2O_4$.

At the base of the spinel adjacent to the metal there was a thin (<10nm) layer of Si oxide. The EDX data from Figure 12 (b) includes some of the base metal so the relative ratio of Mn\Cr\Fe in the oxide was not precisely determined.

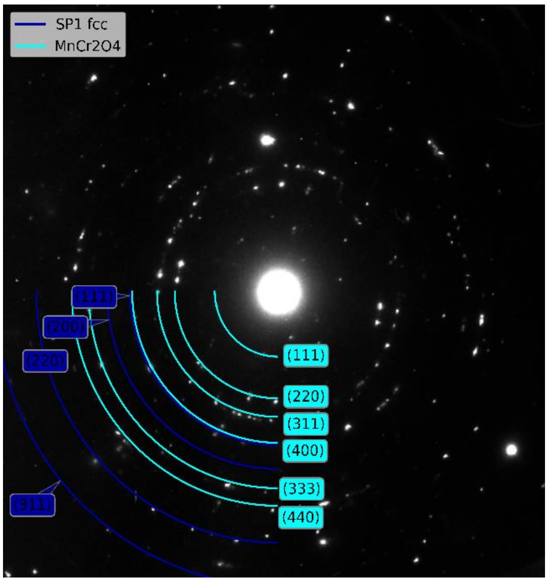

Figure 11 - SAED pattern of oxide layer grown on SP1 after 1000 hours in vacuum at 700°C. Simulated diffraction rings are for austenite and $MnCr_2O_4$ spinel.

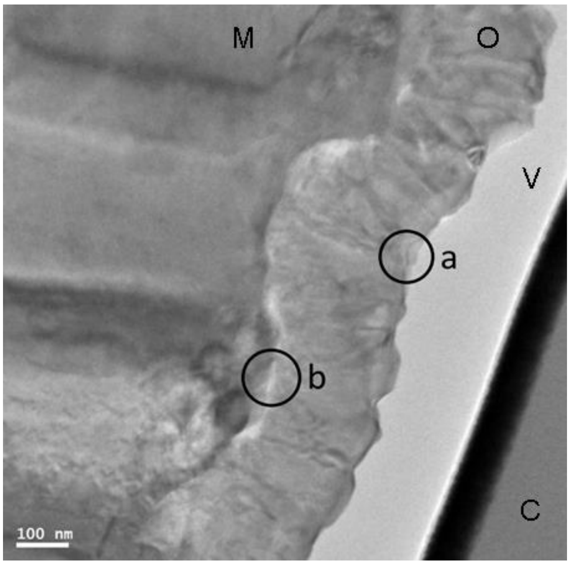

(a) EDX spot analysis of a

Element	Mass %	Atomic %
C *	7.44	17.21
O	28.59	49.66
Cr	39.09	20.89
Mn	19.83	10.03
Cu *	5.04	2.20

(b) EDX spot analysis of b

Element	Mass %	Atomic %
C *	14.76	31.08
O	23.24	36.73
Si	8.30	7.47
Cr	20.89	10.16
Mn	5.60	2.58
Fe	19.47	8.82
Ni	2.39	1.03
Cu *	5.35	2.13

Figure 12 - Brightfield TEM image of oxide layer formed on SP1 in vacuum after 1000hrs at 700°C. Tables show EDX Point analysis from (a) and (b) regions. M = metal, O = oxide, V = void, C = tungsten coating. Elements marked (*) are observed due to equipment/software error and are not part of the sample.

5.3.2 Steam (Atmospheric Pressure)

Figure 13 shows an SEM image of the oxidized surface of SSP after exposure to atmospheric pressure steam. Two visually distinct types of oxide were found across the sample surface, usually divided into separate 'regions'. Figure 13 shows the border between two oxide regions.

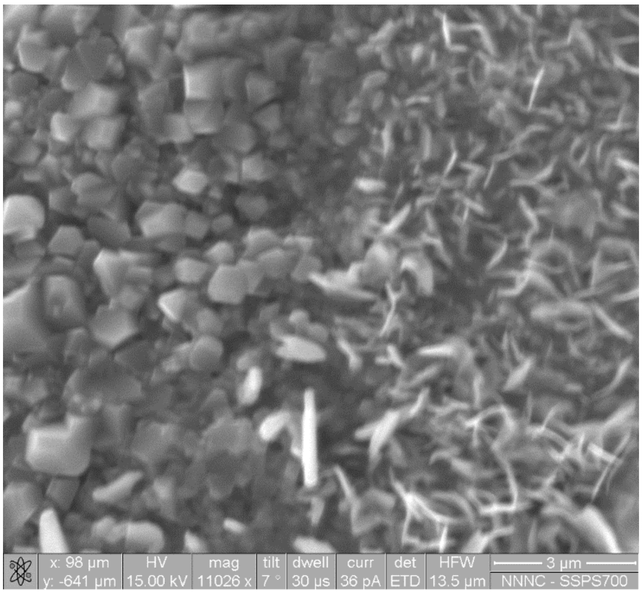

Figure 13 - SEM image of SSP surface oxidized in atmospheric pressure steam at 700°C for 1000hrs. The left of the image shows a polyhedral oxide and the right shows a platelet oxide.

TEM BF imaging of the oxide was performed after performing in-situ lift-out with FIB. The oxide layer was found to be a made of primarily small grains with some larger grains protruding outwards, as observed in Figure 14.

TEM EDX found that some grains were rich in Mn, Cr and O (Figure 14(a)) and the other grains closer to the metal/oxide interface were generally rich in Cr and O (Figure 14(b)).

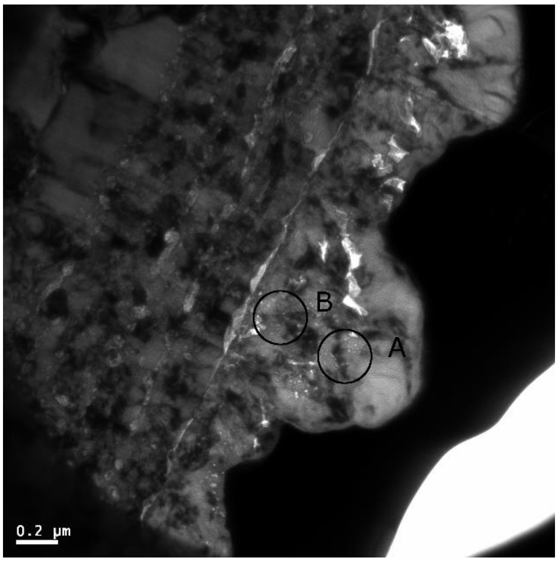

(a) EDX spot analysis of A

Element	Mass %	Atomic %
O	28.49	57.27
Cr	43.22	26.74
Mn	20.79	12.17
Fe	0.41	0.24
Cu *	7.09	3.59

(b) EDX spot analysis of B

Element	Mass %	Atomic %
O	32.95	61.97
Cr	57.38	33.21
Mn	3.18	1.74
Cu *	6.49	3.07

*Figure 14 - Brightfield TEM image of oxide grown on SP1 exposed to atmospheric pressure steam at 700°C for 1000hrs. *Cu signal is enhanced by background levels in the equipment.*

TEM DF imaging found that the grains were a mixture of chromia and spinel structures such as the two grains highlighted in Figure 15. A set of DF images was used to provide data for Figure 16, which colours areas highlighted by DF images of different crystal structures.

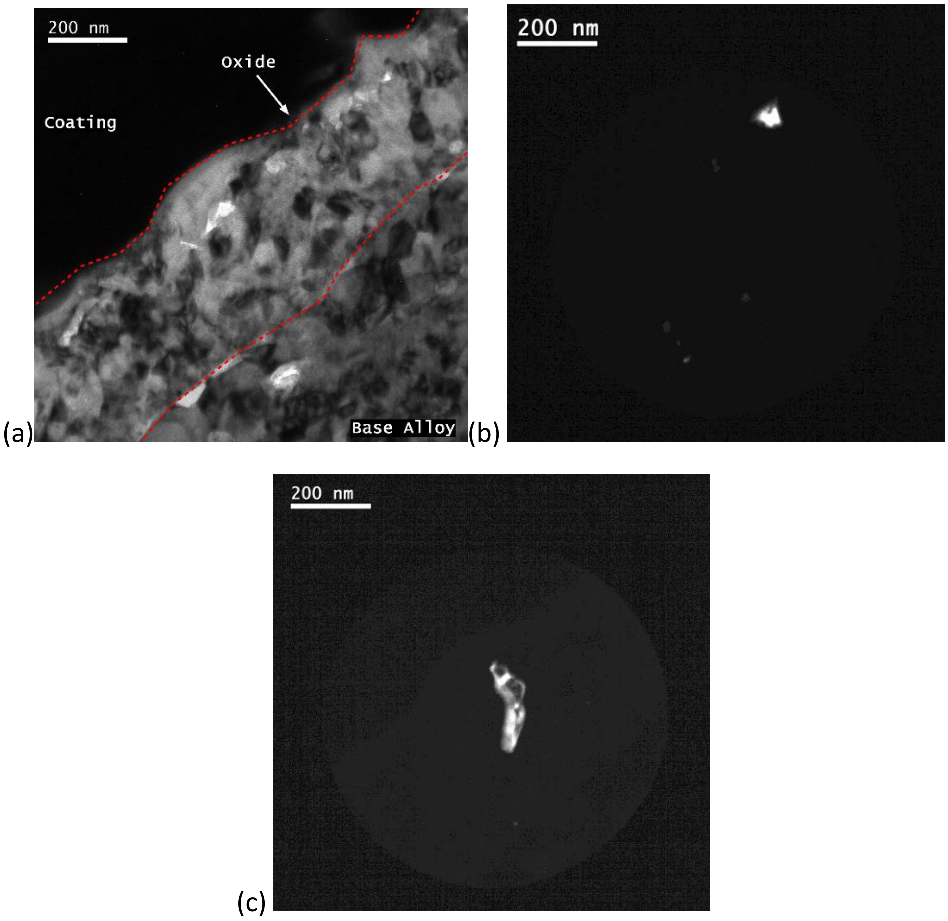

Figure 15 - (a) TEM brightfield image of the metal/oxide interface grown on SP1 exposed to atmospheric pressure steam at 700°C for 1000hrs. (b) Darkfield image of the same region made by electrons diffracted by spinel [111] planes. (c) Darkfield image of the same region made by electrons diffracted by chromia [011] planes. Coating is W deposited on the surface during TEM foil preparation to protect the oxide layer.

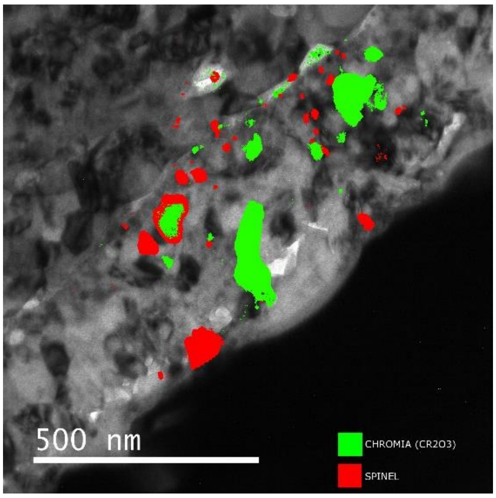

Figure 16 - TEM brightfield image of the metal/oxide interface grown on SP1 exposed to atmospheric pressure steam at 700°C for 1000hrs overlaid with regions that appeared in darkfield images made with electrons diffracted by chromia and spinel planes.

TKD mapping of the oxide layer is shown in Figure 17 and showed that both spinel and chromia crystal structures were present, but the majority of the grains were too small to index.

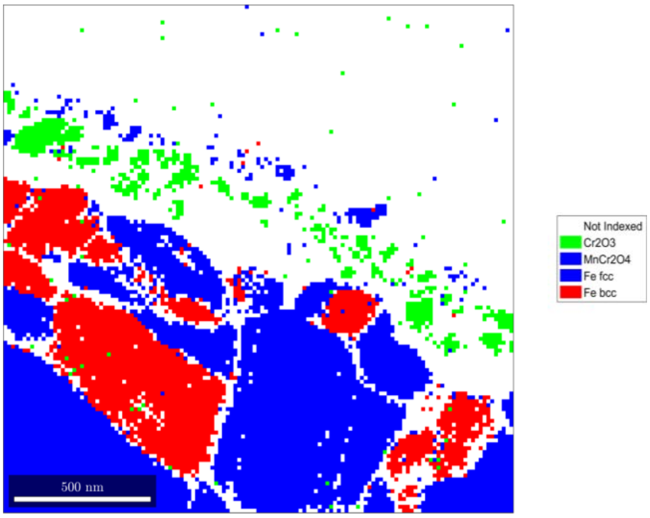

Figure 17 – TKD map of the metal/oxide interface grown on SP1 exposed to atmospheric pressure steam at 700°C for 1000hrs. The TKD patterns for austenite and $MnCr_2O_4$ are both the same colour because they could not be reliably distinguished. Base alloy is at the bottom of the image.

BF and DF images and TKD mapping suggests that the oxide layer is composed of two types of region; a thin layer topped with chromia and a thicker layer topped with $MnCr_2O_4$ spinel. This is shown schematically in Figure 18.

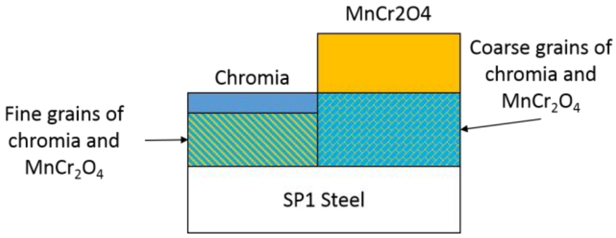

Figure 18 - Schematic of SP1 steel oxidized in atmospheric pressure steam at 700°C for 1000 hours showing the fine grain and coarse grain regions.

5.3.3 Steam (70bar)

Exposing the materials to high pressure (70bar) steam changed the proportion of the types of oxide on the surface. Figure 19 - Figure 21 show that the polyhedral oxide grains are isolated, with the majority of the surface being covered by platelet-type oxide. EDX data from the oxide surface are shown in Figure 21. The elemental compositions indicate that the polyhedral shapes are $MnCr_2O_4$ and the thin platelets are chromia, though the base alloy is close enough to the top of the chromia layer to generate Fe, Ni and Cu signals. The presence of 6%wt P in the oxide at Site A in Figure 21 is unexplained.

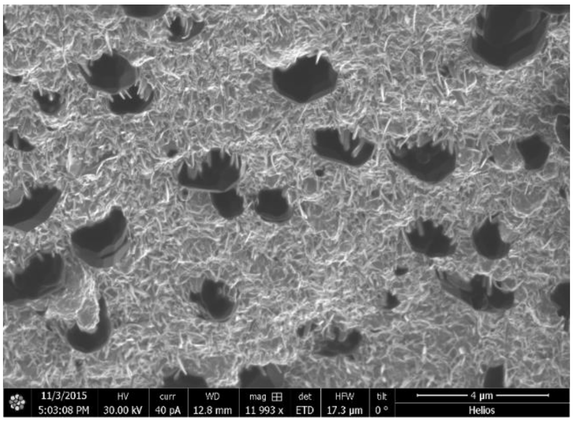

Figure 19 - FIB image of oxide grown on SP1 exposed to high-pressure steam at 700°C for 1000hrs. Platelet (chromia) and polyhedral (spinel) oxides are visible.

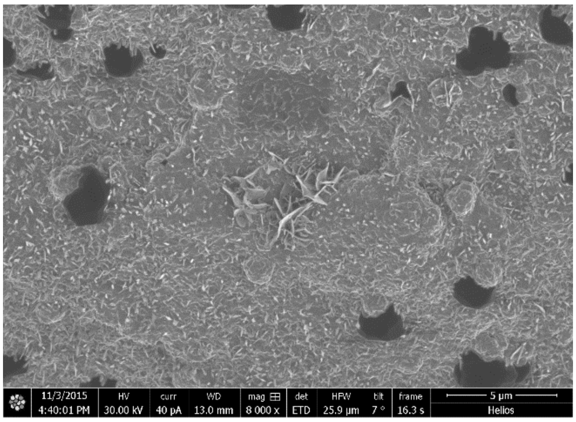

Figure 20 - FIB image of oxide grown on SP1 exposed to high-pressure steam at 700°C for 1000hrs. Platelet (chromia) and polyhedral (spinel) oxides are visible.

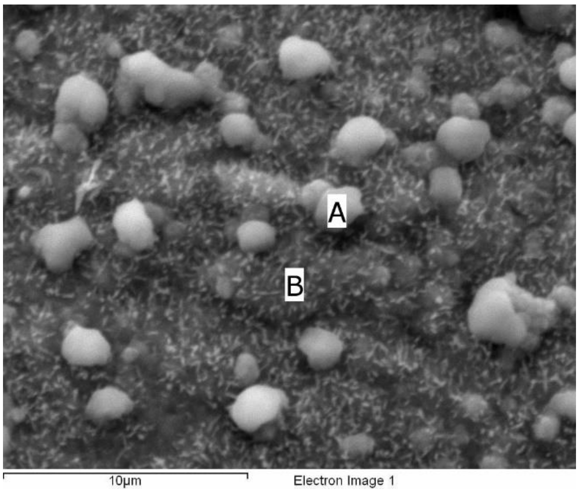

Site	O	Si	P	Cr	Mn	Fe	Ni	Cu
A	38.10	0.34	6.18	30.13	15.24	9.09	0.93	
B	21.00	0.76		30.18	1.98	40.35	4.80	0.93

Figure 21 - SEM image of oxide grown on SP1 exposed to 70bar steam at 700°C for 1000hrs. EDX data from points A & B are shown in wt%.

It should be noted that the EDX data in Figure 21 was generated at an accelerating voltage of 20kV and therefore the interaction volume of the electron beam should include material from 1μm up to 5μm beneath the surface, depending on the electron penetration characteristics of the material [2]. The oxide thickness was measured to be <1μm and so a significant portion of the X-ray signal would be expected to be from the base alloy and not the oxide in this instance. The base alloy was certainly a large part of the signal observed at site B, on the thin oxide, but very little Fe was detected at site A. It is possible that the oxide at site A was unusually thick, or that the sample/detector geometry reduced the electron beam current that reached the base alloy.

Figure 19 also features short whiskers growing from the oxide surface. EDX data for the oxide and an oxide whisker is shown in Figure 22. The fine-grained region below the whisker is made primarily of chromium with very little Mn. The concentration of Mn increases at the metal/oxide interface and the oxide/gas interface. Fe is also present above the chromium-rich layer, most likely in a (Fe,Mn) spinel. The whisker has a chromium-rich core in its centre surrounded by (Fe,Mn) material. A layer of Si-oxide is present at the metal/oxide interface, below the chromium-rich layer.

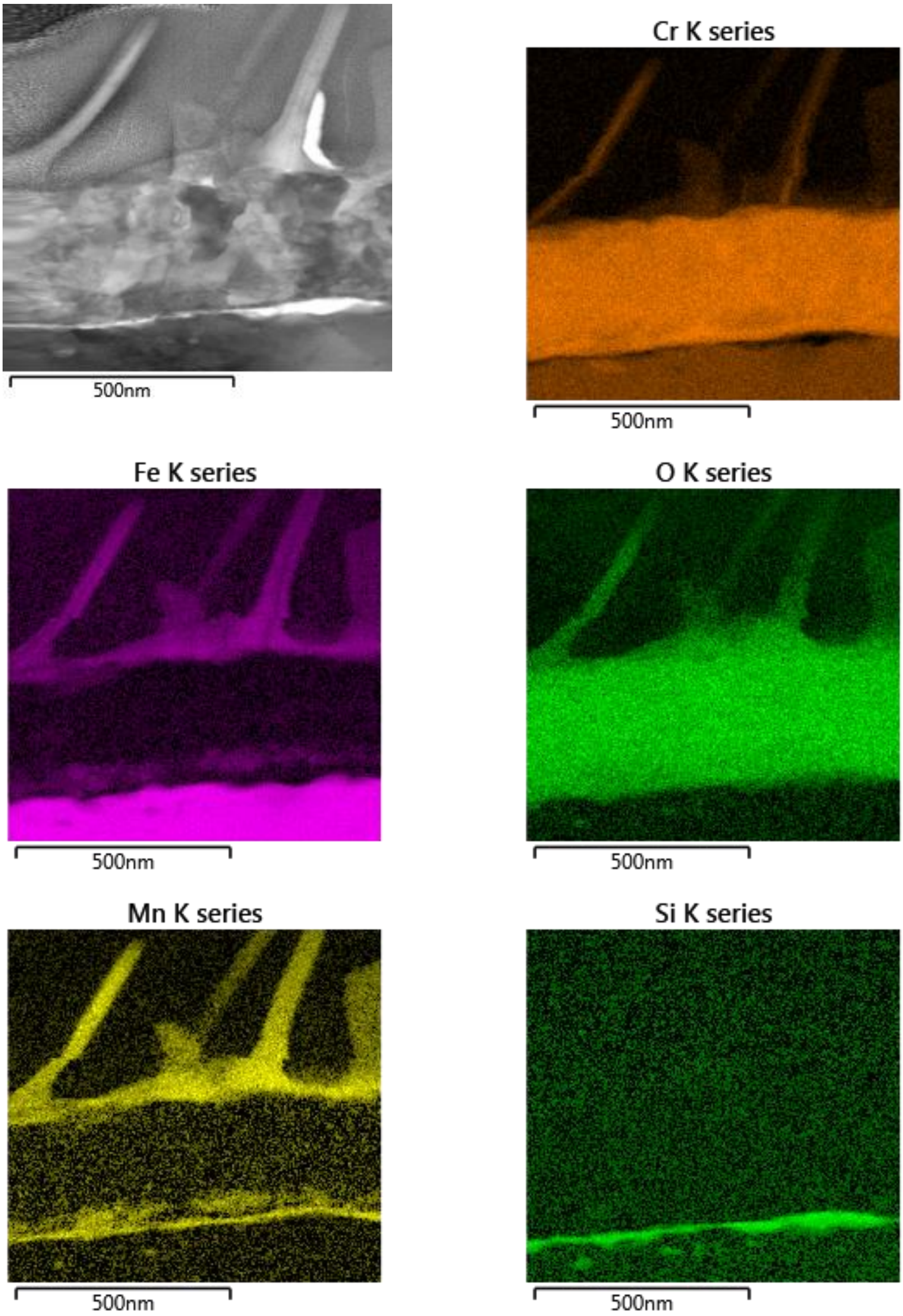

Figure 22 - TEM-EDX element maps of oxide grown on SP1 exposed to high-pressure steam at 700°C for 1000hrs. Image at Top-Left is SE.

A cross section and SEAD pattern of the oxide layer grown in high pressure steam is shown in Figure 23. Both the spinel and the chromia crystal structures are identified in the SAED pattern, suggesting that the oxide is structured in the same way as the samples exposed to atmospheric pressure steam. However, TKD and EDX maps of the oxide layer, shown in Figure 24, show that the centre of the oxide is primarily chromia and that $MnCr_2O_4$ is present both above and below the chromia.

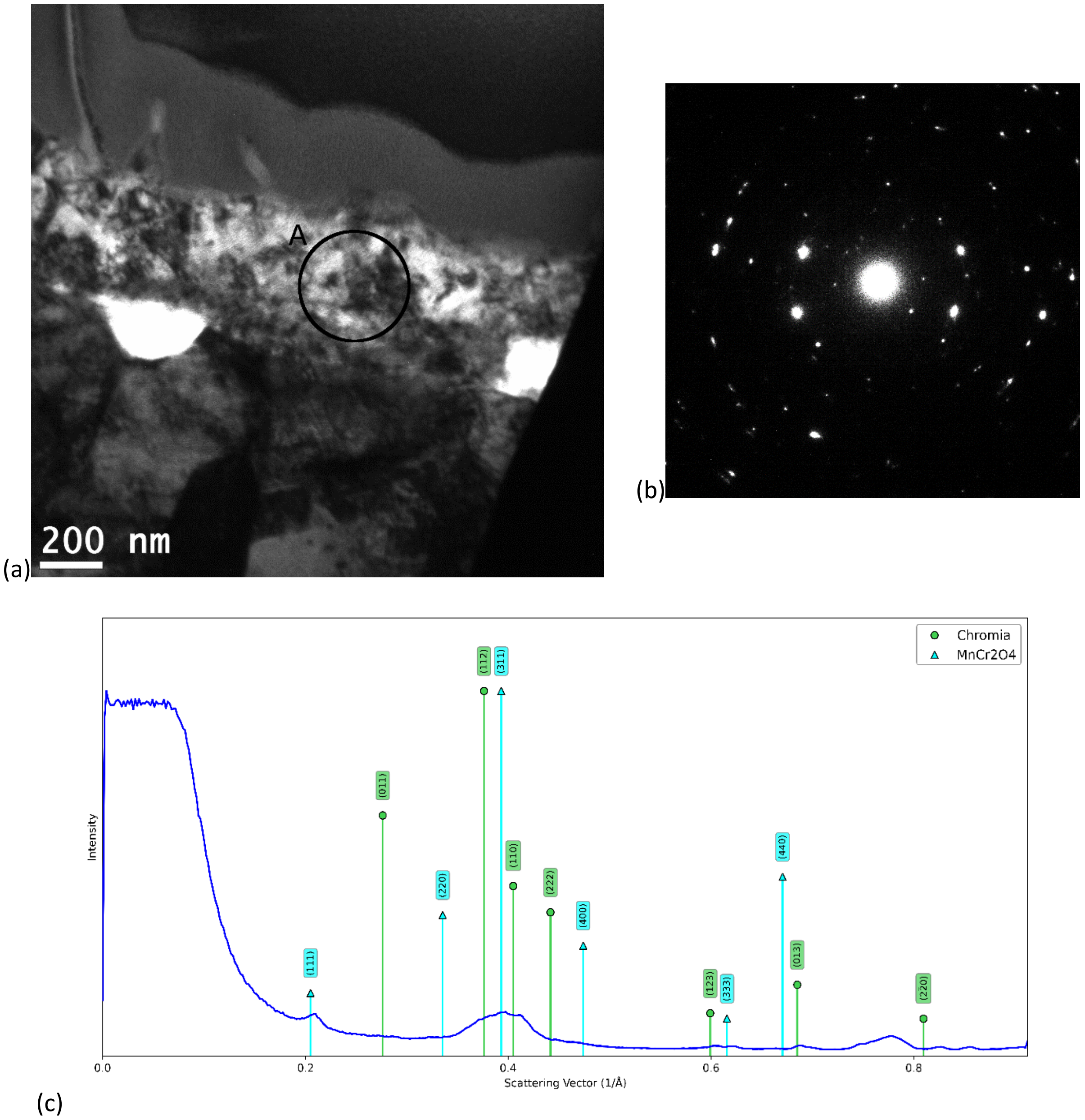

Figure 23 – (a)Brightfield TEM image of oxide grown on SP1 exposed to high pressure steam at 700°C for 1000hrs. (b)An SAED pattern taken from area A. (c)The radial profile of the SAED pattern correlates to $MnCr_2O_4$ [111],[311] and chromia [112], [110] peaks.

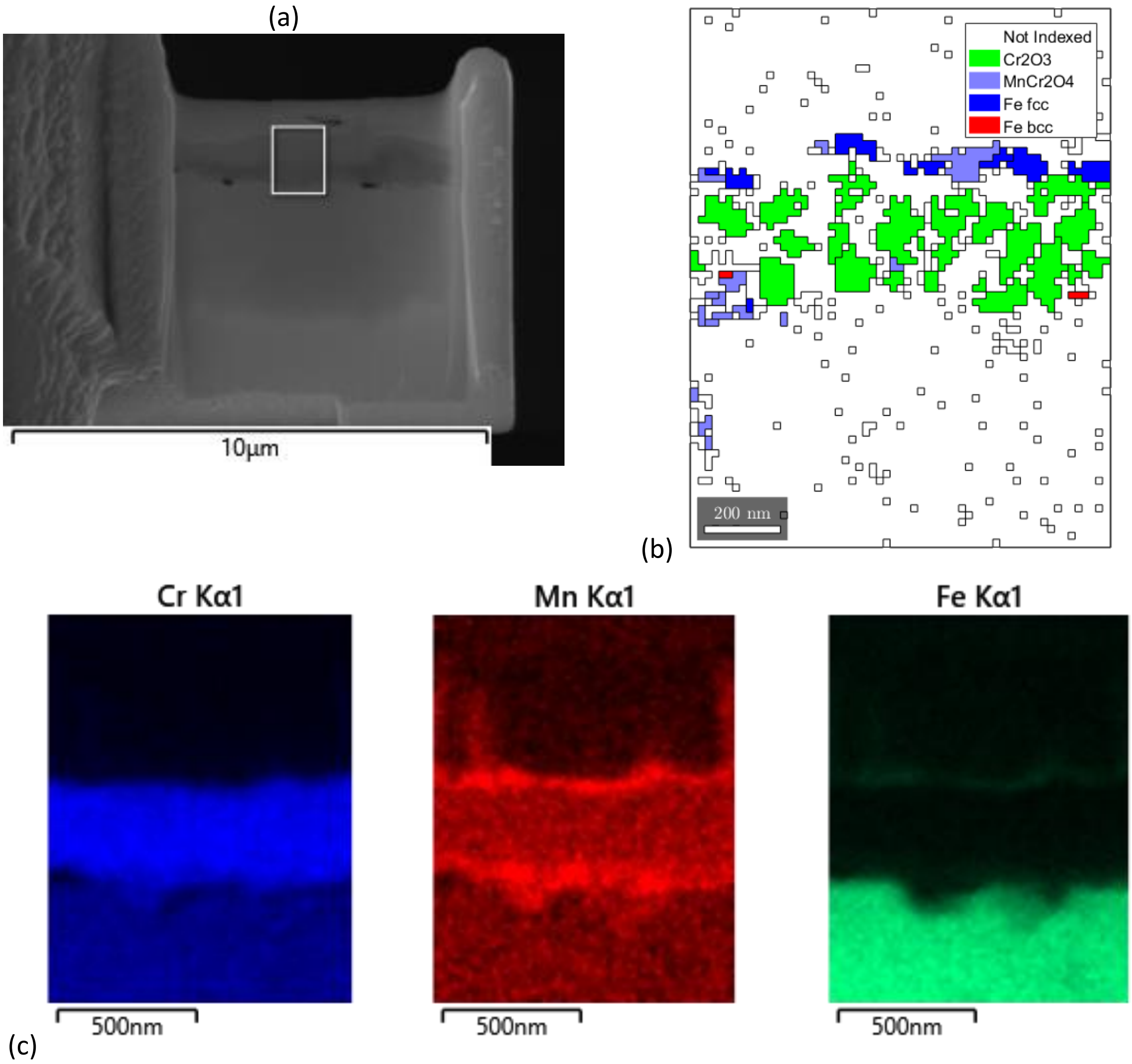

Figure 24 - SEM image of SP1 exposed to high pressure steam at 700°C for 1000hrs. (b) TKD phase map of highlighted oxide region. (c) EDX maps of highlighted oxide region.

A schematic of the oxide layer grown in high-pressure steam is shown in Figure 25.

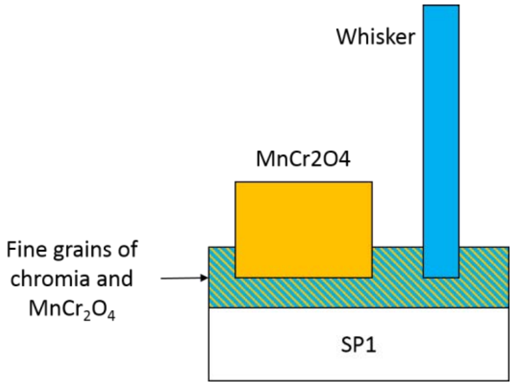

Figure 25 - Schematic of SP1 steel oxidized in 70bar steam at 700°C for 1000 hours.

5.4 Summary of Oxidation Results

SP1, SP2 and SSP exposed to 700°C temperatures in a vacuum grew an oxide made of columnar $MnCr_2O_4$. After 1000hrs the oxide layers were 150-250nm in thickness depending on the sample material. The order of oxide thicknesses was SSP > SP1 > SP2.

SP1 exposed to atmospheric pressure deoxygenated steam at 700°C for 1000hrs grew an oxide layer (482.5 ± 131.7)nm thick. Two morphologies of oxide were identified across the sample surface; a fine grained layer topped with chromia and a coarse grained layer topped with $MnCr_2O_4$. Both morphologies contained a mixture of chromia and $MnCr_2O_4$.

SP1 exposed to 70bar deoxygenated steam at 700°C for 1000hrs grew an oxide layer (520.5 ± 134.0)nm thick. The oxide was fine grained and consisted mostly of chromia at the metal/oxide interface. Above the chromia layer was a thin (Fe,Mn) spinel layer. Whiskers with a central core of chromia covered in (Fe,Mn) spinel were observed to grow outwards from the oxide layer.

5.5 References

1. Kjellqvist, L., & Selleby, M. (2010). Thermodynamic assessment of the Cr-Mn-O system. *Journal of Alloys and Compounds*, *507*(1), 84–92. doi:10.1016/j.jallcom.2010.04.252

2. Goldstein, J. I., Yakowitz, H., Newbury, D. E., Lifshin, E., Colby, J. W., & Coleman, J. R. (1975). *Practical Scanning Electron Microscopy*. (J. I. Goldstein & H. Yakowitz, Eds.). New York: Plenum Press.

6 Discussion

6.1 Bulk Microhardness

The bulk Vickers microhardness of SP1, SP2 and SSP materials were all found to increase during heat treatment at 600-750°C, lasting up to 100hrs. This increase could be explained by the precipitation of elemental Cu in the alloy matrix, which is well documented in the literature. (See section 2.2.6.3 of the literature review.) A further possibility is that the materials underwent a phase transformation from austenite to ferrite because at temperatures below ≈650°C ferrite is more thermodynamically stable than austenite, as shown in Results section 4.3.3. However, the same increase in hardness in the first 100hrs is observed in material heat treated at 750°C, which would not be expected to undergo such a transformation. The increase in bulk microhardness is therefore very likely to be the result of copper precipitation.

In order to prove this hypothesis, the copper precipitates would have to be observed by TEM. Work by Chi et al. [1] found that after 1000hrs of heat treatment at 650°C Cu precipitates in Super304 (the same alloy as the S304 and SSP samples) had grown to an average diameter of ≈10nm and were within metal grains as substitutional groups of atoms. These precipitates would therefore be theoretically resolvable in the TEM images used in this study, but they were not identified. The Cu precipitates would be of a similar size to the grains themselves in shot peened material and inside the grains; they therefore would not stand out in the TEM-BF images. The lattice constant and crystal structure of Cu are almost identical to those of austenite so the precipitates would also be indistinguishable from austenite in TEM-DF images. The only technique used in this study that might reasonably identify Cu precipitates was TEM-EDX and this was primarily used to observe external oxides, not internal precipitates. Therefore, Cu precipitates could have been present, even though they were not observed by TEM and TKD in this study.

At 1000hrs the bulk microhardness of all of the materials is lower than at 100hrs, but in most cases is still above the initial value. The largest reduction in hardness from 100hrs is observed in SP2 samples heat-treated at 700°C and 750°C and SSP samples heat-treated at 650°C and 750°C.

It could be that the Cu precipitates formed by heat treatment are growing larger and that this is causing the reduction in bulk hardness. Cu precipitates in Super304 have been observed to grow from ≈3nm to 10nm over 1000hr of heat treatment at 650°C[1]. In the work of Ou et al. [2] it was shown that heat treating Super304H at temperatures above 300°C lowers the tensile yield stress compared to heat treatment ≤300°C. The effectiveness of the Cu precipitates in hardening SSP, SP1 and SP2 will decrease as the precipitates grow larger, and this process occurs more rapidly at higher temperatures. To investigate this hypothesis would require TEM-EDX observations of samples heat-treated at different temperatures and for different times. The present study was only able to create TEM foils from material heat treated at 700°C for 1000hrs, due to time constraints.

6.2 Microhardness Profiles

Microhardness profiles of SP1, SP2 and SSP materials all showed that the shot peening process affected the hardness of the material down to 200µm below the surface. This value agrees with other investigations of shot peened material in the literature. The microhardness profiles also correlate with the expected profiles of the residual stress in the material, as discussed in section 2.3.1.2.

The peak microhardness was rarely found at the closest indentation to the surface and instead occurred at some depth below the shot peened surface. The grain size becomes smaller the closer it is to the shot peened surface, so the Hall-Petch relationship predicts that the peak microhardness will be at the surface. However, as was described in section 4.1.3, taking hardness measurements so close to the sample edge underestimates the hardness.

In order to take hardness readings closer to the sample edge it would be necessary to use nanohardness indentation, and this was attempted. However, equipment and sample preparation issues led to nano-indentations only being made >10µm below the shot peened surface. The closest nano-indentation to the surface of as-peened SSP recorded the peak nanohardness, and was ≈2x the hardness of the material >200µm below the surface.

The peak nano-hardness of as-peened SSP was (5.0±0.1) GPa at 20µm from the surface, which was converted to a Vickers hardness number of (501±14). The peak Vickers microhardness of as-peened SSP was 428(HV0.05), and was at a distance from the surface of ≈20µm. This illustrates how the microhardness measurements underestimate hardness at points close to the surface.

A chart was made in order to assess the reliability of a Vickers microhardness measurement taken close to an edge using a load of 0.05kg, and this is reproduced in Figure 1. It is feasible that the measured microhardness profiles could be adjusted to correct the hardness values that are closer than 2.5x the indentation diagonal from the sample edge. However, such a recalculation of the measured microhardness values would need to be compared with other hardness measurements, such as nanohardness indentation tests, to confirm if the method is valid.

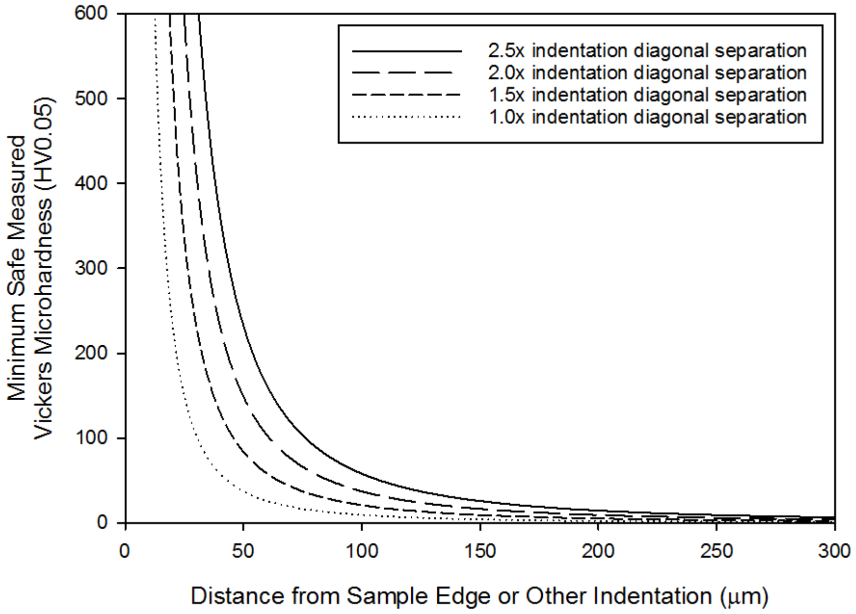

Figure 1 - Minimum Vickers microhardness that can be reliably measured at a given distance between indentations or from the sample edge for an indentation load of 0.05kg. Indentations and a sample edge must be separated by at least 2.5x the indentation diagonal in order to comply with the ASTM standard for Vickers microhardness testing.

6.2.1 Changes in Microhardness Profiles During Heat Treatment

The peak microhardness of the shot peened materials tended to decrease during heat treatment, but these values were almost all observed too close to the sample edge to be taken at face value. For example, after heat treatment at 600°C the microhardness profile of SP1 showed little change, especially at distances >2.5x the indentation diagonal from the edge, as shown in Figure 2.

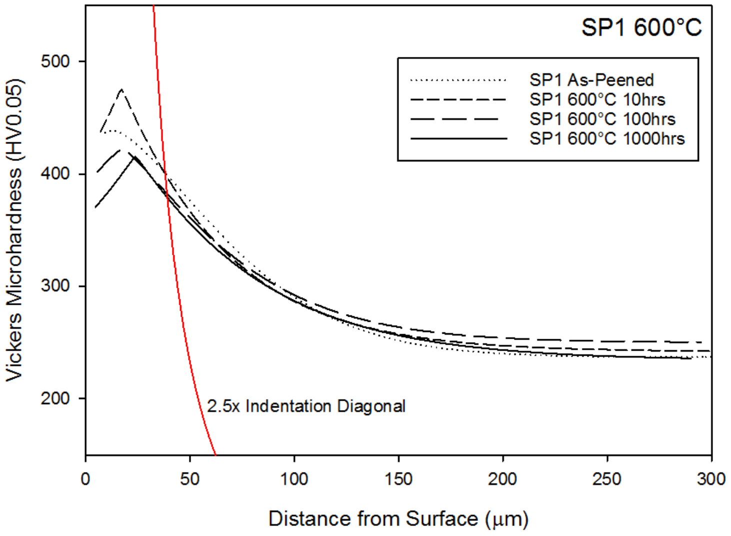

Figure 2 - Microhardness profiles of SP1 after heat treatment in vacuum at 600°C for 10, 100 and 1000hrs. The distance from the sample edge corresponding to 2.5x the indentation diagonal is shown in red. Only points to the right/above the red line satisfy the ASTM standard for minimum distance from the sample edge. Raw data for profiles are shown in Chapter 4, Figure 13.

At a heat treatment temperature of 700°C, as shown in Figure 3, the reduction in hardness with longer heat treatments can be seen at distances >2.5x the indentation diagonal from the edge, in addition to the reduction in peak microhardness. The trend continues during heat treatment at 750°C, shown in Figure 4.

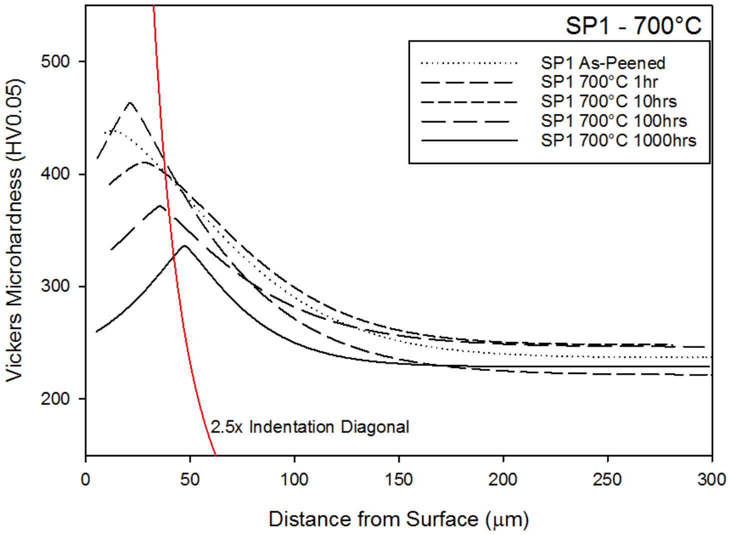

Figure 3 - Microhardness profiles of SP1 after heat treatment in vacuum at 700°C for 1, 10, 100 and 1000hrs. The distance from the sample edge corresponding to 2.5x the indentation diagonal is shown in red. Only points to the right/above the red line satisfy the ASTM standard for minimum distance from the sample edge. Raw data for profiles are shown in Chapter 4, Figure 15.

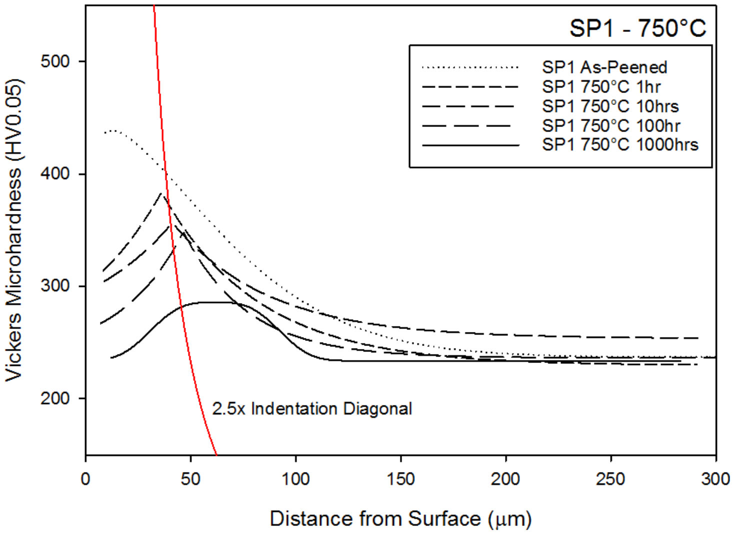

Figure 4 - Microhardness profiles of SP1 after heat treatment in vacuum at 750°C for 1, 10, 100 and 1000hrs. The distance from the sample edge corresponding to 2.5x the indentation diagonal is shown in red. Only points to the right/above the red line satisfy the ASTM standard for minimum distance from the sample edge. Raw data for profiles are shown in Chapter 4, Figure 16.

Therefore, although the peak microhardness values found by Vickers indentation microhardness testing are not representative of the actual peak microhardness values close to the sample edges, the trends in changing peak microhardness do mean something. The trends in changing peak microhardness values after heat treatments correspond to changes in hardness that are observed, more reliably, further from the edges of samples. The changes in peak microhardness can therefore be used to estimate the degree of recrystallization in the heat treated, shot peened material, as discussed in the following section.

6.2.2 Predicting Shot Peened Microstructure Lifetime

Section 2.5.4 described how the recrystallization of shot peened material can be estimated using (1).

$$X_R = \frac{H_0 - H_t}{H_0 - H_{ann}} \tag{1}$$

X_R = Fraction recrystallized
H_0 = Initial microhardness
H_t = Microhardness at time t
H_{ann}= Microhardness when fully annealed

This equation was modified to use the values of peak microhardness and to take values from the as-peened material as the initial values, as shown in (2).

$$X_R = \frac{H_0 - H_t}{H_0 - H_{ann}} \tag{2}$$

X_R = Fraction recrystallized
H_0 = Peak microhardness of as-peened material
H_t = Peak microhardness at time t
H_{ann}= Bulk microhardness of as-peened material

Figure 5 shows the recrystallized fraction of shot peened material when calculated using (2). The figure also includes the estimated fraction of recrystallization using the fitted trend lines of peak microhardness at 600, 650, 700 and 750°C that were found in section 4.1.4.1.

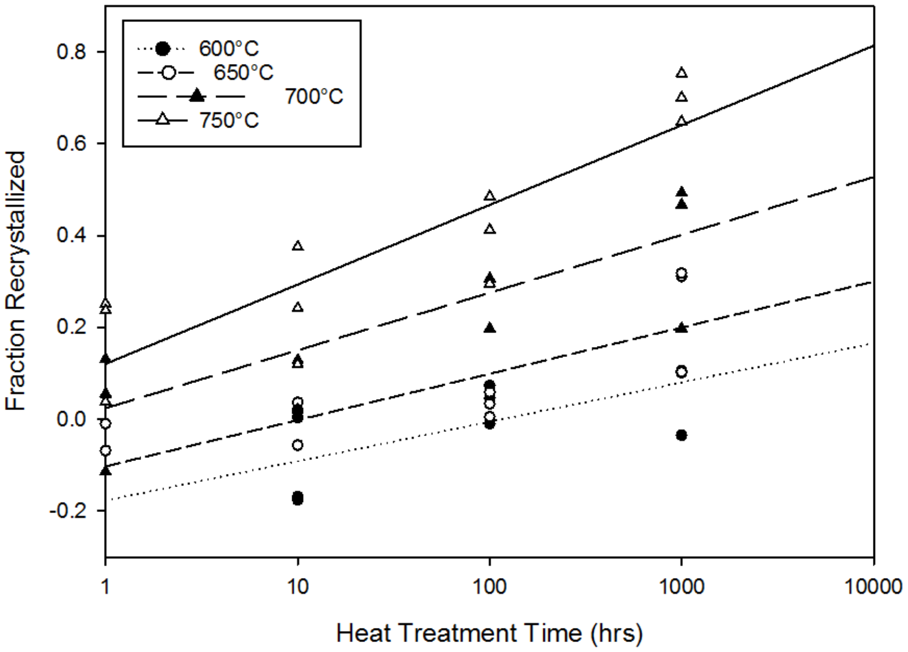

Figure 5 - Calculated fraction of recrystallized material using (2). Trend lines were plotted using fitted curves for peak microhardness (see section 4.1.4.1). Negative values for fraction recrystallized are invalid and are discussed in the text below.

Shot peened materials exposed to temperatures of 600°C and 650°C are predicted to recrystallize by <25% even after 10,000hrs. This suggests that the microstructure may still provide some improved fatigue and oxidation resistance after 10,000hrs. At 700°C and 750°C the predicted fraction of material recrystallized is significantly higher after 10,000hrs, at >40% and >70% respectively. The rate of recrystallization of the shot peened material is approximately doubled by increasing the heat treatment temperature by 50°C. This prediction is an extremely generalized view of the many changes to microstructure occurring during recrystallization, and no conclusions should be drawn on specific aspects of the microstructural changes. For example, it is not clear that this data could be used to predict changes in grain size to any meaningful accuracy.

The recrystallized fraction of material after heat treatment at 600°C and 650°C is given as <0% at some points, which is clearly incorrect. The negative values are caused by an initial increase in hardness during the first 1-10hrs of heat treatment at these temperatures, which is not accounted for in the model being used.

A possible cause of this increased peak microhardness is that the shot peened material heat treated at 600°C and 650°C underwent a phase transformation from austenitic steel to ferritic steel. The thermodynamic calculations in section 4.3.3 support the idea that such a change is possible, and the SAED and TKD observations of shot peened material heat treated at 700°C showed that some fraction of the shot peened surface was ferritic after heat treatment. Ferritic steel has a higher microhardness than austenitic steel of the same composition [3, 4], and so the change in peak microhardness reflected not only the increase in grain size during recrystallization, but also the change in phase. At 700°C and 750°C the ferritic phase of the steel was not thermodynamically stable and no initial increase in peak microhardness was observed. This behaviour is different from the observed increase in bulk microhardness, which occurred at all observed temperatures (600, 650, 700 and 750°C), including those at which ferrite was not stable.

If the initial increase in peak microhardness were to be taken into account in Figure 5 it would decrease the rate of recrystallization of the material at 600°C, 650°C and possibly at 700°C. However, it is not possible to isolate the contribution of the $\gamma \rightarrow \alpha$ transformation from the peak microhardness data without further experimental work.

In other studies that use microhardness to track the process of recrystallization, such as by Kalu & Waryoba [5], there are no phase changes to account for. The method used in this study is therefore not as applicable when studying meta-stable austenitic steels that can undergo phase transformations during experimental work.

6.3 Grain Size

The grain size of the SP1 and SP2 varied with depth according to (3) at depths greater than 10μm.

$$d = \frac{ax}{x+b} \qquad (3)$$

d = Grain size (μm)
x = Depth below shot peened surface (μm)
a = Bulk grain size found by regression (μm)
b = Constant found by regression (μm)

The fitted grain size profiles for as-peened SP1 and SP2 are shown in Figure 6. SP2 has smaller grains but the profiles are within the margin of error. Therefore, this data did not show a difference in the grain size profiles of SP1 and SP2 material. The similarity of both the grain size and microhardness profiles of the as-peened SP1 and SP2 suggest that their microstructures are equivalent within the margin of error for these tests.

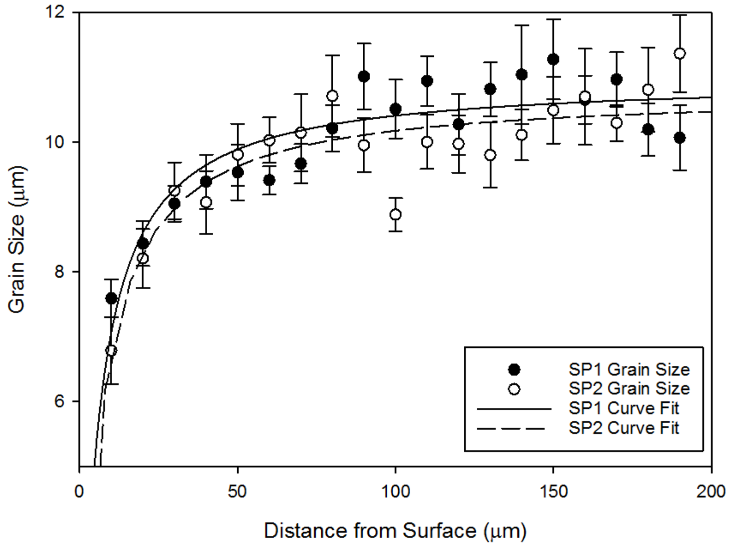

Figure 6 - Grain Size Profiles for SP1 and SP2. Error bars show standard error.

The bulk grain sizes observed directly by SEM are compared to the values found by regression of the grain size profiles in Table 1. Both the observed grain sizes and the calculated values of bulk grain size in SP1 and SP2 are within one standard error of each other. The error on the fitted data is an order of magnitude smaller than the error from direct observations.

Table 1 – Observed Grain Size and Grain Size Predicted by Regression in Bulk SP1 & SP2

	Observed Bulk Grain Size (µm)	**Calculated Bulk Grain Size (µm)**
SP1	10.4 ± 1.5	11.0±0.2
SP2	11.5 ± 1.9	10.8±0.2

The grain size profiles do not make use of data <10µm below the surface and the relationship in (3) could be further examined by using SEM or TEM observations of the region. This investigation did not pursue SEM observation of the region because of difficulties etching samples to highlight the grain structure. TEM observations were limited by the size and number of TEM foils that could be produced by in-situ lift-out. These issues could be overcome with further work.

At distances <10µm from the surface the TEM observations found differences in the grain sizes of as-peened SP1 and SP2. DF imaging failed to observe any grains $>10^{-2}\mu m^2$ in size in SP2, but found an area fraction of ≈34% of SP1 that was made of grains $>10^{-2}\mu m^2$ in size. Unfortunately, the sampled area of SP2 in the as-peened condition was very small and is unlikely to provide a representative view of grain size.

A larger area of the heat-treated SP1 and SP2 was observed in DF images than in the as-peened material, and so these findings are more robust. The heat-treated SP2 had a larger area fraction of grains $>1\mu m^2$ than both SP1 and SSP.

BF imaging and grain mapping of heat-treated SP1 is compared with DF imaging in Table 2. The BF imaging identified a similar grain size distribution to that via the DF methodology and sampled a larger area of material. However, when creating the grain maps using BF images it was more likely that grains $<10^{-4}\mu m^2$ would be missed due to the lower contrast between them and the adjacent grains. The BF and DF imaging methods used in this study can therefore complement each other, but both have limitations. A method that does not share the shortcomings of the BF & DF techniques would be EBSD mapping, provided a high enough resolution could be achieved. TKD could also be used to produce grain maps but in TEM foils the small grains that overlap each other in a 2D map would prevent indexing, similar to the lack of contrast in BF images.

Table 2 - Comparison of BF and DF results for area made up of different grain sizes of SP1 after exposure to vacuum at 700°C for 1000hrs.

Grain Size Lower Limit (um^2)	Grain Size Upper Limit (um^2)	Darkfield Area (um^2)	Darkfield Area Fraction	Brightfield Area (um^2)	Brightfield Area Fraction
0	10^{-5}	0.000	0%	0.00	0%
10^{-5}	10^{-4}	0.011	0%	0.00	0%
10^{-4}	10^{-3}	0.121	3%	0.07	0%
10^{-3}	10^{-2}	0.516	11%	5.09	7%
10^{-2}	10^{-1}	1.523	31%	30.34	43%
10^{-1}	1	2.692	55%	30.27	43%
1	10	0.000	0%	4.62	7%
Total:		4.864	100.0%	70.39	100%

A comparison of the grain sizes in as-peened and heat-treated SP1 and SP2 suggests that the SP2 material <10µm from the surface is more deformed than the same region in SP1, though >10µm below the surface the two materials have the same grain size profile. The more deformed region at the surface of SP2 provides a stronger driving force for recrystallization than in SP1, so heat-treatment causes SP2 to undergo recrystallization more rapidly than SP1 under the same conditions.

Further work could provide support for this hypothesis by comparing the fraction of ferrite/martensite in heat-treated SP1 and SP2. If SP2 undergoes more rapid recrystallization then it will have a higher fraction of ferrite/martensite after heat-treatment than SP1.

The results of DF imaging could not be used to produce grain-size profiles vs depth because of the small number of grains sampled. The grain maps generated with BF imaging were more suited to this purpose, though the intercept method suffered from the 3D nature of the TEM foils. The intercept method assumes that the images are a 2D view of a flat plane of material and TEM foils can approximate this for large grain sizes. However, when grains are small enough multiple grains can appear stacked on top of one another and create additional grain boundaries in TEM images. The grain size identified by using the intercept method on TEM BF images is therefore likely to be an underestimate when used to analyse shot peened material.

Furthermore, TEM foils created by FIB in-situ lift-out can vary in thickness as a function of distance from the upper surface. The final thinning steps use a FIB that is positioned above the foil and directed perpendicular from the original surface, as shown in Figure 7.

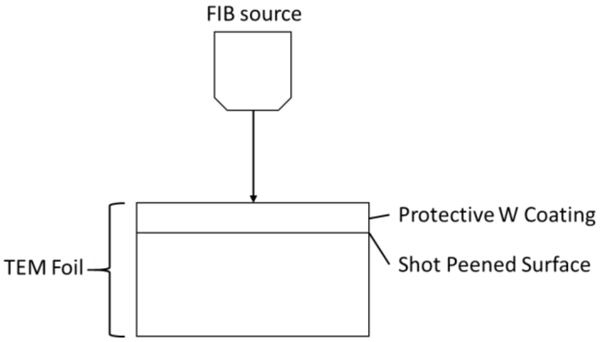

Figure 7 - Orientation of the TEM foil and FIB for final polishing

The shot peened surface is thinned more than material further down. This preferential thinning would result in grain size being underestimated at greater distances from the surface. It is possible that the grain size profile of heat treated SP1 was effected by these limitations of the intercept method. The grain size profile is reproduced here for ease of reference as Figure 8.

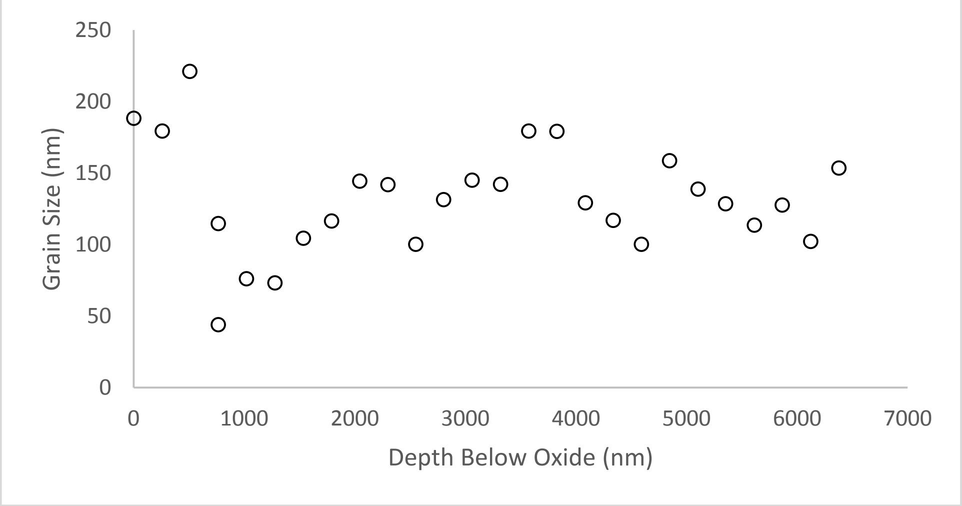

Figure 8 - Grain Size Profile of SP1 after heat-treatment in vacuum at 700°C for 1000hr. The data is based on intercept analysis of a grain map produced from TEM-BF images. Depth is relative to the metal/oxide interface

In Figure 8 the grain size from the metal/oxide interface to ≈500nm is significantly larger than the grain size at a depth of ≈1000nm. This is not the result of a shortcoming of the intercept method and will be discussed in a later section. Between a depth of 500-1500nm the grain size is at its lowest values and it is likely over-estimated; as discussed previously, BF images are unlikely to resolve grains so small due to the contrast mechanism. At a depth of 2000-6000nm the grain size varies between 100-150nm without a clear trend. If the factors that are expected to affect BF imaging and the intercept method are taken into account then Figure 8 would have the form shown in Figure 9. This is closer to the grain size seen in the SP1 exposed to steam, with the exception of the large grains close to the metal/oxide interface. However, the modified grain size profile is only an estimate and further work to confirm the assumptions made would be necessary.

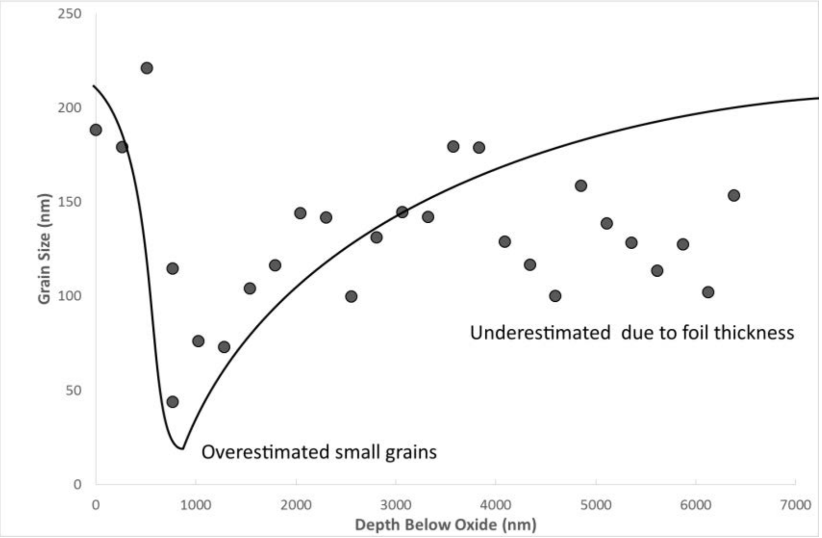

Figure 9 – Estimated plot of grain size based on Figure 8 and corrections for bias caused by BF imaging and analysis techniques

In SP1 exposed to atmospheric steam at 700°C for 1000hrs it was found that the grain size profile could be modelled by (4) to a depth of ≈6µm using data from TEM observations.

$$d = 0.028D + 93.1 \qquad (4)$$

d = grain size (nm)
D = distance from metal/oxide interface (nm)

SEM observations of the grain size of as-peened SP1 began at ≈10µm from the shot peened surface and were described previously. The two data sets are plotted in Figure 10 using logarithmic scales to aid comparison.

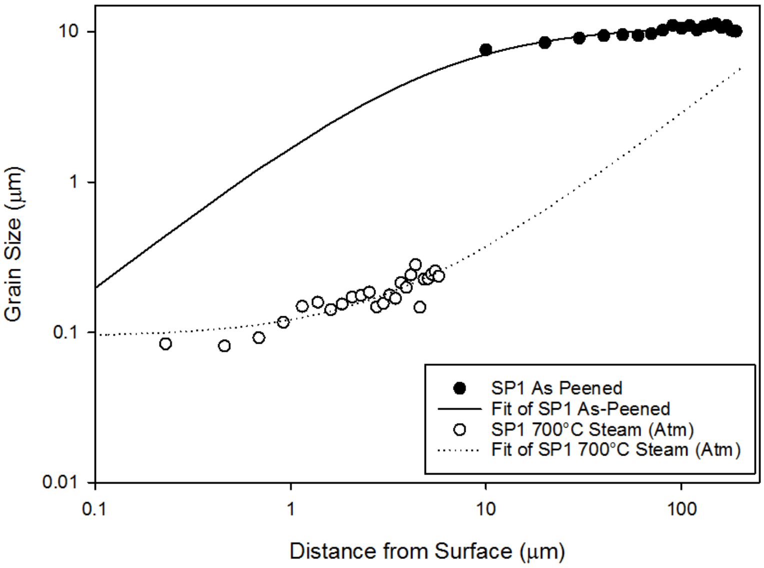

Figure 10 - Grain sizes of as-peened SP1 identified by SEM and grain sizes of SP1 exposed to atmospheric pressure steam at 700°C for 1000hrs identified by TEM. The data are from sections 4.2.2 and 4.2.3 respectively.

The difference between the predicted trends and observations show that the grain size is changing more rapidly than predicted 6-10µm from the shot peened surface. A more conclusive grain size profile could be made by creating TEM foils from this region. TEM foils could also be taken from material >10µm from the shot peened surface to compare TEM and SEM observations. Unfortunately, such TEM foils were not made in this study due to time constraints.

6.3.1 Large grains at the metal/oxide interface

After heat treatment for 1000hrs at 700°C all of the shot peened materials showed a significant growth of the grains at the metal/oxide interface compared to the as-peened material, and different from the grains >500nm below the interface, such as in Figure 9. In SP1 exposed to high pressure steam the grains at the metal/oxide interface are also much larger than in as-peened SP1, but there was not a layer of smaller grains further below the surface. SP1 exposed to atmospheric pressure steam developed grains of approximately the same size as the fine oxide grains, showing no evidence of grain enlargement at the metal/oxide interface.

The difference between the fine grain and large grain structure of the SP1 exposed to steam is discussed in section 6.4 and may be caused by a difference in cooling rate. However, this does not explain the large grains observed at the metal/oxide interface in heat-treated samples.

The two primary differences between the heat-treated and steam exposures were the oxygen partial pressures and the presence of water. If either of these factors is responsible for the difference in recrystallization behaviour then it could be related to oxide pinning. Internal oxides would slow down the rate of grain growth, particularly during primary recrystallization. The finer grains present after steam exposure could hypothetically be caused by a more rapid formation of internal oxides because of the higher P_{O2} or the presence of water accelerating oxidation, the latter of which is observed in the literature (see sections 2.7.5 and 2.7.6).

However, no internal oxides were observed using either TEM or TKD in this study. In order to investigate the hypothesis that oxide pinning is responsible for the larger grains, it would be necessary to look for very fine oxides in the shot peened material before and after heat treatment/steam exposure.

6.4 Austenite/Ferrite Content

The literature firmly establishes that austenitic stainless steels undergoing stress and strain can undergo martensitic transformation, which by definition creates 'martensite'. However, some of the resultant martensite shares the same structure as ferritic iron and this leads to a question of the difference between martensite and ferrite in recrystallization studies. For example, in the work of Guy et al. [6], it is shown that the DIM content in 18/8 and 18/12 steels increased when the materials were heated at 400°C. However, the phase transformation of austenite to ferrite by diffusional processes is not a martensitic transformation. DIM can also include small amounts of ε-martensite (hcp), while martensite created by the rapid cooling of carbon-rich steels has a bct structure and delta/sigma-phase iron is bcc, so there is a possible overlap of many different phases when referring only to the crystal structure. In the context of this thesis, martensite always refers to a bcc structure identical to ferrite, and the terms martensite and ferrite may be used interchangeably.

SAED and TKD mapping of as-peened SP1, SP2 and SSP showed that the shot peened surface to a depth of ≈5µm was fully austenitic. According to the literature, shot peened austenitic steels contain upwards of 70% DIM at the surface, so the metal tubes must have undergone further processing after shot peening and before being received. DIM reverts to austenite at temperatures >400°C and work with cold-rolled 304 steels shows 99% of the DIM can undergo reversion in less than a minute at temperatures >800°C. Unfortunately, it is not possible to know the temperatures or time scales of the post-shot peening processing that are responsible here for the DIM reversion; shot peening in industry is often performed under conditions of trade secrecy.

After heat-treatment at 700°C for 1000hrs the shot peened materials contained both austenite and ferrite. TKD mapping showed that the heat-treated SP1 and SP1 exposed to atmospheric-pressure deoxygenated steam for 1000hrs at 700°C were primarily composed of γ. SP1 exposed to 70bar deoxygenated steam was mostly α.

The thermodynamic simulations for DMV304HCu steel (see section 4.3.3) did not predict this because ferrite was found to be thermodynamically unstable at 700°C. However, the structure could have changed during cooling from 700°C, or the heat treatment temperature of the sample could have been lower than expected. If the temperature was responsible for the differences in α-content then the SP1 exposed to high-pressure steam must have either been held at a lower temperature than the heat treatments or cooled more slowly. The oxide layer grown in high-pressure steam was thicker than the oxide layer grown in atmospheric pressure steam so it is unlikely that the high-pressure steam temperature was significantly cooler than the atmospheric pressure exposures. Further evidence for the cooling rate being responsible for the higher α content is that there was less fine-grained material in the high-pressure steam exposures. A slower cooling rate can allow larger grains of α to form throughout the shot peened region before the temperature is too low to allow further recrystallization. In the heat-treated material, the cooling rate was higher and so the γ→α transformation was halted at an earlier stage when the grains were still very fine.

6.4.1 Effects of γ→α Transformation on Oxidation

The diffusion rate of cations through α is higher than through γ. In models of the oxidation of austenitic stainless steels this must be taken into account if the material is held below or near 627°C (900K), the point at which ferrite is able to form in austenitic material. The α fraction of a 304 steel can reach up to ≈80% according to thermodynamic calculations, as shown in section 4.3.3. The rate at which a material recrystallizes to form α will be dependent on not only the chemical composition, but the grain size, presence of precipitates, and possibly the DIM content. In shot peened material the grain size is sufficiently small to accelerate the recrystallization of γ, and the initial DIM content may provide nucleation sites for α to grow, reducing the nucleation time.

In SP1 exposed to high-pressure steam at 700°C the α content was observed to be higher than in heat-treated samples of SP1. This factor is a possible explanation for the Fe-rich spinel that grew on the SP1 exposed to high-pressure steam, but not on SP1 in atmospheric pressure steam. Unfortunately, it is not yet possible to confirm that the high α content is responsible for the increased rate of Fe diffusion to the oxide/gas interface, or if both were caused separately by a difference in exposure conditions. More work on the recrystallization of SP1 is needed to isolate the cause of the high α content and any differences in sample treatment that could have affected the oxide layers because the high-pressure exposure was carried out at NPL without the author being present.

6.5 Oxide Thermodynamics

The EDX and TKD data taken from heat-treated SP1 showed that a uniform layer of $MnCr_2O_4$ had grown at the metal/gas interface after 1000hrs in vacuum at 700°C. The low partial pressure of oxygen in the vacuum produced a slowly growing oxide and matched the thermodynamic calculations that showed that $MnCr_2O_4$ would be the most stable oxide present if there was Mn in the steel. Traces of silicon oxide were present and this would be expected in areas with sufficient Si because SiO_2 is more stable than both chromia and $MnCr_2O_4$ (see section 5.1, Figure 1). Chromia was detected in SAED patterns in very small amounts which lends support to the predicted mixed chromia/$MnCr_2O_4$ phase (see section 5.1, Figure 3) in a low oxygen environment.

SP1 grew a mixture of chromia and $MnCr_2O_4$ when oxidized in atmospheric pressure steam at 700°C for 1000hrs. SAED patterns and DF imaging showed that the oxides were not separated into discrete layers, so the oxide growth was not only controlled by the relative thermodynamic stability of the oxides, as observed in the heat-treated samples. The steam-oxidized samples were growing oxide based on the diffusion rate of ions into and out of the material and were not in thermodynamic equilibrium.

SP1 oxidized in 70bar steam formed a chromium-rich oxide at the metal/oxide interface which appeared to be chromia, with less spinel mixed in with it than on SP1 oxidized in atmospheric steam. Above this chromia layer a layer of Fe-Mn oxide grew, which SAED patterns showed is spinel. The higher pressure steam increased the amount of Fe observed above the chromium-rich oxide layer. The presence of Fe invalidated the use of Mn-Cr-O phase diagrams to predict the stable oxides and required Cr-Fe-Mn-O phase diagrams to be used instead. The author was unsuccessful in calculating Cr-Fe-Mn-O phase diagrams with Thermo-Calc and did not find any published phase diagrams of this system. Figure 11 and Figure 12 show related phase diagrams taken from the literature; they suggest that the oxides formed from Mn, Fe and O in this study would be expected to be made primarily of spinel with some corundum-type (M_2O_3) and halite-type (MO) oxides possible.

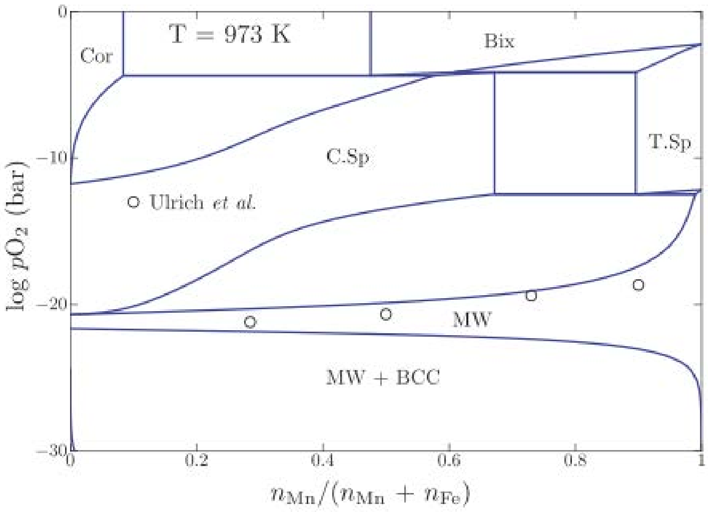

(a) T = 973 K

Figure 11 - Phase diagram of the Fe-Mn-O system. MW = (Fe,Mn)1-xO. C.Sp = fcc spinel. T.Sp = tetragonal spinel. Cor = corundum. Bix = Bixbyite. BCC = bcc metal. Taken from [7].

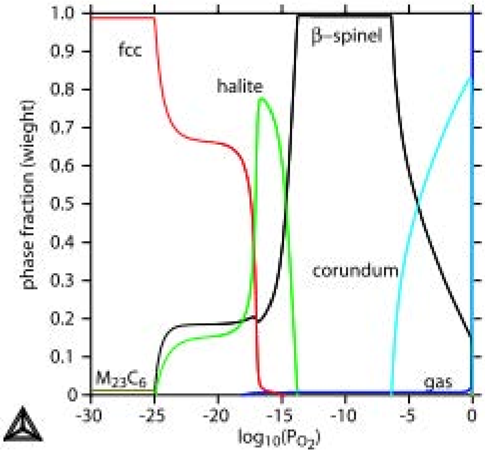

Figure 12 - Phase diagram for austenitic steel (17.8% Mn, 9.5% Cr, 1.0% Ni, 0.27% C, balance Fe) at 900°C. Taken from [8].

The oxides formed on SP1 exposed to deoxygenated steam vary between the atmospheric pressure exposures and the 70bar exposures. The two most likely causes of this are the difference in partial oxygen pressure and a difference in temperature caused by the calibration of the experiments. However, the possibility of the higher α content of the sample, compared to other steam exposures, causing an enhanced rate of Fe transport was discussed in 0.

If the temperature of the atmospheric steam was lower than the temperature of the 70bar steam then the diffusion rates of all of the alloy components would be higher in the 70bar steam. This could allow Fe to pass through the protective chromia layer more quickly, but it would also increase the diffusion rates of Mn and Cr. It is therefore not clear how such a different group of oxides would form because of a small difference in temperature in this system.

The partial pressure of oxygen in the 70bar steam will theoretically be higher than in atmospheric pressure steam, assuming that they have the same fraction of oxygen in the steam after deoxygenation. Figure 12 shows that if $\log_{10}(p_{O2})$ is increased from -10, where the spinel is dominant, to -5, the stability of corundum is increased. The chromia layer could therefore be more stable when grown in high pressure steam and contain less $MnCr_2O_4$ than oxides grown in atmospheric pressure steam. This could explain the low Mn content/Cr-enrichment of the oxide grown at the metal/oxide interface in high pressure steam, but it does not clarify how more Fe passes through the chromia layer.

6.6 Oxide Layer Thickness

In both heat-treated and steam oxidized samples of shot peened material, no significant internal oxidation was observed. The heat-treated samples showed outward, columnar growth of $MnCr_2O_4$ of 150-250nm thickness.

SP1 oxidized in atmospheric pressure steam grew an oxide layer of 482.5nm thickness composed of fine and coarse-grained regions. The oxide was a mixture of chromia and $MnCr_2O_4$ in both coarse-grained and fine-grained areas; the size of the grains was not simply a function of their chemical composition. However, the oxide layer was up to twice as thick in coarse-grained regions compared to the fine-grained oxide layer.

The difference in oxide thickness between fine and coarse-grained regions is likely caused by a lower availability of Cr in the coarse-grained material. In fine-grained regions the grain boundary diffusion enhances the Cr flux sufficiently to create a chromia layer and to prevent any internal oxidation. In coarse-grained areas the Cr flux is lower and the chromia layer will contain more $MnCr_2O_4$. The diffusion rate of Cr and Mn will be enhanced in areas containing more spinel, allowing oxide to form at the oxide/gas interface and grow outwards more rapidly.

SP1 oxidized in deoxygenated steam at 70bar was 520nm thick and composed of the fine-grained oxide seen in the SP1 exposed to atmospheric pressure steam with a thinner layer of Fe and Mn rich oxide at the oxide/gas interface. Whiskers of chromia encased in the Fe-Mn oxide grew on the oxide surface.

The relative thicknesses of the oxide layers are heat-treated < atmospheric pressure steam < 70bar steam, which is the expected behaviour of a 304 stainless steel based on the literature. The rate of oxidation was much lower in shot peened 304 than in coarse-grained 304, and SP1 did not suffer from any internal oxidation after 1000hrs at 700°C in steam, which was seen in the wet-air experiments of Halvarsson et al [9] after only 168hrs at 600°C.

6.7 Modelling Oxidation Behaviour

Essuman et al. [10] used (5), below, to calculate the molar fraction of Cr in the alloy that is required to prevent internal oxidation. (6) was used to calculate the molar fraction of Cr that must be present to form a protective chromia layer on the metal/gas interface. A number of limitations of the model were discussed in section 2.7.3.1, but the model is still useful in order to identify some key variables and to discuss their effects.

$$N_{Cr}^{(1)} > \left[\frac{\pi g^*}{3} N_O^{(S)} \frac{D_O V_m}{\widetilde{D}_{Fe-Cr} V_{CrO_{1.5}}}\right]^{\frac{1}{2}} \qquad (5)$$

$N_{Cr}^{(1)}$ = Molar fraction of Cr in alloy
$N_O^{(s)}$ = Oxygen solubility in alloy
D_O = Diffusivity of oxygen in alloy (cm^2/s)
$\widetilde{D}_{Fe-Cr}$ = Alloy interdiffusion coefficient (cm^2/s)
V_m = Molar volume of alloy
$V_{CrO_{1.5}}$ = Molar volume of oxide
g^* = factor, approximated to 0.3

$$N_{Cr}^{(2)} = \frac{V_m}{32 v_O}\left(\frac{\pi k_p}{\widetilde{D}_{Fe-Cr}}\right)^{\frac{1}{2}} \qquad (6)$$

$N_{Cr}^{(2)}$ = Molar fraction of Cr in alloy
$\widetilde{D}_{Fe-Cr}$ = Alloy interdiffusion coefficient
V_m = Molar volume of alloy
v_O = Molar volume of oxide
k_p = parabolic rate constant (in terms of scale thickness) (cm^2/s)

6.7.1 Effect of Shot Peened Material Grain Size on Oxidation

Shot peening changes the value for $\widetilde{D}_{Fe-Cr}$ by changing the ratio of GB to bulk material. The effective interdiffusion coefficient can therefore be expressed in its simplest form by (7).

$$\widetilde{D}_{Eff} = V_t^{IC}\widetilde{D}_{Fe-Cr}^{GB} + (1 - V_t^{IC})\widetilde{D}_{Fe-Cr} \qquad (7)$$

$\widetilde{D}_{Eff}$ = Effective alloy interdiffusion coefficient
V_t^{IC} = Grain boundary volume fraction
$\widetilde{D}_{Fe-Cr}^{GB}$ = Alloy interdiffusion coefficient of Cr in Fe GB
$\widetilde{D}_{Fe-Cr}$ = Alloy interdiffusion coefficient of Cr in Fe Matrix

$\widetilde{D}_{Eff}$ was calculated with (7) for a range of grain sizes and temperatures and this is shown in Figure 13. This can be used to predict the qualitative change in N_{Cr}^{Crit} with changing grain size even if the other variables in (7) are not known. The Relative $N_{Cr}^{(2)}$ line in Figure 13 shows how $N_{Cr}^{(2)}$ changes when grain size is changed, but all other values in (6) are kept constant. Relative $N_{Cr}^{(2)}$ was set to 1 at a grain size of 10μm, representing the bulk grain size, and was then calculated for different grain sizes. Under these assumptions (7) predicts that shot peening will reduce the fraction of Cr required to form a protective chromia layer by ≈50x.

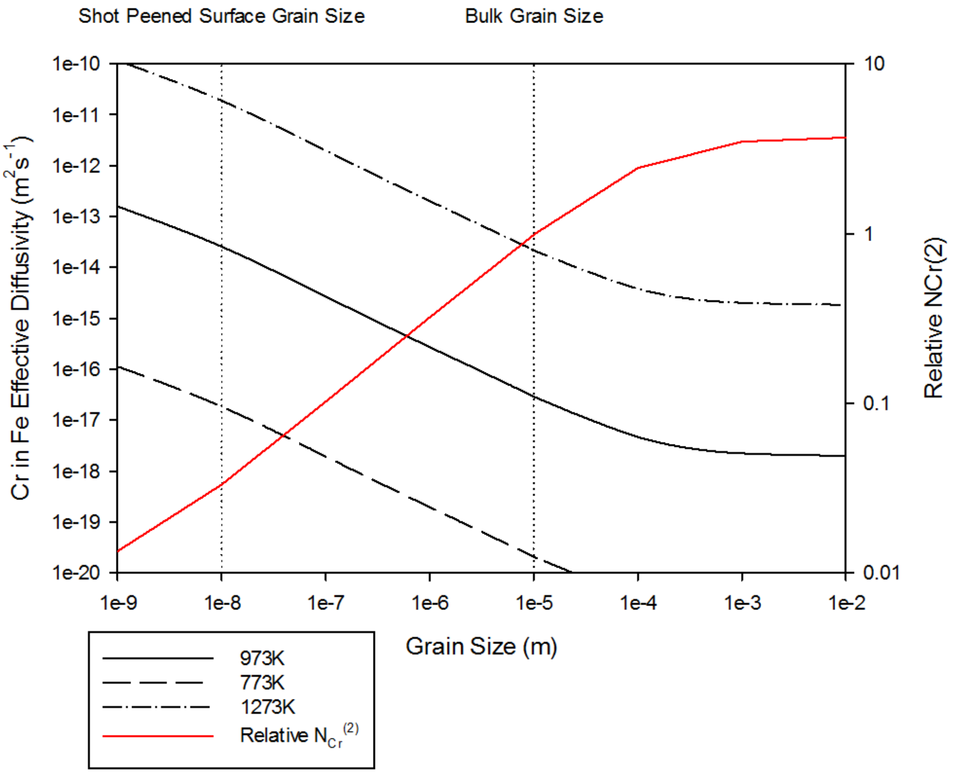

Figure 13 - Effective Diffusivity of Cr in Fe. Relative $N_{Cr}^{(2)}$ *shows the change in* $N_{Cr}^{(2)}$ *if grain size is changed by setting Relative* $N_{Cr}^{(2)} = 1$ *at a grain size of 10µm (Bulk grain size). Reducing the grain size from 10µm to 10nm causes a reduction in Relative* $N_{Cr}^{(2)}$ *of ≈50x*

Such a model of effective diffusivity is too simple to provide predictive results because it neglects the effects of 'segregation' in the grain boundaries. The GB diffusivity is usually described using the Fisher model, as discussed in section 2.6.2. Using the Fisher model, GB diffusivity is given in units of $s\delta D_b$, were δ is the grain boundary width, D_b is the enhanced diffusion rate within the GB and s is the segregation factor that accounts for impurities in the GB. In pure metals s=1, but this assumption cannot realistically be made for 304 steel. Each element diffusing through the alloy will have a different segregation factor, which will also be affected by the concentration of the other elements in the GB. There are diffusion models capable of predicting Cr diffusion in a simple austenitic steel such as that of Hansson et al [11], but these are outside the scope of this thesis.

This study has also shown that the oxide layer grown on SP1 is a mixture of chromia and spinel instead of pure chromia. The relatively high diffusivity of $MnCr_2O_4$ will change $\widetilde{D}_{Eff}$ in ways that are not taken into account in models that assume a pure chromia layer is formed.

6.8 Role of Manganese

Mn is included in commercial 304-grade steels in amounts up to 2wt%, but DMV304HCu and Super304H contain less than half of this (≈0.8wt%). Despite the relatively small Mn content in the materials it has a significant effect on the oxide growth and cation diffusion processes. The oxides grown on DMV304HCu in the first 1000hrs of exposure had Mn as a key component in both wet and dry environments and such a role suggests that further research is needed that focuses on Mn-content. There are two fundamental roles that Mn plays in SS oxidation; altering the diffusion rates of Cr and Fe in the alloy/oxides and changing the oxides grown.

This study cannot bring any new information to light on the diffusion rates of the elements in the alloy matrix, but it does highlight the different oxidation behaviour of Mn-containing alloys when compared to model Fe-Cr alloys investigated in the literature. In the work of Essuman et. al [10] the Fe-Cr alloys formed a chromia layer at the initial gas/metal interface at 900°C in dry atmospheres and this was protective enough to prevent or greatly slow any other oxide growth. The only other oxides observed in the study were Cr-Fe spinels, Fe_2O_3 and Fe_3O_4. The outward growth of Fe_2O_3 and Fe_3O_4 were controlled by the presence of a chromia layer, while Fe-Cr spinel grew inwardly if water was present in the atmosphere. The outward growth of iron oxides is to be expected because Fe cations diffuse more quickly through chromia than do Cr cations. If the rate of oxygen diffusion increases beyond the ability for Cr to migrate to the oxide/metal interface, Fe will oxidize internally and form the observed Fe-Cr spinels, which are much less protective and further accelerate oxidation and diffusion.

Using the model of chromia formation in (6) is less valid in a system containing Mn because it will not form only chromia at the surface. The protective oxide layer will consist of both chromia and $MnCr_2O_4$ and this will need to be taken into account. The simplest case is assuming that there is already enough Mn available at the surface to form $MnCr_2O_4$, so only the diffusion of Cr is considered, just as in the original model. The changes to (6) are that V_O becomes the molar volume of $MnCr_2O_4$ instead of chromia, given in Table 3, and the value for K_p is for the growth of $MnCr_2O_4$.

Table 3 - Molar mass and molar volume of chromia and $MnCr_2O_4$

	Molar Mass (g/mol)	**Density (g/cm^3)**	**Molar Volume (cm^3/mol)**
Cr_2O_3	152	5.22	29.1
$MnCr_2O_4$	223	4.80 [12]	46.4

The molar volume of $MnCr_2O_4$ is almost twice that of chromia so if $MnCr_2O_4$ is grown instead of chromia it will decrease the value $N_{Cr}^{(2)}$ by ½ if all other values are the same. The rate of oxide growth is likely to vary between the oxides, but Mn will be beneficial as long as the condition $K_P(MnCr_2O_4) < 4K_P(Cr_2O_3)$ is met and sufficient Mn can reach the metal/gas interface.

Conversely, the presence of Mn could be detrimental to the formation of a chromia layer if $K_P(MnCr_2O_4) > 4K_P(Cr_2O_3)$. If this were the case then more Cr would be required to form the oxide layer than in the case of a pure chromia layer. Unfortunately, the author has not located any K_p values for $MnCr_2O_4$ growth on stainless austenitic steels and does not have enough data points from this study to calculate them.

This model suggests that the Mn could be able to reduce the critical Cr concentration in the alloy needed to grow a protective oxide layer. However, in order to take on this role the flux of Mn must be high enough to enhance the Mn concentrations at the metal/oxide interface and the parabolic rate constant of the oxide layer must remain less than 4x the value for pure chromia.

The rate of diffusion of Mn in the shot peened material was enough to allow a layer of $MnCr_2O_4$ to grow in a vacuum at 700°C. However, the oxide layers grown on material oxidized in steam was more chromia rich, which may be the result of a faster growth rate and a limited supply of Mn. A detailed model of the diffusion of the various elements in the shot peened region of the steel is outside the scope of this work, but a rough calculation can be made to estimate the availability of Mn to an oxide growing on the steel surface.

The diffusivity of Mn in the bulk of stainless steel at 700°C was given as $2.51 \times 10^{-15} cm^2s^{-1}$ (see section 2.6.1, Table 12). This can be used with (8) to find the diffusion length of Mn in the material for different time scales, which approximates the distance travelled by Mn atoms in the material by diffusion .

$$x \approx \sqrt{Dt} \qquad (8)$$

x = Diffusion length (cm)
D = Diffusivity (cm^2s^{-1})
t = Time (s)

On a $1cm^2$ area of the steel surface, the number of moles of oxide in the oxide layer is given by (9). This is also the number of moles of Mn that must diffuse from the steel alloy to grow a layer of $MnCr_2O_4$. SP1 contains 0.8%(wt) Mn and has a density of ≈8g/cm^3. This gives a density of Mn in the SP1 alloy of 0.064g/cm^3, or 1.2×10^{-3}moles/cm^3.

$$Y = \frac{X}{46.4cm^3mol^{-1}} \qquad (9)$$

X = Thickness of $MnCr_2O_4$ oxide layer (cm)
Y = Moles of $MnCr_2O_4$ (per cm^2)

Therefore, the growth of an oxide layer will require that Mn diffuses through the steel for at least the distance given in (10), or there will not be enough Mn available. This value can then be compared to the estimated diffusion length of Mn.

$$Z = \frac{X}{46.4cm^3mol^{-1}} \times \frac{1}{1.2 \times 10^{-3}mol\ cm^{-3}} \qquad (10)$$

$$Z \approx 18 \times X$$

X = Thickness of $MnCr_2O_4$ oxide layer (cm)
Z = Minimum diffusion length for Mn (cm)

The oxide grown on SP1 heat treated in a vacuum at 700°C for 1000hr was ≈200nm thick. The required diffusion length would therefore be of the order 3.6µm. The oxide grown on SP1 exposed to atmospheric steam at 700°C for 1000hrs was ≈500nm thick, which would require a diffusion length of the order 9µm.

The diffusion length calculated using (8) for SP1 exposed to temperatures of 700°C for 1000hrs is ≈1µm. This suggests that the diffusion rate of Mn in bulk SP1 would not be high enough to allow the growth of an $MnCr_2O_4$ layer. This finding explains the absence in the literature of $MnCr_2O_4$ layers being seen in oxidation studies of Mn-containing stainless steels that are neither peened nor extremely fine-grained.

The minimum diffusion lengths calculated for SP1 in vacuum and steam environments were 3.6µm and 9µm respectively. These values are of the same order of magnitude as the distance from the surface of peak microhardness in the as-peened materials. This region consists of much smaller grains than in the bulk of the steel and so has a higher proportion of grain boundaries. As discussed in section 2.6.2, the diffusion rate of material in grain boundaries can be several orders of magnitude higher than in the bulk. This provides a more rapid diffusion pathway for the Mn close to the surface of shot peened material to travel to the metal/oxide interface.

However, the diffusion length estimates suggest that the Mn in the shot peening affected region will not be replaced by Mn from the bulk of the material as quickly as it is being incorporated into the oxide. Therefore, the Mn present in the shot peening affected region of the steel surface is likely to be depleted by oxide formation, if the oxidation rates remain high enough. $MnCr_2O_4$ and chromia are protective oxides and would be expected to grow with a parabolic rate (see section 2.7.3). It is therefore possible that, if the rate of oxide growth was low enough at longer time scales (>>1000hrs), the Mn content of the shot peened region could recover. The oxide thickness was only observed for samples oxidized for 1000hrs in this study, so it is outside the capabilities of this study to estimate which of these scenarios are applicable for a given exposure temperature or time.

When the shot peened region undergoes recrystallization, the metal grains will grow and the grain boundaries that act as diffusion shortcuts will become less common. Therefore, the rate of Mn diffusion to the steel surface will be reduced by the recrystallization of the shot peened material. It is therefore a possibility that the $MnCr_2O_4$ oxides observed in this study will not be able to form in significant amounts after the shot peened region of the material is either depleted of Mn or recrystallized. This will have an effect on the lifetime of shot peened components if the growth of an $MnCr_2O_4$ layer is found to significantly affect their oxidation rate. Unfortunately, this study is unable to provide an answer to the question of how beneficial (or otherwise) $MnCr_2O_4$ formation is to the oxidation performance of shot peened austenitic stainless steels.

6.9 References

1. Chi, C., Yu, H., Dong, J., Liu, W., Cheng, S., Liu, Z., & Xie, X. (2012). The precipitation strengthening behavior of Cu-rich phase in Nb contained advanced Fe–Cr–Ni type austenitic heat resistant steel for USC power plant application. *Progress in Natural Science: Materials International*, *22*(3), 175–185. doi:10.1016/j.pnsc.2012.05.002

2. Ou, P., Xing, H., Wang, X. L., & Sun, J. (2014). Tensile yield behavior and precipitation strengthening mechanism in Super304H steel. *Materials Science and Engineering A*, *600*, 171–175. doi:10.1016/j.msea.2014.01.085

3. Argandoña, G., Palacio, F. J., Berlanga, C., Biezma, V. M., Rivero, J. P., Peña, J., & Rodriguez, R. (2017). Effect of the Temperature in the Mechanical Properties of Austenite, Ferrite and Sigma Phases of Duplex Stainless Steels Using Hardness, Microhardness and Nanoindentation Techniques. *Metals* , *7*(6). doi:10.3390/met7060219

4. Wang, X., Yang, X., Guo, Z., Zhou, Y., & Song, H. (2007). Nanoindentation Characterization of Mechanical Properties of Ferrite and Austenite in Duplex Stainless Steel. In Chang, YW and Kim, NJ and Lee, CS (Ed.), *ADVANCED MATERIALS AND PROCESSING* (Vol. 26–28, p. 1165+). KREUZSTRASSE 10, 8635 DURNTEN-ZURICH, SWITZERLAND: TRANS TECH PUBLICATIONS LTD. doi:10.4028/www.scientific.net/AMR.26-28.1165

5. Kalu, P. N., & Waryoba, D. R. (2007). A JMAK-microhardness model for quantifying the kinetics of restoration mechanisms in inhomogeneous microstructure. *Materials Science and Engineering: A*, *464*(1–2), 68–75. doi:10.1016/j.msea.2007.01.124

6. Guy, K. B., Butler, E. P., & West, D. R. F. (1983). Reversion of bcc (alpha) martensite in Fe-Cr-Ni austenitic stainless steels. *Metal Science*, *17*(April), 167–176.

7. Kang, Y.-B., & Jung, I.-H. (2016). Thermodynamic modeling of oxide phases in the Fe–Mn–O system. *Journal of Physics and Chemistry of Solids*, *98*, 237–246. doi:10.1016/j.jpcs.2016.07.017

8. Kjellqvist, L. (2009). *Thermodynamic description of the Fe-C-Cr-Mn-Ni-O system*. KTH Stockholm.

9. Halvarsson, M., Tang, J., Asteman, H., Svensson, J., & Johansson, L. (2006). Microstructural investigation of the breakdown of the protective oxide scale on a 304 steel in the presence of oxygen and water vapour at 600°C. *Corrosion Science*, *48*(8), 2014–2035. doi:10.1016/j.corsci.2005.08.012

10. Essuman, E., Meier, G. H., Żurek, J., Hänsel, M., & Quadakkers, W. J. (2008). The Effect of Water Vapor on Selective Oxidation of Fe–Cr Alloys. *Oxidation of Metals*, *69*(3–4), 143–162. doi:10.1007/s11085-007-9090-x

11. Hansson, A. N., Hattel, J. H., Dahl, K. V, & Somers, M. A. J. (2009). Modelling Cr depletion under a growing Cr2O3 layer on austenitic stainless steel: the influence of grain

boundary diffusion. *Modelling and Simulation in Materials Science and Engineering*, *17*(3), 35009. doi:10.1088/0965-0393/17/3/035009

12. Parmelee, C. W., Badger, A. E., & Ballam, G. A. (1932). A study of a group of typical spinels. *University of Illinois Bulletin*, *29*(84). Retrieved from http://hdl.handle.net/2142/4420

7 Conclusions

The aims of this project were:

1. Estimate the lifespan of the shot peened microstructure in the industrially important 600-700°C temperature range
2. Characterize the oxides grown in deoxygenated steam on a 304HCu-grade stainless steel alloy
3. Characterize the oxides grown on the same alloys in high-pressure deoxygenated steam

7.1 Estimating the lifespan of the shot peened microstructure

Material from shot peened 304HCu grade stainless steel tubes was heat treated at 600-750°C for 1-1000hrs in vacuum. The shot peened microstructure was found to recrystallize at a rate linked to temperature, with higher temperatures causing faster recrystallization.

The recrystallization rate of shot peened 304HCu-grade stainless steel was predicted for exposures to temperatures of 600°C, 650°C, 700°C and 750°C using Vickers microhardness profiles. This information was used to estimate how much of the shot peened microstructure remains in shot peened material made of 304HCu during its life cycle. The applicability of this method was found to be questionable because of the presence of a phase change in the shot peened material on exposure to elevated temperatures.

Shot peened 304HCu-grade stainless steel was observed to undergo a phase change from austenitic (γ) steel to ferritic (α) steel during exposure to temperatures of 600°C and 650°C. This change increased the Vickers microhardness of the shot peened material.

The project aim of estimating the lifespan of shot peened microstructure in 600°C-700°C temperatures was therefore partially met using Vickers microhardness tests. However, the applicability of these results was questionable and models that are more suitable could be developed using other experimental results from this study.

The grain size of a heat-treated, shot peened 304HCu-grade stainless steel was found using TEM with a combination of darkfield imaging and brightfield imaging. A comparison of the two methods showed that darkfield imaging was more able to identify grains <1nm in size, but could only image a very small fraction of the available material. Brightfield imaging allowed many more grains to be included in the analysis, but processing the images into a useful form was extremely time consuming and suffered from bias introduced by TEM foil thickness and 3D structure.

Grain sizes increased during heat-treatment, but the grain size near the surface of a shot peened 304HCu-grade stainless steel that was heat treated for 1000hrs at 700°C was still <50nm. The same material that was oxidized in deoxygenated steam at atmospheric pressure for 1000hrs at 700°C had a grain size <100nm at the metal/oxide interface.

Shot peened 304HCu-grade stainless steel samples exposed to elevated temperatures in any atmosphere became a mixture of α and γ phases. The relationship between the sample processing and ratio of these phases is not yet known, but it is suggested that a higher fraction of α in samples exposed to high-pressure steam could have been caused by a slower cooling rate.

The predictions based on Vickers microhardness tests do not make use of grain size observations to estimate microstructure recrystallization. However, these observations could be used in further work to model oxidation and diffusion processes in these temperature ranges. Such models could also take into account the γ→α phase transformation that was observed in this work.

7.2 Characterization of Oxides

The project succeeded in characterizing the oxides grown on 304HCu-grade steel during the first 1000hrs at 700°C in deoxygenated steam at both atmospheric and high (70bar) pressure, in addition to the oxides grown in vacuum.

Samples of shot peened 304HCu-grade stainless steel that were heat treated in vacuum all showed the growth of $MnCr_2O_4$ at the metal/gas interface. The spinel was generally uniform in coverage and grew outwards from the surface as columnar grains.

Samples of a shot peened 304HCu-grade stainless steel exposed to deoxygenated steam at 700°C formed mixed phase oxides made of Cr_2O_3 and $MnCr_2O_4$. High-pressure steam caused the growth of Fe-rich spinel and Cr_2O_3 oxide whiskers on the oxide/gas interface. The behaviour of the material in high-pressure steam could theoretically be related to the higher ratio of α:γ of the material, or to Fe and/or O transport through the oxide layer being enhanced by the higher pressures.

Current oxidation models used to estimate the concentration of Cr required to prevent internal oxidation and breakaway oxidation are not suitable for use in industry standard austenitic stainless steels. Of particular importance, the presence of Mn in production steels enables the formation of $MnCr_2O_4$ and invalidates the assumption used in Wagner's model that only Cr_2O_3 and Cr diffusion rates are needed to predict oxidation behaviour.

The low Mn content of the 304HCu-grade steels used in this study (≈0.8%) may be insufficient to support the growth of $MnCr_2O_4$ at longer timescales (>1000hrs) or temperatures other than 700°C. This study does not have the information necessary to model the growth of $MnCr_2O_4$, as the oxide growth will be dependent on the diffusion rate of Mn from the steel to the metal/oxide interface. Calculating the diffusion rate of Mn through the shot peened region to the metal/oxide interface is complex and has not been undertaken here.

This study was not able to confirm if the growth of $MnCr_2O_4$ was beneficial or detrimental to the oxidation performance of shot peened 304HCu steel.

8 Further Work

One of the most limiting factors of this study was the number of TEM observations that could be made. TEM foils were prepared by FIB and as a result, a relatively small number of samples were made, only representing the as-peened 304HCu-grade stainless steels, and heat treatments/steam exposures at 700°C for 1000hrs.

If TEM foils were created from the oxidized surfaces of material exposed for different lengths of time, such as 1, 10 and 100hrs then the change in oxide layer thickness could be used to confirm if the oxide growth was parabolic. This data could also be used to find the parabolic oxidation constant (K_p) for the material, which would provide a way to predict the oxidation rate of the shot peened metal and compare it to other materials in the literature.

TEM samples were taken from materials exposed to a temperature of 700°C because it was expected that lower temperatures would grow a very small amount of oxide and make studying the material more difficult. However, it would be beneficial to make TEM foils of samples exposed to 600°C and 650°C in order to study the ratio of austenite/ferrite in the shot peened surfaces, as well as to gather more data on oxidation rates.

The literature did not include much discussion of the effects of $\gamma \rightarrow \alpha$ phase transformation of shot peened austenitic steels. However, this study has found that metastable 304HCu-grade austenitic steels can undergo a phase transformation to ferritic steel in shot peened regions when held at 600°C-700°C. This phase change alters the hardness of the shot peened region during heat treatments of only 1-10hrs. It should therefore be of interest to any industry using shot peened austenitic steel, as the mechanical performance of the shot peened material is being altered and may be affecting its oxidation performance.

Vickers microhardness tests did not show the same phase changes occurring in the bulk of the material, though thermodynamic calculations showed that such a change is energetically favourable. The larger grains and the lower residual stress/strain in the bulk of the metal may slow down the rate of phase transformation, possibly to the point of it being negligible. Further work could be undertaken to confirm the rate of $\gamma \rightarrow \alpha$ transformation in the bulk of the material using EBSD.

More generally, further studies are required of the diffusion rates of Fe, Cr and Mn in $MnCr_2O_4$ spinel. The diffusion rates are needed to inform oxidation models that can include both chromia and spinel growth and predict the chances of breakaway oxidation and internal oxidation. The current data in the literature is incomplete and does not include the 600-700°C temperature range, which is the range in which austenitic steels are being investigated for use in supercritical thermal plant.

More data on the oxidation rates of steels in supercritical steam are needed to improve oxidation models. K_p values are calculated from empirical tests and there has been relatively little work done in supercritical steam due to practical limitations. The effects of the following variables on oxidation rates in supercritical steam are still not known:

1. Steam temperature
2. Oxygen content
3. Pressure
4. Flow rate

Oxidation models of shot peened austenitic steel also require an improvement in understanding grain boundaries and grain boundary diffusion. The Fisher model used to describe grain boundary diffusion relies on finding the grain boundary thickness and the segregation factor, but it is unclear how reliably this can be done without extensive empirical testing. The Fisher model and its limitations are discussed in more detail in literature review section 2.6.2. A more developed model of GB diffusion could be key to making oxidation models more reliable and predictive for peened and cold worked materials.

Appendix A: Oxidation Studies by Atmosphere

A.1 Studies in ‘Wet’ Oxygen-Containing Atmospheres

Paper	**Material**	**Temp (°C)**	**Pressure**
(Huenert & Kranzmann 2011)	310N	500-700	Atm – 8MPa
(Rother et al. 2012)	T347	800	Atm
(Vangeli et al. 2013)	304H, 304L, 153MA, 253MA, 309S, 310S	900-1150	Atm
(Asteman et al. 2004)	153MA, 310, 353MA	700-900	Atm
(Asteman et al. 2002)	310	600	Atm
(Asteman et al. 2000)	304L	600	Atm
(Brady et al. 2012)	Fe-20Cr, 430	700-800	Atm
(Brady et al. 2011)	347, Fe-20Cr, AFA, 430	800	Atm
(Halvarsson et al. 2006)	304L	600	Atm
(Hansson et al. 2009)	347H	500-700	Atm
(Holcomb et al. 2004)	S304H + Ni alloys	700-800	Atm
(Huntz et al. 2007)	304, 439	850-950	Atm
(Jonsson et al. 2009)	Fe	500	Atm
(Lepingle et al. 2008)	Ferritic Steels	600-650	Atm
(Liu et al. 2008)	310	600	Atm
(Ostwald & Grabke 2004)	18Cr-10Ni, 20Cr-32Ni	600	Atm
(Othman et al. 2009)	Fe-Cr	700	Atm
(Othman et al. 2010)	Fe-Cr	600-950	Atm
(Peraldi & Pint 2004)	Model Fe-Ni-Cr Alloys	650, 800	Atm
(Pettersson et al. 2010)	Sanicro 28	600-800	Atm
(Quadakkers et al. 2009)	Fe-Cr	900	Atm
(Zengwu et al. 2011)	304H, HR3C	650	Atm
(Simms 2011)	P91,P92,304,347	600-700	Atm
(Ennis & Czyrska-Filemonowicz 2003)	9% martensitic steels	600-700	Atm
(Zurek & Quadakkers 2015)	Martensitic Fe, Ni alloys	600-750	Atm

A.2: Studies in Deoxygenated ‘Steam’ Atmospheres

Paper	**Material**	**Temp (°C)**	**Pressure**
(Sato et al. 2002)	SUS316	600-800	<10^{-22}atm
(Rosser et al. 2012)	S304H	600-700	Atm
(Betova et al. 2006)	316, P91	500-700	30MPa
(Penttilä et al. 2011)	316, P91	500-700	30MPa
(Penttilä et al. 2015)	Sanicro 28	650	25MPa
(Bischoff et al. 2013)	HCM12A, NF616	500	10.8MPa, 25MPa
(Zhu et al. 2016)	P92	600-700	25MPa

A.3: Studies in Air / Oxygen

Paper	Material	Temp (°C)	Pressure
(Botella et al. 1998)	304 + Mn-based alloy	700	Atm
(Li et al. 2012)	18Cr-11Ni-3Cu-3Al-MnNb	700-900	Atm
(Rother et al. 2012)	T347	800	Atm
(Vangeli et al. 2013)	304H, 304L, 153MA, 253MA, 309S, 310S	900-1150	Atm
(Wang et al. 2013)	SS304	900	Atm
(Zacchetti et al. 2009)	304	700-1200	Atm
(Asteman et al. 2004)	153MA, 310, 353MA	700-900	Atm
(Asteman et al. 2002)	310	600	Atm
(Asteman et al. 2000)	304L	600	Atm
(Brady et al. 2012)	Fe-20Cr, 430 (ferritic)	700-800	Atm
(Naraparaju et al. 2012)	18-8, 12Cr-steel	750	Atm
(Sabioni et al. 2003)	304, 439	850-950	Atm
(Simms 2011)	P91,P92,304,347		Atm
(Tang et al. 2001)	304L	600	Atm
(Trindade et al. 2005)	347	750	Atm
(Mamede et al. 2016)	304L	750,950	Atm

A.4: References

Asteman, H. et al., 2000. Influence of Water Vapor and Flow Rate on the High-Temperature Oxidation of 304L ; Effect of Chromium Oxide Hydroxide Evaporation. *Oxidation of Metals*, 54(1/2), pp.11–26.

Asteman, H., Svensson, J.-E. & Johansson, L.-G., 2004. Effect of Water-Vapor-Induced Cr Vaporization on the Oxidation of Austenitic Stainless Steels at 700 and 900°C. *Journal of The Electrochemical Society*, 151(3), p.B141. Available at: http://link.aip.org/link/JESOAN/v151/i3/pB141/s1&Agg=doi.

Asteman, H., Svensson, J.-E. & Johansson, L.-G., 2002. Oxidation of 310 steel in H2O/O2 mixtures at 600°C : the effect of water-vapour-enhanced chromium evaporation. *Corrosion Science*, 44, pp.2635–2649.

Betova, I. et al., 2006. Composition, Structure, and Properties of Corrosion Layers on Ferritic and Austenitic Steels in Ultrasupercritical Water. *Journal of The Electrochemical Society*, 153(11), p.B464.

Bischoff, J. et al., 2013. Corrosion of ferritic-martensitic steels in steam and supercritical water. *Journal of Nuclear Materials*, 441(1–3), pp.604–611. Available at: http://dx.doi.org/10.1016/j.jnucmat.2012.09.037.

Botella, J., Merino, C. & Otero, E., 1998. A Comparison of the High-Temperature Oxidation of 17Cr-2Ni and 18Cr-8Ni Austenitic Stainless Steels at 973 K. *Oxidation of Metals*, 49(3–4), pp.297–324. Available at: http://link.springer.com/article/10.1023/A%3A1018830424480.

Brady, M.P. et al., 2012. Comparison of Short-Term Oxidation Behavior of Model and Commercial Chromia-Forming Ferritic Stainless Steels in Dry and Wet Air. *Oxidation of Metals*, 78(1–2), pp.1–16. Available at: http://www.springerlink.com/index/10.1007/s11085-012-9289-3 [Accessed July 30, 2012].

Brady, M.P. et al., 2011. Wet oxidation of stainless steels: New insights into hydrogen ingress.

Corrosion Science, 53(5), pp.1633–1638. Available at: http://linkinghub.elsevier.com/retrieve/pii/S0010938X11000941 [Accessed August 22, 2012].

Ennis, P.J. & Czyrska-Filemonowicz, a., 2003. Recent advances in creep-resistant steels for power plant applications. *Sadhana*, 28(3–4), pp.709–730. Available at: http://www.springerlink.com/index/10.1007/BF02706455.

Halvarsson, M. et al., 2006. Microstructural investigation of the breakdown of the protective oxide scale on a 304 steel in the presence of oxygen and water vapour at 600°C. *Corrosion Science*, 48(8), pp.2014–2035. Available at: http://linkinghub.elsevier.com/retrieve/pii/S0010938X05002647.

Hansson, a. N. et al., 2009. Microstructure Evolution During Steam Oxidation of a Nb Stabilized Austenitic Stainless Steel. *Oxidation of Metals*, 73(1–2), pp.289–309. Available at: http://www.springerlink.com/index/10.1007/s11085-009-9182-x.

Holcomb, G.R. et al., 2004. *Ultra supercritical steamside oxidation*, Albany. Available at: http://www.osti.gov/bridge/servlets/purl/859328-sO62ee/859328.pdf.

Huenert, D. & Kranzmann, a., 2011. Impact of oxyfuel atmospheres H2O/CO2/O2 and H2O/CO2 on the oxidation of ferritic–martensitic and austenitic steels. *Corrosion Science*, 53(6), pp.2306–2317. Available at: http://linkinghub.elsevier.com/retrieve/pii/S0010938X11001697 [Accessed November 14, 2011].

Huntz, A.M. et al., 2007. Oxidation of AISI 304 and AISI 439 stainless steels. *Materials Science and Engineering A*, 447, pp.266–276.

Jonsson, T. et al., 2009. An ESEM in situ investigation of the influence of H2O on iron oxidation at 500°C. *Corrosion Science*, 51(9), pp.1914–1924. Available at: http://linkinghub.elsevier.com/retrieve/pii/S0010938X0900211X [Accessed August 3, 2010].

Lepingle, V. et al., 2008. Steam oxidation resistance of new 12%Cr steels: Comparison with some other ferritic steels. *Corrosion Science*, 50(4), pp.1011–1019. Available at: http://linkinghub.elsevier.com/retrieve/pii/S0010938X07003368.

Li, D. et al., 2012. High-Temperature Oxidation Resistance of Austenitic Stainless Steel Cr18Ni11Cu3Al3MnNb. *Journal of Iron and Steel Research, International*, 19(5), pp.74–78. Available at: http://dx.doi.org/10.1016/S1006-706X(12)60103-4.

Liu, F. et al., 2008. Investigation of the Evolution of the Oxide Scale Formed on 310 Stainless Steel Oxidized at 600 °C in Oxygen with 40% Water Vapour Using FIB and TEM. *Oxidation of Metals*, 71(1–2), pp.77–105. Available at: http://www.springerlink.com/index/10.1007/s11085-008-9130-1.

Mamede, A.S. et al., 2016. Multitechnique characterisation of 304L surface states oxidised at high temperature in steam and air atmospheres. *Applied Surface Science*, 369, pp.510–519.

Naraparaju, R. et al., 2012. Dislocation engineering and its effect on the oxidation behaviour. *Materials at High Temperatures*, 29(2), pp.116–122. Available at: http://openurl.ingenta.com/content/xref?genre=article&issn=0960-3409&volume=29&issue=2&spage=116 [Accessed October 25, 2012].

Ostwald, C. & Grabke, H., 2004. Initial oxidation and chromium diffusion. I. Effects of surface working on 9–20% Cr steels. *Corrosion Science*, 46(5), pp.1113–1127. Available at: http://linkinghub.elsevier.com/retrieve/pii/S0010938X03002257.

Othman, N.K., Zhang, J. & Young, D.J., 2010. Temperature and water vapour effects on the cyclic oxidation behaviour of Fe-Cr alloys. *Corrosion Science*, (April). Available at: http://linkinghub.elsevier.com/retrieve/pii/S0010938X10002118.

Othman, N.K., Zhang, J. & Young, D.J., 2009. Water Vapour Effects on Fe–Cr Alloy Oxidation. *Oxidation of Metals*, 73(1–2), pp.337–352. Available at: http://www.springerlink.com/index/10.1007/s11085-009-9183-9.

Penttilä, S. et al., 2011. Estimation of kinetic parameters of the corrosion layer constituents on steels in supercritical water coolant conditions. *Corrosion Science*, 53(12), pp.4193–4203.

Penttilä, S. et al., 2015. Oxidation model for construction materials in supercritical water-Estimation of kinetic and transport parameters. *Corrosion Science*, 100, pp.36–46. Available at: http://dx.doi.org/10.1016/j.corsci.2015.06.033.

Peraldi, R. & Pint, B. a., 2004. Effect of Cr and Ni Contents on the Oxidation Behavior of Ferritic and Austenitic Model Alloys in Air with Water Vapor. *Oxidation of Metals*, 61(5/6), pp.463–483. Available at: http://www.springerlink.com/openurl.asp?id=doi:10.1023/B:OXID.0000032334.75463.da.

Pettersson, C. et al., 2010. High Temperature Oxidation of the Austenitic (35Fe27Cr31Ni) Alloy Sanicro 28 in O2 + H2O Environment. *Oxidation of Metals*, 74(1–2), pp.93–111. Available at: http://www.springerlink.com/index/10.1007/s11085-010-9199-1 [Accessed August 13, 2010].

Quadakkers, W.J., Żurek, J. & Hänsel, M., 2009. Effect of water vapor on high-temperature oxidation of FeCr alloys. *JOM*, 61(7), pp.44–50. Available at: http://apps.isiknowledge.com/full_record.do?product=UA&search_mode=Refine&qid=24&SID=X1G2B9anONIKmPinakl&page=4&doc=34&colname=WOS.

Rosser, J.C. et al., 2012. Steam oxidation of Super 304H and shot-peened Super 304H. *Materials at High Temperatures*, 29(2), pp.95–106. Available at: http://openurl.ingenta.com/content/xref?genre=article&issn=0960-3409&volume=29&issue=2&spage=95 [Accessed August 14, 2012].

Rother, G. et al., 2012. Small-angle neutron scattering study of the wet and dry high-temperature oxidation of alumina- and chromia-forming stainless steels. *Corrosion Science*, 58, pp.121–132. Available at: http://dx.doi.org/10.1016/j.corsci.2012.01.024.

Sabioni, A.C.S. et al., 2003. Comparative study of high temperature oxidation behaviour in AISI 304 and AISI 439 stainless steels. *Materials Research*, 6(2), pp.179–185. Available at: http://www.scielo.br/scielo.php?script=sci_arttext&pid=S1516-14392003000200012&lng=en&nrm=iso&tlng=en.

Sato, I., Momoda, M. & Namekawa, T., 2002. Oxidation behavior of modified SUS316 (PNC316) stainless steel under low oxygen partial pressure. *Journal of Nuclear Materials*, 304, pp.21–28.

Simms, H.G., 2011. *Oxidation Behaviour of Austenitic Stainless Steels At High Temperature in Supercritical Plant*. University of Birmingham.

Tang, J. et al., 2001. The microstructure of the base oxide on 304L steel. *Micron*, 32(8), pp.799–805. Available at: http://linkinghub.elsevier.com/retrieve/pii/S0968432800000871.

Trindade, V.B. et al., 2005. Oxidation mechanisms of Cr-containing steels and Ni-base alloys at high-temperatures -. Part I: The different role of alloy grain boundaries. *Materials and Corrosion*, 56(11), pp.785–790. Available at: http://doi.wiley.com/10.1002/maco.200503879.

Vangeli, P.S., Ivarsson, B. & Pettersson, R., 2013. Comparative behaviour of specialty austenitic stainless steels in high temperature environments. *Oxidation of Metals*, 80(1–2), pp.37–47.

Wang, S.G. et al., 2013. The high-temperature oxidation of bulk nanocrystalline 304 stainless steel in air. *Corrosion Science*, 72, pp.64–72. Available at: http://linkinghub.elsevier.com/retrieve/pii/S0010938X13000875.

Zacchetti, N. et al., 2009. Early stage oxidation of AISI 304 stainless steel: role of temperature and oxygen pressure. *Materials at High Temperatures*, 26(1), pp.31–38. Available at: http://openurl.ingenta.com/content/xref?genre=article&issn=0960-3409&volume=26&issue=1&spage=31 [Accessed November 14, 2011].

Zengwu, Y. et al., 2011. Effect of Shot Peening on the Oxidation Resistance of TP304H and HR3C Steels in Water Vapor. *Oxidation of Metals*, 77(1–2), pp.17–26. Available at: http://www.springerlink.com/index/10.1007/s11085-011-9270-6 [Accessed August 22, 2012].

Zhu, Z. et al., 2016. Temperature Dependence of Oxidation Behaviour of a Ferritic–Martensitic Steel in Supercritical Water at 600–700 °C. *Oxidation of Metals*, 86(5–6), pp.483–496. Available at: http://link.springer.com/10.1007/s11085-016-9647-7.

Zurek, J. & Quadakkers, W.J., 2015. Effect of Surface Condition on Steam Oxidation of Martensitic Steels and Nickel-Based Alloys. *CORROSION*, 71(11), pp.1342–1359. Available at: http://corrosionjournal.org/doi/10.5006/1859.

Appendix B: Automated Measuring of Oxide Thickness

This automated method of measuring the thickness of oxide layers is generally applicable to any image, so is suitable for use with TEM, SEM and optical images. The following software was used:

- GIMP for image manipulation
- ImageJ 2 for taking measurements

B.1 Highlighting an Oxide Layer

1. Open the image in GIMP and change the image mode to Greyscale. This will reduce the memory required for image editing and simplify colour selection.
2. Create a new blank layer over the top of the image and use the Pencil tool to draw *solid* lines around the base metal in **Black**. Use the fill tool to colour in this area.
3. Highlight the layer to be measured in **Grey** using the same method.
4. Highlight the area above the layer in **White**.
5. Optional: Put a scale bar in the base metal region for future reference.
6. Export this layer as a PNG file. It should be between 10-500Kb in size, even if a large area is highlighted.

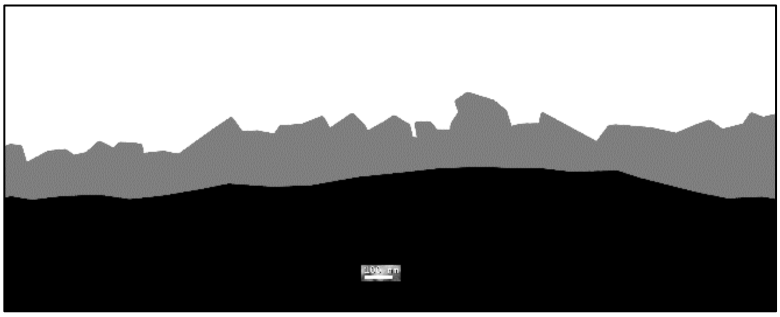

Figure 1- Example PNG image with scale bar

B.2 Measuring the Oxide Layer

1. Open the PNG file in **ImageJ 2**.
2. Calibrate the image scale.
3. Open the Javascript Script Editing tool by going to Plugins → New → Javascript
4. Paste in the Oxide Thickness Measurement script text into this window. This is normally stored in a .JS or .txt file. The script is included below with comments.
5. Go to Macro → Run Macro to activate the script.
6. The script will run and output the results of its measurements into the ImageJ results window.
    - The results show the thickness of the oxide layer measured from the top of the oxide layer to the closest point of the base metal.
    - A measurement is taken every 25 pixels across the image from Left to Right. This can be adjusted by changing the “lineSpacing” variable in the script text.
7. Save these results as a comma separated value file. This can be opened in Excel or any other data analysis tool.

B.3 Oxide Thickness Measurement script

```
importClass(Packages.ij.IJ);
importClass(Packages.ij.plugin.frame.RoiManager);
importClass(Packages.ij.gui.GenericDialog);
importClass(Packages.ij.ImagePlus);
importClass(Packages.ij.measure.ResultsTable);
importClass(Packages.ij.measure.Calibration);
importClass(Packages.ij.gui.ProfilePlot);
importClass(Packages.ij.gui.Roi);
importClass(Packages.ij.gui.Line);

var source = IJ.getImage();
calibrationObject = source.getCalibration();
// For drawing lines
var x1 = 0;
var y1 = 0;
var x2 = 0;
var y2 = 0;
var imageWidth = source.getWidth();
var imageHeight = source.getHeight();

// Go down from the image top until there is a change in colour
// Set this point as the centre of a circle.
// Expand the circle by 1px.
// Look at each point of the circle's colour value
// If the colour becomes the designated 'base' value then make a line between start
and the new point
// Measure the line length
// Continue to the next X-spacing and repeat until no X-spacings left.

// Above layer = white (255);
// Base layer = black (0);

// Line spacing is the amount moved along the X axis to properly space the sequential
lines.
// The value in Units is entered by the user, so this must be changed to pixel
values.
var lineSpacing = 25;
// Calculate the number of lines to make (i)
var iMax = (imageWidth / lineSpacing);

   //Start plotting and store the x,y coordinates of the circle centres.
var circleCoords = new Array();
for(var i=0; i<iMax ;i++){
   // Calculate the line coordinates
   x1 = i * lineSpacing;
   y1 = 0;
   x2 = x1;
   y2 = imageHeight;
   var lineID = IJ.makeLine(x1, y1, x2, y2);
   // Build a profile to be examined
   var profileObject = new ProfilePlot(source);
   var profile = profileObject.getProfile();
   var startCol = profile[0];
   // Find the value when the colour changes from 'above' colour
   // If there was no layer there at all then make y=0;
   var yCoord=1;
   circleCoords[i] = [x1, 0];
```

```
  for(yCoord; yCoord < profile.length; yCoord++){
    if(profile[yCoord]!=startCol){
      if(profile[yCoord] == 0){
        circleCoords[i][1] = 0;
        break;
      } else {
      circleCoords[i][1] = yCoord;
      break;
      }
    }
  }
// If no colour change then the y-cord will be 0. Delete these later once the array
has been built.
  }
// Delete y = 0 values
for(var i=0; i<circleCoords.length; i++){
  if(circleCoords[i][1] == 0){
    circleCoords.splice(i, 1)
    i = i - 1; // since the array has shrunk
  }
}
resultsToDisplay = new ResultsTable();
resultsToDisplay.incrementCounter();
resultsToDisplay.addValue("Thickness (pixels)", 0);
resultsToDisplay.addValue("Thickness (Chosen units)", 1);
// We now have the start points of our circles in the form of  circleCoords[i][x,y].
For each one start drawing a circle outwards until we meet the 'base' colour.
for(var i=0;i<circleCoords.length; i++){
  var centreX = circleCoords[i][0];
  var centreY = circleCoords[i][1];
  for(var radius=1; radius < imageWidth; radius++){
    // check pixels for base colour in larger radius circles
    var increment = 0.1; // size of angle to rotate each step
    var radianMax = (2 * Math.PI);
    var found = false;
    for(var angle=0; angle < radianMax; angle += increment){
      var checkX = centreX + (radius * Math.cos(angle))
      var checkY = centreY + (radius * Math.sin(angle))
      var pixelValueArray = source.getPixel(checkX, checkY);
      // Convert to Grayscale (assuming RGB for now)
      // The X and Y values must be within the image bounds.
      if(checkX>=imageWidth || checkY>=imageHeight || checkX<0 || heckY<0){
        continue; // skip this one if not on canvas.
      }

      var   pixelValue   =   (pixelValueArray[0]   +   pixelValueArray[1]   +
pixelValueArray[2]) / 3
      if(pixelValue == 0){
        found = true;
        /* Draw the line */
        var lineID = IJ.makeLine(centreX, centreY, checkX, checkY);
        var dx = Math.abs(centreX - checkX);
        var dy = Math.abs(centreY - checkY);
        var lineLength = Math.sqrt((dx*dx)+(dy*dy))
        resultsToDisplay.incrementCounter();
        resultsToDisplay.addValue(0, lineLength);
        var unitLineLength = calibrationObject.getX(lineLength)
        resultsToDisplay.addValue(1, unitLineLength);
        break;
```

```
         }
      }
      if(found == true){
         break;
      }
   }
   resultsToDisplay.show("Results");
}
```

Appendix C Grain Boundary Maps

The following grain maps were created by hand using composite TEM brightfield images as described in section 3.13. The grain maps presented here are at a significantly reduced resolution in order to be printed on a single A4 page. As such, there are fine details that may not appear in the images that were identified in the original format. An attempt to create a grain map of as-received SP1 failed because the grains were too small to create a 2D map by eye.

C.1 DMV304HCu shot peened once and exposed in vacuum to 700°C for 1000hrs

Oxide layer is at top of image and has been removed for grain analysis

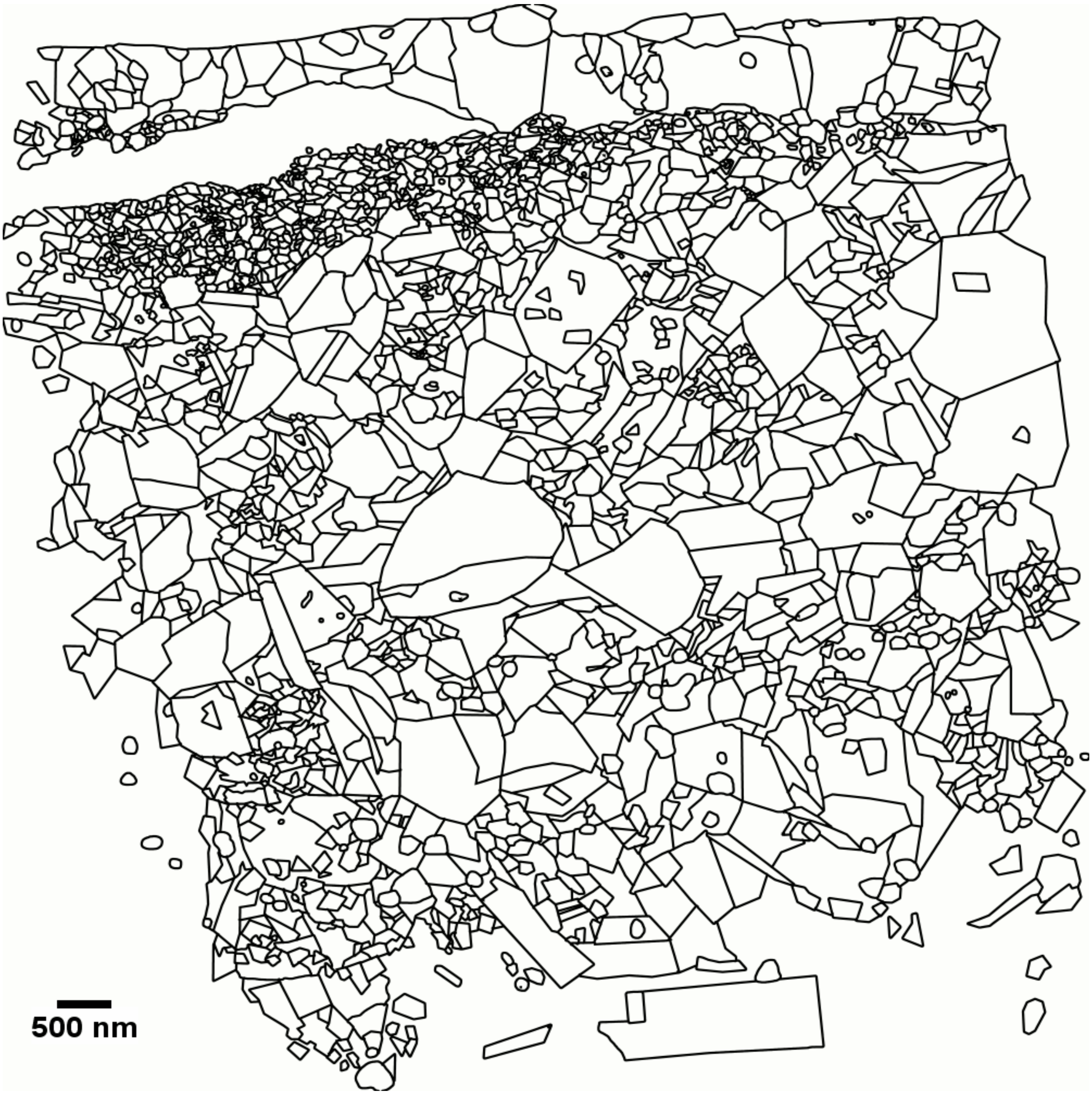

C.1.1 Oxide Layer of C.1

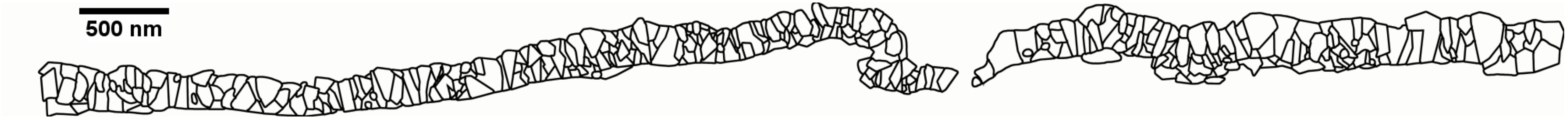

Base alloy at bottom of image

C.2 DMV304HCu shot peened once and exposed to steam at atmospheric pressure and 700°C for 1000hrs

Oxide is at top of image and is included here. Grain size analysis excluded the oxide layer from the alloy

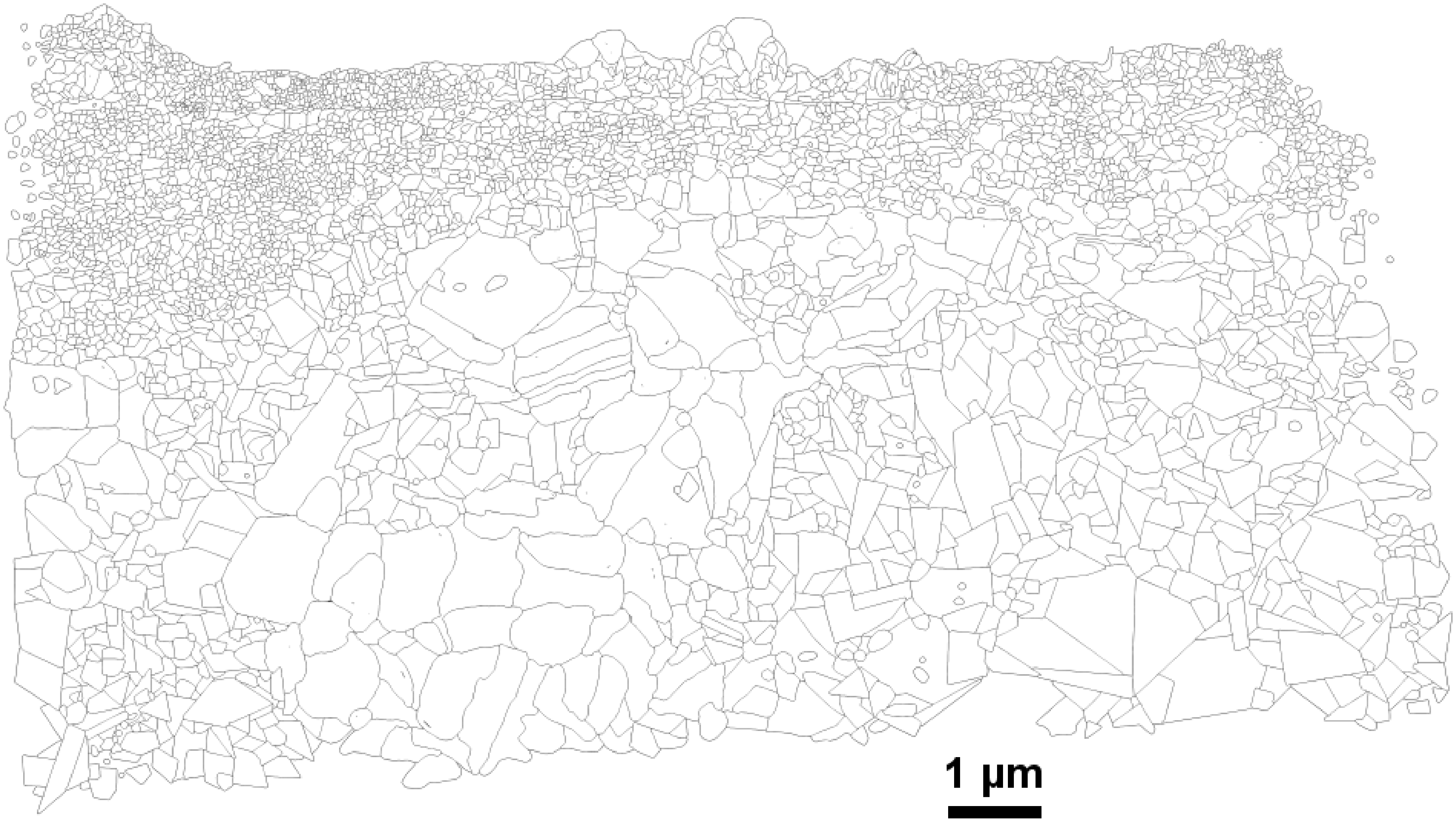

C.2.1 Oxide Layer of C.2

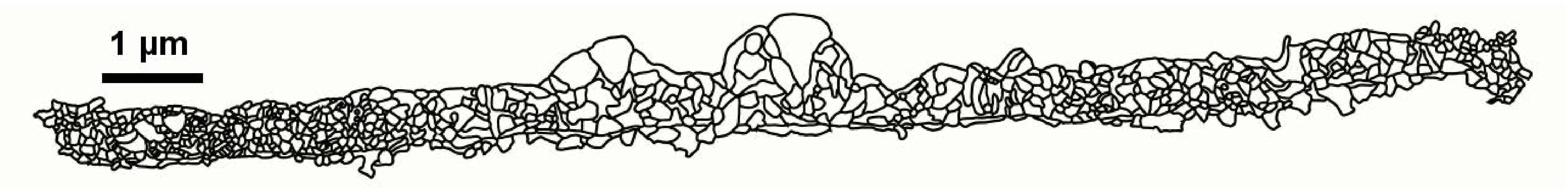

Base alloy at bottom of image

Appendix D: Oxygen Activity Calculations for Cr-Mn-O Phase Diagrams

Thermocalc was used to create Cr-Mn-O phase diagrams in air and a theoretical power plant steam. The steam conditions used are given in table D.1. Thermocalc allows the activity (a) of a gas to be set when calculating phase equilibrium without forcing the resultant phase/s to contain a set mass of oxygen or considering non-reactant gas components. The activity of a component of an ideal gas is found using (1).

$$a_i = \frac{p_i}{p} = X_i \qquad (1)$$

a_i = activity of component i
p_i = partial pressure of component i
p = overall gas pressure
X_i = molar fraction of component i

It is common practice when using thermocalc to use the natural log of activity, ln(a), to improve code readability, so this value is also provided in table D.1.

Table D.1 – Atmosphere characteristics

	Air	Power Plant Steam
Gas Pressure	1×10^5 Pa / 1 Bar	24×10^6 Pa / 26 Bar
Oxygen Content	20.95 %	10 ppb
Oxygen Partial Pressure	2.095×10^4 Pa	2.4×10^{-2} Pa
Activity (O_2)	0.2095	10×10^{-9}
Activity (O)	0.419	2×10^{-8}
Ln(a_O)	-0.87	-17.7